LUMINESCENT PROBES FOR ORGANELLE TARGETED IMAGING, PHOTODYNAMIC THERAPY AND THERANOSTIC APPLICATIONS

THESIS SUBMITTED TO **AcSIR** FOR THE AWARD OF THE DEGREE OF
DOCTOR OF PHILOSOPHY IN CHEMISTRY
UNDER THE FACULTY OF SCIENCE

By
SUDHEESH K. V.
Enrollment No: 10CC12J39006

Under the Supervision of
Prof. A. AJAYAGHOSH

PHOTOSCIENCES AND PHOTONICS SECTION
CSIR-NATIONAL INSTITUTE FOR INTERDISCIPLINARY
SCIENCE AND TECHNOLOGY (CSIR-NIIST)
THIRUVANANTHAPURAM - 695019, KERALA

June, 2018

Dedicated to

Achan, Amma, Teachers and Friends

DECLARATION

I hereby declare that the matter embodied in the thesis entitled: "**Luminescent Probes for Organelle Targeted Imaging, Photodynamic Therapy and Theranostic Applications**" is the result of the investigations carried out by me at the Photosciences and Photonics Section, Chemical Sciences and Technology Division, CSIR-National Institute for Interdisciplinary Science and Technology (CSIR-NIIST), Thiruvananthapuram, under the supervision of Prof. A. Ajayaghosh and the same has not been submitted elsewhere for any other degree.

In keeping with the general practice of reporting scientific observations, due acknowledgement has been made wherever the work described is based on the findings of other investigators.

Sudheesh K. V.

Thiruvananthapuram
June 12, 2018

National Institute for Interdisciplinary Science and Technology (NIIST)
(Formerly Regional Research Laboratory)
Council of Scientific & Industrial Research (CSIR)
Industrial Estate P.O., Trivandrum - 695 019
Kerala, INDIA

Tel: 91-471-2490324
Fax: +91-471-2491 712
Email: ajayaghosh62@gmail.com
ajayaghosh@niist.res.in

Dr. A. Ajayaghosh FASc., FNASc., FNA., FTWAS
Director

June 12, 2018

CERTIFICATE

This is to certify that the work incorporated in this Ph. D. thesis entitled "**Luminescent Probes for Organelle Targeted Imaging, Photodynamic Therapy and Theranostic Applications**" submitted by **Mr. Sudheesh K. V.** to the Academy of Scientific and Innovative Research (AcSIR) in fulfillment of the requirements for the award of the Degree of Doctor of Philosophy in Chemical Sciences embodies original research work carried out by him under my supervision. I further certify that this work has not been submitted to any other University or Institution in part or full for the award of any degree or diploma. Research material obtained from other sources has been duly acknowledged in the thesis. Any text, illustration, table etc., used in the thesis from other sources, have been duly cited and acknowledged.

Prof. A. Ajayaghosh

(Thesis Supervisor)

ACKNOWLEDGEMENTS

It is with great pleasure that I extend my deep sense of gratitude to Prof. A. Ajayaghosh, my thesis supervisor, for suggesting the research problem, for his valuable guidance, support, encouragement and scientific freedom, leading to the successful completion of this work. I also want to thank him for the expression of faith in my abilities.

I would like to express my gratitude to Prof. M. V. George for his inspiration.

I thank Dr. Suresh Das (former Director) and Dr. Gangan Pratap (former acting Director) of CSIR-NIIST, Thiruvananthapuram, for providing the necessary facilities for carrying out this work.

My sincere thanks are also due to:

- *Dr. Mangalam S. Nair and Dr. R. Luxmi Varma, former and present AcSIR co-ordinators.*
- *Dr. K. R. Gopidas, for his scientific discussions and valuable suggestions.*
- *Dr. Narayanan Unni, Dr. J. D. Sudha, Dr. Joshy Joseph, Dr. K. Yoosaf, Dr. C. Vijayakumar, Dr. B. Deb and Dr. V. Karunakaran, scientists of the Photosciences and Photonics Section, Chemical Sciences and Technology Division (CSTD), for their help and support.*
- *Dr. D. Ramaiah. Dr. K. V. Radhaakrishnan, and Dr. Madhavan Nampoothiri, the Doctoral Advisory Committee (DAC) members and the whole AcSIR faculty for the successful completion of course work.*
- *Dr. Animesh Samantha and Dr. V. K. Praveen for their valuable suggestions, help, support and care for manuscript and thesis preparation.*
- *Dr. K. K. Maiti and Dr. Manu Joseph for fluorescence imaging studies.*
- *Dr. R. S. Jayasree and Mr. Jayaram Prasad of the Sree Chitra Tirunal Institute for Medical Sciences and Technology, for cell imaging and photodynamic therapy studies.*
- *Dr. C. H. Suresh, CSTD, CSIR-NIIST, for Density Functional Theory calculations.*

- *Dr. Jayamurthy and Dr. Vandana for helping in the initial stages of imaging work.*
- *Mr. Sreejith and Dr. Sumesh Babu for transient absorption studies.*
- *Mr. Ashish Aravind and Mr. Yoosaf for cyclic voltammetry studies.*
- *Dr. Bejoymohondas K. S. for his help in the synthesis of iridium complexes.*
- *Dr. Krishnan Kartha and Dr. Rakesh K Mishra for scientific discussions.*
- *Mr. Satyajith and Mr. Gourab for life time studies.*
- *All former and present group members for their help, guidance and support.*
- *All former and present members of Photosciences and Photonics Section for their cooperation and help.*
- *Mr. Robert Philip and Mr. Kiran J. S. for their general help and support.*
- *Mr. Kiran Mohan for TEM analysis.*
- *Ms. Saumini, Mr. Adarsh, Mr. Arun, Mr. Sharan and Mr. Gokul for NMR and Ms. Viji for mass spectral analyses.*
- *Dr. K. V. Radhakrishnan and Nanma Kudumbasree for the successful completion of CSIR-800 project.*
- *All my teachers for leading the way and their encouragement at different stages of my academic career.*
- *Council of Scientific and Industrial Research (CSIR) and Department of Science and Technology (DST), Government of India for financial assistance.*

A special word of thanks to my seniors, Mr. Sandeep A, Dr. Adarsh N, Dr. Hari Shankar, Dr. Sandeep Cherumukkil, Dr. Jatish Kumar, Dr. Rahul Dev Mukhopadhyay for helping me in all ways at the early stages of my research and their support and suggestions in the research activities.

I am profoundly thankful to the generous help, support, discussions as well as the care rendered by my colleagues, Dr. Divya Susan Philips and Dr. Samrat Ghosh throughout my research in its length and breadth.

I am deeply and forever indebted to my family for their love, care and their blessings. Finally, I would like to thank all my dear friends and teachers from my school and college, my room-mates and each and every person who has made my life bright and *cheerful. And above all, I place my thanks to God Almighty for every blessing that has been given to me.*

Sudheesh K. V.

CONTENTS

Chapter 2 pH-Controlled Nanoparticles Formation and Tracking of Lysosomal Zinc Ions in Cancer Cells by Fluorescent Carbazole–Bipyridine Conjugates

Chapter 4 A Cyclometalated Ir(III) Complex as Lysosome Targeted Photodynamic Therapeutic Agent for Integrated Imaging and Therapy in Cancer Cells

List of Abbreviations

1PM	One-photon microscopy
2P	Two-photon
2PA	Two-photon absorption
3P	Three-photon
3T3 L1	Mouse embryo cell line
2P PDT	Two-photon photodynamic therapy
A549 cells	Adenocarcinomic human alveolar basal epithelial cells
ABDA	9,10-Anthracenediyl-bis-(methylene)dimalonic acid
ACN	Acetonitrile
ACQ	Aggregation caused quenching
ADP	Adenosine diphosphate
AFM	Atomic force microscopy
AIBN	Azobisisobutyronitrile
AIEE	Aggregation induced enhanced emission
AO	Acridine orange
ATP	Adenosine triphosphate
BF	Bright field
Bodipy	Boron-dipyrromethane
bpy	2,2'-bipyridine
BSA	Bovine serum albumin
C6 glioma	Brain tumor cell lines of Rattus norvegicus

c.a.	Calculated approximately
CA	Carbonic anhydrase
$CDCl_3$	Deuterated chloroform
CD_3CN	Deuterated acetonitrile
CO_2	Carbon dioxide
CV	Cyclic voltametry
CW	Continuous wave
Cys	Cysteine
D-A-D	Donor-acceptor-donor
DAPI	4′,6-diamidino-2-phenylindole
DCM	Dichloromethane
DCFDA	2',7'-Dichlorodihydrofluorescein diacetate acetyl ester
DFT	Density functional theory
D_h	Hydrodynamic diameter
DLS	Dynamic light scattering
DMA	9,10-Dimethyl anthracene
DMEM	Dulbecco’s modified eagle’s medium
DMF	Dimethylformamide
DMSO	Dimethyl sulfoxide
DNA	Deoxyribo nucleic acid
DPA	Dipicolylamine
DPBF	1,3-Diphenylbenzo[*c*]furan
DPEN	*N*,*N*-di-(2-picolyl)ethylenediamine
EDTA	Ethylenediaminetetraacetic acid
eq.	Equivalent

ESIPT	Excited state intramolecular proton transfer
ESR	Electron spin resonance
et al.	*Et allii/alia*
EtOAc	Ethyl acetate
FBS	Fetal bovine serum
FACS	Fluorescence assisted cell sorting
FITC	Fluorescein isothiocyanate
FRET	Forster resonance energy transfer
GM	Goppert Mayer
GMP	Guanosine monophosphate
h	Hour
hCA	Human carbonic anhydrase
Hcy	Homocysteine
HeLa	Human cervical cancer cell line
HEPES	4-(2-hydroxyethyl)-1-piperazineethanesulfonic acid
HOMO	Highest occupied molecular orbital
HRMS	High resolution mass spectrometry
HSA	Human serum albumin
Hz	Hertz
ICT	Intramolecular charge transfer
ILCT	Interligand charge transfer
IR	Infrared
ISC	Inter system crossing
K_d	Dissociation constant
LMP	Lysosomal membrane permeabilization

LTR	Lyso Tracker Red
LUMO	Lowest unoccupied molecular orbital
LyTMC	Lysosome-targeting metal complex
M	Molar
M^+	Molecular ion peak
MCF-7	Breast cancer cell line
MDA-MB-231	Breast cancer cell line
MeOH	Methanol
MES	2-(N-morpholino)ethanesulfonic acid
min	Minutes
MiTMC	Mitochondria targeting metal complexes
mL	Millilitre
MLCT	Metal to ligand charge transfer
mmol	Millimole
MNO	2-Mercaptopyridine N-oxide
MRI	Magnetic resonance imaging
MTT	(3-(4,5-Dimethylthiazol-2-yl)-2,5-Diphenyltetrazolium Bromide
NBS	*N*-Bromosuccinimide
NIR	Near-infrared
nm	Nano meter
nM	Nano molar
NMR	Nuclear magnetic resonance
OPM	One photon micoscopy
PBI	Perylene bisimide
PBS	Phosphate buffered saline

PDT	Photodynamic therapy
PEG	Poly(ethylene glycol)
PET	Photoinduced electron transfer
pH	Hydrogen ion concentration at logarithmic scale
phen	Phenanthroline
pH_i	Intracellular pH
PI	Propidium iodide
pK_a	Acid dissociation constant at logarithmic scale
PLIM	Phosphorescence lifetime imaging
pM	Picomolar
ppm	Parts per million
ppy	2- Phenylpyridyl
PS	Photosensitizer
QD	Quantum dot
R	Mander’s overlap coefficients
r	Pearson’s correlation coefficient
RNA	Ribonucleic acid
RNS	Reactive nitrogen species
ROS	Reactive oxygen species
rpm	Rotation per minute
rt	Room temperature
s	Seconds
SD	Standard deviation
SOC	Spin-orbit coupling
T	Temperature

TBET	Through bond energy transfer
TEM	Transmission electron microscopy
THF	Tetrahydrofuran
TICT	Twisted intramolecular charge transfer
TPA	Two-photon absorption
TPEF	Two-photon excited fluorescence
TPEN	(*N,N,N′,N′*-tetrakis(2-pyridinylmethyl)-1,2-ethanediamine
TPM	Two-photon microscopy
TPP	Triphenylphosphonium
UV-Vis	Ultraviolet-visible
δ	Chemical shift
^{o}C	Degree Celsius
ϕ_F	Fluorescence quantum yield
ϕ_P	Phosphorescence quantum yield
ϕ_T	Triplet quantum yield
ϕ_Δ	Singlet oxygen quantum yield
ε	Molar extinction coefficient
λ_{abs}	Wavelength of absorption
λ_{ex}	Wavelength of excitation
λ_{em}	Wavelength of emission
µ	Micro
Z	Atomic number

SYNOPSIS

Molecules which emit light upon photoexcitation are useful as luminescent probes for bioimaging whereas photosensitizers that generate singlet oxygen are useful for photodynamic therapy (PDT). However, design of biocompatable, photochemicaly stable and long wavelength emitting probes is a challenge. Similarly, molecules with high singlet oxygen generation efficiency are required for PDT applications. Even though there are several reports on individual luminescent probes and PDT agents, molecules, which are useful for both imaging and PDT are rare. Therefore, design of luminescent probes for simultaneous imaging and therapy in cancer cells are essential for diagnostic and therapeutic applications. Inspired by the recent progress in the design of synthetic molecular probes for organelle targeted imaging and therapeutic applications, we explored a few fluorescent organic molecules and cyclometalated Ir(III) complexes having bipyridyl moieties for bioimaging for PDT applications. The work described in the present thesis is organized into four chapters. In the first chapter, an introduction and recent developments in the area of molecular probes for bioimaging and PDT applications are described. Especially, the bipyridine based ligands are well explored in the literature for the preparation of Zn^{2+} sensors and metal complexes. The mechanism of bipyridine based probes for organelle targeted Zn^{2+} imaging by showcasing various examples are described followed by the different types of photosensitizers used for PDT applications. In the present context, cyclometalated Ir(III) based photosentizers and their importance in imaging and PDT applications were discussed.

In the second chapter, synthesis and studies of lysosome targeting carbazole-bipyridine conjugates, **CBL1-3** and **CBG**, where bipyridine acts as the receptor for Zn^{2+} and morpoline acts as the lysosome targeting agent are described. Zn^{2+} is a biologically relevant cation and is involved in various cellular processes including immune function, signal transduction, neurotransmission, etc. The **CBL** probes form nano-aggregates in aqueous medium and these nano-aggregates were successfully used for monitoring the variations in pH and for sensing of Zn^{2+}. Detailed studies revealed that **CBL2** is the best candidate for imaging and Zn^{2+} sensing. Fluorescent imaging experiments on cancer cells revealed that the **CBL2** nanoprobe is capable of localizing at lysosomes and facilitates the detection of endogenous Zn^{2+} and pH variations. Furthermore, the lysosomal Zn^{2+} variation with external stimuli induced programmed cell death was visualized using the nanoprobe.

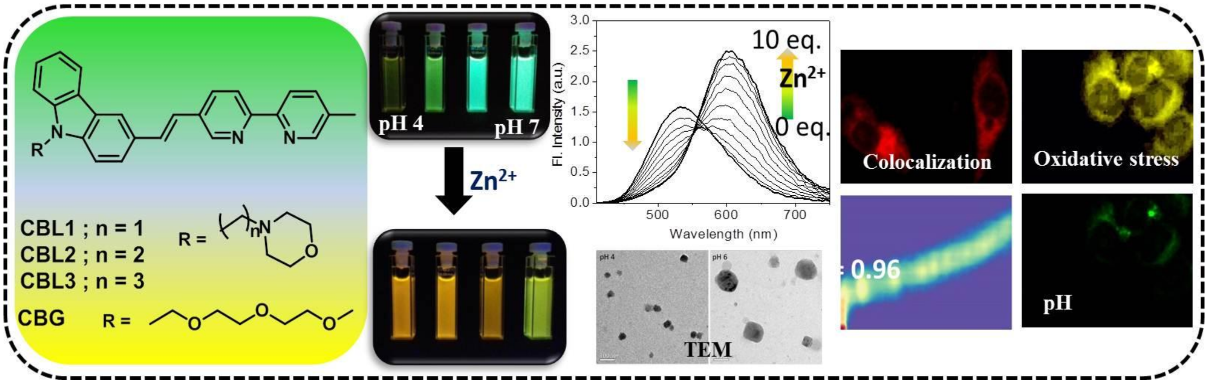

In Chapter 3, the synthesis and studies of cyclometalated Ir(III) complexes, **IrL1** and **IrL2** are described. Since **CBL2** (described in Chapter 2) was found to localize in lysosome, we used it as the ancillary ligand to prepare **IrL1**, to target lysosome which is identified as one of the most effective organelles for apoptotic cell death during PDT. We found that **IrL1** serves as a good photosentizer for lysosomal targeting PDT applications. For a comparative study, we used a highly conjugated ancillary ligand and synthesized another complex **IrL2**. The detailed tansient absorption studies and singlet oxygen quantum yield measurement showed better efficiency for **IrL2**. The HOMO – LUMO and triplet energy calculation revealed that the energy transfer from the probe to ground state oxygen is highly favaourable in the case of **IrL2**. The cellular studies were also conducted with the same probe. The apoptotic experiments were conducted with MD-MBA-231 cell lines and the mechanism of the cell death was analyzed by flow cytometry and caspace-3/7 detection agent. However, the luminescence quantum yield was found to be low which limited its application as a theranostic probe.

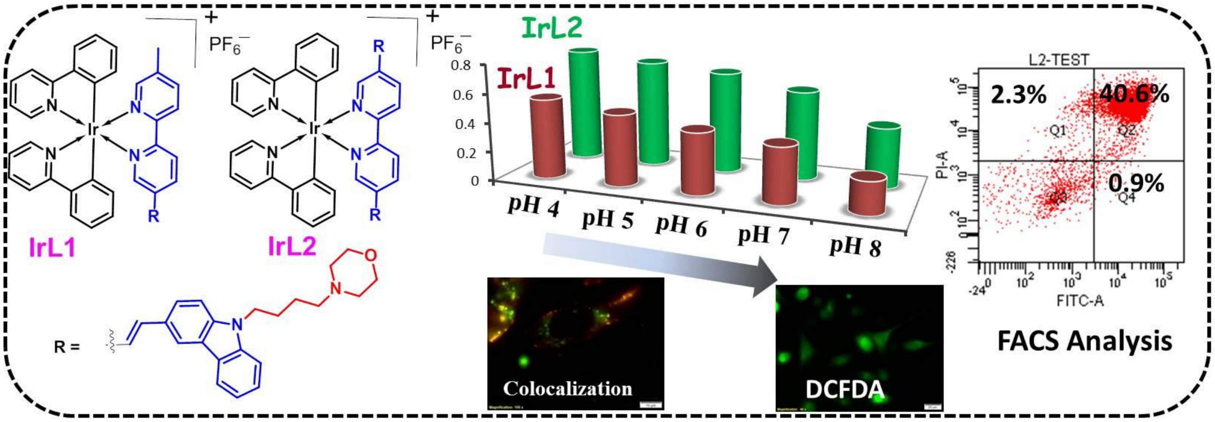

In Chapter 4 we designed and synthezied a cyclometalated Ir(III) complex for organelle targeted theranostic application. The synthesized photosentitizer, **Ir-Bp-Ly** showed good luminescence (11%) and singlet oxygen quantum yields (79% at pH 4) under aqueous condition. It showed strong energy transfer to triplet oxygen leading to efficient generation of singlet oxygen. The singlet oxygen quantum yield was unaffected by changes in pH and hence was successfully used for imaging applications. The complex was found to localize well in lysosomes which was confirmed by co-localization experiments. The detailed theranostic investigations were done in the Rat brain tumor C6 glioma cells. The cell death mechanism followed the apoptotic pathway which was studied through flow cytometry analysis. Thus, the developed Ir(III) complex was identified as an efficient photosensitizer with high singlet oxygen quantum yield that can localize in lysosomes and induce cell death via apoptosis which is highly favorable for therapeutic applications.

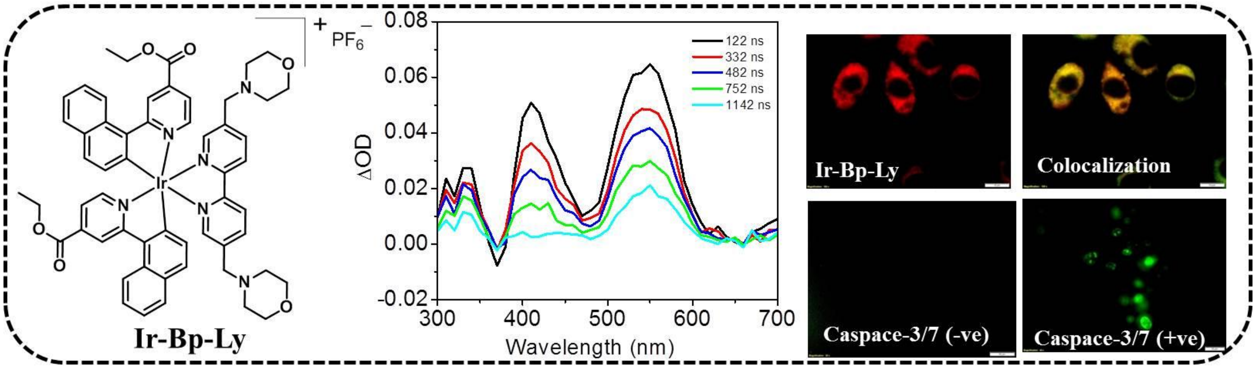

In summary, the present thesis describes detailed investigation on organic fluorophores namely **CBL1-3** and **CBG**, for lysosomal pH and Zn^{2+} imaging and cyclometalated Ir(III) complexes namely **IrL1**, **IrL2** and **Ir-Bp-Ly** for photodynamic therapeutic and theranostic applications. These probes were designed to target the subcellular organelle, lysosome which serves as the main site for macromolecule degradation and apoptosis. The incorporation of morpholine moiety to the probe helps to accumulate in lysosome through lysosomotropism. The higher co-localization values, sensing properties and efficient singlet oxygen generation are the advantages of the described probes. The insights gained from these studies are expected to help the development of new and efficient theranostic probes for diagnostic and therapeutic applications.

References

1. pH-Controlled Nanoparticles Formation and Tracking of Lysosomal Zinc Ions in Cancer Cells by Fluorescent Carbazole–Bipyridine Conjugates. **Sudheesh, K. V**.; Joseph, M. M.; Philips, D. S.; Samanta, A.; Maiti, K. K.; Ajayaghosh, A. *ChemistrySelect* **2018**, *3*, 2416 – 2422
2. A Cyclometalated Ir(III) Complex as Lysosome Targeted Photodynamic Therapeutic Agent for Integrated Imaging and Therapy in Cancer Cells.

Sudheesh, K. V.; Jayaram, P. S.; Samanta, A.; Bejoymohandas, K. S.; Jayasree, R. S.; Ajayaghosh, A. *Chem. -A. Eur. J*. **2018** (Accepted article. DOI: 10.1002/chem.201801918).

3. Lysosome Targeting Cyclometalated Ir(III) Complexes with Extended π-Conjugation as Potential Sensitizer for Photodynamic Therapeutic Applications. **Sudheesh, K. V**.; Jayaram, P. S.; Samanta, A.; Jayasree, R. S.; Ajayaghosh, A. (under preparation)

Chapter 1

Luminescent Probes for Organelle Targeted Imaging, Photodynamic Therapy and Theranostic Applications: An Overview

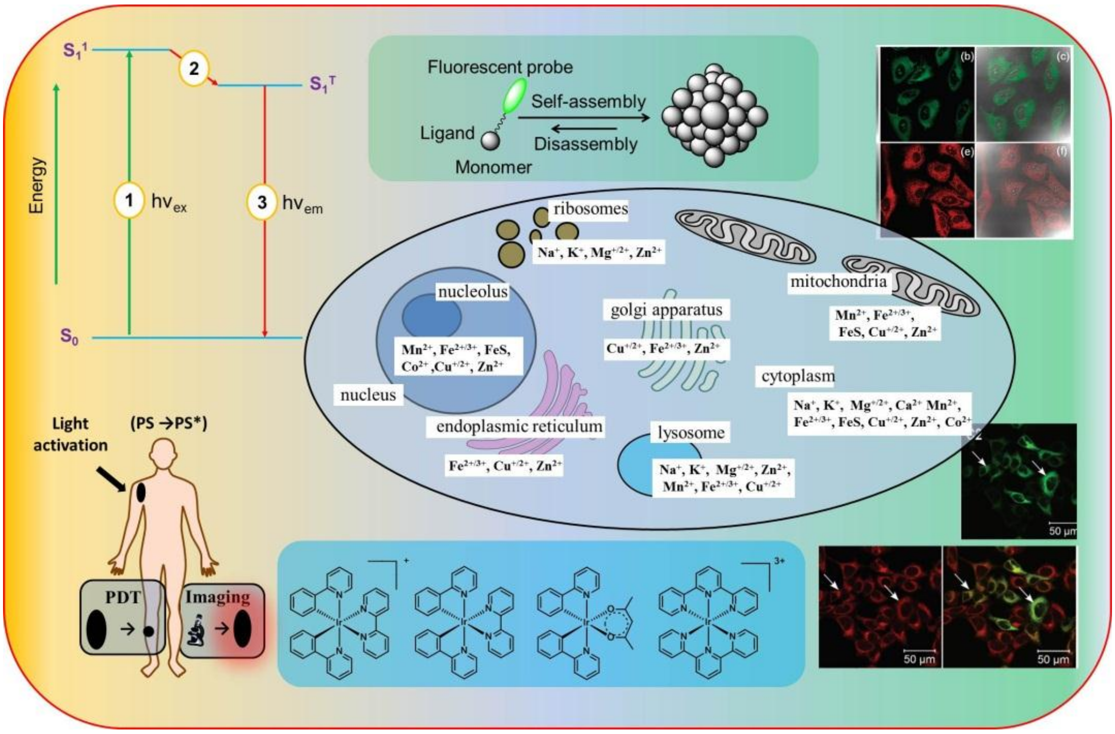

1.1. Abstract

Fluorescent probes for simultaneous detection of organelle specific multiple analytes in cancer cells are essential for diagnostic applications. Among various analytes present in the biological systems, Zn^{2+} is involved in many biological processes including regulation of immune function, signal transduction, neurotransmission, etc. The detection of Zn^{2+} in specific subcellular organelle helps to evaluate subcellular functions and other related diseases. Therefore, detection of Zn^{2+} in specific subcellular organelle is of great significance. Therapy is the attempted remediation of a health problem usually following diagnosis. However, in photodynamic therapeutic applications photosensitizers with essential

properties like high singlet oxygen quantum yield are required. Recently, Ir(III) based metal complexes are well explored in this area because of its exceptional photophysical properties and good cell compatibility. This introductory chapter will first give an overview of the different fluorescence based sensors and organelle targeted imaging of Zn^{2+}*. This will be followed by different types of photosensitizers and recent advances in the use of Ir(III) complexes in the biological systems. The aim and the outline of the thesis are then discussed.*

1.2. Introduction

Bioimaging aims to detect and monitor various biomolecular processes in cells, tissues, and living organisms in clinical studies. Contrast agents make molecular processes visible, quantifiable, and traceable over time. Various contrast agents are used to assess specific molecular targets in different imaging modalities such as positron emission tomography, magnetic resonance imaging, fluorescence imaging, etc.[1,2]

Among various analytical techniques, optical assay based on fluorescence has been extensively studied owing to its advantage including high sensitivity, fast response time, visual signal transduction, real-time *in situ* responses and low cost. Numerous signaling mechanisms have been developed and widely used for the optical detection of different species. These include photoinduced electron transfer (PET), fluorescence resonance energy transfer (FRET), intramolecular charge transfer (ICT), twisted intramolecular charge transfer (TICT), excited state intramolecular proton transfer (ESIPT), excimer/exciplex formation, aggregation induced enhanced emission (AIEE) and many others.[3-5]

Apart from molecular sensors, molecular self-assembly has also been widely used for analyte sensing and imaging.[6-8] Quantitative determination of specific analytes is essential for a variety of applications ranging from diagnosis to therapy. Among various metal ions present, Zn^{2+} plays essential roles in various physiological processes in living systems, and the investigations on Zn^{2+} related physiology and pathology are major research interest.[9] 2,2'-Bipyridine, dipicolylamine and terpyridine, are the key receptors for Zn^{2+}. Among them, bipyridine based probes have got much attention and have several Zn^{2+} imaging probes including multi-photon active probes were developed.[10] The subcellular localization of the newly developed probes is helpful for deeper understanding of biological processes.[11]

Therapy is the attempted remediation of a health problem usually following diagnosis. Among various therapeutic techniques, photodynamic therapy, which involves the generation of highly toxic and reactive oxygen species (ROS) upon excitation of a photosensitizer (PS) which ultimately destroy the tumor tissue, is a widely accepted clinical technique.[12] Transition metal based PSs are commonly used in PDT due to their efficient spin orbit coupling induced by heavy atom effect. Among the various transition metal based PSs, Ir(III) complexes offer multiple advantages compared to poor cell permeability of Ru(II) complexes and labile ligands of Pt(II) complexes. The detailed investigations about the uptake efficiency and cytotoxicity helps to increase the efficiency of newly synthesized Ir(III) complexes.[13]

Luminescent PSs are not only restricted to therapeutic generation of singlet oxygen but also for imaging to improve drug’s efficacy and its distribution to the tumor tissue. High photostability, high singlet oxygen quantum yield and efficient cellular uptake of the complexes make them a potential candidate for theranostic applications. By attaching specific targeting group or the modification in the ligand itself will help the complex to target the specific organelle like lysosome, mitochondria, etc.[14]

1.3. Bioimaging

Understanding the molecular interactions in living system in their native habitat is a great challenge, particularly in the area of chemical biology and clinical diagnostics. Much of the qualitative understanding of molecular processes came from the traditional test tube biochemical experiments using purified or isolated biomolecules. These kinds of approaches are highly useful but the cellular conditions are fundamentally different from the experimental conditions. In order to understand the chemistry of living cells, we have to consider the cell itself as the test tube which helps to visualize cellular process and cell diagnosis. Light microscopes allow visualizing various molecular events within the cells, which are about 20-50 times smaller than the smallest thing that we can see with our naked eye. A simple light microscope displays the cell surface in a monochromatic fashion from which one cannot discriminate the working and constituents of the individual cells.[1]

Use of contrast agents along with highly sensitive instrumentation is a successful strategy to detect, localize and monitor critical molecular processes in cells, tissues, and living organisms. Contrast agents make molecular processes visible, quantifiable and traceable over time, aiming to probe molecular abnormalities. The key is to scrutinize the molecular abnormalities that are the basis of disease rather than to image the end effects of these molecular alterations. This will help in earlier detection of disease, direct molecular assessment of treatment effects, and a more fundamental understanding of the disease. Various contrast agents are used to assess specific molecular targets in different imaging modalities such as positron emission tomography, single photon emission computed tomography, magnetic resonance imaging, fluorescence imaging, ultrasound, etc. Fluorescence imaging technique allows real-time, non-invasive monitoring of biomolecules of interest in their native environments with high spatial and temporal resolutions.[8]

1.4. Fluorescence Imaging

Fluorescent chemosensors for ions and neutral analytes have been widely applied in many diverse fields such as biology, physiology, pharmacology, and environmental sciences. Fluorescence is the dissipation of energy in the form of light from electronically excited states generated by the excitation of a molecule or material by providing suitable energy. The fluorescence processes is directed by three important events, all of which occur on time scales that are separated by several orders of magnitude (Figure 1.1a). Initially, a photon of energy (h*v*) is supplied to the susceptible molecule, which results in the absorption of light, creating an excited electronic singlet state (S_1^1). This process occurs in femtosecond (10^{-15} s) timescale, and then the molecule partially dissipates the energy *via* vibrational relaxation of excited state electrons to the lowest energy level (S_1), which is measured in picoseconds (10^{-12} s). Finally a longer wavelength photon is emitted (hv_{em}) when the molecule returns to the ground state, which occurs in the relatively long time period of nanoseconds (10^{-9} s). The entire molecular fluorescence lifetime, from excitation to emission, is measured only in one billionth of a second; the phenomenon is a remarkable indicator of the interaction between light and matter that forms the basis for fluorescence microscopy. Because of the extremely sensitive emission profiles, spatial resolution, and high specificity of fluorescence investigations, the technique has become an important tool in understanding cell biology.[1,2]

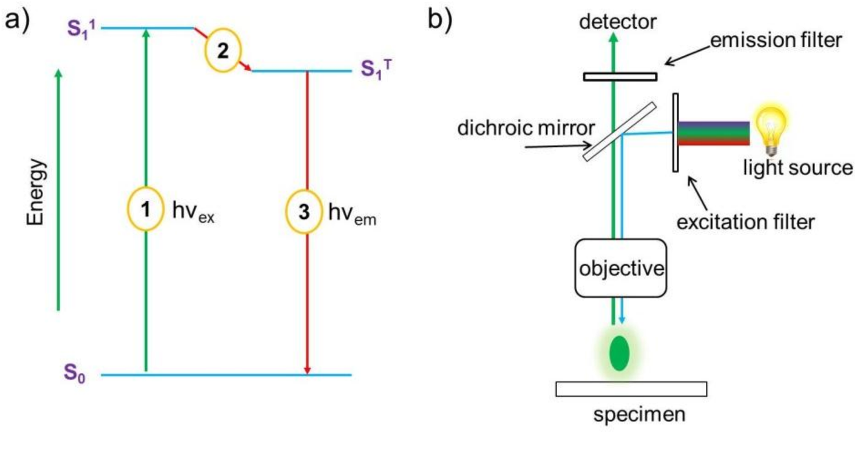

Figure 1.1: (a) Jablonski diagram illustrating fluorescence. (b) Fundamental concept under pinning fluorescence microscopy

The majority of fluorescence microscope, especially those used in the life sciences are of epifluorescence design, where excitation of the fluorophore and detection of the fluorescence are done through the same light path (*i.e.*, through the objective) as shown in the Figure1.1.b. Light of the excitation wavelength produced by passing light from a lamp through a wavelength selective exciter filter is reflected through the microscope objective lens to the specimen using a dichroic mirror. If the specimen fluoresces, the collected emission then passes through the dichromatic mirror and is subsequently filtered by a barrier filter that blocks the excitation light from the fluorescent light.

1.4.1 Small Molecular Fluorogenic Probes for Sensing and Imaging

Fluorogenic probes are described as reagents for which the physicochemical properties change upon interaction with a chemical species so that a change in fluorescence is produced, which in turn can detect the presence of an analyte. They have been extensively investigated and widely explored in many fields because of their exquisite sensitivity, and in particular in offering greater temporal and spatial visualizing capability for *in vivo* imaging studies. Significant effort has been devoted to the development of new fluorogenic probes, based on small fluorescent organic molecules[15], fluorescent proteins[16], polymers[17], metal nanoparticles[18], quantum dots[19], etc. To date, the most popular fluorogenic probes are small molecular dyes owing to their good biocompatibility and small sizes that are ideal for intracellular target labeling. Typically, small molecular fluorogenic probes are comprised of three different moieties: (1) a recognition moiety that provides selective binding with target analytes; (2) a transducer component for signaling the binding event; (3) a suitable spacer or linker that connects the two former moieties (sometimes the two moieties are integrated without any linker (Figure 2a)). The selectivity in sensing event is largely determined by the affinity between target analyte and recognition units, where the sensitivity usually depends on the fluorescence brightness of the probe and the contrast between the emission before and after the binding of the probe to an analyte. So far, various small molecular fluorogenic probes with superior properties have been developed to creatively couple the recognition process with the photophysical behaviors.[2]

A “turn-on” emission or a shift in excitation/emission profiles is preferred over a turn-off quenching response. A “turn-on” response gives a bright signal against a dark background, which maximizes spatial resolution. The fluorescence measurement by an increase of the fluorescence intensity without much shift of either excitation or emission wavelength can be influenced by many factors, such as the localization of the probe, changes of environment around the probe (pH, polarity, temperature, and so forth), emission collection efficiency, effective cell thickness in the optical beam and changes in the excitation intensity. To reduce the influence of such factors, ratiometric measurement is utilized, namely, simultaneous recording of the fluorescence intensities at two wavelengths and calculation of their ratio. Likewise, a shift in excitation/emission maxima can be used for ratiometric imaging, which allows for internal calibration of reacted and unreacted probe to minimize artifacts that may arise from variations in light intensity, sample thickness and heterogeneity, and dye distribution.[20] This technique provides greater precision than measurement at a single wavelength and is suitable for cellular imaging studies. In the context of ratiometric fluorescence sensing, a number of strategies, including internal charge transfer, excited state intramolecular proton transfer, fluorescence resonance energy transfer, through-bond energy transfer, and monomer-excimer formation, have long been the subject of study.[21] The schematic representation of various methods for the analyte detection through photophysical methods are summarized in Figure 1.2.

1.4.2 Self-assembled Molecular Probes for Sensing and Imaging

Molecular self-assembly refers to the spontaneous association of molecules to create a larger aggregate species through a number of non-covalent interactions.[7] These molecules undergo self-association forming hierarchical structures. To make use of this molecular self-assembly, the molecules should be designed in such a way to ensure that its building blocks are capable of undergoing stepwise interactions and assemblies through the formation of numerous non-covalent chemical bonds. The primary interactions which drive these molecules to assemble into well-defined and stable hierarchical macroscopic structures include hydrogen bonds, electrostatic and van der Waals interactions. Although each of these interactions are rather weak, their collective interactions can result in very stable structures and materials. Once the molecules are aggregated they will not be easily distorted until there is a drastic change in their environment.

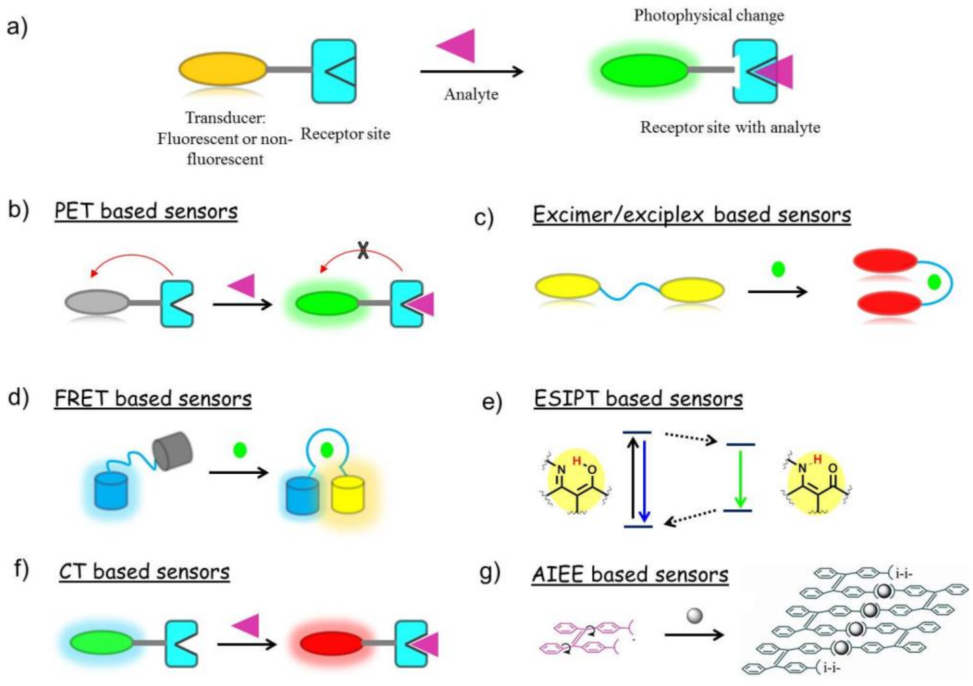

Figure 1.2: (a) Schematic representation of fluorescence based sensing. (b) to (g) Schematic representations of mechanisms for analyte sensing based on fluorescence.

Molecular self-assembly is not much exploited in sensing applications because of the aggregation caused quenching (ACQ) which is the quenching of emission when a fluorophore undergoes aggregation. Therefore, aggregation is generally considered detrimental in the probe development and is generally unfavorable. Recently some research groups have utilized ACQ to design fluorescent probes by using the disaggregation nature of the assembly in the presence of a specific analyte that bring “turn-on” fluorescence.[8] The sensing mechanism based on signal amplification using disaggregation of probes has several advantages. First, due to the formation of aggregates, the original signal of the monomer is largely quenched which makes this kind of probe to exhibit negligible background signal and large fold enhancement in the signal intensity upon binding with analytes. Second, the enhancement or the recovery of the signal by disaggregation renders the probe with “turn-on” property with high sensitivity. Third, ACQ is a very common phenomenon among most of the fluorophore; therefore, aggregation-disaggregation process would be applicable to a variety of probes. Based on the mechanism, the aggregation based probes are classified into two, which are discussed in the following sections.

1.4.3 Disaggregation from Template-Aggregate

The aggregate formation usually occurs at high concentration of the probe. However, in some cases, molecules can be deliberately brought together and allowed to form aggregates using a template (induced aggregation). Such a template can serve as an assembling core (e.g., metal ion) or backbone (e.g., nucleobases in DNA) and its disaggregation occurs specifically in presence of a particular analyte. The stronger interaction of the analyte with the template results in the breakage of the interaction between the probe and the template, which releases the monomer molecule with a “turn-on” fluorescence response.

Many fluorescent molecules such as rhodamine, cyanine and styryl derivatives are positively charged. They tend to form aggregates in the presence of negatively charged polyanions, (e.g., nucleic acids) due to electrostatic interaction. In contrast, when the interaction is disturbed or weakened by the addition of an analyte, the aggregates will disassemble. Utilizing such a mechanism, Yu and co-workers, designed an aptamer induced aggregate of PBI derivative (**1**) as a “turn-on” sensor for lysozyme (Figure 1.3).[22] An aqueous solution of **1** containing both monomeic and aggregated species exhibit strong fluorescence due to the existence of the free monomer of the dye. Addition of an anti-lysozyme aptamer (5'-ATC AGG AAA GAG TGC AGA GTT ACT TAG-3') resulted in the aggregation of **1** due to the strong electrostatic interaction between the dye and the multiple negatively charged phosphate functional groups in the backbone of aptamer molecule. The enhanced dye aggregation resulted in a significant decrease in the fluorescence intensity of the dye. Addition of lysozyme to this solution, however, would weaken the interaction between **1** and the aptamer due to the specific binding of lysozyme to the anti-lysozyme nucleic acid aptamer resulting in the regeneration of the fluorescence of **1** at 545 nm. This method achieved a detection limit of 70 pM.

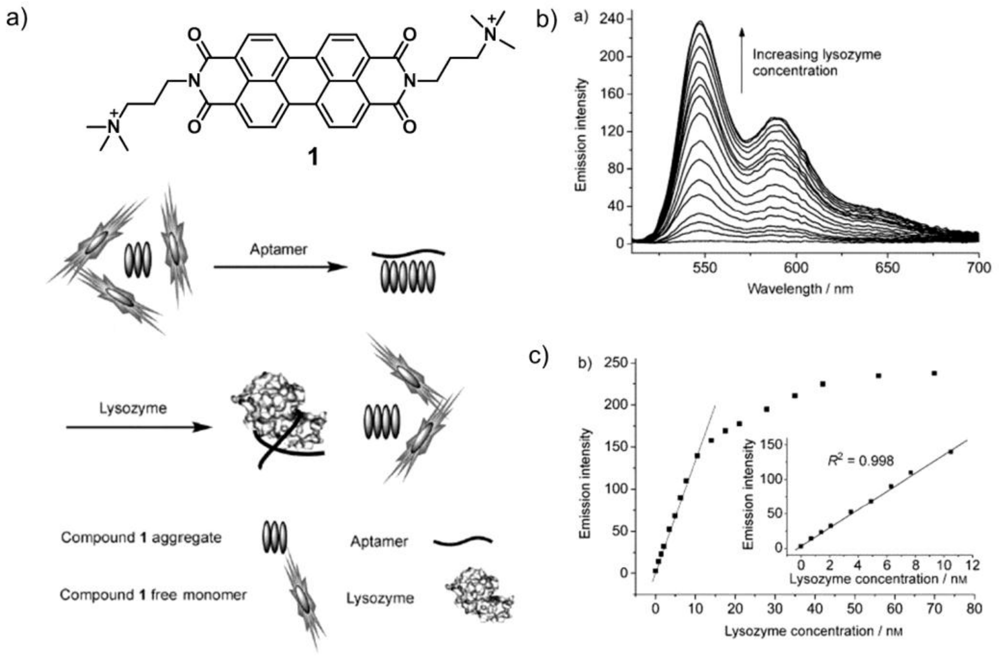

Figure 1.3: (a) Schematic representation of the strategy for selective lysozyme sensing based on the aggregation of **1** mediated by DNA aptamer and disaggregation in the presence of lysozyme. (b) Changes in emission spectrum upon addition of different concentrations of lysozyme to the mixture of compound **1** (5 nM) and the anti-lysozyme aptamer (0.5 nM). (c) Plot of the fluorescence intensity at 545 nm against the lysozyme concentration; inset: expanded linear region of the curve.

1.4.4 Disaggregation from Self-Aggregates

The inherent tendency of certain molecules to form aggregates has been used as a specific strategy to develop probes in several cases.[23] For example, Hamachi and co-workers introduced the disassembly approach for specific sensing of proteins.[23] The fluorescent probe **2** consists of a fluorophore tethered to a recognition ligand, which self-assembles in buffer, resulting in significant red-shift of the absorption maximum and quenching of fluorescence. Atomic force microscopy (AFM) measurement revealed the formation of spherical particles with diameters ranging from 100 to 200 nm. When the probe binds to the specific protein (human carbonic anhydrase I, hCA), a clear fluorescence "turn-on" signal was detected due to the recognition-driven disassembly of the nanoprobes. This probe provides good selectivity to hCA with a detection limit of 70 nM. Researchers have succeeded in developing these probes for specific visualization of over expressed folate receptor (FR) and hypoxia-inducible membrane bound carbonic anhydrases (CA) on the surface of live cancer cells, both of which are tumor specific biomarkers (Figure 1.4).

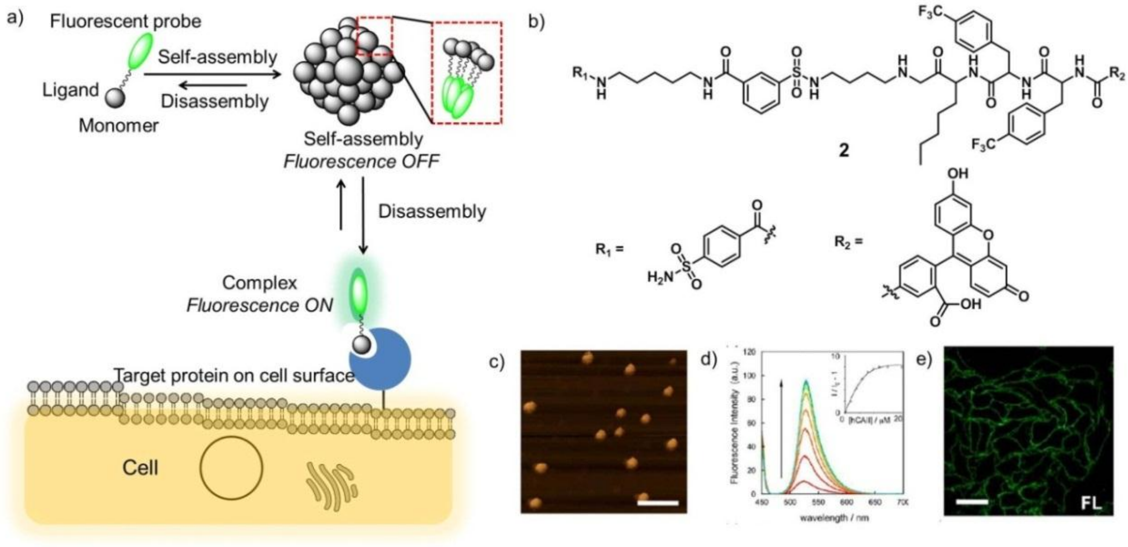

Figure 1.4: (a) Schematic presentation of recognition driven disaggregation approach to design "turn-on" fluorescent probe for cell surface protein imaging. (b) Chemical structure of self-assembling probe **2**. (c) AFM image of probe **2** (10 μM, HEPES buffer (pH 7.2, 150 mM NaCl)). (d) Fluorescent spectral changes of probe 2 (10 μM) upon addition of hCA1 (0−20 μM). (e) Fluorescence images of hypoxia-cultured A549 cells treated with probe **2** (10 μM) in the presence of CA inhibitor EZA (100 nM). Scale bar, 40 μm.

Squaraine molecules are well exploited in aggregation based probes. For example, there is a recent report on a self-assembled squaraine nanoprobe for the selective sensing of a protein in blood serum.[24] The dye self-assembles to form nonfluorescent nanoparticles (D_h = 200 nm) which selectively respond to human serum albumin (HSA) in the presence of other thiol-containing molecules and proteins by triggering a green fluorescence. This selective response of the dye nanoparticles allowed detection and quantification of HSA in blood serum with a sensitivity limit of 3 nM. The sensing mechanism involves HSA specific controlled disassembly of the squaraine nanoparticles to the molecular dye by a non-covalent binding process and its subsequent reaction with the thiol moiety of the protein, triggering the green emission of the fluorophore present in the dye (Figure 1.5).

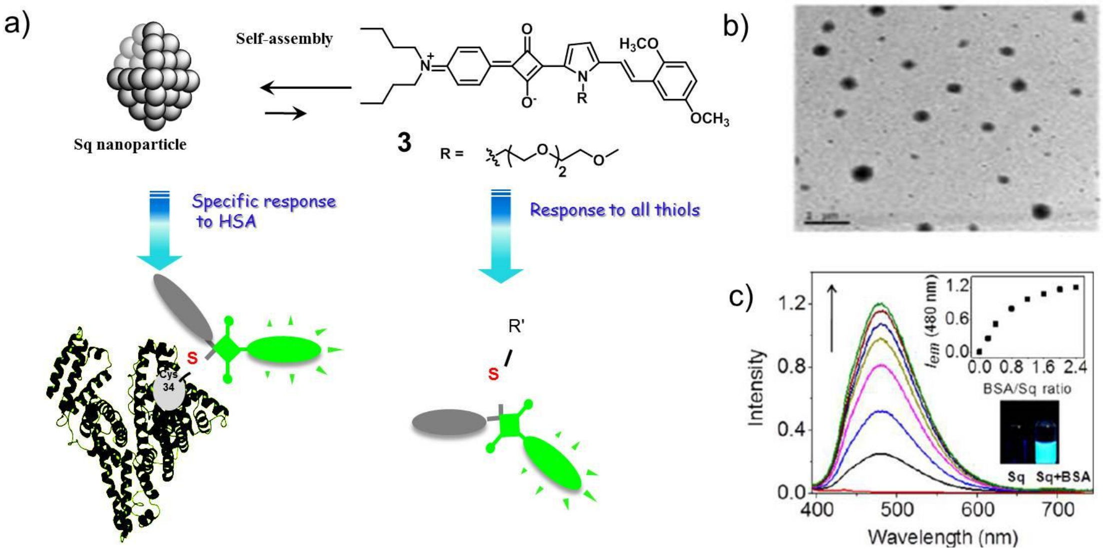

Figure 1.5: (a) Schematic representation of the specific recognition of the probe **3** towards thiols. (b) TEM images of **3** showing spherical assemblies obtained from 25 mM phosphate buffer at a pH of 8.0.(c) Emission spectral changes of the squaraine nanoparticles upon addition of BSA protein (0−14 μM) (λ_{exc} = 380 nm) and photograph showing the corresponding fluorescence turn-on. (The authors choose BSA instead of HSA since the former is easily available and cheaper but structurally similar to the latter.)

1.5 Metal Ion Imaging in Biological System

All life forms have an absolute requirement for metals, as metals play critical roles in fundamental processes such as osmotic regulation, catalysis, metabolism, biomineralization, signaling etc.[25] Group I and II metals (alkali and alkaline earth metals such as sodium, potassium, calcium, and magnesium) are abundant in most biological organisms. Transition metals that are generally recognized to play critical roles in biological process include iron, zinc, copper, manganese, cobalt, nickel, molybdenum, tungsten, chromium, and vanadium. These elements are often referred to as trace elements because they are present at much lower amounts than the group I and II metals. However, iron and zinc are often found in substantial amounts. While biologically relevant metals occur ubiquitously throughout the cell, higher concentrations are found in certain organelles depending on their biological role.[25] The details are given in the Figure 1.6.[26,27]

Biological metals may exist in different forms, including as hydrated ions, tightly bound forms such as metal-bound co-factors and protein or nucleic-acid bound species, or loosely bound forms in association with a diverse heterogeneous buffer, which can consist of low molecular weight species such as amino acids, glutathione, or citric acid, and labile species. The total metal content comprises of the sum of all of these diverse forms.[28,29] Zinc is the second-most abundant transition metal ion in the human body following iron.[30] The total amount of zinc in an adult human body is estimated to be 2-3 g. Long term insufficient intake of zinc will cause stunted growth in children.[31,32] The total zinc concentration in a mammalian cell is reported to be in several hundreds of micromolar range. The homeostasis of Zn^{2+} in living systems is exquisitely regulated by three classes of proteins, namely, Zn^{2+} buffer proteins, Zn^{2+} transporters and Zn^{2+} sensor proteins. The thiol-rich metallothioneins, which can bind a large number of Zn^{2+} and release Zn^{2+} in the presence of oxidative stress, act as Zn^{2+} buffers and storage proteins. Zn^{2+} transporters have opposite functions, and they control the cellular uptake and excretion of Zn^{2+}.

It has been proposed that labile Zn^{2+} in living systems initiates transient signals that stimulate various physiological processes. Substantial evidence have demonstrated that Zn^{2+} plays an important role in apoptosis[33], and that both labile Zn^{2+} regulation and Zn^{2+}-associated DNA/RNA polymerases are involved in apoptosis.[34] Labile Zn^{2+} are also associated with the regulation of gene expression and insulin secretion. Moreover, labile Zn^{2+} is believed to play important neurological roles and is considered to be a neurotransmitter.[35] In a complete synaptic transmission, labile Zn^{2+} ions are co-released with glutamate from synaptic vesicles of a presynaptic neuron; they traverse the synaptic cleft and then arrive at a postsynaptic neuron. In this signalling pathway, Zn^{2+} is recognized to be a second messenger, similar to Ca^{2+} in the hippocampus, for long-term potentiation.[36]

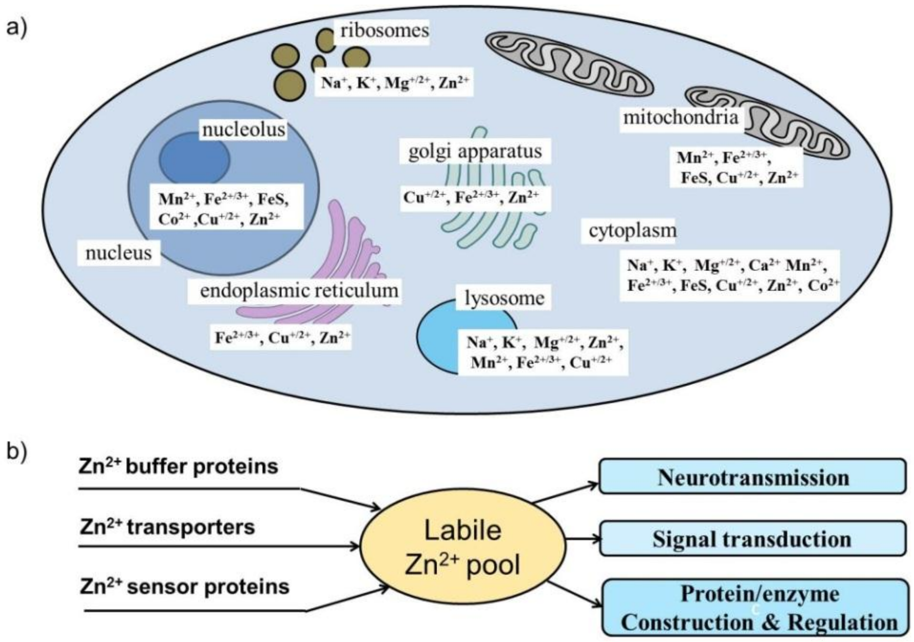

Figure 1.6: (a) Organelle-specific metal distribution in a eukaryotic cell. (b) Proposed scheme of Zn^{2+} homeostasis in living systems.

1.6 Fluorescent Chemosensor for Zinc Ions

Of all the methods known for the detection of any analyte, fluorescence technique outstands owing to its high sensitivity, fast response, simple instrumentation and reliability. A large number of zinc ion sensors are available based on efficient chromophoric systems and a wide range of receptors are also known for efficient binding of Zn^{2+}.[27] The most well studied and mostly applied mechanisms of fluorescence signal transduction in the design of Zn^{2+} chemosensors are based on photoinduced electron transfer and intramolecular charge transfer based. Also, the most widely used receptors for Zn^{2+} binding are 2,2'-bipyridine, dipicolylamine and terpyridine. In the following sections, we will briefly discuss the mechanism of sensing and bipyridine receptor used for Zn^{2+} sensing and imaging.[27]

1.6.1 Mechanism of Sensing of Zinc Ions

A general design for a PET based fluorescent sensor has a ‘fluorophore-spacer-receptor’ format (Figure 1.7).[37] Upon photoexcitation of the fluorophore, an electron transfer occurs from the receptor to the fluorophore resulting in a quenched emission of the fluorophore. The binding of the analyte with the receptor restricts this processes leading to the regeneration of the native fluorescence. A rule of thumb deduced from various literature reports till date shows that for efficient PET to occur the receptor should have a lower oxidation potential than the fluorophore leaving the sensor system in an off-mode and the reverse happens when PET is arrested.

In an ICT based fluorescent sensor system, the design strategy comprises of an electron acceptor unit (A) in conjugation with an electron donor (D) generating a push-pull π system (Figure 1.7).[38] The metal binding to the acceptor part enhances the acceptor strength creating an efficient push-pull system and ultimately leading to a bathochromic shift in the absorption and emission spectrum. However, if the metal binds to the donor, the electron donating character is decreased leading to a hypsochromic shift in the spectrum.

1.6.2 Bipyridine Based Zn^{2+} Sensors

Binding-induced conformational restriction of biaryl fluorophores can efficiently increase the fluorescence intensity. For hetero biaryl fluorophores (e.g., bipyridyl), the coordination of metal ions, through the combination of two signaling mechanisms, that is conformational restriction and intramolecular charge transfer, will produce an enhanced red-shift in fluorescence emission.[39] Since bipyridine ligands bind with different transition metal ions producing similar absorption spectral responses, it is difficult to use them as specific sensors. However, excited state dynamics may vary widely, depending upon the metal ion and hence the fluorescence signature in each case can be the tool to identify the nature of the metal ion. Generally, binding induced conformational changes leads to planarization which induces a red-shifted emission.

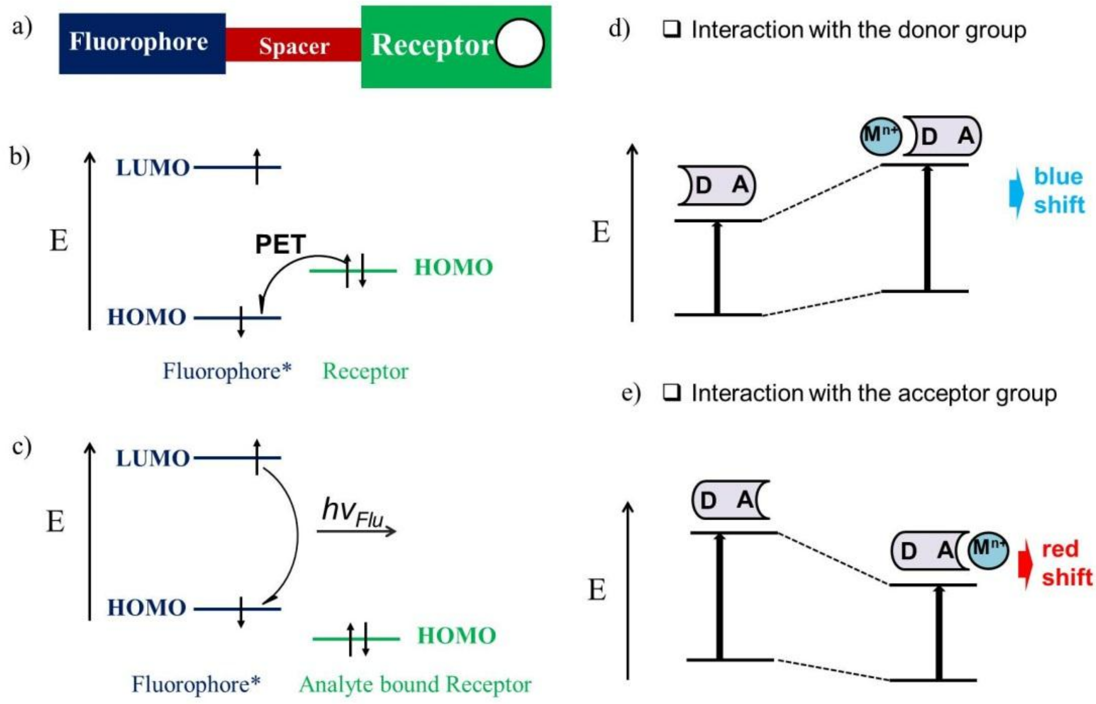

Figure 1.7: (a) Fluorophore-spacer-receptor design strategy for fluorescent PET sensors. (b) Fluorescence 'off' state due to PET. (c) Fluorescence 'on' state upon binding of analyte due to the restriction of PET. (d) and (e) Ratiometric sensing behavior in ICT-based fluorescent probes.

Ajayaghosh and co-workers have developed several 2,2'– bipyridine receptor based Zn^{2+} probes that are ratiometric in nature (Figure 1.8).[40,41] Pyrrole end-capped divinyl aromatic systems are known to be strongly fluorescent building blocks for the synthesis of electrochromic and low band gap polymers. Hence, the high fluorescence of such systems was exploited for metal ion sensing by introducing a bipyridyl moiety for the metal chelation. The probe **4** showed an emission maximum at 547 nm in buffered aqueous acetonitrile solution (1:9) which was shifted bathochromically to 635 nm upon titration with Zn^{2+}.[40] The titration with Cu^{2+}, on the other hand, led to quenching of emission. However, the addition of Zn^{2+} to the non-fluorescent Cu^{2+}-complex caused the appearance of emission corresponding to that of the Zn^{2+} complex. The probe, thus facilitated the ratiometric and visual sensing of Zn^{2+} amidst other competing metal ions.

The role of donor moiety linked to the bipyridyl unit in modulating the fluorescence behavior upon interaction with Zn^{2+} has been reported.[42] Different derivatives having different donor groups such as pyrrole (**4**), thiophene (**5**) and aniline (**6**) were prepared and their fluorescence response towards Zn^{2+} were investigated. The excited state charge transfer behavior of **4** and **5**, and the generated fluorescent states with Zn^{2+} renders them excellent fluorescent ratiometric Zn^{2+} probes. However, the enhanced charge transfer process in **6** ultimately quenches the emission with Zn^{2+} as well as a variety of other cations, and hence is not suitable for the sensing of these ions.

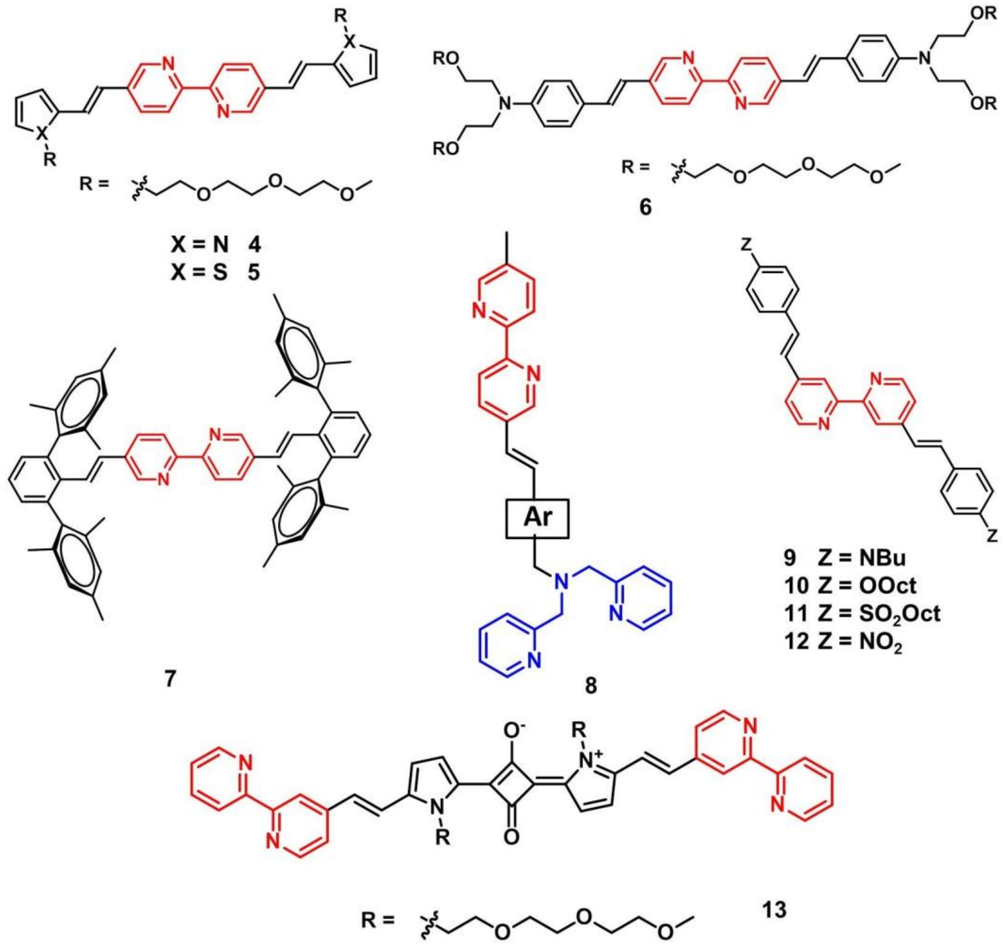

Figure 1.8: Bipyridine based ratiometric sensors for Zn^{2+}, **4 -13**.

Smith and co-workers have reported a fluorescent sensor **7** for the selective detection of zinc ion by a sterically-encumbered bipyridyl based receptor.[43] In this case, a meta-terphenyl moiety was selected as a steric shield for the chromophore-derivatised bipyridyl ligand. The zinc ion binding resulted in a red-shifted absorption and an immediate 21-fold increase in the emission intensity. Later, Zhu and co-workers incorporated two zinc ion binding ligands to develop a highly efficient fluorescent system **8** for Zn^{2+}.[44] The ditopic ligand, however, is nonfluorescent due to the PET from the electron donating high affinity Zn^{2+} binding site (dipicolylamino site) to the excited arylvinyl-bipy fluorophore. Their experiments revealed a sequential binding of the metal implying a higher affinity of Zn^{2+} towards the dipicolylamino site over the bipyridyl unit giving a certain fluorescence output. Gradually, as the concentration of Zn^{2+} increased, they observed co-ordination to the bipyridyl unit with an entirely different fluorescence output. Larger number of different 4,4'-disubstituted-[2,2']-bipyridine based fluorophores **9-12** have been reported as Zn^{2+} sensors.[45] Bipyridine receptor was also integrated on to a squaraine backbone for the ratiometric sensing of Zn^{2+} by Fu and coworkers. The probe **13** was found to detect Zn^{2+} in acetone with a 22 nm bathochromic shift in the emission with a limit of detection of 6.1×10^{-8} M.[46]

Ajayaghosh and co-workers have reported a ratiometric two photon (2P) probe **14** carrying a bipyridine moiety at the center (acting as the acceptor) with carbazole units on either side (acting as the donor) (Figure 1.9).[47] Spectrochemical titration of a solution of **14** in 1:1 acetonitrile/water (HEPES, pH 7.2) with $Zn(ClO_4)_2$ caused a red-shift in the emission from 530 nm to 610 nm. A 13-fold enhancement in 2PA cross section and a 9-fold enhancement in 2P brightness upon interaction with Zn^{2+} as compared to the free ligand were observed. The probe was then used for the detection of Zn^{2+} and its significantly high 2P brightness was utilized for *in vivo* 2P tissue imaging of live hepatocytes of rats.

Zhao and co-workers have reported a donor-acceptor system as a three photon active probe for the imaging of Zn^{2+}.[48] Their molecular system, **15** comprises of aniline and pyrrole as the two donor units, each of which is connected to 2,2'-bipyridine acceptor *via* vinyl linkage and bridged together using a triazole unit. The molecule exhibited a 1:2 binding stoichiometry upon addition of Zn^{2+} with a red-shift in both absorption and emission profiles. They observed intense emission features at respective emission wavelengths, 426 nm for the probe and 591 nm for the Zn^{2+} bound complex when excited at 1200 nm, proving the 3P activity of the system. The 3P absorption cross section was found to be 1.38

x 10^{-78} cm^6 s^2 photon^{-2} for the probe and 3.03 x 10^{-78} cm^6 s^2 photon^{-2} for the complex. The ability of the probe for the detection of exogenous Zn^{2+} in live HeLa cells by 3P excitation was also demonstrated. Later, Ajayaghosh and co-workers have developed a 3P active donor-π-acceptor type fluorophor that can effectively signal and image Zn^{2+} in biological specimens.[49] The GMP probe, (**16)** exhibited selective ratiometric response to Zn^{2+} in the visible region upon excitation at 1150 nm. The observed σ_3 and $\sigma_3\eta_3$ values are among the highest of reported 3P active fluorophores. Good cell viability, high fluorescence quantum yield, large 3P cross-section and high 3P brightness of GMP facilitate the 3P imaging of free zinc ions in live cells. The demonstration of the 3P hippocampal slice imaging further indicates the viability of GMP as an efficient ratiometric 3P fluorescent probe for deep tissue Zn^{2+} imaging.

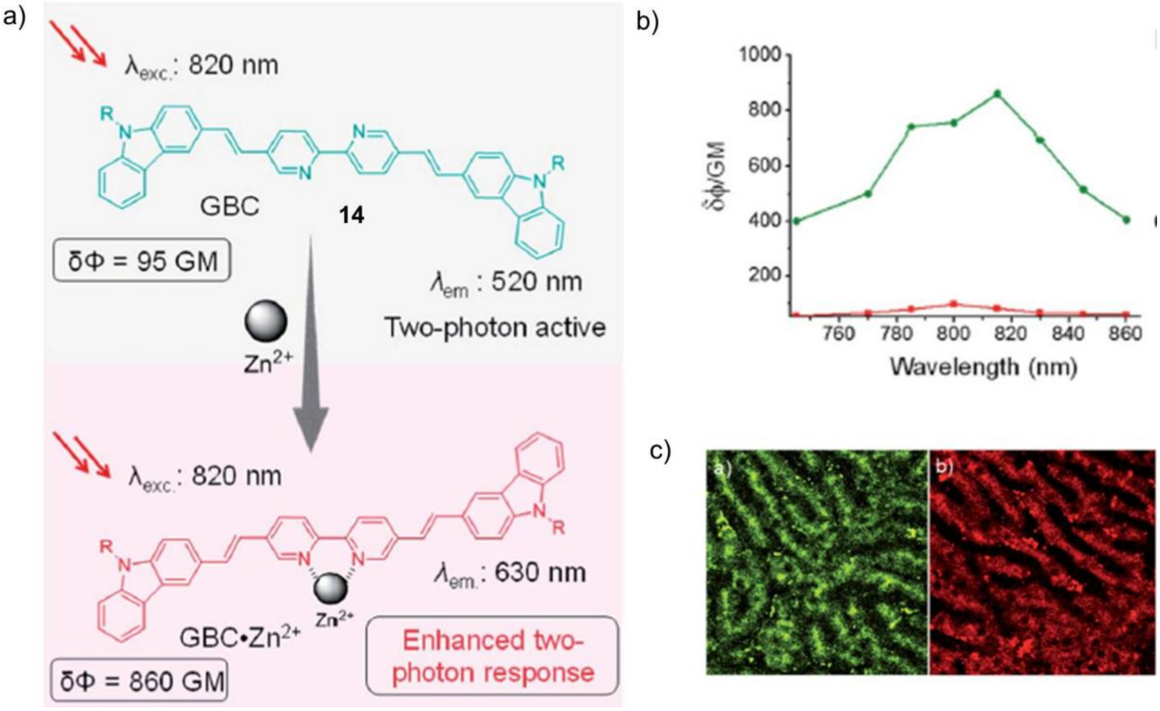

Figure 1.9: (a) Schematic illustration of 2P response of **14** before and after addition of Zn^{2+}, (b) corresponding 2P action spectra and (c) in vivo 2P imaging using **14** (λ_{ex} = 820 nm, λ_{em} = 530 nm) and **14** + Zn^{2+} (λ_{ex} = 820 nm, λ_{em} = 650 nm) in hepatocytes in live rat after intravenous injection.

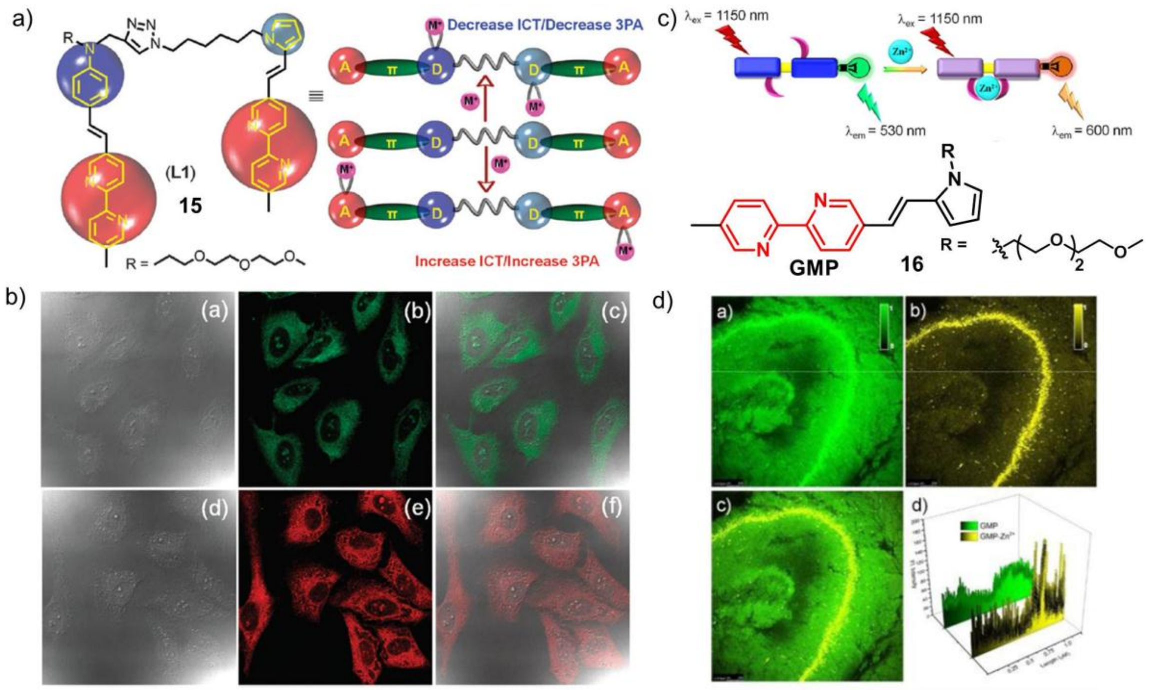

Figure 1.10: (a) Chemical structure of **15** and schematic representation for the modulation of the 3P absorption upon interaction with Zn^{2+}. (b) 3P Micrscopy images of Hela cells incubated with **15** under excitation at 1200 nm before (upper panel) and after (lower panel) Zn^{2+} binding. (c) Zn^{2+} chelation induced emission changes from GMP (**16**) upon 3P excitation at 1150 nm; molecular structure and scheme. (d) 3P microscopy images of hippocampal slices of Wistar rats after incubating GMP (**16**). 3P excited fluorescence from **16** (λ_{ex}= 1150 nm, λ_{em}= 530 nm) **16**·+ Zn^{2+} (λ_{ex} = 1150 nm, λ_{em} = 600 nm), Overlay image of slices and 3P excited fluorescence intensity profiles. Scale bars are 250 µm.

1.6.3 Subcellular Zn^{2+} Imaging Using Organelle Targeting Groups

Mammalian cells are the most commonly used biological specimens for intracellular Zn^{2+} imaging. These cells contain many subcellular compartments such as mitochondria, lysosome, Golgi apparatus, and endoplasmic reticulum (ER) which play different roles in intracellular Zn^{2+} homeostasis.[50] Labile Zn^{2+} concentrations in these organelles vary from one to another. It is reported that the labile Zn^{2+} levels in the ER and Golgi apparatus of HeLa cells were in the range of ~ 1 pM, and those in cytosol and nucleus were about two-orders of magnitude higher, whereas in mitochondria, the level was 10-fold lower.[38] Moreover, labile Zn^{2+} level in the same organelle vary with the cell lines, cell phases, and physiological processes. Therefore, it is highly appealing to visualize labile Zn^{2+} within specific subcellular compartments for the study of inter- and intra-organelle Zn^{2+} physiology. Considerable efforts have been devoted to this subject during the past few years. The subcellular localization of a tested sensor can be evaluated by co-staining experiments with commercially available fluorescent markers with known specific subcellular localization patterns, but with no emission (or excitation) overlap with the tested sensors. Colocalization parameters, such as Pearson's correction coefficient, which is given by imaging software, are used to quantify the degree of colocalization between sensor and organelle marker.[51]

Mitochondria, the energy-generating primary subcellular compartments in eukaryotic cells play vital roles in various physiological processes including proliferation and apoptosis.[52,53] Many Zn^{2+}-dependent enzymes are located in mitochondria, and Zn^{2+} pools are essential for maintaining mitochondrial protein functions.[54] Most of the ROS/RNS in living systems are generated in the mitochondria during the production of ATP, which mobilizes mitochondrial Zn^{2+}. Mitochondria have a slightly basic pH value of ~ 8.0 with a negative cross membrane potential (c.a. -180 mV, outer to inner). In general, fluorescent sensors with a lipophilic cationic nature tend to accumulate in mitochondria driven by the cross inner membrane potential within the mitochondria.[55] The first mitochondrial Zn^{2+} imaging was reported by Weiss and co-workers in 2003 using a Zn^{2+} sensor rhodZin-3, which exhibited a 75-fold fluorescence enhancement upon Zn^{2+} binding with a dissociation constant of 65 nM.[56,57] Triphenylphosphonium (TPP), another lipophilic cationic group, is one of the most commonly used targeting groups for mitochondria.[58] Sensors containing a TPP group, such as SZn-Mito, SZn2-Mito, and FZn-Mito,[59,60] have been tested for TPM turn-on Zn^{2+}. SZn-Mito (**17**) showed a 7-fold TPEF enhancement in response to Zn^{2+} with a dissociation constant (K^{TP}_d) of 3.1 nM. SZn2-Mito (**18**) exhibited a 70-fold TPEF enhancement in response to Zn^{2+} with a K^{TP}_d of 1.4 nM. The TPEF intensity of FZn-Mito increased by 16-fold upon Zn^{2+} addition and the related K^{TP}_d was determined to be 17 nM. These sensors were found to localize in mitochondria with Pearson’s correction coefficients ranging from 0.85 to 0.89.

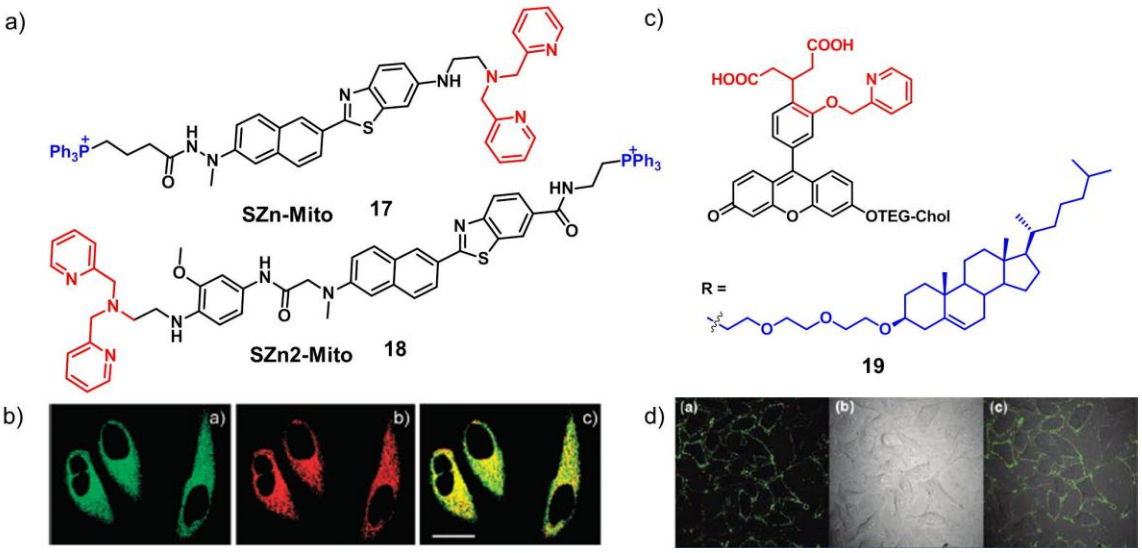

Figure 1.11: (a) Structures of SZn-Mito (**17**) and SZn2-Mito (**18**). (b) TPM and OPM images of HeLa cells co-labeled with **18** (1 mM) and Mitotracker Red FM (1 mM) respectively and colocalized image. (c) Molecular structure of **19**. (d) Confocal fluorescence image of HeLa cells loaded 2.5 μM **19**, bright-field transmission image of the cells and overlay of images.

Lysosomes containing various acidic hydrolases serve as the main sites for macromolecule degradation.[61] Zn^{2+} appears to be a link between oxidative stress and lysosomal membrane permeabilization (LMP).[62] Fluorescent Zn^{2+} sensors for lysosomal Zn^{2+} are developed to study the lysosomal Zn^{2+}-related oxidative stress and downstream markers for LMP. Considering the acidic pH of lysosomes (4.5–6.0), weakly basic aliphatic amines tend to accumulate in lysosomes through a lysosomotropism process.[63] It is worth noting that the interference from protons should be considered while designing the Zn^{2+} sensors, especially the PET based ones. The protonation of the electron donor (usually as Zn^{2+} chelator) could also induce a fluorescence enhancement, which will lead to false signaling. To minimize the interference from protons in lysosomal Zn^{2+} imaging, a Zn^{2+} sensor should have a lower pK_a, which keeps its fluorescence unchanged even in a slightly acidic environment. The detailed discussion is given in the Chapter 2, section 1.

Imaging of labile Zn^{2+} at the cell membrane is crucial for investigating the equilibrium between intracellular and extracellular Zn^{2+}, which requires sensors with cell membrane-targeting ability. Cholesterol tail or long alkyl chains are common targeting groups that anchor cell membrane because of their strong hydrophobic affinity to membrane lipids.[64] A cholesterol-conjugated fluorescence Zn^{2+} sensor based on the fluorescein platform **19** was synthesized by Yamamoto and co-workers and successfully imaged Zn^{2+} in the cell membrane.[64] Several probes achieved the specific localization at Golgi apparatus and ER,[65,66] however, there was no specific targeting group observed for these organelle. Zn^{2+} plays essential roles in numerous nuclear proteins such as transcription factors, polymerases, and DNA remodeling factors. The penetrating ability of most of the synthesized probes are very less to the nucleus and there are very less number of Zn^{2+} probes reported for nucleus.[67]

1.7 Basic Aspects of Photodynamic Therapy

Therapy is the attempted remediation of a health problem usually following diagnosis. There are hundreds of different therapeutic techniques available today and most of them are in clinical use. In this section, we will be discussing the importance, photophysical aspects, classification and applications of photodynamic therapy.

Photodynamic therapy research draws much attention as it is an alternative to the traditional cancer treatments due to its high selectivity in the destruction of tumor cells over normal cells. Over the past decade, the clinical use of PDT has greatly increased. The use of PDT to treat bacterial and fungal infections is in practice for over 30 years.[68,69] PDT involves the generation of highly toxic and reactive oxygen species upon excitation of a photosensitizer which ultimately destroy the tumor tissue. It has several advantages over conventional therapies because of its noninvasive nature, selectivity, ability to treat patients with repeated doses without initiating resistance or exceeding total dose limitations (as associated with radiotherapy), fast healing process resulting in little or no scarring, ability to treat patients in an outpatient setting, and less side effects associated. PDT comprises mainly four stages- first stage involves the administration of the sensitizer into the body.[70,71] The sensitizer will then selectively accumulate around the tumor tissue when allowed for a suitable period of incubation in the stage 2. The target tissue will be irradiated in the stage 3 using a light stimulus, and the cytotoxic agents such as ROS will be generated due to the excitation of the sensitizer. These species react with the biological targets such as proteins, amino acids, lipids, nucleotides and nucleic acids thereby disrupting the normal functions of the cell and causing cell death in stage 4. A sensitizer in PDT can, therefore, be regarded as a ‘stimuli-responsive system’, being inactive in dark and becomes active only when irradiated with light of an appropriate wavelength.

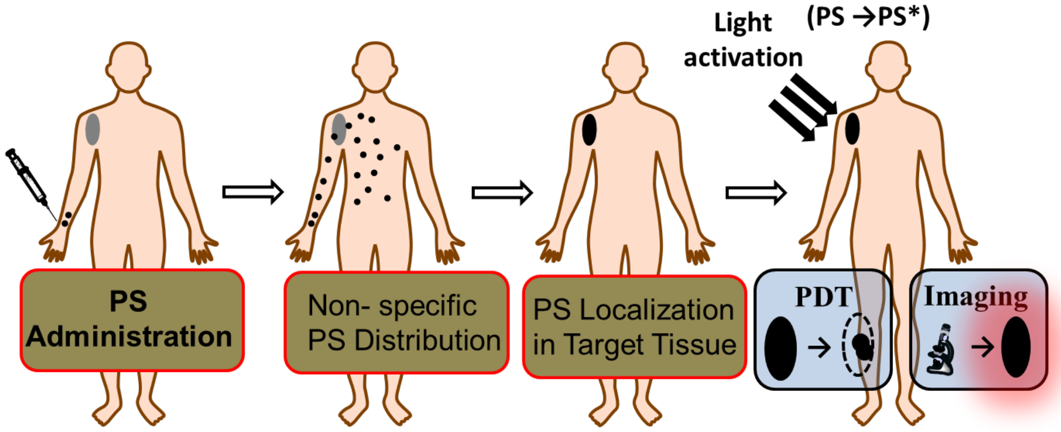

Figure 1.12: Schematic representation of the sequence of administration, localization and light activation of the PS for PDT or fluorescence imaging.

Although most PDT processes are oxygen-dependent and are only initiated in oxygenated conditions, PDT can take place even in hypoxic environments, without the presence of oxygen.[72] Based on the different photochemical reaction processes, PDT can be divided into two types: type I PDT and type II PDT. After light activation, the PS is transformed from the ground singlet state (S_0) to the excited singlet state (S_1), and then to an electronically excited triplet state (T_1); T_1 triggers the photochemical reaction via two different (type I and type II) paths (Fig.). For type I PDT, T_1 participates in a hydrogen- or electron-transfer process to react directly with a biological substrate to form free radicals, which can interact with triplet oxygen ($^3O_2$) and water to produce superoxide anions ($O_2^{\cdot-}$) and hydroxyl radicals ($OH^{\cdot}$), respectively. During the type II PDT process, T_1 undergoes a type II photochemical reaction to convert the surrounding $^3O_2$ into cytotoxic singlet oxygen ($^1O_2$) *via* direct energy transfer. Therefore, type II PDT dominates in well-oxygenated environments, while type I PDT can occur under hypoxic conditions (Figure 1.13).[73]

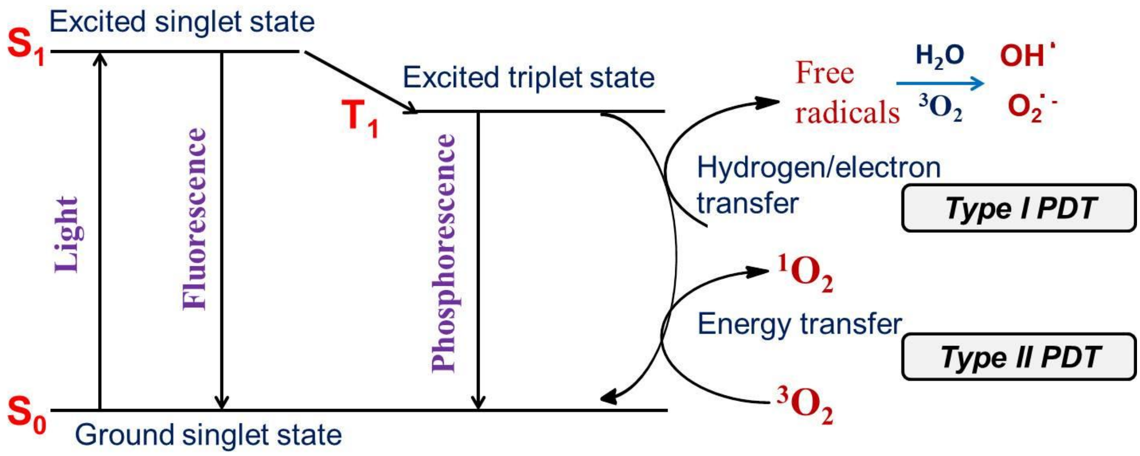

Figure 1.13: Scheme of the photochemical reactions for type I and type II PDT.

The mechanism of cell death, whether occuring through apoptosis or necrosis, is dependent upon the localization of the photosensitizer within the cell and the amount of singlet oxygen generated. Some evidence suggests a photosensitizer localized in the mitochondria or the endoplasmic reticulum is a better inducer of apoptosis, whereas a photosensitizer localized in the plasma membrane or in lysosomes is more condusive to necrosis. PDT cause acute local inflammation, inducing an immune response against cancer cells.[74]

1.8 Generation of Singlet Oxygen

Singlet oxygen generation can be achieved either chemically or photochemically. The major chemical reactions include the decomposition of triethylsilyl hydrotrioxide generated *in situ* from triethylsilane and ozone, aqueous reaction of hydrogen peroxide with sodium hypochlorite and from phosphite ozonides.[75] An advantage of this method is that it is amenable to non-aqueous conditions.

Photosensitized generation is a simple and controllable method for $^1O_2$ production which requires oxygen, light of an appropriate wavelength, and a photosensitizer capable of absorbing and using that energy to excite oxygen to its singlet state.

The PS is the key element involved in PDT, and takes responsibility for ROS generation upon wavelength-selected light irradiation. Generally, a PS is a single chemical compound with pure quality and good stability. An ideal PS should have a high singlet-to-triplet intersystem crossing efficiency, extremely low dark toxicity, minimized phototoxic damage to normal tissues, and maximum absorption at a long wavelength. The principal photophysical processes involved in triplet excited state (S_0-S_1-T_1 or S_0-S_1-T_n-T_1) are basically quantum mechanically forbidden.

Population of the T_1 state of an organic chromophore requires a non-radiative transition S_1-Tn or S_1-T_1, *i.e.*, inter system crossing. This transition involves two different spin states. Energy and the total angular momentum (orbital and spin) have to be conserved during ISC. The most important interaction that couples two spin states and that provides a means of conserving the total angular momentum is the coupling of the electron spin with the orbital angular momentum, *i.e.*, the spin-orbit coupling (SOC).[76] The various factors that enhance ISC are:

- Heavy atom effect
- Low-lying n-π* transitions
- Exciton coupling
- Intramolecular spin conversion

1.8.1 Heavy Atom Effect

Atoms with large atomic number can induce strong SOC leading to an enhanced ISC. An electron moving in the vicinity of a nucleus with a positive charge Z will be accelerated to relativistic velocity resulting in a strong coupling of the spin (μ_S) and orbital (μ_L) magnetic momentum. This heavy atom effect is a nuclear charge effect and scales with Z^4 (Z is the nuclear charge). Typical heavy atoms include Ir, Pt, Ru, Os, Re, Rh, I and Br, etc.[77]

1.8.2 Low-Lying n-π* Transitions

For n-π* transition, the exchange integral and consequently the energy gap between S_1/T_1 states is small. The energy difference between S_1 and T_1 states is large for the compounds with low lying π-π* transitions. According to El-Sayed's selection rule for ISC, $S_1(n, \pi^*) \rightarrow T_1(\pi\text{-}\pi^*)$ is an allowed transition because the angular momentum is conserved and the S_1/T_1 state energy gap is small.[77a]

1.8.3 Exciton Coupling

When two identical chromophores are incorporated into one molecule in close vicinity without π-conjugation, the exciton coupling, i.e. the interaction of the transition dipole moments of the chromophores, can lead to two delocalized excited states for every local excitation of the singlet chromophore. If the lower of the two singlet exciton states is closer in energy to the triplet state, ISC can be enhanced.[77a, 78]

1.8.4 Intramolecular Spin Conversion

The development of a general molecular motif for triplet PSs is highly desired for chromophores which lack heavy atom effect, and thus ISC property cannot be predicted. Generally, a dyad as a triplet PS can be constructed, in which an intramolecular energy acceptor with intrinsic ISC property is used as a spin convertor together with a light harvesting energy donor. The most promising aspect of this strategy is that the ISC of these heavy atom free chromophores is predictable. At present C_{60} is used as a spin convertor.[79]

1.9 Types of Photosensitizers

There are several groups of UV-vis absorbing molecules that have shown singlet oxygen generating ability. The different classes of photosensitizers include:

- Organic dyes and aromatic hydrocarbons
- Porphyrins, phthalocyanines, and related tetrapyrroles
- Semiconductors
- Transition metal complexes

1.9.1 Organic Dyes and Aromatic Hydrocarbons

Dyes such as Rose Bengal (**20**), eosin (**21**), and methylene blue (**22**) are very effective photosensitizers, as they possess triplet states of appropriate energies for sensitization of oxygen. Methylene blue is a phenothiazinium dye with strong absorbance in the range of 550-700 nm, and a significant singlet oxygen quantum yield ($\phi_\Delta = 0.52$).[80] Aromatic hydrocarbons such as napthalenes, anthracenes, and biphenyls have also been studied for their photosensitizer ability. These studies found that the competition of charge transfer interactions with the energy transfer pathway was of greater importance for biphenyls than for the napthalenes.[81] Guiterez *et al*. have obtained the singlet oxygen quantum yields from a range of quinone and anthraquinone derivatives (**23**) and these compounds were found to be excellent sensitizers for singlet oxygen in aprotic solvents (ϕ_Δ= 0.69 for anthraquinone-2- sulfonic acid and 1,8-dihydroxyanthraquinone, for example), as well as moderate quenchers of $^1O_2$ by physical deactivation.[82] Hypocrellins have sizeable singlet oxygen quantum yield values, for example, hypocrellin B (**17**) has ϕ_Δ= 0.76, but they lack strong absorptivity at energies greater than 600 nm, which has limited their application to date.[83] Boron dipyrromethene (Bodipy) is one of the most extensively investigated organic chromophores for their triplet state studies also. The formation of the triplet state of Bodipy upon photoexcitation, can be achieved *via* the well-known approach such as the heavy atom effect (including I, Br, Ru, Ir, etc.), and the new methods, such as using a spin converter (e.g., C_{60}), charge recombination, exciton coupling, etc. All the Bodipy-based triplet photosensitizers show strong absorption in visible or near IR light and the long-lived triplet excited state, which are important for PDT. For example, Ramaiah and co-workers reported iodinated azaBodipy as a triplet photosensitizer (**25**) shows absorption at 666 nm, with a molar absorption coefficient of 69 900 M^{-1} cm^{-1}.[84]

1.9.2 Porphyrins, Phthalocyanines and Related Tetrapyrroles

Recently, the attention on photosensitizers has been focused on porphyrins and their analogues (**26** and **27**) because their presence in natural systems makes them ideal candidates for use in biological singlet oxygen generation. These photosensitizers generally lack cytotoxicity in the absence of light, which makes them important in certain applications.

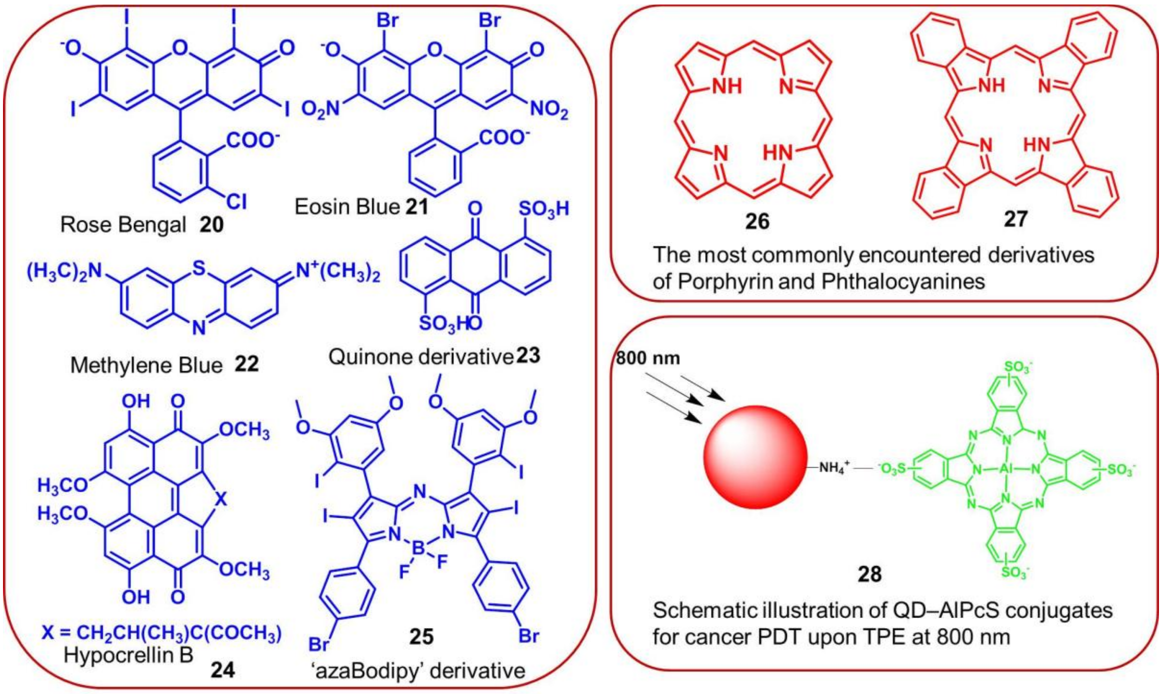

The most commonly encountered derivatives of Porphyrin and Phthalocyanines

Schematic illustration of QD–AlPcS conjugates for cancer PDT upon TPE at 800 nm

Figure 1.14: Some common examples of triplet photosensitizers.

A well-studied porphyrin used in the photosensitized production of singlet oxygen is haematoporphyrin. Although its triplet quantum yield and singlet oxygen production quantum yields are high (0.83 and 0.65 respectively) its absorption at 630 nm ($\varepsilon = 3500\ M^{-1}\ cm^{-1}$) is weaker than that of an ideal photosensitizer.[85a] A long triplet lifetime and a relatively high triplet quantum yield, which are useful qualities for a photosensitizer and metallophthalocyanines containing diamagnetic metal ions such as Al^{3+} or Zn^{2+} possess these properties.[85c] The major problems associated with these systems are aggregation and bleaching in presence of singlet oxygen. Napthalocyanines are macrocycles with a second benzene ring added on the periphery of the phthalocyanine ring. This additional conjugation leads to the absorption of longer wavelength light than the phthalocyanines (770 compared with 680 nm) that could prove useful in the treatment of highly pigmented tumors in PDT.[86]

1.9.3 Semiconductors

Singlet oxygen production from photoexcited semiconductors such as TiO_2 and ZnO has received little attention when compared to that of active oxygen species such as hydroxyl radicals and superoxide anion.[87a] Two-photon excitation nanoparticle-based PSs that combine the advantages of TPE and nanotechnology have emerged as attractive therapeutic agents for NIR light excited PDT for cancer treatment. For example, In 2013, Chou *et al.*, used a core-shell CdSe/CdS/ZnS quantum dot as the TPE energy donor to sensitize electrostatically absorbed sulfonated aluminum phthalocyanine (**28**) molecules upon two-photon irradiation with an unfocused 800 nm femtosecond pulsed laser beam.[87b] The FRET mediated $^1O_2$ generation and PDT was subsequently studied *in vitro* in cultured human HeLa and KB cancer cells.

1.9.4 Transition Metal Complexes

Most of the studies in singlet oxygen photosensitization involve organic molecules but there are also inorganic complexes that have shown to be efficient photosensitizers. Atoms with large atomic number can induce strong SOC, and as a result enhance ISC. Therefore, one straightforward approach to prepare triplet PSs is to attach heavy atoms to a chromophore and these complexes can be used as triplet PSs if the absorption in the visible region is strong.[88] PSs with bromo- or iodo- substituents and the transition metal complexes belong to this category. Due to heavy atom effect of transition metal atoms such as Pt(II), Ir(III), Ru(II), etc., efficient ISC were usually observed for these complexes. Dramatic developments have occurred in the use of metal complexes for PDT in biomedical research in the last few years. Among several organometallic complexes, Ir(III) complexes offer multiple advantages when compared to poor cell permeability of Ru(II) complexes and labile ligands of Pt(II) complexes. In addition, high photostability, long lifetime, good phosphorescence quantum yield, large stokes shift, colour tunability and importantly ROS generation under normoxic or hypoxic conditions of Ir(III) organometallic complexes offer a potential PSs candidate for diagnosis *via* imaging and therapeutic applications in cancer.[76] The common classes of Ir(III) complexes used for photodynamic therapy and imaging applications is given in the Figure 1.15.

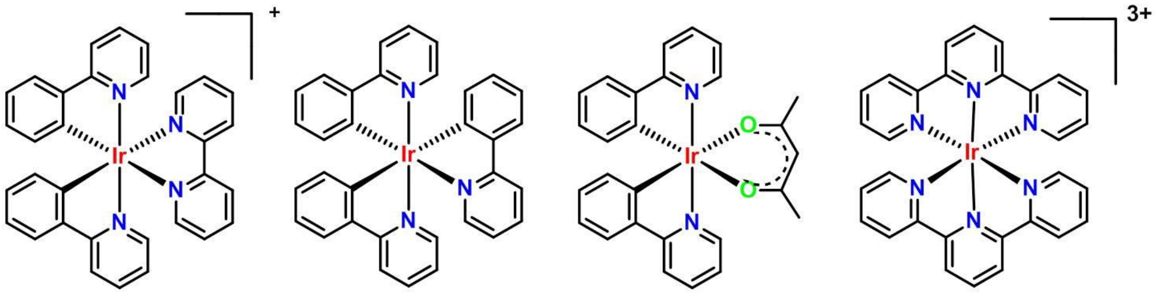

29 **30** **31** **32**

Figure 1.15: Examples of common classes of Ir(III) complexes used for photodynamic therapy and imaging applications.

1.10 Singlet Oxygen Generation by Iridium Complexes

Several classes of Ir(III) complexes are now been developed with a view to study singlet oxygen generation.[13] You and Nam reviewed the rapid expansion of chemistry and application of cyclometalated Ir(III) complexes, including a handful studies that have looked at the photogeneration of singlet oxygen.[89] As with selected Ru(II) species, Ir(III) complexes can show impressive ϕ_Δ value upto unity. Ir(III) complexes incorporating two cyclometalated ligands and an ancillary diketonate (*i.e.* [Ir(C^N)$_2$(O^O)]) (**31**) have shown both energy and electron transfer pathways to yield singlet oxygen.[90] Murata has extensively studied about Ir(III) complexes (**33-36**) and looked at the influence of ligand type upon photooxidation performance. ϕ_Δ values range from 0.26 for [Ir(pip)$_2$(acac)] (pip = 2-phenylimidazo-4,5-f-1,10-phenanthroline) (**33**) to 0.97 for [Ir(ppy)$_2$(bpy)] (ppy = 2-phenylpyridine) (**36**) and the authors propose that difference in oxidation potential of the sensitizer and the triplet energy levels influence $^1O_2$ generating efficiency.[91] For these studies, 1,5-dihydronaphthalene was used as a $^1O_2$-scavanging agent, allowing the photodegradation kinetics of $^1O_2$ to be determined.

Importantly, the cationic complexes in the series [Ir(ppy)$_2$(N^N)]$^+$ (**29**) did not show any photodegradation, whilst impaired photooxidation performances from some of the neutral species was attributed to poor photochemical stability.

Sun *et al*., have extended this work and studied a range of Ir(III) complexes based on the [Ir(ppy)$_2$(phen)]$^+$ core, investigating the influence of extended conjugation of the phenanthroline ligand, thereby increasing the absorption coefficient of the visible region bands around ε_{465nm} = 50000 M^{-1} cm^{-1} (**37**).[92] This enhancement in absorption efficiency was also accompanied by a dramatic extension in the triplet lifetimes of the complex and singlet oxygen production *via* energy transfer. In a subsequent development, together with Zhao, Pope and co-workers investigated the photooxidation characteristics of the first example of pyrene based chromophores cyclometalated to Ir(III) (**38**).[93] Complexes of the neutral cyclometalated [Ir(C^N)$_3$] or heteroleptic cationic [Ir(C^N)$_2$(N^N)]$^+$ were synthesized and showed singlet oxygen photogeneration. Of the complexes studied, the cationic species performed most effectively.

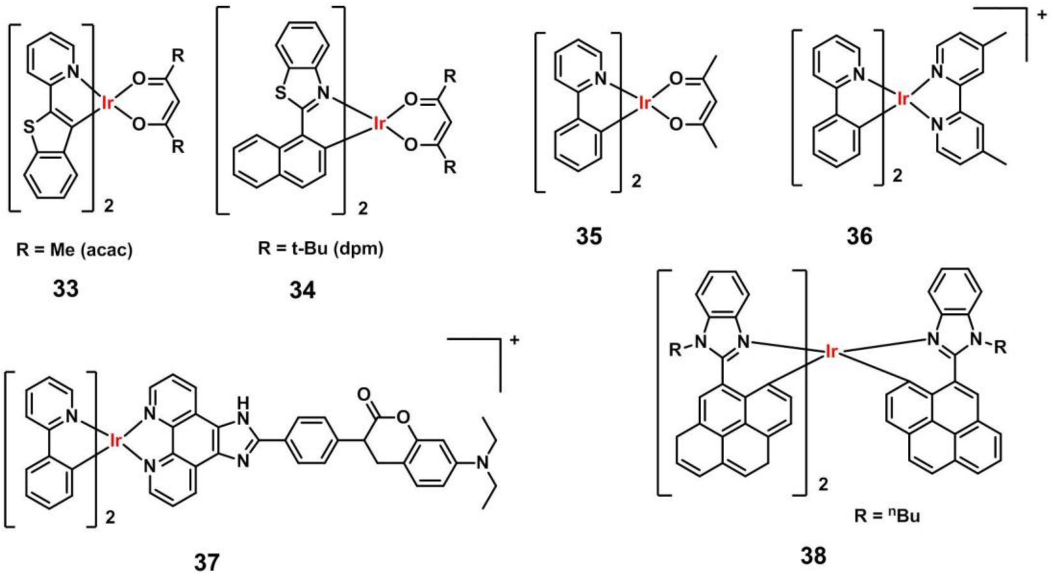

Figure 1.16: Examples of various types of Ir(III) complexes used for the generation of singlet oxygen **33-38**.

Recently, several modification was done in Ir(III) complexes which improved its efficiency. A polymer complex (**39**) was synthesized by binding bis(cyclometalated) Ir(ppy)$_2^+$ fragments (ppy = 2-phenylpyridyl) to phenanthroline (phen) pendants of a poly-(amidoamine) copolymer (PhenISA, in which the phen pendants involved ~6% of the repeating units) (**39**) by Maggioni and co-workers.[94] The corresponding molecular complex $[Ir(ppy)_2(bap)]^+$ (1_M, bap = 4-(butyl-4-amino)-1,10-phenanthroline) (**40**) was also prepared for comparison. In water solution **39** gives nanoaggregates with a hydrodynamic diameter of 30 nm in which the lipophilic metal centers are presumed to be segregated within polymer tasks to reduce their interaction with water. Photoreaction of O_2 with 1,5-dihydroxynaphthalene showed that **39** is able to sensitize $^1O_2$ generation but with half the quantum yield of **40**. Cellular photodynamic therapy tests showed that both **40** and **39** are able to induce cell apoptosis upon exposure to Xe-lamp irradiation. The fraction of apoptotic cells for **40** was higher than that for **39** (74 and 38%, respectively) 6 h after being irradiated for 5 min, but cells incubated with **39** showed much lower levels of necrosis as well as lower toxicity in the absence of irradiation. More generally, the results indicate that cell damage induced by **40** was avoided by binding the iridium sensitizers to the poly(amidoamine).

Natrajan *et. al.*, developed a new Ir(III) cyclometalated complex bearing a fluorenyl 5-substituted-1,10-phenanthroline ligand ($[Ir(ppy)_2(L1)][PF_6]$, ppy = 2-phenylpyridine, L1 = ancillary ligand given in the Figure 1.17) which exhibits enhanced triplet oxygen sensing properties up on two-photon excitation (**41**).[95] The complex $[Ir(ppy)_2(L1)][PF_6]$ exhibit relatively high two photon absorption efficiencies for the lowest energy MLCT electronic transitions with two-photon absorption cross sections that range from 50 to 80 GM between 750 to 800 nm. Also, Sun and co-workers studied the photodynamic therapeutic effect of six cationic biscyclometalated Ir(III) complexes with extended π-conjugation on the diimine ligand and/or the cyclometalating ligands.[96] Extending the π-conjugation on the cyclometalating ligand affects both ground-state absorption and the nature of the emitting triplet excited states. The phototherapeutic margin for complex **42** is observed to be very high for an Ir(III) complex PS having broad visible or red light activation, and its interaction with plasmid DNA suggests that a photocytotoxicity mechanism other than singlet oxygen sensitization may be operative.

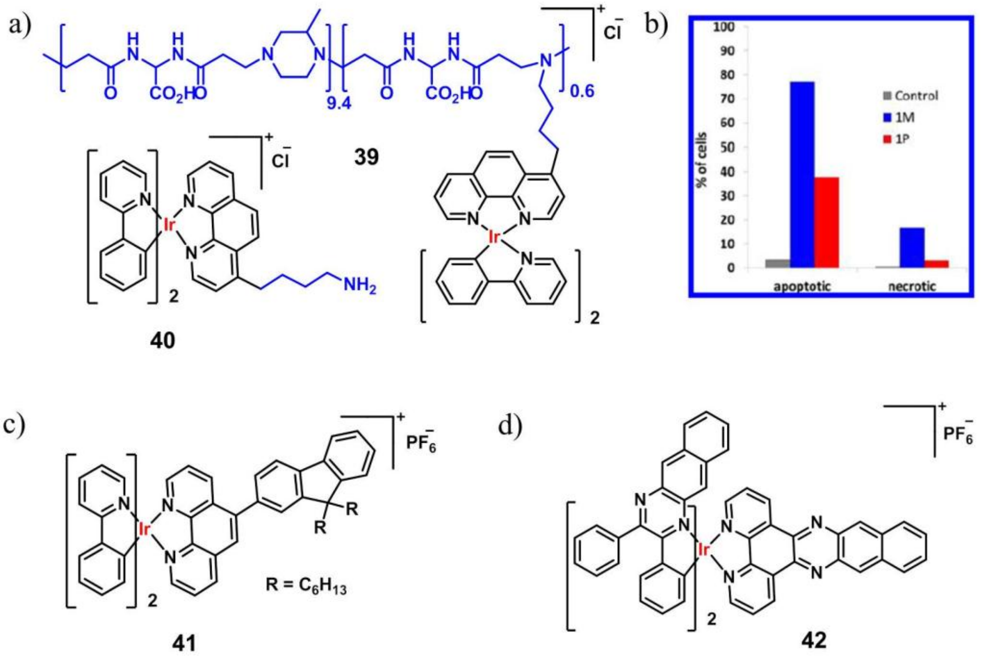

Figure 1.17: (a) Molecular structures of I_P and I_M (**39** and **40**), (b) Percentages of dead cells resulting from apoptotic or necrotic events upon PDT treatments (6 h after being irradiated for 5 min) in control samples and samples sensitized by **39** or **40**. (c) Molecular structure of **41** and (d) Molecular structure of **42**, having highest singlet oxygen quantum yield among the six complexes prepared by Sun and co-workers

1.11 Use of Iridium (III) Complexes in Biological System

There are several requirements for the synthesized complex to use in the biological system and several modifications in the ligand helps to attain more efficiency. Three major criteria are discussed below.

1.11.1 Uptake Efficiency

An important requirement for an intracellular PDT/imaging reagent is efficient uptake by cells, preferably in a controlled manner. The cellular uptake of Ir(III) complexes is known to be closely related to lipophilicity, and therefore cyclometalated Ir(III) polypyridine complexes show more efficient cellular uptake when compared to their chloro counterparts, as a result of increased lipophilicity caused by the cyclometalating and polypyridine complexes.[97] Velders *et. al.*, reported a series of Ir(III) mono-, bis- and tris- amino acid complexes, **43-51** which show variable cellular uptake.[98] The number (mono-, bis-, tris-) and type (glycine, alanine, lysine) of amino acids influence both the cellular uptake and, to a lesser extent, intracellular localization of the complex. All three mono substituted Ir(III) complexes gave a remarkably higher cellular uptake than the bis- and tris- substituted complexes. Ir (III) complexes conjugated to lysine in general exhibit a higher uptake with respect to the correspondingly substituted glycine and alanine derivatives (**43**). These differences are believed to be due to the lipophilicity of the complexes. The lipophilicity of the complexes $[Ir(N^\wedge C)_2(bpy\text{-}C_nH_{2n+1})]^+$ (n = 18, 10, 2) bearing an aliphatic alkyl chain ranges from -0.34 to 9.89.[99] Although efficient internalization of the complex is supposed to be assisted by high lipophilicity, the most liphophilic complex of this family is taken up least efficiently by cells due to higher degree of self-aggregation in aqueous solution.

1.11.2 Uptake Mechanism

The cellular uptake mechanism of Ir(III) polypyridine complexes have been investigated by studying uptake efficiency at different temperature using various uptake inhibitors. The complex $[Ir(ppy)_2(bpy\text{-}(C_4)_2]^+$ forms a diffuse emissive background with cytoplasmic granules upon internalization into HeLa cells at 37 ^oC.[100] The disappearance of the cytoplasmic foci upon incubation of HeLa cells with this complex, either at 4 ^oC or in the presence of endocytic inhibitors, suggest that the complex enters cells by both passive diffusion and endocytosis pathways. The attachment of biological substrates to Ir(III) polypyridine complexes is found to affect their intracellular distribution and cellular uptake mechanisms.[101] For example, the internalization of the indole complexes is *via* an energy requiring process such as endocytosis. Mao *et al.*, reported four different biscyclometalated Ir(III) complexes **52 - 55** where no biological substrates were attached. Incubation of A549 cells with **52** at lower temperature (4 ^oC) results in a reduced cellular uptake efficiency as revealed by confocal microscopy.[102] Pretreatment of the cells with metabolic inhibitors, 2-deoxy-D-glucose and oligomycin, can lower the cellular uptake levels of the complexes, while the endocytosis modulator chloroquine shows no effect on the ability of complexes to cross the plasma membrane. Thus it is clear that **52** penetrate the cell membrane through an energy dependent mechanism and do not rely on the endocytic pathways. The same group reported similar observations in other similar derivatives.[102]

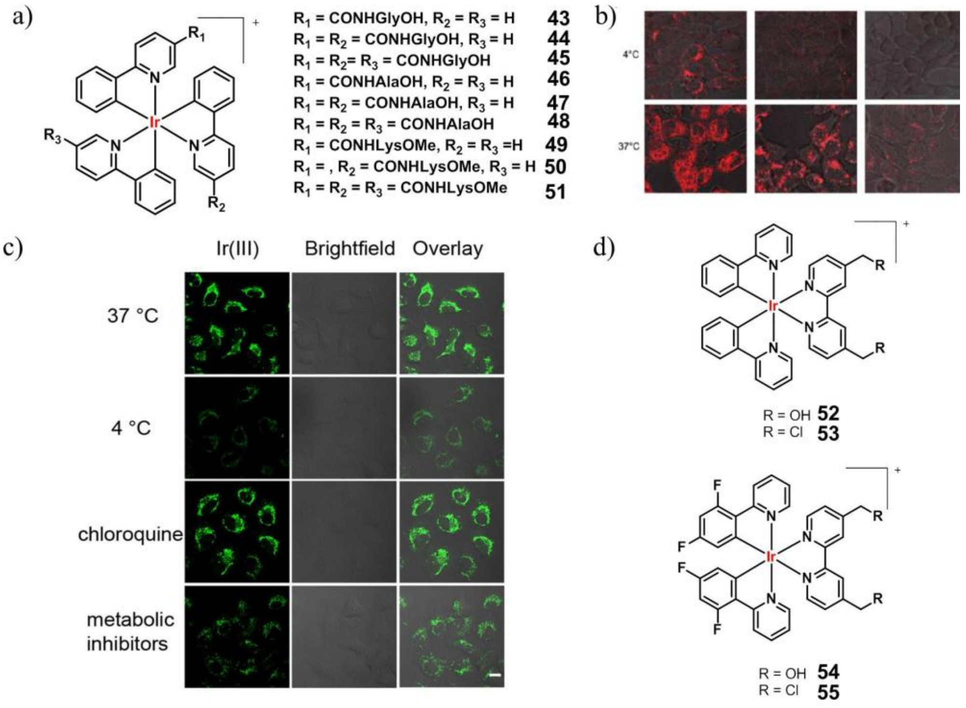

Figure 1.18: (a) Molecular structures of mono-, bis- and tris- amino acid substituted Ir(III) complexes (**43-51**). (b) Confocal microscopy images of the cellular distribution of the various lysine substituted Ir(III) complexes **43-45**. Difference in distribution of the number of lysine residues from left to right: mono- (**43**), bis- (**44**), and tris- (**45**) substituted complexes. Cells were incubated for 1 h at 4 °C (top row) or 37 °C (bottom row) with 10 μM complex in 0.3% DMSO/cell culture medium. Cell transmission images were overlaid with the luminescence image. (c) Cellular uptake mechanisms of complex **52**. A549 cells were incubated with **52** (10 μM, 1 h) under different temperature, pretreated with chloroquine (50 μM) or metabolic inhibitors (2-deoxy- D-glucose (10 mM) and oligomycin (3 μM)). λ_{ex} = 405 nm; λ_{em} = 630 ± 20 nm. Scale bar: 10 μm. (d) Molecular structures of complexes **52 -55**.

1.11.3 Cytotoxicity

Many Ir(III) complexes suffer from high cytotoxicity, which limits their use as live cell imaging/PDT agents. Decreasing lipophilicity of these complexes can efficiently reduce the cytotoxicity by lowering their uptake efficiency. This problem of high cytotoxicity has been circumvented by the incorporation of poly(ethyleneglycol) (PEG) into complexes. The long PEG chains protect the complexes from interacting nonspecifically with intracellular biomolecules and/or organelles.[103] Recently complexes with specific organelle targeting moieties also found to have less cytotoxicity because of the specific localization of the probe.

1.12 Activatable Photosensitizers for Imaging and Therapy - Theranostic Applications

Photosensitizers are not restricted solely on therapeutic generation of singlet oxygen. Many of the photosensitizers tend to emit in the near infrared region of the spectra in addition to the bright fluorescence which are useful for *in vivo* imaging.[70,71] Theranostic refers to an appealing formulation of combining therapy and diagnosis to improve drug’s efficacy and its distribution to the tumor-affected site. Theranostics play a key role in the assessment of chemotherapy by visualizing the tumor size and providing feedback information on the therapy status. Fluorescent signals may also be used as optical biopsy, that differentiate between benign and malignant cell and avoiding standard histological evaluation. In addition, evaluation of the success or failure of treatment may be monitored through the photosensitizer fluorescence (as target cells are destroyed, fluorescence signal decreases), which may be a useful dosimetric guide for real time modification during therapy.[71]

Luminescent photosensitizers can aid in determining photosensitizer localization and degree of photosensitizer uptake by diseased tissue. These photosensitizer characteristics can be further exploited in photosensitizers that are only active in the presence of target molecule upon which fluorescence and singlet oxygen production occur. While conventional photosensitizers often can serve as fluorophores suitable for *in vivo* studies, extraneous phototoxicity to non-target tissues can occur in the course of imaging and photosensitizer localization. Photosensitizers that are not phototoxic outside activation or target site would therefore be more powerful imaging probes due to a reduction in non-specific phototoxicity. Activatable photosensitizers are ideal imaging probes as molecular activation distinguishes target cells from normal cells. Another utility of photosensitizers is that they may be conjugated to agents from other imaging modalities. Radio-labeled photosensitizers and MRI contrast agent-conjugated photosensitizers have been described and provide a multifunctional probe with the capability of two imaging modalities as well as therapeutic function.[14]

Ir(III) complexes possess many advantageous characteristics for their use as biological reagents; for example, the possible utilization of a wide range of ligands enables fine tuning of their physical and chemical properties. Many of these complexes, especially those with polypiridine ligands, show intense, long lived and environmental sensitive emission, which would allow the complexes to serve as reporters of their local surroundings and intracellular biological events. The intracellular trafficking and distribution of these complexes can also be followed conveniently by fluorescence method such as laser scanning confocal microscopy. The long-lived phosphorescence of these complexes facilitates the use of phosphorescence life time imaging (PLIM), which offers very high sensitivity. The detailed examples are discussed in the following sections.[14]

1.13 The Basic Organelle-Targeting Methods of Metal Complexes

Cells are the fundamental functional units of all life on earth, and organelles are essential part of a cells structure and its function. The various organelles found in eukaryotic cells include the cytomembrane, lysosome, mitochondrion, Golgi apparatus, ER, and nucleus, located from the periphery to the core. Each organelle plays its respective role to support the normal functions of cells and thus the life of the whole body. Organelle dysfunction can lead to a series of diseases, including cancer, Parkinson’s disease, Alzheimer’s disease, and diabetes.[104]

As a result of the clinical success of cisplatin in the early 1960s, metal complexes for biological applications have made considerable progress over the past half-century.[105,106] In recent years, anticancer metal complexes have been designed to specifically target organelles in order to increase their therapeutic effect.[107] Meanwhile, for high photostability, large Stokes shifts, and long luminescence lifetimes, luminescent metal complexes have been employed as organelle-targeting probes to study the functions of organelles.

There are two basic methods for metal complex targeting of organelles: one of them is the coordination of a metal center with organelle-targeting moieties, and the other is regulating the relative properties of a metal complex to satisfy the requirements of organelle-targeting. The above mentioned organelle-targeting moieties can be divided into peptides and small molecules. A major difference between the above two is that the efficacy of peptides as targeting moieties be degraded by enzymes where small molecules remain unaffected. Despite this problem, the two different moieties are used widely. Another strategy for targeting of organelles involves varying the ligands of a complex to regulate the relevant property desired for the targeting of a specific organelle.[14]

There are two strategies for designing lysosome-targeting metal complexes (LyTMCs). First one is the incorporation of lysosome targeting moieties in the metal complex. These moieties generally include amine groups, among which morpholine is the commonly used moiety. Once lipophilic LyTMCs diffuse into lysosomes, the acidic environment will protonate the amine groups and the positively charged LyTMCs accumulate inside the lysosome trapped by their inability to cross the membrane. It is believed that the amine groups could achieve a 100-fold enrichment in the lysosomes. The second strategy depends on the endocytic pathway. Hydrophilic cationic metal complexes cannot freely diffuse into cells but can enter cells by endocytosis. As lysosomes are the final destinations of endocytosis, the process can be used to selectively target metal complexes to lysosomes.[108]

Mao *et al.,* developed two Ir(III) complexes that can specifically image lysosomes and induce an autophagic response in live cells. These two features make them ideal probes to track autophagic lysosomes.[109] The probe, **56** exhibit

TPA and emission properties, which greatly enhance their sensitivity and expand their compatibility with other staining methods by minimizing the interference with the background noises and other labeling agents. The same probe has been used for photodynamic therapeutic applications and serves as theranostic agents. The detailed description is given in Chapter 4, section 2. Chao and co-workers also worked on the organelle targeted Ir(III) complexes and recently reported a water soluble effective two-photon phosphorescent lysosomal probe **57** for long-term tracking.[110] Due to its large Stokes shift, low cytotoxicity, superior photostability, long-term specifically localized in the lysosomes, and excellent two-photon properties, **57** has been used to track lysosomes during cell migration and apoptosis.

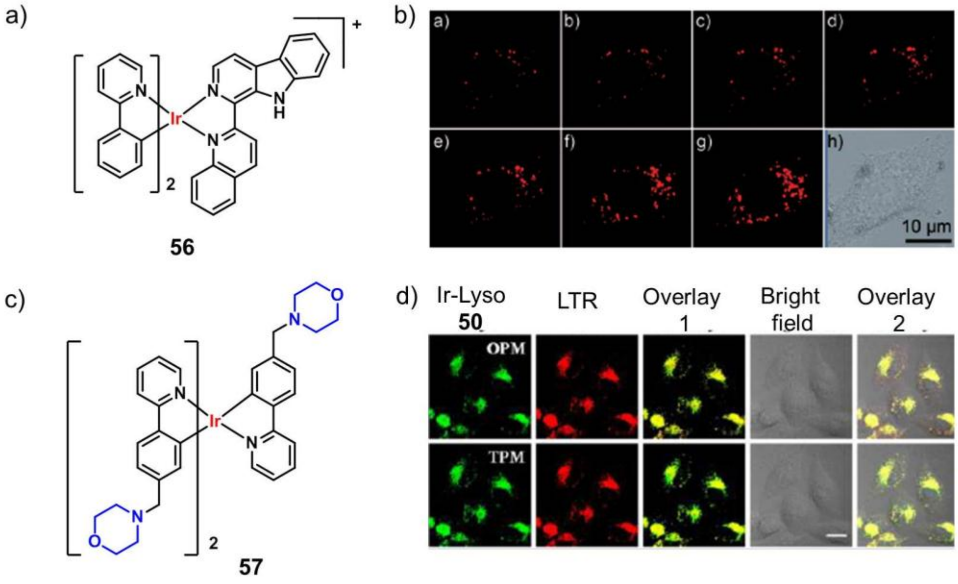

Figure 1.19: (a) Molecular structure of lysosome targeting probe, **56**. (b) Two-photon excited real-time tracking of lysosomes in A549 cells stained with **56** (10 μm) at 37 °C for different time intervals; 0.25 h, 0.5 h, 1 h, 1.5 h, 2 h, 4 h, 6 h, and bright field. (c) Molecular structure of lysosome targeting probe, **57**. (d) OPM and TPM images of HeLa cells colabeled with **57** (2 μM, 0.5 h) and LTR (50 nM, 0.5 h). Scale bar: 20 μm.

Horobin *et al.*, suggested that a molecule with a log(P) value (probe lipophilicity) between 0 and 5 and a cation number greater than 0 showed a high probability of mitochondrial localization and that the cation with a log(P) value between −5 and 0 showed a high probability of lysosomal localization.[111] Thus, Chao and co-workers synthesized five different biscyclometalated Ir(III) complexes were the ancillary ligand was 4-(4-pyridin-2-yl)benzyl)-morpholine **58-62**.[112] The size of the conjugated aromatic rings of the main ligands decreased gradually. The complexes **58** and **59** were found in the mitochondria because of their lipophilicity and **60-62** were found in the lysosomes because of their hydrophilicity.

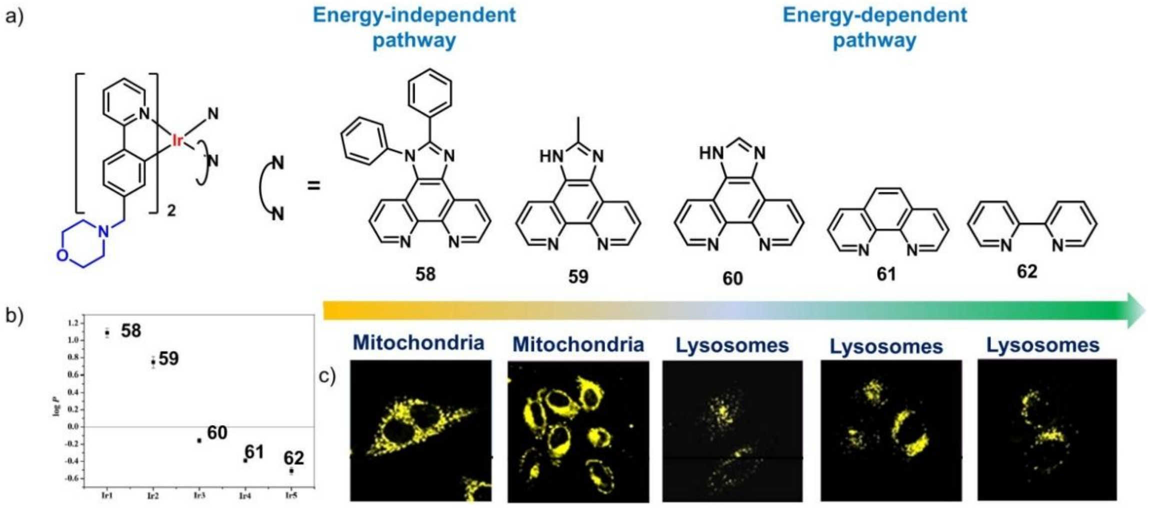

Figure 1.20: (a) Chemical structures, (b) n-octanol/water partition coefficients, (c) cellular localization, and cellular uptake mechanisms of complexes **58-62** (λ_{ex} = 405 nm, λ_{em} = 570 ± 20 nm). "Energy-independent pathway" means the complex (**58**) do not need energy to enter cells, "energy-dependent pathway" means the complexes (**59-62**) need energy to enter cells.

Due to the proton pumping effect induced by mitochondrial oxidative phosphorylation, the mitochondrial outer membrane possesses a strong negative potential as high as 180-200 mV.[113] Considering also the lipophilicity of the outer membrane, most MiTMCs (Mitochondria targeting metal complexes) that have been developed are lipophilic cations. Some MiTMCs have intrinsic cationic lipophilicity and can target mitochondria without any modification. The extrinsic MiTMCs have no preference towards mitochondria and must be modified with a mitochondrial targeting group. The group could be a lipophilic cation to take advantage of the mitochondrial membrane potential or a mitochondrial targeting peptide to take advantage of the protein import machinery. Currently, TPP is considered to be most popular lipophilic cation for mitochondrial targeting.[114] The positive charge of TPP makes an effective electrostatic attraction between TPP to the negatively charged mitochondrial membrane.

A new class of phosphorescent cyclometalated Ir(III) polypyridine poly(ethylene glycol) complexes for mitochondria targeted PDT (**63**) has been reported by Lo and co-workers.[115] Their PEG free counterparts were also studied. Compared to their counterparts, the PEG complexes did not show cytotoxicity in dark, but were highly toxic under light. The localization of these complexes in mitochondria allows rapid necrotic cell death upon light activation. Generally complex incorporates a minimum planar aromatic system and an overall positive charge that tends to localize inside the nucleus.[116] The Li research group designed a new strategy to fabricate a non-emissive reaction based Ir(III) complex for visualizing nuclei of living cells (**64**).[117] The complex was able to rapidly and selectively illuminate the nuclei and showed very low dark cytotoxicity. A cellular uptake assay indicated that the complex entered the nucleus *via* an energy-dependent pathway within a few minutes.

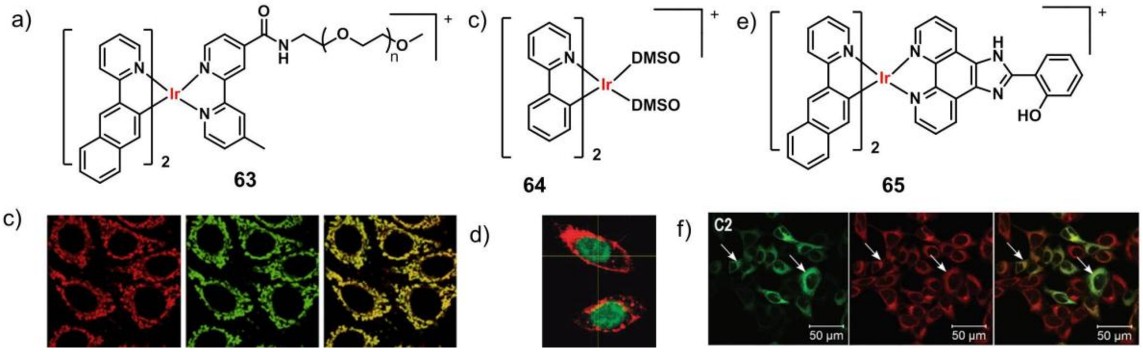

Figure 1.21: (a) Molecular structure of mitochondria targeting probe, **63**. (b) Laser-scanning confocal microscopy images of HeLa cells upon incubation with complex **63** (λ_{ex} = 405 nm) and then by MitoTracker Red (λ_{ex} = 633 nm) at 37 °C. (c) Molecular structure of nucleus targeting probe, **64**. (d) Three-dimensional luminescence images of live KB cells loaded with 10 μM **64** in DMSO/PBS (pH 7.4, 1:99, v/v) for 10 min at 25 °C. (e) Molecular structure of ER targeting probe, **65**. (f) Confocal fluorescence images of MCF7 cells treated with **65** (λ_{ex} = 405 nm and λ_{em} = 550–610 nm). CellLight ER-GFP (λ_{ex} = 488 nm and λ_{em} = 490–540 nm) and merged image.

Recently, the ER was also chosen as a target for PDT. For the large lipophilic membrane of the ER, the required features of intrinsic ER targeting metal complexes are lipophilicity, a positive charge and moderately-sized conjugated ligands.[118] Extrinsic ER targeting complexes are made by addition of ER-targeting signal peptides, which can avoid lysosomes *via* the clathrin-independent pathway. In 2014, Gupta and Ray developed a series of heteroleptic phosphorescent cyclometalated Ir(III) complexes as photosensitizers with an imidazolyl modified phenanthroline ligand.[105b] Due to strong intramolecular hydrogen bonding interactions and cationic nature, complex, **65** was found in the ER by coloalization study. The use of Ir(III) complexes for imaging and PDT applications is now a rapidly growing area.

1.14 Objectives and Methodologies of the Present Investigation

Inspired by the recent progress in the design of synthetic molecular probes for organelle targeted sensing and therapeutic applications, we decided to explore the possibility of utilizing a few fluorescent organic molecules having bipyridine moieties for sensing and imaging. In addition, a few cyclometalated Ir(III) complexes were designed for photodynamic therapeutic and theranostic applications. The bipyridine based ligands are well explored in the literature for sensing applications and for the preparation of metal complexes. Therefore, we focused on developing a few bipydine based ligands incorporated with organelle targeting moieties to achieve targeted imaging as well as some photosensitizers for efficient PDT applications.

With the above objectives, we performed the synthesis of lysosome targeting carbazole-bipyridine conjugates, **CBL1-3** and **CBG**, where bipyridine is a well-known receptor for Zn^{2+} and morpoline is identified as the best organic moiety to target lysosome. We carried out a detailed investigation on the photophysical and sensing properties. The dual analyte sensing was achieved due to the formation of nano-aggregates. After the detailed investigations, we choose the best probe, **CBL2** to use in the biological system. HeLa cells were employed for pH and Zn^{2+} imaging in lysosome and we studied the effect of pH regulators, oxidative stress and apoptotic studies.

Next we choose the probe **CBL2** as the ancillary ligand to make Ir(III) complex, **IrL1** for photodynamic therapeutic applications. For a comparative study, we used a highly conjugated ancillary ligand and synthesized another complex **IrL2**. The detailed triplet state studies and singlet oxygen quantum yield measurement showed better efficiency for **IrL2**. The morpholine moiety attached to the complex helps to target lysosome. The cellular studies were also conducted with the same probe. The luminescence intensity was found to be less for this molecule. The apoptotic experiments were planned with MD-MBA 231 cell lines and the mechanism of the cell death was analyzed by flow cytometry and caspace-3/7 detection agent.

We then designed a lysosome targeting cyclometalated Ir(III) complex for both imaging and photodynamic theraperutic applications. The synthesized probe, **Ir-Bp-Ly** showed good luminescence and singlet oxygen quantum yields with high water solubility. The detailed investigations were done in the C6 glioma cells. In short, we discuss the synthesis and detailed investigation of organic molecules and cyclometalated Ir(III) complexes for diagnostic, therapeutic and theranostic applications.

1.7. References

(1) Kobayashi, H.; Ogawa, M.; Alfrod, R.; Choyke, P. L.; Urano, Y. *Chem. Rev*. **2010**, *110*, 2620–2640.

(2) Yao, J.; Yang, M.; Duran, Y. *Chem. Rev*. **2014**, *114*, 6130–6178.

(3) Kim, C.; Favazza, C.; Wang, L. V. *Chem. Rev*. **2010**, *110*, 2756–2782.

(4) Nie, L.; Chen, X. *Chem. Soc. Rev*. **2014**, *43*, 7132–7170.

(5) Yuan, J; Lin, W.; Zheng, K.; He, L.; Huang, W. *Chem. Soc. Rev*. **2013**, *42*, 622–661.

(6) Busseron, E.; Ruff, Y.; Moulin, E. Giuseppone, N. *Nanoscle* **2013**, *5*, 7098–7140.

(7) Whitesides, G. M.; Mathias, J. P.; Seto, C. T. *Science* **1991**, *254*, 1312–1319.

(8) Zhai, D.; Xu, W.; Zhang, L.; Chang, Y. T. *Chem. Soc. Rev*. **2014**, *43*, 2402–2411.

(9) Tomat, E.; Lippard, S. J. *Curr. Opin. Chem. Biol.* **2010**, *14*, 225–230.

(10) Kim, H. M.; Cho, B. R. *Chem. Rev*. **2015**, *115*, 5014−5055.

(11) Xu, Z.; Yoon, J.; Spring, D. R. *Chem. Soc. Rev*. **2010**, *39*, 1996–2006.

(12) Zhou, Z.; Song, J.; Nie, L; Chen, X. *Chem. Soc. Rev*. **2016**, *45*, 6597–6626.

(13) Stacy, O. J.; Pope, S. J. A. *RSC Adv*. **2013**, *3*, 25550–25564.

(14) Qiu, K.; Chen, Y.; Rees, T. W.; Ji, L.; Chao, H. *Coord. Chem. Rev.,* **2018**, doi: 10.1016/j.ccr.2017.10.0220010-8545.

(15) Li, X.; Gao, X.; Shi, W.; Ma, H. *Chem. Rev*. **2014**, *114*, 590–695.

(16) Newman, R. H.; Fosbrink, M. D.; Zhang, J. *Chem. Rev*. **2011**, *111*, 3614–3666.

(17) Kim, H. N.; Guo, Z.; Zhu, W.; Yoon, J.; Tian, H. *Chem. Soc. Rev*. **2011**, 40, 79–93.

(18) Wolfbeis, O. S. *Chem. Soc. Rev*. **2015**, *44*, 4743–4768.

(19) Biju, V. *Chem. Soc. Rev*. **2014**, *114*, 744–764.

(20) Chan, J.; Dodani, S. C.; Chang, C. J. *Nat. Chem.* **2012**, *4*, 973–983.

(21) (a) Yang, Y.; Zhao, Q.; Feng, W.; Li, F. *Chem. Rev*. **2013**, *113*, 192−270. (b) Boe1ns, N.; Leen, V.; Dehaen, W. *Chem. Soc. Rev*. **2012**, *41*, 1130–1172. (c) Lee, M. H.; Kim, J. S.; Sessler, J. L. *Chem. Soc. Rev*. **2015**, *44*, 4185–4191.

(22) Wang, B.; Yu, C. *Angew. Chem. Int. Ed*. **2010**, 49, 1485–1488.

(23) Mizusawa, K.; Takaoka, Y.; Hamachi, I. *J. Am. Chem. Soc*. **2012**, *134*, 13386–13395.

(24) Anees, P.; Sreejith, S.; Ajayaghosh, A. *J. Am. Chem. Soc*. **2014**, *136*, 13233−13239.

(25) (a) Duponta, C. L.; Butcherb, A.; Valasc, R. E.; Bourned, P. E.; Caetano-Anollése, G. *Proc. Natl.Acad. Sci. U.S.A.* **2010**, *107*, 10567–10572. (b) Dupont, C. L.; Yang, S.; Palenik, B.; Bourne, P. E. *Proc. Natl. Acad. Sci. U.S.A*. **2006**, *103*, 17822-17827.

(26) Frederickson, C. J.; Koh, J.-Y.; Bush, A. I.; *Nat. Rev. Neurosci*. **2005**, *6*, 449–462.

(27) Chen, Y.; Bai, Y.; Han, Z.; He, W.; Guo, Z. *Chem. Soc. Rev*. **2015**, *44*, 4517–4546.

(28) Burdette, S. C.; Lippard, S. J. *Coord. Chem. Rev*. **2001**, *216*, 333–361.

(29) Sensi, S. L.; Paoletti, P.; Bush, A. I.; Sekler, I. *Nat. Rev. Neurosci.* **2009**, 10, 780–792.

(30) Mills, C. F. *Zinc in Human Biology*; Springer-Verlag, New York, **1989**

(31) Cotton, F. A.; Wilkinson, G.; Murillo, C. A.; Bochmann, M.; Grimes, R. *Advanced Inorganic Chemistry*, Wiley New York; **1988**, Vol. 5

(32) Krezel, A.; Maret, W. *Arch. Biochem. Biophys*. **2016**, *611*, 3–19.

(33) Truong-Tran, A. Q.; Carter, J.; Ruffin, R. E.; Zalewski, P. D. *BioMetals* **2001**, *14*, 315–330.

(34) Lippard, S. J.; Berg, J. M.; *Principles of Bioinorganic Chemistry*, University Science Books, Mill Valley, **1994**

(35) Frederickson, C. J.; Suh, S. W.; Silva, D.; Frederickson, C. J.; Thompson, R. B. *J. Nutr*. **2000**, *130*, 1471S–1483S.

(36) Li, Y.; Hough, C. J.; Frederickson, C. J.; Sarvey, J. M. *J. Neurosci*. **2001**, *21*, 8015–8025.

(37) de Silva, A. P.; Moody, T. S.; Wright, G. D. *Analyst* **2009**, *134*, 2385–2393.

(38) Carter, K. P.; Young, A. M.; Palmer, A. E. *Chem. Rev*. **2014**, *114*, 4564–4601.

(39) Mello, J. V.; Finney, N. S. *Angew. Chem., Int. Ed*. **2001**, *40*, 1536–1538.

(40) Carol, P.; Sreejith, S.; Ajayaghosh, A. *J. Am. Chem. Soc*. **2005**, *127*, 14962–14963.

(41) Sreejith, S.; Divya, K. P.; Ajayaghosh, A. *Chem. Commun*. **2008**, *44*, 2903–2905.

(42) Sreejith, S.; Divya, K. P.; Jayamurthy, P.; Mathew, J.; Anupama, V. N.; Philips, D. S.; Anees, P.; Ajayaghosh, A. *Photochem. Photobiol. Sci*. **2012**, *11*, 1715–1723.

(43) Dennis, A. E.; Smith, R. C. *Chem. Commun*. **2007**, 4641–4643.

(44) Maury, O.; Guegan, J. P.; Renouard, T.; Hilton, A.; Dupau, P.; Sandon, N.; Toupet, L.; Bozec, H. L. *New. J. Chem*. **2001**, *25*, 1553–1566.

(45) Zhang, L.; Clark, R. J.; Zhu, L. *Chem. Eur. J*. **2008**, *14*, 2894–2903.

(46) Huang, Y.; Lin, Q.; Wu, J.; Fu, N. *Dyes Pigm*. **2013**, *99*, 699–704.

(47) Divya, K. P.; Sreejith, S.; Ashokkumar, P.; Yuzhan, K.; Peng, Q.; Maji, S. K.; Tong, Y.; Yu, H.; Zhao, Y.; Ramamurthy, P.; Ajayaghosh, A. *Chem. Sci*. **2014**, *5*, 3469–3474.

(48) Mandal' A. K.; He, T.; Maji, S. K.; Sun, H.; Zhao, Y. *Chem. Commun*. **2014**, *50*, 14378–14381.

(49) Philips, D. S.; Sreejith, S.; He, T.; Menon, N. V.; Anees, P.; Mathew, J.; Sajikumar, S.; Kang, Y.; Stuparu, M. C.; Sun, H.; Zhao, Y.; Ajayaghosh, A. *Chem. Asian J*. **2016**, *11*, 1523–1527.

(50) Haase, H.; Beyersmann, D. *Biochem. Biophys. Res. Commun*. **2002**, *296*, 923–928

(51) Emmerson, K.; Roehrig, K. *Comp. Biochem. Physiol., Part B: Biochem. Mol. Biol*., **1992**, *103*, 663.

(52) Ow, Y.-L. P.; Green, D. R.; Hao, Z.; Mak, T. W. *Nat. Rev. Mol. Cell Biol*. **2008**, *9*, 532–542.

(53) Murphy, M. P.; Smith, M. P. *Adv. Drug Delivery Rev*. **2000**, *41*, 235–250.

(54) Pierrel, F.; Cobine, P. A.; Winge, D. R. *BioMetals* **2007**, 20, 675-682.

(55) Hoye, A. T.; Davoren, J. E.; Wipe, P. *Acc. Chem. Res*. **2008**, *41*, 87–97.

(56) Sensi, S.; Ton-That, D.; Sullivan, P. G.; Jonas, E. A.; Gee, K. R.; Kaczmarek, L. K.; Weiss, J. H. *Proc. Natl. Acad. Sci. U. S. A*. **2003**, **100**, 6157–6162.

(57) Sensi, S. L.; Ton-That, D.; Weiss, J. H.; Rothe, A.; Gee, K. R. *Cell Calcium* **2003**, *34*, 281–284.

(58) Dickinson, B. C.; Srikun, D.; Chang, C. J. *Curr. Opin. Chem. Biol*. **2010**, *14*, 50–56.

(59) Masanta, G.; Lim, C. S.; Kim, H. J.; Han, J. H.; Kim, H. M.; Cho, B. R. *J. Am. Chem. Soc*. **2011**, *133*, 5698–5700.

(60) Baek, N. Y.; Heo, C. H.; Lim, C. S.; Masanta, G.; Cho, B. R.; Kim, H. M. *Chem. Commun*. **2012**, *48*, 4546–4548.

(61) Luzio, J. P.; Pryor, P. R.; Bright, N. A.; *Nat. Rev. Mol. Cell Biol*. **2007**, *8*, 622–632.

(62) Liu, F.; Wu, T.; Cao, J; Cui, S.; Yang, Z.; Qiang, X.; Sun, S.; Song, F.; Fan, J.; Wang, J.; Peng, X. *Chem. -Eur. J*. **2013**, *19*, 1548–1553.

(63) Goldman, S. D.; Funk, R. S.; Rajewski, R. A.; Krise, J. P. *Bioanalysis* **2008**, *1*, 1445–1459.

(64) Iyoshi, S.; Taki, M.; Yamamoto, Y.; *Org. Lett*. **2011**, *13*, 4558–4561.

(65) Qin, Y.; Dittmer, P. J.; Park, J. G.; Jansen, K. B.; Palmer, A. E. *Proc. Natl. Acad. Sci. U. S. A*. **2011**, *108*, 7351–7356

(66) Ellis, C. D.; MacDiarmid, C. W.; Eide, D. J. *J. Biol. Chem*. **2005**, *280*, 28811–28818

(67) Zhang, C.; Liu, Z.; Li, Y.; He, W.; Gao, X.; Guo, Z.; *Chem. Commun*. **2013**, *49*, 11430–11432.

(68) (a) Lo, K. K.-W.; Ng, D. C.-M.; Chung, C.-K. *Organometallics* **2001**, *20*, 4999–5001. (b) Lo, K. K.-W.; Hui, W.-K.; Chung, C.-K.; Tsang, K. H.-K.; Lee, T. K.-M.; Li, C.-K.; Lau, J. S.-Y.; Ng, D. C.-M. *Coord. Chem. Rev*. **2006**, *250*, 1724–1736. (c) Stinner, C.; Wightman, M. D.; Kelley, S. O.; Hill, M. G.; Barton, J. K. *Inorg. Chem*. **2001**, 40, 5245–5250.

(69) (a) Barry, N. P. E.; Sadler, P. J. *Chem. Soc. Rev*. **2012**, *41*, 3264–3279. (b) Kastl, A.; Wilbuer, A.; Merke;, A. L.; Feng, L.; Di Fazio, P.; Ocker, M.; Meggers, E. *Chem. Commun*. **2012**, *48*, 1863–1865.

(70) Celli, J. P.; Spring, B. Q.; Rizvi, I.; Evans, C. L.; Samkoe, K. S.; Verma, S.; Pogue, B. W.; Hasan, T. *Chem. Rev*. **2010**, *110*, 2795–2838.

(71) Lovell, J. F.; Liu, T. W. B.; Chen, J.; Zheng, G. *Chem. Rev*. **2010**, *110*, 2839–2857.

(72) Lv, W.; Zhang, Z.; Zhang, K. Y.; yang, H.; Liu, S.; Xu, A.; Guo, S.; Zhao, Q.; Huang, W. *Angew. Chem. Int. Ed*. **2016**, *55*, 9947–9951.

(73) Shen, Y.; Shuhendler, A. J.; Ye, D.; Ji Xua, J.-J.; Chen, H.-Y. *Chem. Soc. Rev*. **2016**, *45*, 6725–6741.

(74) (a) Spring, b. Q.; Rizvi, I.; Xu, N.; Hasan, T. *Photochem Photobiol Sci*., **2015**, *14*, 1476–1491. (b) Bottone, M. G.; Santin, G.; Aredia, F.; Bernocchi, G.; Pellicciari, C.; Scovassi, A. I. *Cells* **2013**, *2*, 294–305. (c) Zhou, Z.; Song, J.; Nie, L.; Chen, X. *Chem. Soc. Rev*. **2016**, *45*, 6597–6626.

(75) (a) Greer, A. *Acc. Chem. Res*. **2006**, *39* (11), 797–804; (b) Corey, E. J.; Mehrotra, M. M.; Khan, A. U. *J. Am. Chem. Soc*. **1986**, *108*, 2472–2473.

(76) Zhao, J.; Wu, W.; Sun, J.; Guo, S. *Chem. Soc. Rev*. **2013**, *42*, 5323–5351.

(77) (a) Turro, N. J.; Ramamurthy, V.; Scaiano, J. C. Principles of Molecular Photochemistry: An Introduction, University Science Books, Sausalito, CA, **2009**. (b) Gorman, A.; Killoran, J.; O’shea, C.; Kenna, T.; Gallagher, W. M.; O’shea, D. F. *J. Am. Chem. Soc*. **2004**, 126, 10619–10631. (c) Yogo, T.; Urano, Y.; Ishitsuka, Y.; Maniwa, F.; Nagano, T. *J. Am. Chem. Soc*. **2005**, *127*, 12162–12163. (d) Awuah, S. G.; Polreis, J.; Biradar, V.; You, Y. *Org. Lett*. **2011**, *13*, 3884–3887. (e) Awuahab, S. G.; You, Y. *RSC. Adv*. **2012**, *2*, 11169–11183.

(78) (a) Broring, M.; Kruger, R.; Link, S.; Kleeberg, C.; Kohler, S.; Xie, X.; Ventura, B.; Flamigni, L. *Chem. -Eur. J*. **2008**, *14*, 2976–2983. (b) Ventura, B.; Marconi, G.; Broring, M.; Kruger, R.; Flamigni, L. *New. J. Chem*. **2009**, *33*, 428–438.

(79) (a) Huang, L.; Yu, X.; Wu, W.; Zhao, J. *Org. Lett*. **2012**, *14*, 2594–2597. (b) Liu, Y.; Zhao, J. *Chem. Commun.* **2012**, *48*, 3751–3753. (c) Wu, W.; Zhao, J.; Sun, J.; Guo, S. *J. Org. Chem*. **2012**, *77*, 5305–5312.

(80) Redmond, R.W.; Gamlin, J.N. *Photochem. Photobiol*. **1999**, *70* ,391–475.

(81) (a) Wilkinson, F.; Abdel-Shafi, A.A. *J. Phys. Chem. Sect. A* **1997**, *101*, 5509–5516. (b) McGarvey, D. J.; Szekeres, P.G.; Wilkinson, F. *Chem. Phys. Lett*. **1992**, *199*, 314–319. (c) Grewer, C.; Brauer, H. *J. Phys. Chem.* **1994**, *98*, 4230–4235. (d) Olea, A.F.; Wilkinson, F. *J. Phys. Chem*. **1995**, *99*, 4518–4524.

(82) Gutierrez, I.; Bertolotti, S.G.; Biasutti, M.A.; Soltermann, A.T.; Garcia, N.A.; *Can. J. Chem*. **1997**, *75*, 423–428.

(83) Diwu, Z.J. *J. Photochem. Photobiol.*, **1995**, *61*, 529–539.

(84) Adarsh, N.; Shanmugasundaram, M.; Avirah, R. R.; Ramaiah, D. *Chem. Eur. J.* **2012**, *18*, 12655–12662.

(85) (a) Wohrle, D.; Hirth, A.; Bogdahn-Rai, T.; Schnurpfeil, G.; Shopova, M. *Russ. Chem. Bull.*, **1998**, *47*, 807–816. (b) Soncin, M. *J. Photochem. Photobiol. B: Biol.*, **1998**, *42*, 202–210. (c) Darwent, J. R.; Douglas, P.; Harriman, A.; Porter, G.; Richoux, M.C. *Coord. Chem. Rev.* **1982**, 44, 83–126.

(86) DeRosa, M. C.; Crutchley, R. J. *Coord. Chem. Rev.* **2002**, *233-234*, 351-371

(87) (a) Yamamoto, Y.; Imai, N.; Mashima, R.; Konaka, R.; Inoue, M.; Dunlap, W. *Methods in Enzymology*, vol. 319, Academic Press, New York, **2000**, 29. (b) Chou, K. L.; Won, N.; Kwag, J.; Kim, S.; Chen, J. Y. *J. Mater. Chem. B* **2013**, *1*, 4584–4592.

(88) (a) Demas, J.N.; Harris, E.W.; McBride, R.P. *J. Am. Chem. Soc.* **1977**, *99*, 3547–3551. (b) Mulazzani, Q. G.; Jiun, H.; Hoffmann, M.Z.; Ford, W.E.; Rodgers, M.A. *J. Phys. Chem.* **1994**, 98, 1145–1150. (c) Connick, W. B.; Gray, H.B. *J. Am. Chem. Soc.* **1997**, *119*, 11620–11627; (d) Anhalagan, V.; Srivastava, T.S.; *J. Photochem. Photobiol. A: Chem.* **1995**, *89*, 113–119.

(89) (a) You, Y.; Nam, W. *Chem. Soc. Rev.* **2012**, *41*, 7061–7084. (b) Ruggi, A.; van Leeuwen, F. W. B.; Velders, A. H. *Coord. Chem. Rev.* **2011**, *255*, 2542–2554.

(90) Djurovich, P. I.; Murphy, D.; Thompson, M. E.; Hernandez, B.; Gao, R.; Hunt, P. L.; Selke, M. *Dalton Trans.* **2007**, 3763–3770.

(91) Takizawa, S.; Aboshi, R.; Murata, S. *Photochem. Photobiol. Sci.* **2011**, *10*, 895–903.

(92) Sun, J.; Zhao, J.; Guo, H.; Wu, W. *Chem. Commun.* **2012**, *48*, 4159–4161.

(93) Hallet, A. J.; White, N.; Wu, W.; Cui, X.; Harton, P. N.; Coles, S. J.; Zhao, J.; Pope, S. J. A. *Chem.Commun.* **2012**, *48*, 10838–10840.

(94) Maggioni, D.; Galli, M.; D’Alfonso, L.; Inverso, D.; Dozzi, M. V.; Sironi, L.; Iannacone, M.; Collini, M.; Ferruti, P.; Ranucci, E.; D’Alfonso, G. *Inorg. Chem.* **2015**, *54*, 544−553.

(95) Boreham, E. M.; Jones, L.; Swinburne, A. N.; Blanchard-Desce, M.; Hugues, V.; Terryn, C.; Miomandre, F.; Lemercier, G.; Natrajan, L. S. *Dalton Trans*. **2015**, *44*, 16127–16135.

(96) Li, Y.; Dandu, N.; Liu, R.; Li, Z.; Kilina, S.; Sun, W. *J. Phys. Chem. C* **2014**, *118*, 6372−6384.

(97) (a) Yu, M.; Zhao, Q.; Shi, L.; Li, F.; Zhou, Z.; Yang, H.; Yi, T.; Huang, C.; *Chem. Commun*. **2008**, 2115–2117. (b) Zhao, Q.; Yu, M.; Shi, L.; Liu, S.; Li, C.; Shi, M.; Zhou, Z.; Huang, C.; Li, F. *Organometallics* **2010**, *29*, 1095–1100.

(98) Steunenberg, P.; Ruggi, A.; van den Berg, N. S.; Buckle, T.; Kuil, J.; van Leeuwen, F. W. B.; Velders, A. H. *Inorg. Chem*. **2012**, *51*, 2105−2114.

(99) Lo, K. K.-W.; Lee, P.-K.; Lau, J. S.-Y. *Organometallics* **2008**, *27*, 2998–3006.

(100) Zhang, K. Y.; Lo, K. K.-W. *Inorg. Chem*. **2009**, *48*, 6011–6025.

(101) (a) Lau, J. S.-Y.; Lee, P.-K.; Tsang, H.-K.; Ng, C. H.-C.; Lam, Y.-W.; Cheng, S.-H.; Lo, K. K.-W. *Inorg. Chem*. **2009**, *48*, 708-718. (b) Liu, H.-W.; Zhang, K. Y.; Law, H.-T.; Lo, K. K.-W. *Organometallics* **2010**, *29*, 3474–3476.

(102) Cao, J.-J.; Tan, C.-P.; Chen, M.-H.; Wu, N.; Yao, D.-Y.; Liu, X. -G.; Jia, L.-N.; Mao, Z. -W. *Chem. Sci*. **2017**, *8*, 631–640.

(103) Li, S. P.-Y.; Liu, H. -W.; Zhang, K. Y.; Lo, K. K.-W. *Chem. -Eur. J*. **2010**, *16*, 8329–8339.

(104) (a) Satori, C.P.; Henderson, M.M.; Krautkramer, E.A.; Kostal, V.; Distefano, M.D.; Arriaga, E. A. *Chem. Rev*. **2013**, *11*3, 2733–2811. (b) Lodish, H.; Berk, A.; Matsudaira, P.; Kaiser, C.A.; Krieger, M.; Scott, M.P.; Zipursky, S.L.; Darnell, J. *Molecular Cell Biology*, 5th ed., WH Freeman, New York, NY, **2004**. (c) Thomas, J. A. *Chem. Soc. Rev*. **2015**, *44*, 4494–4500.

(105) (a) Rosenberg, B.; VanCamp, L.; Trosko, J. E.; Mansour, V. H. *Nature* **1969**, *222*, 385–386. (b) Mandal, S.; Poria, D. K.; Ghosh, R.; Ray, P. S.; Gupta, P. *Dalton Trans*. **2014**, *43*, 17463–17474.

(106) (a) Happ, B.; Winter, A.; Hager, M.D.; Schubert, U. S. *Chem. Soc. Rev*. **2012**, *41*, 2222–2255. (b) Ma, D.-L.; Wang, M.; Liu, C.; Miao, X.; Kang, T.-S.;

Leung, C.-H. *Coord. Chem. Rev*. **2016**, *324*, 90-105. (c) Lo, K.K.-W. *Acc. Chem. Res*. **2015**, *48*, 2985–2995.

(107) (a) Ma, D.-L.; Lin, S.; Wang, W.; Yang, C.; Leung, C.-H. *Chem. Sci.* **2017**, *8*, 878–889; (b) Kumar, N.; Bhalla, V.; Kumar, M. *Coord. Chem. Rev*. **2013**, *257*, 2335–2347.

(108) (a) Galindo, F.; Burguete, M.I.; Vigara, L.; Luis, S.V.; Kabir, N.; Gavrilovic, J.; Russell, D.A. *Angew. Chem. Int. Ed*. **2005**, *117*, 6662–6666; (b) Huang, H.; Yu, B.; Zhang, P.; Huang, J.; Chen, Y.; Gasser, G.; Ji, L.; Chao, H. *Angew. Chem. Int. Ed*. **2015**, *54*, 14049–14052.

(109) He, L.; Tan, C.-P.; Ye, R.-R.; Zhao, Y.-Z.; Liu, Y.-H.; Zhao, Q.; Ji, Y.-H.; Mao, Z.-W. *Angew. Chem. Int. Ed.* **2014**, *53*, 12137–12141.

(110) Qiu, K.; Huang, K.; Liu, B.; Liu, Y.; Huang, Z.; Chen, Y.; Ji, L.; Chao, H. *ACS Appl. Mater. Interfaces* **2016**, *8*, 12702−12710.

(111) (a) Horobin, R. W.; Rashid-Doubell, F. *Biotech. Histochem*. **2013**, *88*, 461-476. (b) Horobin, R. W.; Rashid- Doubell, F.; Pediani, J. D.; Milligan, G. *Biotech. Histochem*. **2013**, *88*, 440-460.

(112) Qiu, K.; Liu, Y.; Huang, H.; Liu, C.; Zhu, H.; Chen, Y.; Ji, L.; Chao, H. *Dalton Trans*. **2016**, *45*, 16144–16147.

(113) Cao, L.; Zhang, R.; Zhang, W.; Du, Z.; Liu, C.; Ye, Z.; Song, B.; Yuan, J. *Biomaterials* **2015**, *68*, 21–31.

(114) Yamamoto, Y.; Imai, N.; Mashima, R.; Konaka, R.; Inoue, M.; Dunlap, W. *Methods in Enzymology*, vol. 319, Academic Press, New York, **2000**, 29.

(115) Li, S. P.-Y.; Lau, C. T.-S.; Louie, M.-W.; Lam, Y.-W.; Cheng, S. H.; Lo, K. K. -W. *Biomaterials* **2013**, *34*, 7519-7532.

(116) Li, G.; Sun, L.; Ji, L.; Chao, H. *Dalton Trans*. **2016**, *45*, 13261–13276.

(117) Li, C.; Yu, M.; Sun, Y.; Wu, Y.; Huang, C.; Li, F. *J. Am. Chem. Soc*. **2011**, *133*, 11231–11239.

(118) (a) Butler, S. J. ; Lamarque, L.; Pal, R.; Parker, D. *Chem. Sci*. **2014**, *5*, 1750-1756. (b) Sahay, G.; Gautam, V.; Luxenhofer, R.; Kabanov, A.V. *Biomaterials* **2010**, *31*, 1757–1764.

Chapter 2

pH-Controlled Nanoparticles Formation and Tracking of Lysosomal Zinc Ions in Cancer Cells by Fluorescent Carbazole–Bipyridine Conjugates

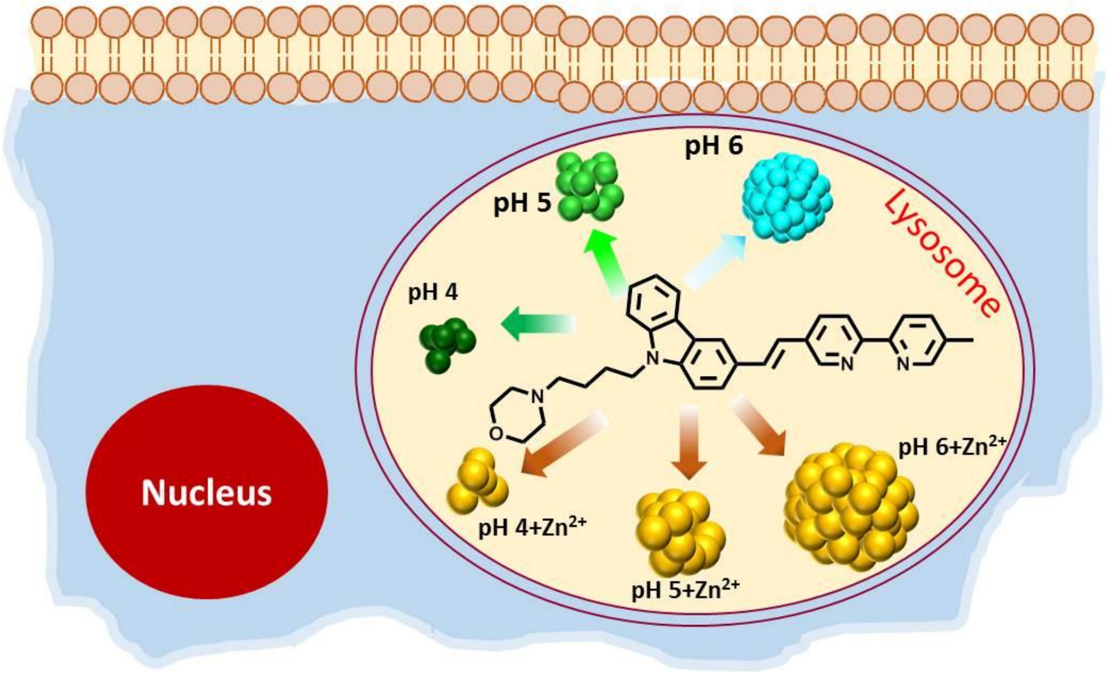

2.1. Abstract

Fluorescent probes for simultaneous detection of multiple organelle specific analytes in cancer cells are essential for bioimaging applications. During abnormalities in cells, among other important parameters (metal ions, reactive oxygen species, enzymes, etc.), pH and Zn^{2+} *are also altered. Herein, we report the formation of nanoparticles of fluorescent molecules, based on carbazole-bipyridine conjugates (**CBL1-3**) and their use as nanoprobes to simultaneously detect Zn*$^{2+}$ *and pH variations in lysosome. Upon increasing the pH from 4-6,*

these probes form nanoparticles with increased size and enhanced fluorescence at 510 nm. Among ***CBL1-3****, nanoparticles of* ***CBL2*** *upon* Zn^{2+} *binding, exhibit pH responsive intensity change only at lysosomal pH window at 610 nm and become silent above pH 7. Fluorescent imaging experiments on cancer cells revealed that the* ***CBL2*** *nanoprobe is capable of localizing at lysosomes and facilitates the detection of endogenous* Zn^{2+} *and pH variations. Furthermore, the lysosomal* Zn^{2+} *variation with external stimuli induced programmed cell death was visualized using the nanoprobe.*

2.2. Introduction

Lysosomes, as membrane-bound organelles, contain a large variety of hydrolytic enzymes and secretory proteins that are active at an acidic pH range (~4.0 to 5.5). They are primarily responsible for degrading bio-macromolecules into low-molecular-weight materials.[1,2] To degrade bio-macromolecules (malfunctioning organelles, obsolete biomolecules and foreign species) from different pathways (autophagy and endocytosis), more than 60 types of acid hydrolases exist in lysosomes, including specific membrane proteins, lipases, sulfatases, peptidases, proteases, glycosidases, nucleases, and phosphatases.[3] Aside from their role as the cells garbage disposal units, lysosomes are also involved in a number of key life activities including intracellular transportation, apoptosis, cholesterol homeostasis, and plasma membrane repair.[4] Lysosomal dysfunction can lead to lysosomal storage disease, cardiovascular disorders, neurodegenerative disorders, silicosis, and inflammation.[5] In addition, tumor invasion and metastasis are largely associated with altered lysosomal trafficking, as are increased lysosomal enzyme expression and activity. Effective techniques to fluorescently label lysosomes of cancer cells and solid tumor models are therefore of significant interest to study lysosomal trafficking and its role in invasion.[6]

In order to understand the biological activities of lysosomes, a limited number of fluorescent probes derived from Neutral Red (toluylene red) and acridine orange (*N,N,N′,N′*-tetramethylacridine-3,6-diamine) have been developed.[7] However, most of the commercial probes require a rather short excitation wavelength (seriously limiting their use in tissue imaging due to low penetration depth), the need for biomolecular conjugation, pH sensitivity, poor water solubility, and poor photostability.[8] In 2010, Belfield and co-workers reported very effective hydrophilic fluorine derivative, LT1 (**1**), as a lysosomal marker for two-photon fluorescence cell imaging.[9] The probe has a number of properties that far exceed those of commercial lysotracker probes, including higher two-photon action cross section, high lysosomal selectivity, good fluorescence quantum yield, and importantly, high photostability, all resulting in a superior figure of merit. The tertiary amine group present in the fluorophore helps the probe to accumulate in the lysosome through lysosomotropism as discussed in Chapter 1, section 1.6.3.

Later Peng *et al.*, chose Nile Blue as a new type of fluorophore for designing lysosomal probes by using 2-morpholinoethylamine as the targetable group.[10] The authors developed a Nile Blue based NIR lysotracker, NBM (**2**) with excellent photostability and biocompatibility. It can easily localize in lysosomes of various live cells quickly with a relatively low concentration (25 nM) and emit strong fluorescence which was observed using laser confocal microscopy. More importantly, **2** was successfully used to observe the morphological changes of lysosomes during cell apoptosis and the disappearance and reproduction of lysosomes during cell division. Apart from small molecule based targeting groups, scientists have developed peptide based sensor for imaging lysosome. Tian, Wu and co-workers have demonstrated that synthetic peptide with spiropyran units (**3**) can be used as a switchable sensor to reversibly track lysosomes in live cell lines in real-time.[11] Upon accumulation in intracellular lysosomes, the low pH of lysosomal lumen promotes the ring-opening of the spiropyran units, which, as a result, makes it possible for **3** to serve as a lysosomal sensor. Moreover, as the process can be tuned by pH and visible light, it enables us to reversibly label lysosomes.

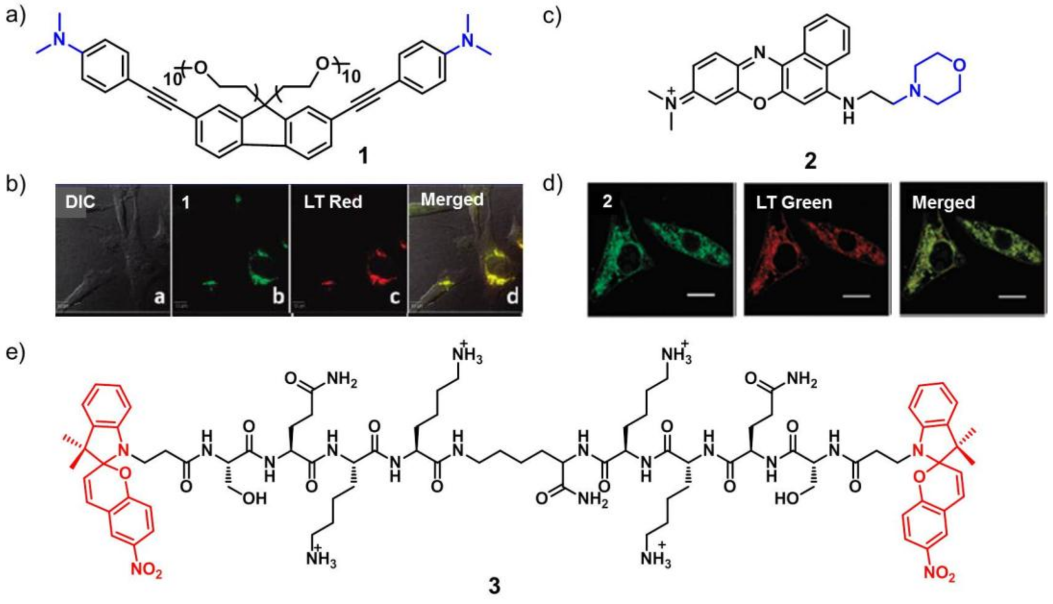

Figure 2.1: (a) Molecular structure of two-photon active fluorescent probe for lysosome imaging, **1**. (b) Colocalization images of HCT 116 cells incubated with **1**. (c) Molecular structure of NIR active fluorescent probe for lysosome, **2**. (d) Intracellular distribution of **2** compared to LysoTracker Green in MCF-7 co-cultured with **2**. Scale bars represent 10 μm. (e) Molecular structure of peptide based lysosome targeting probe, **3**.

Intracellular pH (pH_i) plays many critical roles in cell, enzyme, and tissue activities, including proliferation and apoptosis, multidrug resistance, ion transport, endocytosis, and muscle contraction.[12] Monitoring the pH changes inside living cells is also important for studying cellular internalization pathways, such as phagocytosis, endocytosis, and receptor ligand internalization.[13] Changes of pH_i affect the nervous system too, by influencing synaptic transmission, neuronal excitability, cell-cell coupling *via* gap junctions, and signal cascades.[14] Abnormal pH_i values are associated with inappropriate cell function, growth, and division and are observed in some common disease types such as cancer and Alzheimer's.[15] The acidic environments in lysosomes (pH 4.5-5.5) can facilitate the degradation of proteins in cellular metabolism. Thus, cellular dysfunction is often associated with abnormal pH values in organelles and there are many probes developed for the imaging of lysosomal pH.[1-3]

Peng and co-workers developed a fluorogenic rhodamine-lactam pH sensor, Rlyso (**4**), which exhibited high selectivity and sensitivity for intracellular pH.[16]

The probe can selectively stain lysosomes in live cells and this staining ability is due to the presence of methylcarbitol group, which avoids the ‘alkalizing effect’ on lysosomes by the current lysosomal sensors with nitrogen-containing side chains (Figure 2.2). There is more than a 50-fold increase in the emission intensities within the pH range of 7.4-4.5. It has a pK_a of 5.47, which is useful to detect minute pH changes in 4.5–6.0 range, and that covers both normal and abnormal lysosome pH. Again, **4** was used to quantitatively detect the chloroquine induced increase in lysosomal pH and monitor changes in the acidity of lysosomes during apoptosis in live cells.

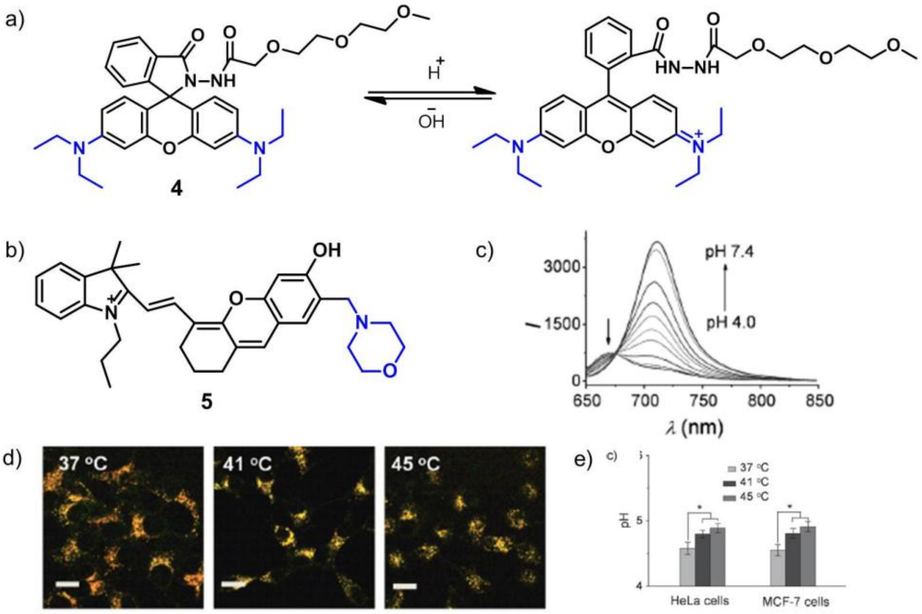

Figure 2.2: (a) Chemical structure of **4** and its proton triggered ring opening. (b) Chemical structure of lysosomal pH imaging probe **5**. (c) Fluorescence emission spectra of **5** (10 μm) in phosphate buffer (0.2 M) at different pH values. (d) Relationship between lysosomal pH and heat shock in HeLa cells monitored by **5**. (e) Lysosomal pH changes with temperature in HeLa and MCF-7 cells.

Recently, Ma *et al.*, developed a new lysosome targeting near-infrared ratiometric pH probe by incorporating morpholine into a stable hemicyanine skeleton (**5**) (Figure 2.2).[17] The probe exhibited maximum absorption band at λ = 598 nm in pH 4.0 medium and is red-shifted to λ = 681 nm in pH 7.4 medium, with a concomitant color change from blue to green. Upon excitation at λ = 635 nm, the near-infrared emission intensity at λ = 670 nm of **5** decreases slightly with the change in pH values from 4.0 to 7.4. This change in intensity is accompanied by a large increase of fluorescence intensity at λ = 708 nm, which provides the basis for achieving a ratiometric (I_{670}/I_{708}) detection. The authors also studied the change of lysosomal pH with temperature. The detailed investigation of heat shock induced irreversible lysosomal pH change was demonstrated for the first time (Figure 2.2).

Zinc, a potential endogenous trigger of oxidative stress in the brain, is abundant in glutamatergic vesicles of the forebrain association pathways and released with neuronal activity or depolarisation.[18] Within brain tissue, zinc is non-uniformly distributed and most abundantly in the hippocampus, amygdala, neocortex and olfactory bulb regions.[19] In the hippocampus, a region of the brain essential for learning and long-term memory storage, Zn^{2+} concentrations can reach up to 300 μM.[19] In hippocampal neurons, the majority of the zinc-containing vesicles are lysosomes. Over the past decade, significant efforts have been made to develop Zn^{2+}-selective probes. However, lysosomal Zn^{2+} detection needs to meet the following requirements: (1) it must reliably monitor Zn^{2+} concentrations under acidic conditions, since the vast majority of reported Zn^{2+} probes are proton-sensitive at a pH range of 4.5 to 6.0 with high pK_a values; (2) it must have high selectivity towards Zn^{2+} over other potential competing species; and (3) it must deliver the Zn^{2+} probes into lysosomes.[21] Also, compared with fluorescence intensity-based probes, ratiometric probes can realize quantitative detection more effectively by measuring the ratio of the fluorescence intensities at two different wavelengths, thus, ratiometric probes are ideal tools for quantitative analysis. There are very less number of probes reported for the sensing and imaging of lysosomal Zn^{2+}.[21]

In 2012, Jiang and co-workers have reported DQZn4 (**7**) as a ratiometric fluorescent probe with a nanomolar level K_d (16 nM) toward Zn^{2+} in acidic aqueous solution (Figure 2.3).[22] Titration of Zn^{2+} resulted in the quenching of emission around 543−700 nm with emergence of a new blue-shifted emission peak at 495 nm (ϕ = 0.17) with an isoemissive point at 543 nm. The ratio of emission intensity at 495 and 542 nm increased linearly from 0.37 to 1.88 upon titration with Zn^{2+} until the $[Zn^{2+}]$/probe ratio reached 1:1, supporting the 1:1 binding stoichiometry as well. The authors applied **7** to detect Zn^{2+} in intracellular lysosomes by using single-excitation dual-emission ratiometry. They prepared another derivative **6** without targeting group, that doesn't show organelle specificity. The imaging experiments were done in the NIH 3T3 cells with **7** (10 μM) (Figure 2.3).

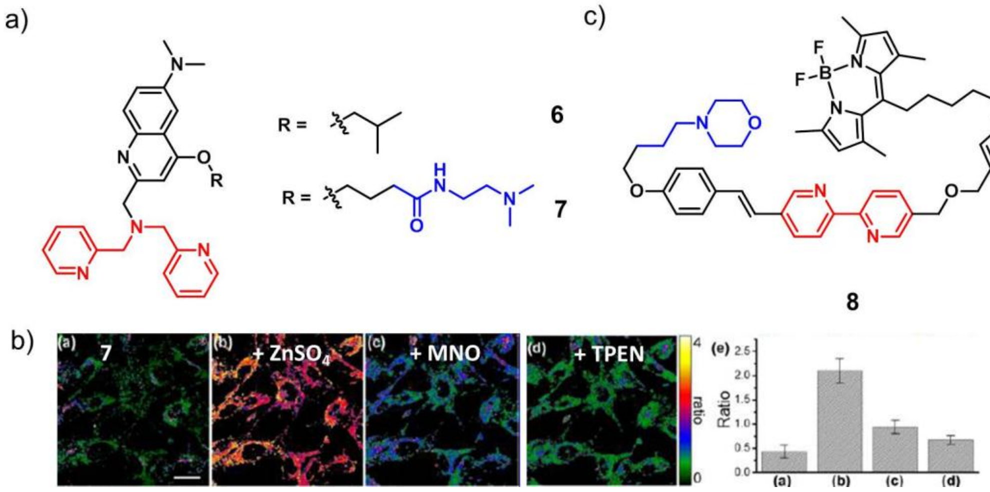

Figure 2.3: (a) Chemical structure of the lysosomal Zn^{2+} imaging probe, **7** and the control **6**. (b) Ratiometric imaging of Zn^{2+} in **7**-labeled NIH 3T3 cells ($ZnSO_4$ = 30 μM, 2- mercaptopyridine *N*-oxide (MNO) = 15 μM and TPEN = 50 μM for 5 min) and average F_{green}/F_{red} ratios (λ_{ex} = 405 nm, scale bar: 20 μm; ratio bar). (c) Chemical structure of FRET based probe, **8** for lysosomal Zn^{2+} imaging.

Later Zhu *et al.*, demonstrated a strategy to modify the Zn^{2+} sensitivity of a fluoroionophore with low photostability and a broad emission band to a bright and photostable fluorophore with a narrow emission band (Figure 2.3).[23] The two fluorophores are covalently connected to afford an intramolecular (FRET) conjugate. The FRET donor in the conjugate is a Zn^{2+}-sensitive aryl-vinyl-bipyridyl fluoroionophore, (**8**), the absorption and emission of which undergo bathochromic shifts upon Zn^{2+} coordination. The broad emission band of the donor/zinc(II) complex is transformed into the strong, narrow emission band of the Bodipy acceptor in the FRET conjugates, which can be captured within the narrow emission window that is preferred for multicolor imaging experiments..

To investigate lysosomal zinc functions in neurons with high spatial and temporal reliability, Peng and co-workers in 2014 reported a ratiometric probe, LysoZn-1(**9**) (Figure 2.4).[24] It is derived from the styryl-Bodipy-DPA (DPA = Di-2-picolylamine) scaffold with a lysosome-targeted 2-morpholinoethylamine moiety to allow localization in lysosomes. Upon Zn^{2+} binding, **9** exhibits obvious fluorescence enhancement ($F_{578\ nm}$) and ratiometric ($F_{578\ nm}/F_{680\ nm}$) changes. The emission intensities of **9** and **9** + Zn^{2+} do not change significantly under lysosomal pH ranging from 4.5 to 6.0. Confocal imaging experiments indicate that **9** is able to localize within the lysosomes in neural stem cells (NSCs), MCF-7 and HeLa cells and detect exogenous Zn^{2+} levels in NSCs and MCF-7 cells (Figure 2.4).

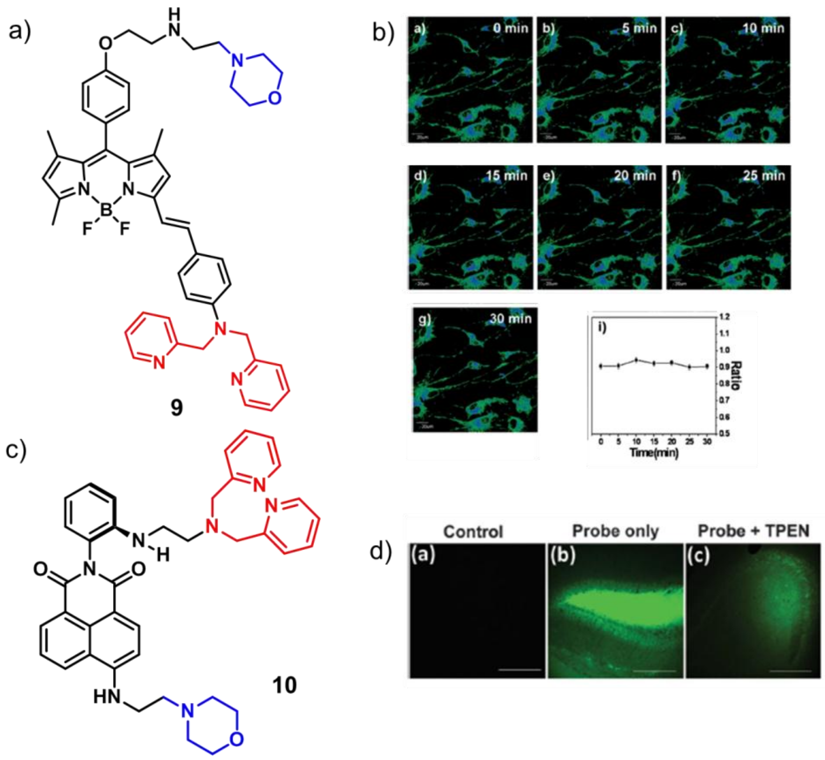

Figure 2.4. (a) Chemical structure of **9**. (b) Fluorescence ratio images ($F_{575–620\ nm}/F_{655–755\ nm}$) of **9** (1 μM) labelled NSCs in the presence of 100 μM chloroquine at different time points and plot of the emission ratio as a function of time after chloroquine was added. (c) Chemical structure of two-photon active lysosomal Zn^{2+} imaging probe, **10**. (d) Two-photon microscopic imaging of Zn(II) in mouse brain (hippocampus) tissues.

Ahn, Cho and co-workers have developed a probe, where a morpholine group and a *N*,*N*-di-(2-picolyl)ethylenediamine ligand were introduced into a naphthalimide dye (Figure 2.4).[25] The probe, detect Zn^{2+} in the lysosomal pH range (pH = 4.5-5.5). The fluorescence measurement at various pH values shows that the molecule **10** has negligible fluorescence, whereas its Zn^{2+} complex emits strong fluorescence in the lysosomal pH range (ϕ_F of probe = 0.03 and ϕ_F of **10**–Zn^{2+} = 0.23 in pH 5 buffer). Also, **10** shows low fluorescence intensity at cytosolic pH (7.4) even after binding with Zn^{2+}. The authors were able to image Zn^{2+} in deep tissues of mouse brain (hippocampal slice) under two-photon excitation conditions at 900 nm. The two photon microscopic images of the tissue slice incubated with probe **10** show strong fluorescence apparently due to endogenous free Zn^{2+} in the mouse brain, whereas the tissue without probe treatment (used as the control) does not show any fluorescence (Figure 2.4).

Self-assembled nanoprobes of small molecules are equally powerful when compared to single molecular probes in terms of the response towards target analytes.[26] Recently, self-assembled gold nanoparticles, small molecular aggregates and polymeric nanoparticles have been extensively applied for sensors design.[27] Although molecular assemblies have been used for sensing certain analytes, they have not been much explored for sensing of bioanalytes in cellular system. External stimuli, especially, pH induced molecular self-assembly that can influence the optical properties may become more attractive to develop novel fluorescent nanoprobes for metal ion sensing and imaging in specific organelle in cellular system.

The precise localization of the probe to the lysosome and selective recognition of the Zn^{2+} which are associated to apoptosis is the prime concern of the present work. Simultaneous, monitoring of pH variations and Zn^{2+} concentration is the major bottleneck to develop a robust diagnostic probe. To date, many attempts have been tried to overcome this issue. So far, very few probes including two-photon probes and FRET based probes have been reported to target lysosomal Zn^{2+}.[22-25]However, none of them endeavor for simultaneous imaging of Zn^{2+} with pH inside lysosome and during apoptosis. The present work is therefore focused on the design and development of a photostable, self-assembled fluorescent nanoprobe for monitoring pH and Zn^{2+} in lysosome under oxidative stress and apoptotic conditions.

2.3. Results and Discussion

2.3.1. Synthesis of CBL1-3 and CBG

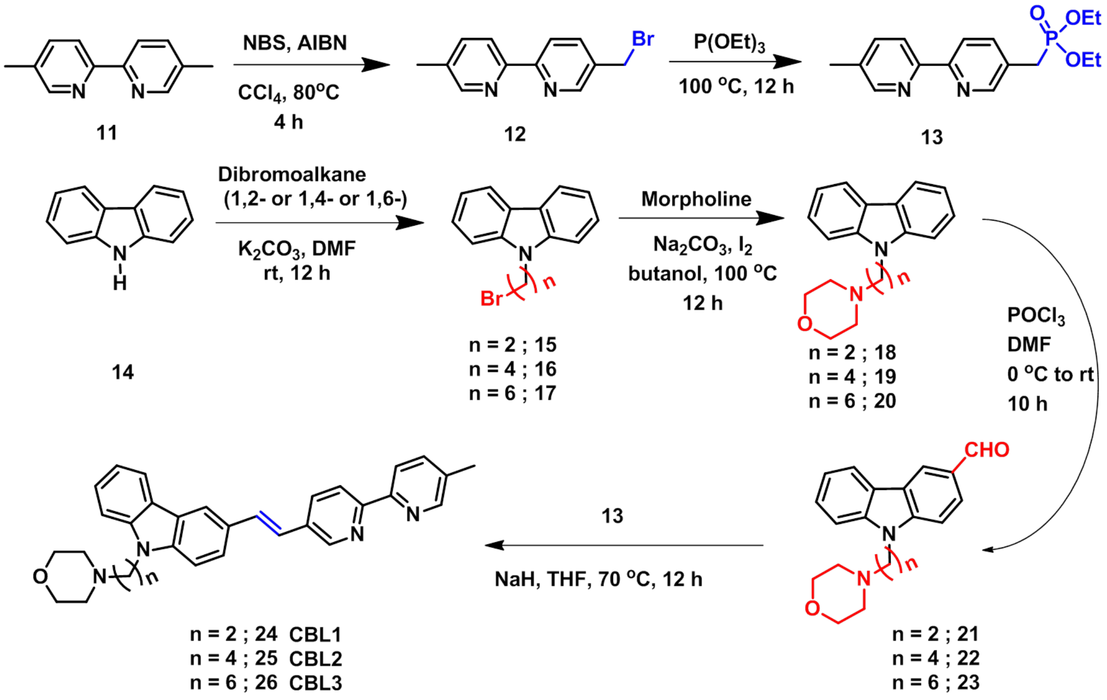

Scheme 2.1: Steps involved in the synthesis of **CBL1-3**

Considering the above aspects, we have designed fluorophores containing a carbazole, linked with a morpholine (pK_a~7.2) which is conjugated to a 2,2'-bipyridine (pK_a~4.2) moiety. The morpholine moiety facilitates targeting of lysosome whereas the 2,2'-bipyridine moiety helps binding of Zn^{2+}. The lysosome targeting carbazole-bipyridine conjugates named **CBL1-3** were synthesized from the phosphonate ester **13** and the corresponding morpholine attached aldehyde of carbazole, **21-23** by Wittig-Horner-Emmons olefination reaction (Scheme 2.1). The *trans* conformation of the vinyl linkage was confirmed from ^1H NMR which showed a coupling constant (*J*) value of 16 Hz. The compound was isolated with 60% yield by column chromatography over silica gel using 6% methanol/dichloromethane as the eluent. The molecule, **CBG** (**28**) was also synthesized by the same strategy as discussed above and the glycol chain is attached instead of morpholine group (Scheme 2.2). All the final molecules were obtained as yellow solid powders. The intermediates and final compounds were characterized by various spectroscopic techniques such as ^{1}H NMR, ^{13}C NMR, HRMS and elemental analyses (**Table 2.1**). The synthetic strategy adopted is represented in **Scheme 2.1** and **2.2**.

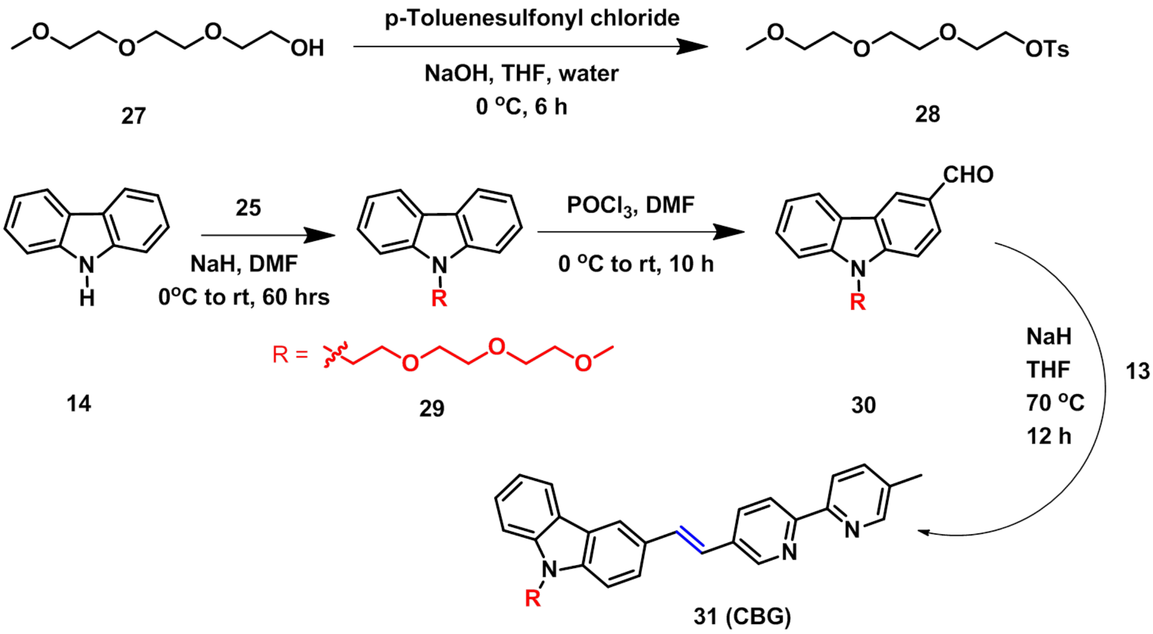

Scheme 2.2: Steps involved in the synthesis of **CBG**

Compound	Melting Point	Elemental Analysis		
		% C [Expt. (Calcd.)]	% H [Expt. (Calcd.)]	% N [Expt. (Calcd.)]
CBL1	218.8 °C ± 1	78.01 (78.45)	6.28 (6.37)	8.20 (8.28)
CBL2	160.7 °C ± 1	78.52 (78.85)	6.53 (6.82)	11.63 (11.81)
CBL3	141.5 °C ± 1	78.95 (79.21)	6.98 (7.22)	10.94 (11.15)
CBG	62.5 °C ± 1	75.28 (75.71)	6.32 (6.55)	10.43 (10.56)

Table 2.1: Melting point and elemental analysis data of **CBL1-3** and **CBG**

2.3.2. Solvent Dependent Absorption, Emission and Aggregation Properties

The photophysical properties of all the molecules were first studied in different solvents. The absorption spectrum of **CBL2 (25)** in acetonitrile (c = 10 μM) showed a maximum at 360 nm (Figure 2.7). However, in phosphate buffer at pH 7, the absorption spectrum is significantly red shifted with broadening, indicating the possible aggregation of the molecule. The emission maximum is found to be at 490 nm in acetonitrile. Also, the solvent dependent emission shift shows the solvatochromic behavior of the molecule. **CBL1**, **CBL3** and **CBG** show similar phenomena in different solvents. **CBL2** has a quantum yield of ϕ = 0.35 in acetonitrile.

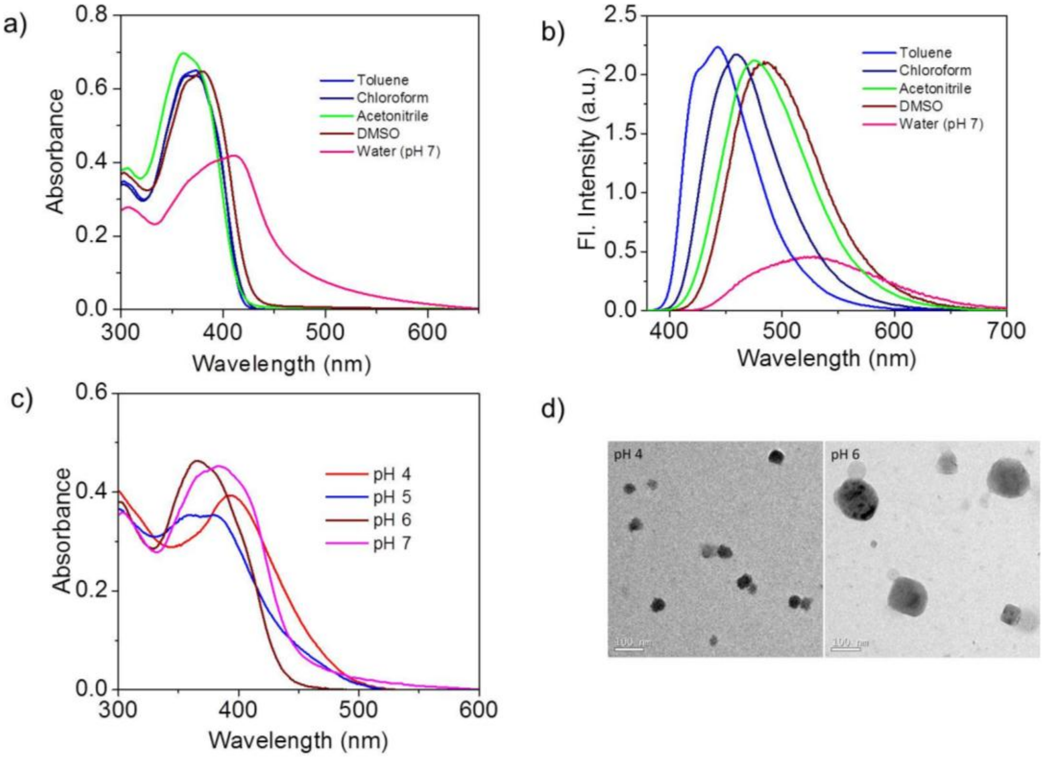

Figure 2.5: (a) Absorption and (b) emission spectra of **CBL2** in different solvents, (c) absorption spectra of **CBL2** in different pH (4 – 7) and (d) pH dependent TEM images of nanoparticles in aqueous solution at pH 4 and 6 (*c* = 10 μM, λ_{ex} = 360 nm).

The absorption spectra of **CBL2** in different pH show broad spectra with different absorption maxima. This is due to the formation of different types of aggregates (or nanoparticles) depending on pH (Figure 2.5). The aggregated molecules formed nanoparticles that are confirmed by transmission electron microscopy (TEM) analysis (Figure 2.5). At pH 4, particles formed were around 50 nm in size whereas at pH 6, the size of spherical particles was significantly increased as it can be seen in Figure 2.5.

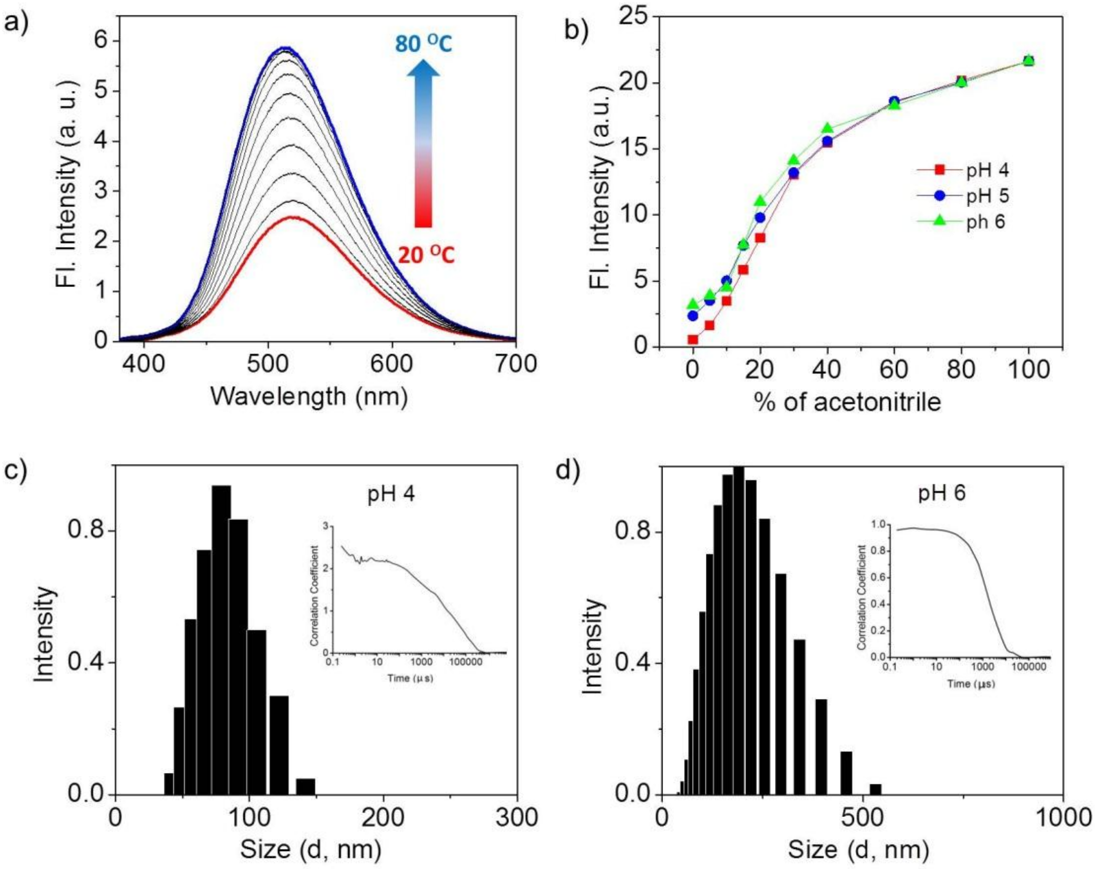

Figure 2.6: (a) Temperature dependent emission spectra of **CBL2** at pH 4, (b) secondary plot of emission intensity monitored at 475 nm in each pH (4, 5 and 6) (c = 10 µM, λ_{ex} = 360 nm) with increasing acetonitrile concentration, (c) and (d) DLS analysis of **CBL2** at pH 4 and 6 (c = 10 µM).

Detailed studies on the pH dependent aggregation are performed with **CBL2** in acetonitrile–water mixture at different pH (4, 5 and 6). The emission maximum at 510 nm corresponding to the aggregates disappeared and the monomeric emission of **CBL2** at 490 nm appeared (Figure 2.6) with increasing the acetonitrile percentage and shows maximum intensity in acetonitrile. Formation of the aggregates is further confirmed by the temperature dependent changes in the emission spectra (Figure 2.6). DLS study confirmed the formation of nanoparticles at pH 4 and 6 (Figure 2.6) as illustrated with the size distribution histograms. The size of the particles was gradually increased with increase in pH of the media. Similar observations were found for other derivatives also.

2.3.3 pH-Dependent Emission Changes.

The absorption maxima of **CBL** derivatives at pH 2 and 3 appear at 395 nm and are almost non-emissive. While increasing the pH from 4 to 6 at lysosomal pH window, the emission intensities at 530 nm were increased by 10 fold with a hypsochromic shift of 20 nm (Figure 2.7). Below pH 4, the morpholine and 2,2'-bipyridine are protonated causing the quenching of the fluorescence intensity. Above pH 4, the protonation may gradually be localized at the morpholine unit. Thus, hypsochromic shift occurs probably due to weaker excited state charge transfer above pH 7.

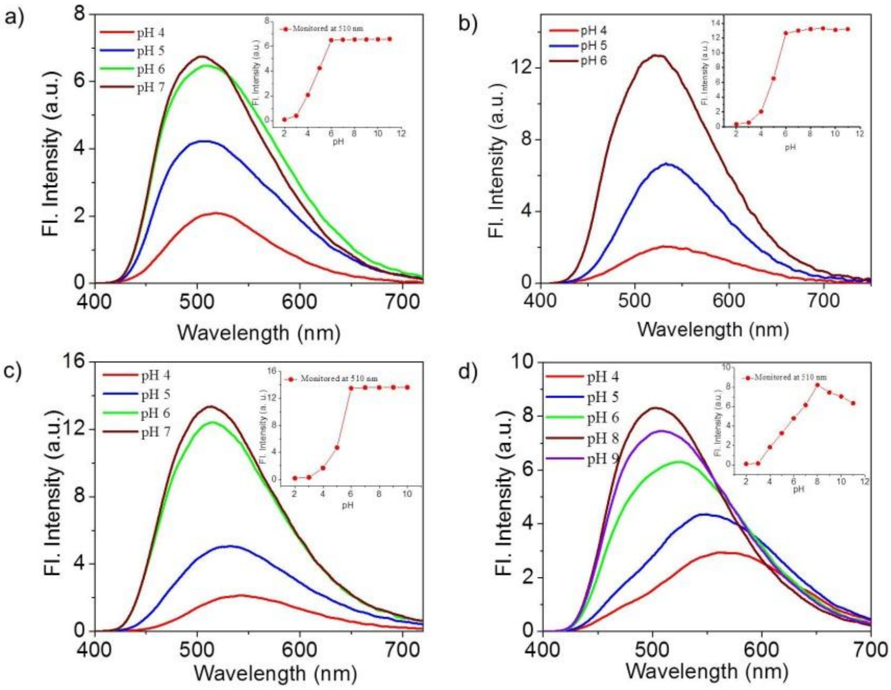

Figure 2.7: pH dependent fluorescence emission spectra of (a) **CBL1**, (b) **CBL2**, (c) **CBL3** and (d) **CBG** (c = 10 μM, λ_{ex} = 365 nm). Insets show the intensity change with pH from 2 - 10.

CBL1 and **CBL3** also show similar behavior (Figure 2.7). However, in the case of **CBG**, the emission intensities increased slowly from pH 4 to 8 at 510 nm as there is no morpholine unit (Figure 2.7). This observation suggests that **CBG** is not suitable for lysosomal analysis. The pH dependent quantum yield values are tabulated in the Table 2.2.

2.3.4 Stability, Reversibility and Photostability of Nanoparticles

To evaluate the stability of these aggregated nanoparticles, we measured the emission properties in buffer solution at different pH for 24 h. Interestingly, there was no significant change for the emission indicating that these nanoparticles are stable in physiological conditions. Also the particles exhibited reversible size variation with change in pH as illustrated with pH 4 and 6 without the loss of fluorescence intensity for at least 10 cycles (Figure 2.8). Notably, prepared aqueous solution was transparent at the experimental conditions and no precipitation was observed for at least one week. This phenomenon suggests that these molecular assemblies are useful in monitoring the pH variations once incubated with lysosome since lysosomal pH can alter during pathologies.

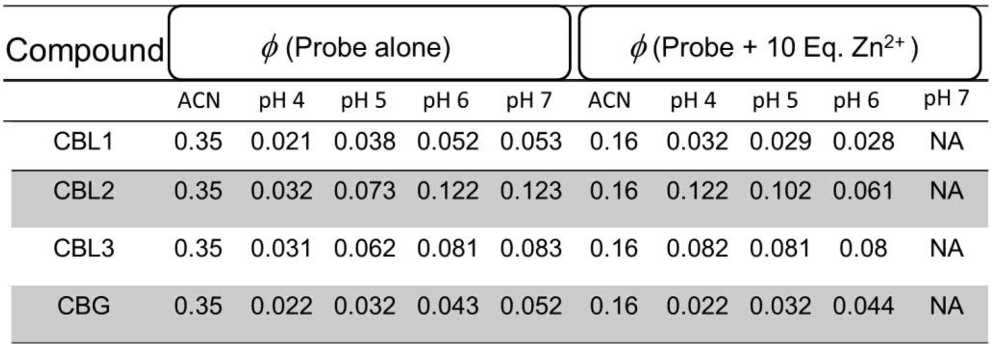

Compound	ϕ (Probe alone)					ϕ (Probe + 10 Eq. Zn^{2+})				
	ACN	pH 4	pH 5	pH 6	pH 7	ACN	pH 4	pH 5	pH 6	pH 7
CBL1	0.35	0.021	0.038	0.052	0.053	0.16	0.032	0.029	0.028	NA
CBL2	0.35	0.032	0.073	0.122	0.123	0.16	0.122	0.102	0.061	NA
CBL3	0.35	0.031	0.062	0.081	0.083	0.16	0.082	0.081	0.08	NA
CBG	0.35	0.022	0.032	0.043	0.052	0.16	0.022	0.032	0.044	NA

Table 2.2: Quantum yield of **CBL1**, **CBL2**, **CBL3** and **CBG** in acetonitrile and different pH (4 to 7) before and after zinc binding (error limit = ±0.001).

At low pH values (pH < 4) due to the protonation at the bipyridyl nitrogen and morpholine nitrogen, molecules become hydrophilic to form non-emissive particles. Above pH 4.2, protonation specifically occurs at the morpholine site, leading to an amphiphilic behavior to the fluorophore. The amphiphilic character of the molecule facilitates spherical assembly in which the hydrophilic morpholine units are aligned towards the outer surface and 2,2'-bipyridine unit stay in the inner part.

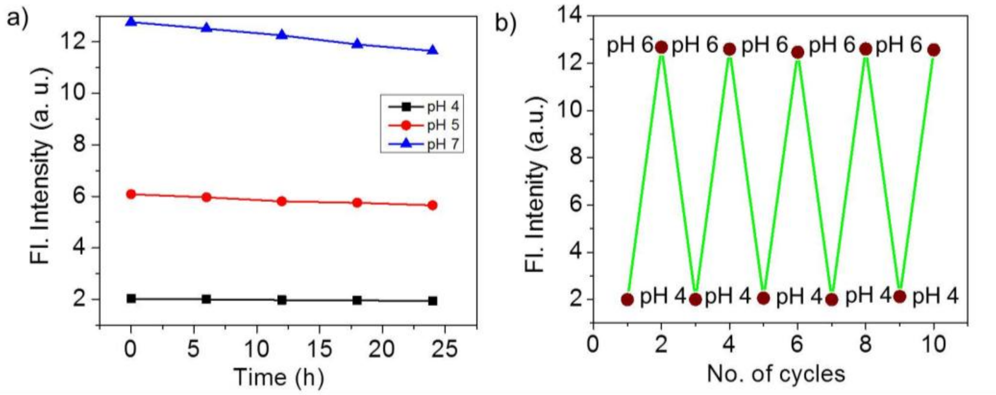

Figure 2.8: (a) Time dependent emission of **CBL2** at pH 4, 5 and 7; (b) Reversibility of the aggregates of **CBL2** in different pH (4 and 6). The pH is changed manually and the emission intensity is measured in each case (PBS buffer, c = 10 μM and λ_{ex} = 365 nm).

On the contrary, above pH 7, molecules are hydrophobic in nature which facilitates π-stacking, leading to large spherical assemblies. In the case of **CBG**, random aggregates were formed at different pH. Interestingly, the molecular assemblies of **CBL** probes show better photostability when compared to the monomer and lysotracker green, and no change of intensities were observed even after 30 min of light irradiation and hence are suitable for bioimaging of long time cellular dynamics in lysosome (Figure 2.9).

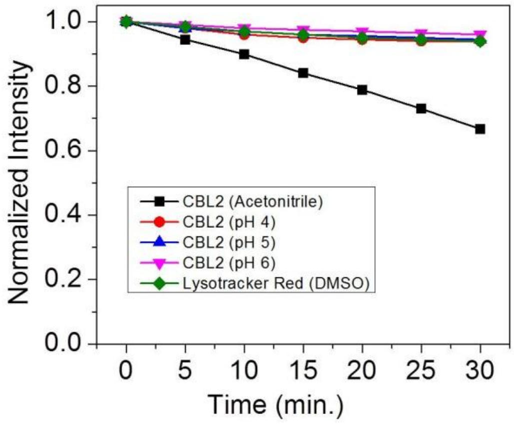

Figure 2.9: The change in emission of **CBL2** (c = 10 μM) monitored in acetonitrile (λ_{em} = 475 nm), pH 4 (λ_{em} = 530 nm), pH 5 (λ_{em} = 525 nm) and pH 6 (λ_{em} = 520 nm) and Lysotracker Red (λ_{em} = 600 nm) in DMSO by irradiating with 370 nm long pass for 30 min.

2.3.5 DFT Calculations of Protonation Effect on CBL2

To understand the absorbance behavior and HOMO-LUMO energy at different pH, DFT calculations of the molecule **CBL2** in the ground states were carried out using M06X/6-311G(d,p) level as implemented in Gaussian09. HOMO energy level of **CBL2** (neutral), **CBL2**(H)$^{+}$ (protonation only at morpholine nitrogen), **CBL2**(HH)$^{++}$ (protonation both at bipyridine and morpholine nitrogen) were found to be nearly unchanged while the LUMO energy level of **CBL2**(HH)$^{++}$ showed significant stabilization compared to that of **CBL2** (Figure 2.10). The calculated absorption spectra are in good agreement with the experiments. A minimal blue shift in absorption maximum was observed for **CBL2**(H)$^{+}$, at pH 6 due to protonation at morpholine nitrogen, whereas a significant red shift of absorbance wavelength was obtained for **CBL2**(HH)$^{++}$, at pH 4 due to protonation of both bipyridine and morpholine units (Figure 2.11).

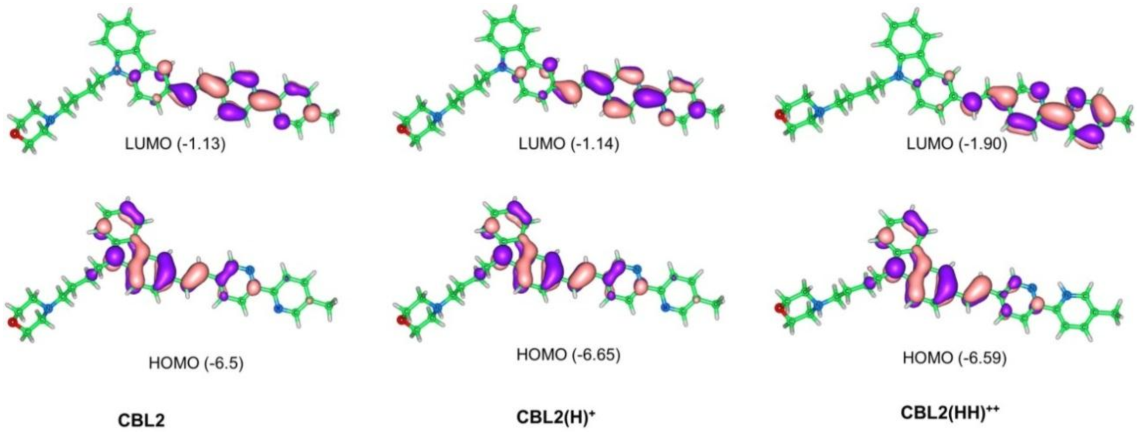

Figure 2.10: HOMO and LUMO features of **CBL2**, **CBL2**(H)$^{+}$ and **CBL2**(HH)$^{++}$. All the optimized structures were confirmed as energy minima by vibrational frequency analysis at 298.15 K and 1.0 atm pressure.

2.3.6 pH-Dependent Zn^{2+} Binding

CBL2 exhibits maximum fluorescence response at the lysosomal pH window of 4-6 and hence is ideal for probing lysosomal pH variations. Upon addition of Zn(ClO$_4$)$_2$, the emission maximum at 530 nm is shifted to 610 nm with 80 nm red shift (ϕ = 0.12). While increasing the pH to 6, the emission intensity was decreased

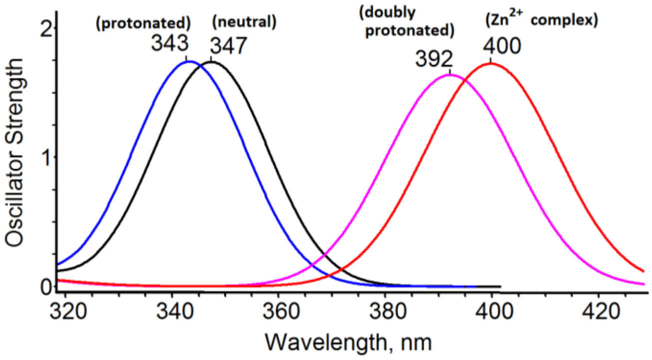

Figure 2.11: The simulated absorption spectra of **CBL2**, **CBL2**(H)+ and **CBL2**(HH)++.

on addition of $Zn(ClO_4)_2$ ($\phi = 0.06$). This observation suggests that after binding to Zn^{2+} the molecular aggregates are even stronger and non-radiative. In the case of **CBL1**, up on Zn^{2+} binding, the intensity is reduced from pH 4 to 5 after which no change is observed. **CBL3** binds with Zn^{2+} and no change in emission intensity at 610 nm was observed depending on pH. For all these cases, above pH 7, the emission is shifted to the molecular aggregates suggesting very less interaction between the aggregates and Zn^{2+}. **CBG** derivative show random behavior in Zn^{2+} binding depending on pH and it is not suitable for imaging in lysosomal pH window.

Among the three derivatives, only **CBL2** shows pH dependent emission changes up on Zn^{2+} binding. Especially at pH 5, the ratio (530 nm / 610 nm) was gradually decreased with increase in Zn^{2+} concentration (Figure 2.14). Similar phenomena were observed at pH 4 and 6. The red shift is due to the internal charge transfer from the donor to the acceptor. At lower pH (pH 4-6), since the particle size is smaller, the surface area available for interaction with Zn^{2+} is more, resulting in faster response. However, in basic pH since the molecule forms strong and larger aggregates, the surface area available for interaction with Zn^{2+} is less and have weaker response by Zn^{2+} (Figure 2.13). Similar phenomenon was observed with other **CBL** derivatives also.

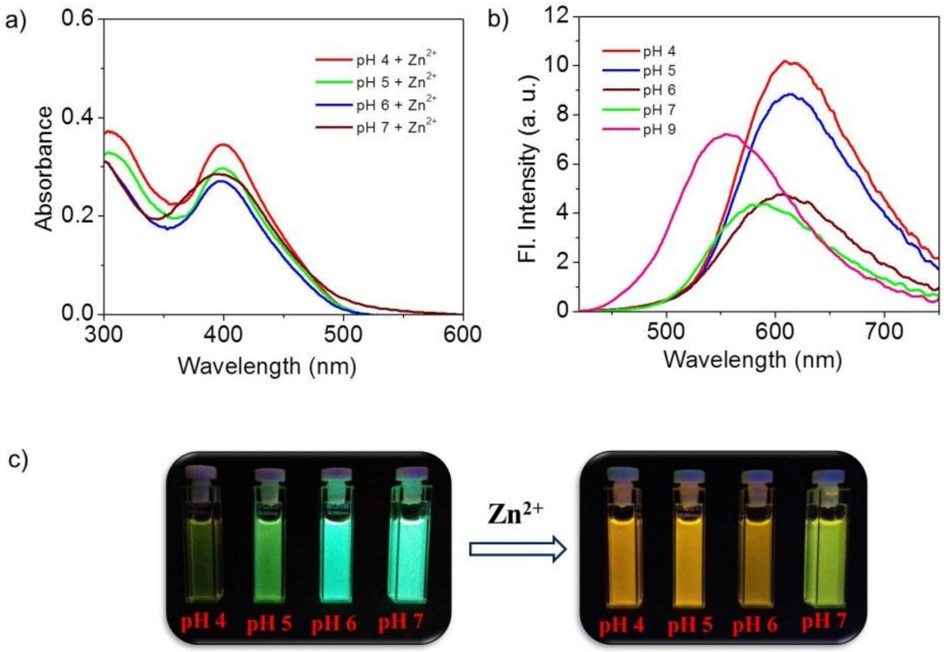

Figure 2.12: (a) Absorption and (b) emission spectra of **CBL2** on addition of 10 equivalent of Zn^{2+} in different pH (c = 10 µM and λ_{ex} = 390 nm); (c) The photograph of fluorescence change with respect to pH and on addition of Zn^{2+}.

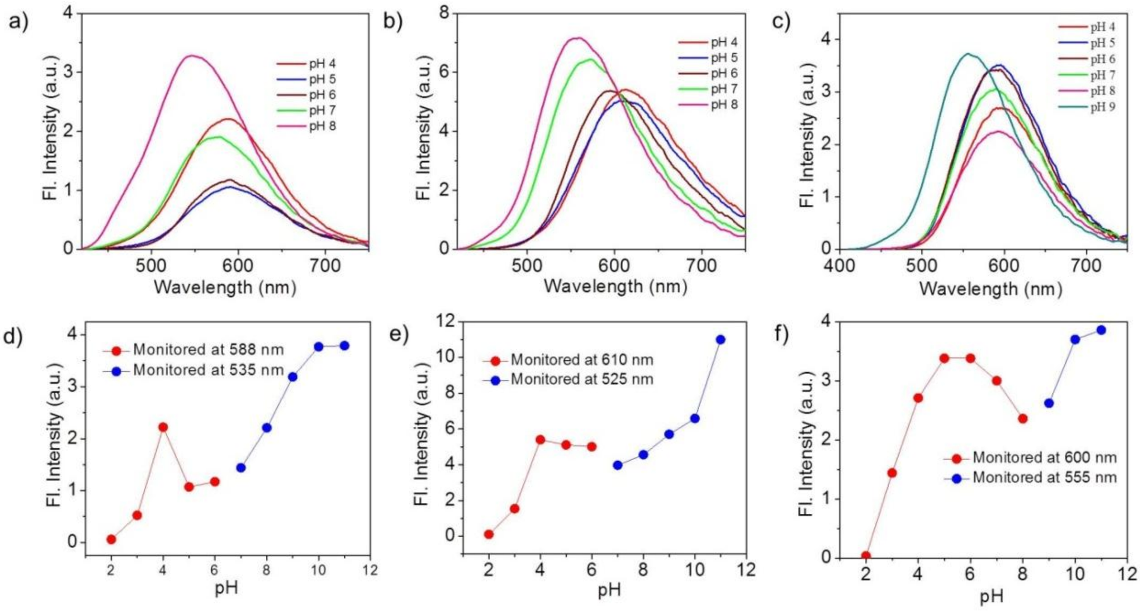

Figure 2.13: The emission intensity change of a) **CBL1**, b) **CBL3** and c) **CBG** with respect to pH (*c* = 10 µM and λ_{ex} = 365 nm) and the corresponding secondary plot for the emission change of d) **CBL1**, e) **CBL3** and f) **CBG** in the pH range 2-11.

Subsequently we studied the Zn^{2+} binding of **CBL2** in different concentration of Zn^{2+}. It was found that, 1.7 eq., 2.8 eq. and 5.4 eq. of Zn^{2+} were required to attain saturation at pH 4, 5 and 6, respectively, suggesting that there may be steric hindrance at higher pH. While increasing the pH, the aggregates are becoming strong and the interaction with Zn^{2+} is less (Figure 2.14). The DLS analysis also show that even after binding with Zn^{2+}, it exists as aggregates but the size varies on changing the pH. The aggregate size increased on binding with Zn^{2+} than the corresponding molecular aggregate at the same pH (Figure 2.15).

We have also tested Zn^{2+} sensing in MES buffer at different pH and the phenomena are similar as in PBS buffer. Thus, we continued rest of the experiments in PBS buffer for mimicking the physiology. In addition, we also measured the dissociation constant of nanoparticles with Zn^{2+} at different pH (pH 4 : $1.03 \pm 0.4 \times 10^{-5}$ M; pH 5 : $1.92 \pm 0.3 \times 10^{-5}$ M; pH 6 : $3.78 \pm 0.4 \times 10^{-5}$ M) and the detection limits of Zn^{2+} ranged from 89 nM, 154 nM, and 369 nM at pH 4, 5 and 6, respectively. The HOMO energy level is nearly unchanged while the LUMO level of the Zn^{2+} complexes shows significant stabilization compared to the neutral form.

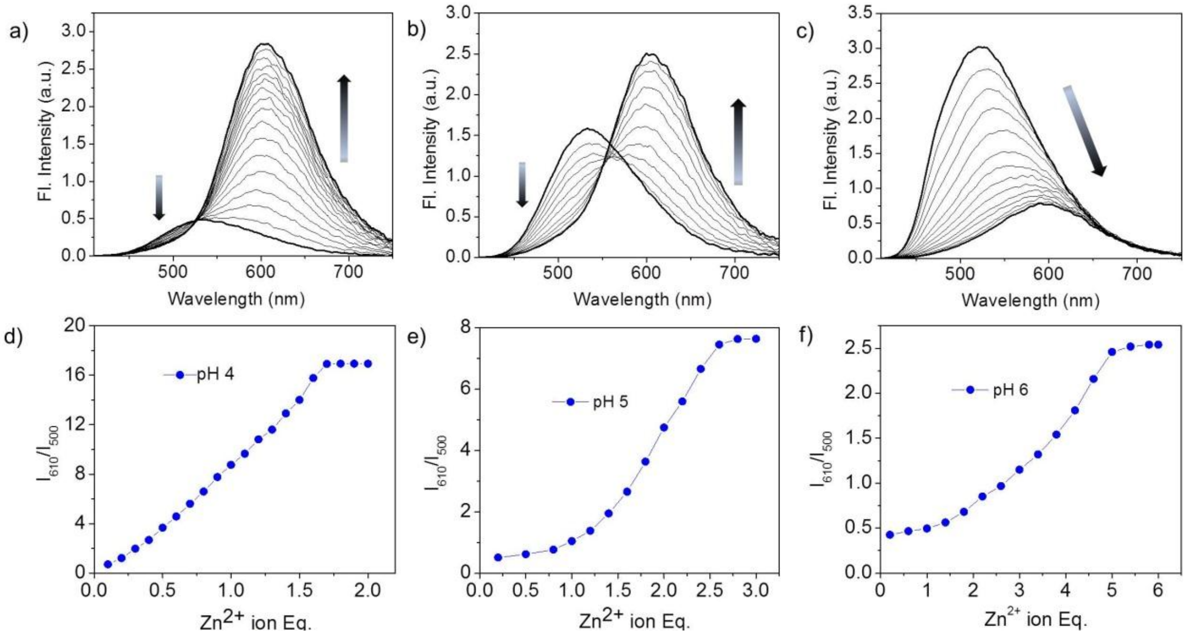

Figure 2.14: The emission intensity change of **CBL2** on reacting with Zn^{2+} at a) pH 4, b) pH 5 and c) pH 6 (c = 5 µM, λ_{ex} = 390 nm, MES buffer). The corresponding secondary plots are shown in d), e) and f).

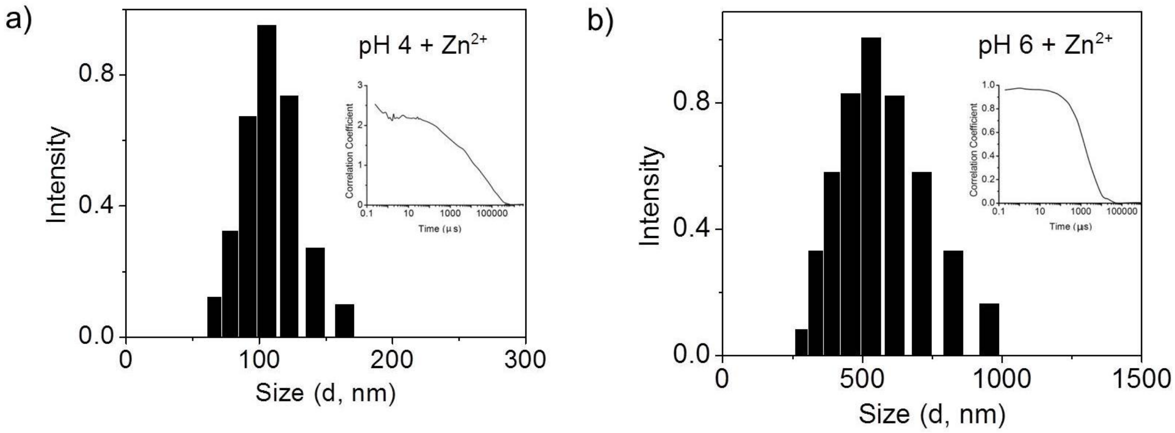

Figure 2.15: pH dependent size distribution of **CBL2** bound with zinc ions in different pH (4, 6) and the insets show the corresponding correlogram.

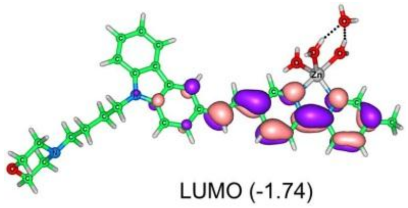

LUMO (-1.74)

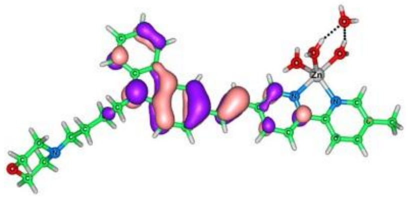

HOMO (-6.49)

Figure 2.16: HOMO and LUMO features of **CBL2-Zn^{2+}**. All the optimized structures were confirmed as energy minima by vibrational frequency analysis at 298.15 K and 1.0 atm pressure.

2.3.7 Selectivity

The selective binding towards Zn^{2+} when compared to other cations was investigated by conducting detailed metal ion titration experiments in the presence of a variety of metal cations at different pH (4 to 6). Biologically relevant and abundant cations such as Na^+, K^+, Mg^{2+}, Cu^{2+}, Fe^{3+}, Co^{2+} and toxic metal ions such as Pb^{2+} and Hg^{2+} showed negligible responses (Figure 2.17). However, Cd^{2+}, a toxic but least abundant cation in cellular component showed a partial fluorescence enhancement, however may not interfere since Cd^{2+} is not a biologically relevant cation. Obviously, the maximum emission intensity at 610 nm in presence of Zn^{2+}

is much higher when compared to other ions and hence **CBL2** nanoprobe is suitable for Zn^{2+} sensing in physiological conditions. Other derivatives also showed the same behavior towards different metal ions but, no distinct emission change in lysosomal pH window. Hence, **CBL2** is selected as the best fluorescent nanoprobe that can be used for the targeted imaging of lysosomal Zn^{2+} and pH simultaneously.

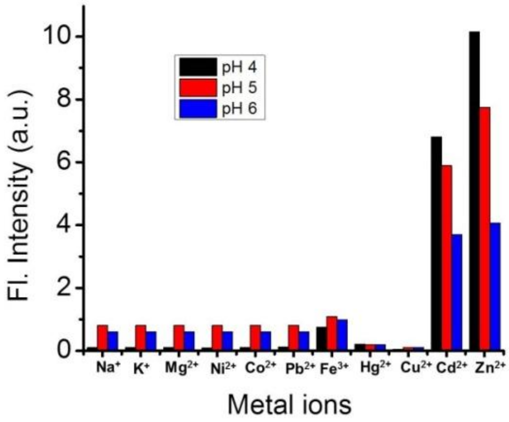

Figure 2.17: Fluorescence intensity change of, **CBL2** on reaction with various metal ions (10 eq.) (c = 10 µM and λ_{ex} = 390 nm).

2.3.8 MTT Assay

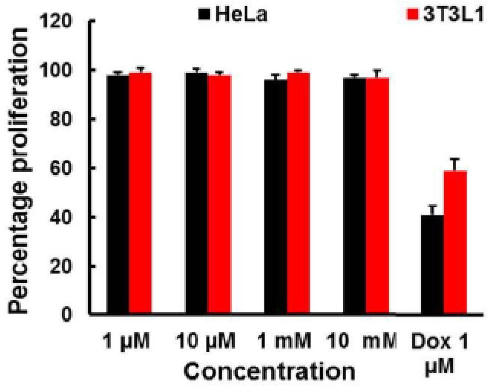

Figure 2.18: Cell viability of normal (3T3L1) and cancer (HeLa) cells after 3 h incubation with **CBL2** at different concentration. Cells were incubated in DMEM (10% FBS) at 37 °C, at 5% CO_2. Spectra were measured at 450 nm.

Cytotoxicity of the nanoprobe was evaluated on human cervical cancer (HeLa), and fibroblast-like murine pre-adipocyte (3T3 L1) cell lines by MTT assay. The cell viability at different concentrations of the probe, **CBL2** is shown in the Figure 2.18. No measurable cytotoxicity was observed even at 10 mM probe concentration.

2.3.9 Colocalization Experiments

Subsequently, cells were co-stained with **CBL2** along with Lysotracker Red, Mito Tracker Red and a nucleus staining dye Hoechst 33342, to check its specificity in cellular organelles. As shown in Figure 2.19, **CBL2** displayed reasonably good colocalization with Lyso Tracker Red with a Pearson coefficient of 0.96. However, there was either very poor or no colocalization observed with Mito Tracker Red and Hoechst 33342, respectively. These results suggest that **CBL2** nanoprobe has great potential for lysosomal study without interference of other cellular organelles in cell. The colocalization was calculated using Pearson's correlation coefficient (r) and Mander's overlap coefficients (R) as given in the Figure 2.19.

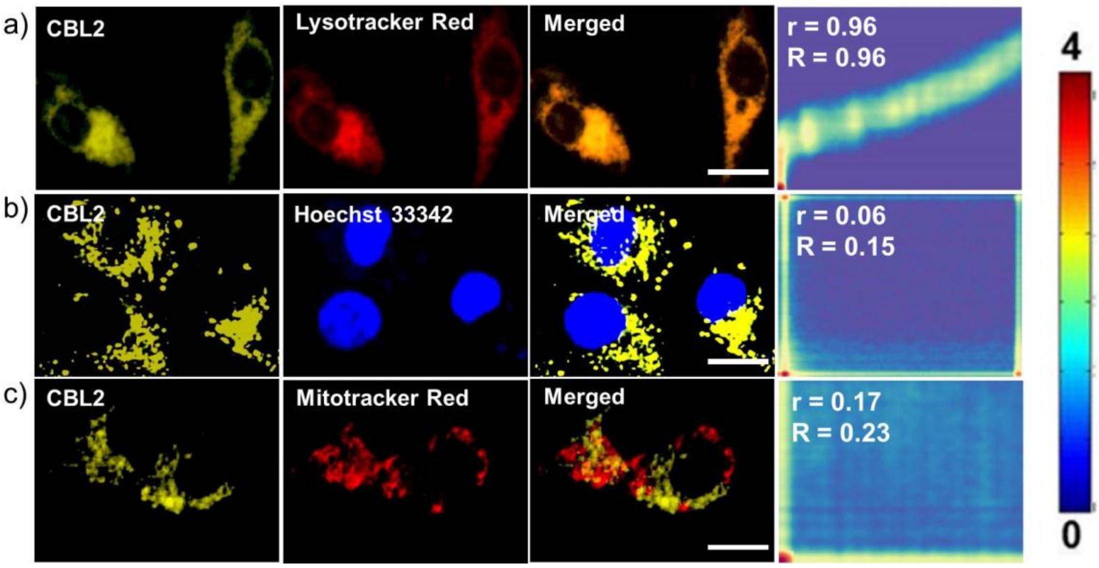

Figure 2.19: Fluorescence images for intracellular localization of **CBL2** (*c* =10 μM, DMEM culture media) in HeLa cells and imaged after counter stained with (a) Lyso-Tracker, (b) Hoechst 33342 and (c) Mito-Tracker. Scale bar corresponds to 50 μm.

Zhu *et.al.*, reported that glycol moiety can be used for targeting lysosome when the fluorescent scaffold was rhodamine.[24] However, in the case of the carbazole derivative **CBG** attached with glycol moiety, no such localization in lysosome was observed. The Pearson's colocalization coefficient was found to be 0.07 (Figure 2.20).

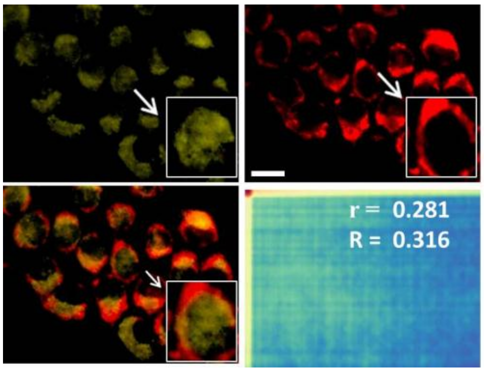

Figure 2.20: Fluorescence images for intracellular localization of **CBG** (*c* = 10 μM) in HeLa cells and imaged after counter staining with Lyso Tracker. Scale bar corresponds to 50 μM.

2.3.10 pH dependent Emission Change

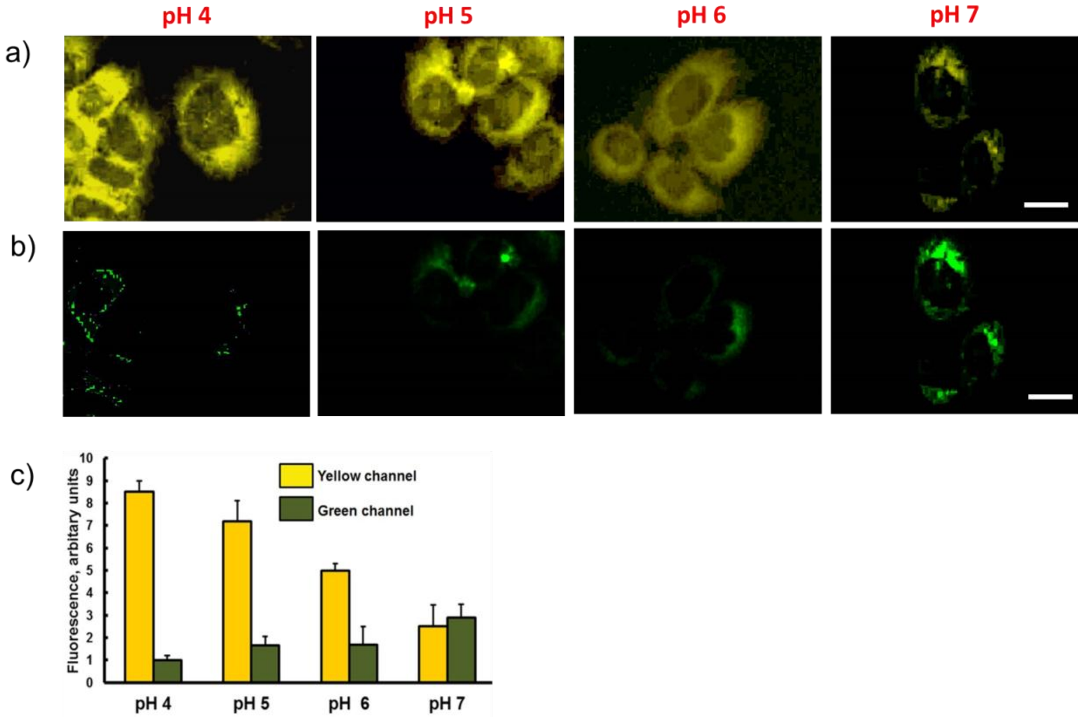

Figure 2.21: Change in fluorescence of HeLa cells incubated for 30 min in K^+ buffer of various pH values with Nigericin (10 μM) and finally treated with **CBL2** (10 μM) under (a) yellow channel and (b) green channel. Scale bar corresponds to 30 μm. Effect of pH on the relative emission intensity (at FITC Channel) of **CBL2** and relative emission intensity (at TRITC Channel) of **CBL2** +Zn^{2+} in HeLa cells. Data are the mean ± SD of three independent experiments.

Detailed studies on pH dependent emission changes were performed at the cellular level. HeLa cells were incubated for 30 min in K^+ buffer of various pH values with Nigericin (10 mM) and finally treated with **CBL2**. The emission intensity was checked in the yellow channel (for zinc complex) and green channel (for the probe). Interestingly, the emission intensity was found to reduce in the yellow channel and increased in the green channel as seen in the fluorescent images and intensity graph in Figure 2.23. These results clearly indicate the use of the probe for monitoring both pH and Zn^{2+} in lysosome since the emission intensity change occurs in the pH range of 4-6.

2.3.11 Effect of pH Regulators

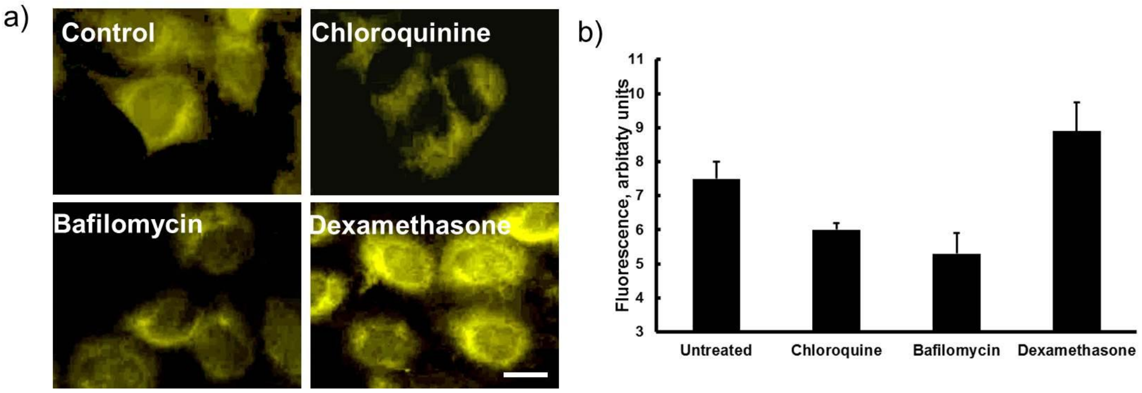

Figure 2.22: Evaluation of pH change using **CBL2** (c = 10 μM) on HeLa cells incubated with intracellular pH regulators such as Chloroquine (200 μM), Bafilomycin (100 nM) and Dexamethasome (2 μM) using (a) fluorescence microscope and (b) its quantification using Image J software. Scale bar corresponds to 30 μM. Data are the mean ± SD of three independent experiments.

Since Chloroquine, a lysomotropic agent and Baflomycin A1, a selective inhibitor of the vacuolar-type H^+ ATPase can cause increase of lysosomal pH, and dexamethasome which decreases the cytoplasmic pH and initiate apoptosis, we examined these external pH regulators for monitoring the emission intensity change in cancer cells. As expected, when pH regulators along with **CBL2** nanoprobe were incubated to study intracellular pH, the fluorescence intensity was decreased for Chloroquine and Baflomycin A1, whereas intensity was increased for Dexamethasome (Figure 2.22) at yellow channel. It is worth noting that **CBL2** probe simultaneously responds to intracellular Zn^{2+} along with pH regulators.

2.3.12 Zn^{2+} Sensing in Oxidative Stress

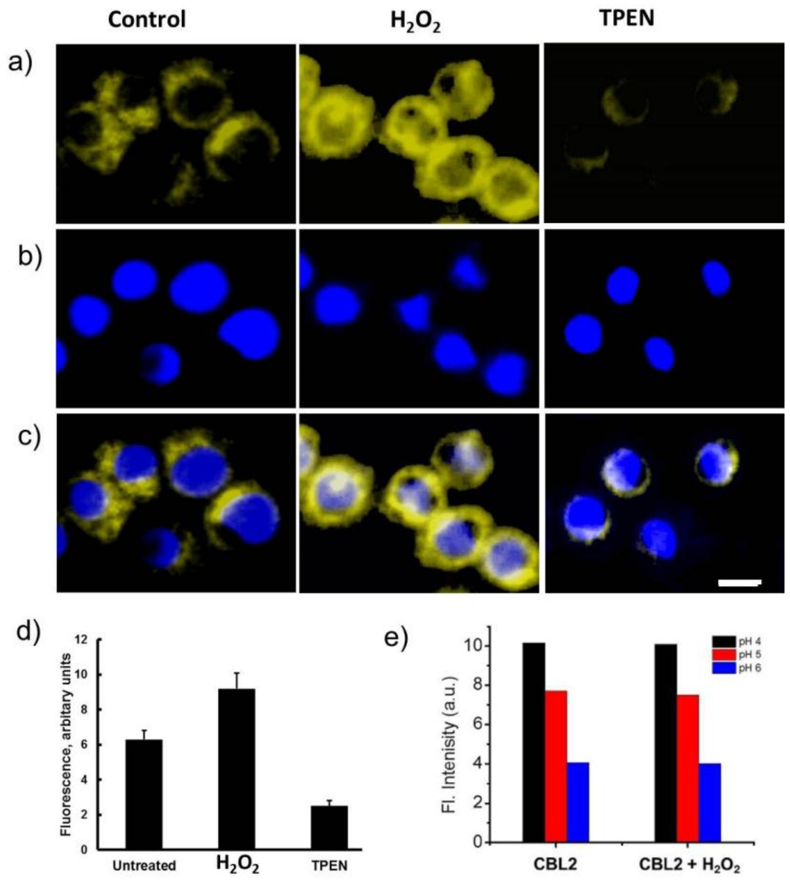

Figure 2.23: Imaging of Zn^{2+} using intracellular Zn^{2+} generators and chelators in HeLa cells. Cells were treated with either hydrogen peroxide (50 μM) for 30 min or TPEN (20 μM) for 20 min. After the respective treatments, cells were incubated with the **CBL2** (*c* = 10 μM) for 30 min, washed and observed under an (a) inverted fluorescence microscope, (b) counter stained with Hoechst 333422 and (c) merged image. (d) Emission intensity change monitored from the cell. (e) Fluorescence intensity change of **CBL2** on reaction with H_2O_2 at different pH.

Imaging of Zn^{2+} in lysosome was performed by incubating **CBL2** in HeLa cells. It was confirmed that the emission intensity of the Zn^{2+} bound nanoprobe was gradually decreased when the pH was changed from pH 4 to 6 in TRITC channel (Figure 2.23). At the same time, the emission intensities were increased at FITC channel. As mentioned earlier, at low pH, the molecules formed weak aggregates and readily interacted with Zn^{2+}, whereas at higher pH, the aggregates are stronger and interact less with Zn^{2+}. Thus at pH 7, we observed intense green emission.

Upon treatment with the cell-permeable metal ion chelator TPEN, the emission intensities were reduced drastically, suggesting the decrease of Zn^{2+} level in the cellular lysosome (Figure 2.23). Furthermore, lysosomal Zn^{2+} under oxidative stress was monitored by addition of H_2O_2 with **CBL2** probe (Figure 2.23). During oxidative stress, a rapid influx of hydrogen peroxide takes place which causes the oxidation of cysteine residues in the Zn-bound metallothioneins and subsequently releases the Zn^{2+}. Thus, the administration of hydrogen peroxide causes to release Zn^{2+} within the cells and rapidly accumulated near the lysosome area. The **CBL2** nanoprobe is capable of detecting this endogenous Zn^{2+} in cancer cells (Figure 2.23). Hydrogen peroxide was administrated at low concentration (50 μM) to elicit any cell membrane damage. This observation clearly suggests that **CBL2** probe can efficiently monitor the intracellular Zn^{2+} release under oxidative stress.

2.3.13 Zn^{2+} Sensing in Apoptotic Conditions

In endothelial cells, Zn^{2+} is occasionally associated to the protection of cells against apoptosis. Kolenko *et al.*, reported that in human peripheral blood T lymphocytes, Zn^{2+} depletion may induce cell death due to DNA fragmentation in nuclei. However, the effect of Zn^{2+} in cancer cell proliferation and the apoptosis are not yet clearly studied. Here we studied the efficiency of **CBL2** probe to monitor the role of Zn^{2+} in apoptosis. Thus, a cell permeable zinc chelator, TPEN that induces apoptosis and alters the Zn^{2+} concentration in cancer cells was treated along with **CBL2** probe to investigate the alteration of Zn^{2+} (Figure 2.24). The apoptotic assays clearly differentiated the viable and nonviable cells at different time interval. It is to be noted that TPEN induced apoptosis was accompanied with a reduction of Zn^{2+} that can be clearly monitored by the probe. Furthermore, a standard chemotherapeutic agent, doxorubicin that induces apoptosis was incubated and the Zn^{2+} concentration was monitored. Interestingly, even though there is significant cell death caused by apoptosis (Figure 2.24) no change of Zn^{2+} concentration was observed. Here, doxorubicin does not alter the Zn^{2+} concentration significantly during apoptosis. In this condition, **CBL2** probe effectively detects the endogenous Zn^{2+}. Thus, **CBL2** probe is successfully used to monitor Zn^{2+} in any biological conditions such as oxidative conditions and apoptosis caused by standard drugs and/or metal chelator.

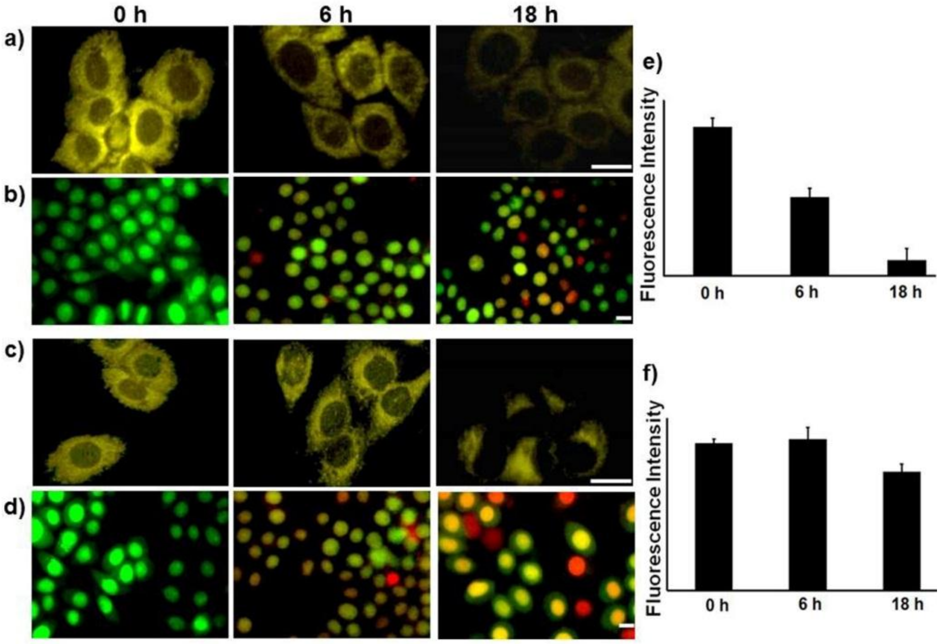

Figure 2.24: Evaluation of Zn^{2+} status using **CBL2** nanoprobe (*c* = 10 μM) during programmed cell death in HeLa cells. Fluorescence images for intracellular Zn^{2+} and live dead assay after (a, b) TPEN (30 μM) or (c, d) Dox (1 μM) treatment for 0 - 18 h. Images were analysed using Image J software and Zn^{2+} concentration were quantified for TPEN (e) and Dox (f) treatment. Scale bar corresponds to 50 μm (a & c) and 20 μm (b & d). Data are the mean ± SD of three independent experiments.

2.4 Conclusions

In conclusion, we have successfully designed fluorescent nanoprobes based on the self-assembled fluorescent molecules, **CBL1-3**. These molecules display pH dependent formation of fluorescent nanoparticles, exhibiting enhanced emission on increasing the pH. They simultaneously respond towards pH and Zn^{2+} in lysosome and are silent above or below pH 6-4. The protonation of nitrogen atoms at the donor and the acceptor sites regulate the hydrophilicity and the self-assembly properties. Interestingly, the **CBL2** nanoprobe display better photostability when compared to the corresponding monomer as well as commercial markers. Among **CBL1-3**, **CBL2** based fluorescent nanoprobe is promising for the imaging of Zn^{2+} and pH variations within lysosomes in cancer cells. In addition, this probe is effectively capable to monitor the alteration of Zn^{2+} under the complex conditions of apoptosis where most reactive oxygen species or free radicals are involved. Thus, **CBL2** nanoprobe turns out to be a potential tool for gaining insights on zinc ion dynamics in cancer cells.

2.5 Experimental Section

2.5.1 Materials and Methods

Unless otherwise stated, all starting materials and reagents were purchased from commercial suppliers (Sigma Aldrich, Alfa Aesar, Fluka, Merck or Spectrochem) and used without further purification. DAPI, Lyso Tracker Red, Mito Tracker Red were also purchased from Sigma Aldrich. Reactions were monitored using thin layer chromatography on silica gel 60 F254 (0.2 mm; Merck) accomplished with UV light source at 254 nm and 365 nm. Normal-phase chromatography was carried out using silica gel (particle size: 60-120 mesh and 100-200 mesh). ^1H NMR spectra were recorded on Bruker Advance 500 NMR spectrometers, and chemical shifts are expressed in parts per million (ppm). Cell imaging was carried out in an Epifluorescent Inverted microscope. Acetonitrile used for photophysical measurements was dried over P_2O_5 and freshly distilled prior to use to ensure extreme dry condition. PBS buffer was used for pH dependent studies and MES buffer was used for the zinc binding studies.

2.5.2. Synthesis and Characterization

Synthesis of 5-(bromomethyl)-5'-methyl-2,2'-bipyridine (12):

To a solution of 5,5'-methyl-2,2'-bipyridine (**11)** (2 g, 10.85 mmol) in 50 mL of dry carbontetrachloride was added *N*-bromosuccinimide (1.93 g, 10.85 mmol) and AIBN (100 mg). The reaction mixture was refluxed for 4 h at 80 °C. After the completion of the reaction, the mixture is filtered in hot condition and the solvent was removed under reduced pressure. The crude was then purified by column chromatography (SiO_2, 5% EtOAc/DCM) to give a white solid. Yield: 72%.

12: ^{1}H **NMR** ($CDCl_3$, 500 MHz, TMS) δ (ppm): 8.60 (d, 1H, *J* = 1 Hz), 8.50 (d, 1H, *J* = 0.5 Hz), 8.36 (d, 1H, *J* = 8.5 Hz), 8.28 (d, 1H, *J* = 8 Hz), 7.83 (dd, 1H, *J* = 8 Hz and 2 Hz), 7.64 – 7.61 (m, 1H), 4.52 (s, 2H), 2.39 (s, 3H); **^{13}C NMR** ($CDCl_3$, 125 MHz,) δ (ppm): 153.2, 150.1, 138.3, 135, 133.2, 129.4, 121.5, 33.4, 18.0. ESI MS (2): **MS** calc. for $C_{12}H_{11}BrN_2$, 263.01; Found 262.01 (100%) and 264.01(98%)

Preparation of diethyl ((5'-methyl-[2,2'-bipyridin]-5-yl)methyl)phosphonate (13)

The monophosphonate (**13**) was prepared by the reaction of the corresponding monobromoethyl derivative (**12**) (1 g, 3.80 mmol) with 1.3 mL (7.60 mmol) of triethyl phosphite at 100 °C for 12 h followed by the removal of the unreacted triethyl phosphite under vacuum. Yield: 90%.

13: **^{1}H NMR** ($CDCl_3$, 500 MHz, TMS) δ (ppm): 8.60 (d, 1H, *J* = 1 Hz), 8.50 (d, 1H, *J* = 0.5 Hz), 8.36 (d, 1H, *J* = 8.5 Hz), 8.28 (d, 1H, *J* = 8 Hz), 7.83 (dd, 1H, *J* = 8 Hz and 2 Hz), 7.64 – 7.61 (m, 1H), 4.2 (q, 4H, *J* = 7 Hz), 2.39 (s, 3H), 1.32 (t, 6H, *J* = 7 Hz); **^{13}C NMR** ($CDCl_3$, 125 MHz,) δ (ppm): 153.2, 150.1, 138.3, 135, 134.2, 128.4, 120.5, 62.3, 39.5, 18.3, 16.3; ESI MS: **MS** Calcd. for $C_{16}H_{21}N_2O_3P$, 320.13 ; Found 321.21; [M + H]+

Synthesis of 9-(2-bromoethyl)-9H-carbazole (15), 9-(4-bromobutyl)-9H-carbazole (16) and 9-(6-bromohexyl)-9H-carbazole (17)

A mixture of carbazole (2 g, 11.97 mmol), the required dibromoalkane (1,2-dibromoethane (23.94 mmol, 2.07 mL), 1,4-dibromobutane (23.94 mmol, 2.87

mL) and 1,6-dibromohexane (23.94 mmol, 3.6 mL)) and K_2CO_3 (9.9 g, 71.82 mmol) in dry DMF (40 mL) was stirred for overnight. Then the reaction mixture was poured into water and extracted with dichloromethane. The organic layer was washed with water and dried over anhydrous sodium sulphate. The crude was then purified by column chromatography (SiO_2, 2% EtOAC/ Hexane). Yield: 81 %.

15: **^{1}H NMR** ($CDCl_3$, 500 MHz, TMS) δ (ppm): 8.10 (d, 2H, *J* = 8 Hz), 7.48 – 7.45 (m, 2H), 7.39 (d, 2H, *J* = 8 Hz), 7.25 – 7.22 (m, 2H), 4.35 (t, 2H, *J* = 7 Hz), 3.37 (t, 2H, *J* = 6.5 Hz); **^{13}C NMR** ($CDCl_3$, 125 MHz,) δ (ppm): 134.3, 121.9, 120.8, 118.0, 110.2, 65.21, 31.9.; **ESI MS**: **MS** Calcd. for $C_{14}H_{12}BrN$, 274.16; Found 273.02(100%) and 275.01 (97%).

16: ^{1}H NMR ($CDCl_3$, 500 MHz, TMS) δ (ppm): 8.10 (d, 2H, *J* = 8 Hz), 7.48 – 7.45 (m, 2H), 7.39 (d, 2H, *J* = 8 Hz), 7.25 – 7.22 (m, 2H), 4.35 (t, 2H, *J* = 7 Hz), 3.37 (t, 2H, 6.5 Hz), 2.09 – 2.03 (m, 2H), 1.94 – 1.88 (m, 2H);**^{13}C NMR** ($CDCl_3$, 125 MHz,) δ (ppm):134.3, 121.6, 120.8, 118.2, 110.5, 58.5, 38.8, 33.4, 31.9.; **MS**: MS calc. for $C_{16}H_{16}Br$, 302.21; Found 302.05 (100%) and 304.04 (97%).

17: **^{1}H NMR** ($CDCl_3$, 500 MHz, TMS) δ (ppm): 8.10 (d, 2H, *J* = 8 Hz), 7.48 – 7.45 (m, 2H), 7.39 (d, 2H, *J* = 8 Hz), 7.25 – 7.22 (m, 2H), 4.35 (t, 2H, *J* = 7 Hz), 3.37 (t, 2H, *J* = 6.5 Hz), 2.09 – 2.03 (m, 4H), 1.94 – 1.88 (m, 4H); **^{13}C NMR** ($CDCl_3$, 125 MHz,) δ (ppm): 134.3, 121.7, 120.4, 118.0, 110.7, 58.3, 33.8, 32.6, 29.5, 27.8, 26.4.; **MS**: MS calc. for $C_{18}H_{20}Br$, 330.26 ; Found 329.08 (100%) and 331.08 (98%).

Synthesis of 4-(2-(9H-carbazol-9-yl)ethyl)morpholine (18), 4-(4-(9H-carbazol-9-yl)butyl)morpholine (19) and 4-(6-(9H-carbazol-9-yl)hexyl)morpholine (20):

The bromoalkyl derivative of carbazole **15** (1.2 g, 4.77 mmol), **6** (1.3 g, 4.32 mmol) and **7** (1.2 g, 3.64 mmol)) was dissolved in 50 mL dry butanol and stirred for 10 minutes. To this solution anhydrous Na_2CO_3 (4.3 g, 40 mmol) and morpholine (1.2 mL, 13 mmol) was added followed by catalytic amount of I_2. The reaction mixture was refluxed at 100 °C for 12 h. The mixture was then cooled to room temperature and the solvent was removed under reduced pressure and then water was added. The organic content extracted with dichloromethane and dried over Na_2SO_4. The crude was then purified by column chromatography (SiO_2, 2 % MeOH/EtOAc). Yield: 84%.

18: **^{1}H NMR** ($CDCl_3$, 500 MHz, TMS) δ (ppm): 8.10 (d, 2H, *J* = 8 Hz), 7.48 – 7.45 (m, 2H), 7.39 (d, 2H, *J* = 8 Hz), 7.25 – 7.22 (m, 2H), 4.34 (t, 2H, *J* = 7 Hz), 3.66 (t, 4H, *J* = 4.5 Hz), 2.56 (t, 2H, *J* = 6.5 Hz), 2.34 -2.32 (m, 4H); **^{13}C NMR** ($CDCl_3$, 125 MHz,) δ (ppm): 134.2, 122.9, 121.4, 109.9, 67.8, 56.9, 55.9, 52.5; **ESI MS** (8) : MS Calcd. for $C_{18}H_{20}N_2O$, 280.16 ; Found 281.18 ; $[M + H]^+$

19: **^{1}H NMR** ($CDCl_3$, 500 MHz, TMS) δ (ppm): 8.10 (d, 2H, *J* = 8 Hz), 7.48 – 7.45 (m, 2H), 7.39 (d, 2H, *J* = 8 Hz), 7.25- 7.22 (m, 2H), 4.32 (t, 2H, *J* = 7 Hz), 3.66 (t, 4H, *J* = 4.5 Hz), 2.34-2.32 (m, 6H), 1.97-1.91 (m, 2H), 1.60-1.54 (m, 2H); **^{13}C NMR** ($CDCl_3$, 75 MHz,) δ (ppm): 134.1, 122.9, 121.4, 109.9, 67.1, 62.9, 58.2, 56.2, 28.1, 26.4; **ESI MS**: MS calc. for $C_{20}H_{24}N_2O$, 308.19; Found 309.20 ; $[M + H]^+$

20: ^{1}H NMR ($CDCl_3$, 500 MHz, TMS) δ (ppm): 8.10 (d, 2H, *J* = 8 Hz), 7.48 – 7.45 (m, 2H), 7.39 (d, 2H, *J* = 8 Hz), 7.25- 7.22 (m, 2H), 4.32 (t, 2H, *J* = 7 Hz), 3.66 (t, 4H, *J* = 4.5 Hz), 2.34 -2.32 (m, 6H), 1.97- 1.91 (m, 4H), 1.60- 1.54 (m, 4H); **^{13}C NMR** ($CDCl_3$, 125 MHz,) δ (ppm): 134.1, 122.9, 121.4, 109.9, 66.7, 62.9, 58.3, 51.2, 29.4, 28.1, 27.0; **ESI MS**: MS Calcd. for $C_{22}H_{28}N_2O$, 336.22 ; Found 337.23 ; $[M + H]^+$

Synthesis of 9-(2-morpholinoethyl)-9H-carbazole-3-carbaldehyde (21), 9-(4-morpholinobutyl)-9H-carbazole-3-carbaldehyde (22) and 9-(6-morpholinohexyl)-9H-carbazole-3-carbaldehyde (23):

$POCl_3$ (6.3 mL, 68.4 mmol) and dry DMF (5 mL, 68.4 mmol) were taken in a two neck round bottom flask in inert atmosphere maintained at 0 °C. The mixture was stirred well for 2 h. Light yellow color indicated the formation of the ylide. After 2 h, the compound **18** (800 mg, 2.85 mmol), **19** (900 mg, 2.92 mmol) or **20** (850 mg, 2.52 mmol) dissolved in dry DMF (10 mL) was added to the ylide at 0 ^{o}C and stirring was continued for 6 h. Then the reaction mixture was poured into ice and stirred well. The mixture was boiled at 80 ^{o}C and then dilute NaOH solution was added. The solution was cooled to room temperature and the crude product was extracted with dichloromethane and dried over anhydrous Na_2SO_4. The purification was done by column chromatography (SiO_2, 4% MeOH/EtOAc). Yield: 71%.

21: ^{1}**H NMR** ($CDCl_3$, 500 MHz, TMS) δ (ppm): 10.08 (s, 1H), 8.61 (d, 1H, *J* = 1 Hz), 8.12 (d, 1H, *J* = 7.5 Hz), 8.09 (dd, 1H, *J* = 7 Hz, and 1.5 Hz), 7.54 – 7.51 (m, 1H), 7.48 – 7.45 (m, 2H), 7.33- 7.26 (m, 1H), 4.34 (t, 2H, *J* = 7 Hz), 3.66 (t, 4H, *J* = 4.5 Hz), 2.56 (t, 2H, *J* = 6.5 Hz), 2.34 -2.32 (m, 4H); ^{13}**C NMR** ($CDCl_3$, 125 MHz,) δ (ppm): 191.0, 139.4, 135.4, 128.7, 126.5, 125.4, 121.7, 119.7, 113.5, 109.8, 66.9, 56.6, 54.0, 41.1; **ESI MS**: MS Calcd. for $C_{19}H_{20}N_2O_2$, 308.15 ; Found 309.26 ; $[M + H]^+$

22: ^{1}**H NMR** ($CDCl_3$, 500 MHz, TMS) δ (ppm): 10.08 (s, 1H), 8.61 (d, 1H, *J* = 1 Hz), 8.12 (d, 1H, *J* = 7.5 Hz), 8.09 (dd, 1H, *J* = 7 Hz, and 1.5 Hz), 7.54- 7.51 (m, 1H), 7.48-7.45 (m, 2H), 7.33- 7.26 (m, 1H), 4.32 (t, 2H, *J* = 7 Hz), 3.66 (t, 4H, *J* = 4.5 Hz), 2.34-2.32 (m, 6H), 1.97-1.91 (m, 2H), 1.60-1.54 (m, 2H); ^{13}**C NMR** ($CDCl_3$, 125 MHz,) δ (ppm): 191.0, 139.4, 135.4, 128.7, 126.5, 125.4, 121.7, 119.7, 113.5, 109.8, 66.9, 58.3, 53.6, 42.9, 26.7, 24.1; **ESI MS**: MS Calcd. for $C_{21}H_{24}N_2O_2$, 336.43 ; Found 337.42 ; $[M + H]^+$

23: ^{1}**H NMR** ($CDCl_3$, 500 MHz, TMS) δ (ppm): 10.08 (s, 1H), 8.61 (d, 1H, *J* = 1 Hz), 8.12 (d, 1H, *J* = 7.5 Hz), 8.09 (dd, 1H, *J* = 7 Hz, and 1.5 Hz), 7.54-7.51 (m, 1H), 7.48-7.45 (m, 2H), 7.33-7.26 (m, 1H), 4.32 (t, 2H, *J* = 7 Hz), 3.66 (t, 4H, *J* = 4.5 Hz), 2.34 - 2.32 (m, 6H), 1.97-1.91 (m, 4H), 1.60-1.54 (m, 4H); ^{13}**C NMR** ($CDCl_3$, 125 MHz,) δ (ppm): 191.0, 139.4, 135.4, 128.7, 126.5, 125.4, 121.7, 119.7, 113.5, 109.8, 66.9, 58.9, 53.7, 43.1, 28.9, 27.2, 27.1, 26.3; **ESI MS**: MS Calcd. for $C_{23}H_{28}N_2O_2$, 364.48 ; Found 365.57 ; $[M + H]^+$

Synthesis of (E)-4-(2-(3-(2-(5'-methyl-[2,2'-bipyridin]-5-yl)vinyl)-9H-carbazol-9-yl)ethyl)morpholine (24), (E)-4-(4-(3-(2-(5'-methyl-[2,2'-bipyridin]-5-yl)vinyl)-9H-carbazol-9-yl)butyl)morpholine (25) and (E)-4-(6-(3-(2-(5'-methyl-[2,2'-bipyridin]-5-yl)vinyl)-9H-carbazol-9-yl)hexyl)morpholine (26)

The monophosphonate ester derivative (**13**) (100 mg, 0.3121 mmol) was taken in a two neck RB flask in an inert atmosphere and dry THF (20 mL) was added to dissolve the content. NaH (37 mg) dissolved in dry THF (10 mL) was added drop wise to it using pressure equalizer at 0 °C. The stirring was continued for 15 min. Then the required aldehyde derivative (**21**) 96.269 mg, 0.3121 mmol or (**22**) 104.99 mg, 0.3121 mmol or (**23**) 113.75 mg, 0.3121 mmol) dissolved in dry THF (20 mL) was added dropwise using a pressure equalizer. The mixture was then refluxed at 60 °C for 12 h. The excess NaH was quenched by adding methanol and the mixture was poured into water and then extracted with DCM. It was dried under reduced pressure and purified by column chromatography (SiO_2, 6 % MeOH/DCM). Yield: 74%.

24: **^{1}H NMR** ($CDCl_3$, 500 MHz, TMS) δ (ppm): 8.78 (d, 1H, *J* = 2 Hz), 8.51 (s, 1H), 8.36 (d, 1H, *J* = 8.5 Hz), 8.30 (d, 1H, *J* = 8 Hz), 8.25 (d, 1H, *J* = 1 Hz), 8.13 (d, 1H, *J* = 7.5 Hz), 8.00 (dd, 1H, *J* = 6 Hz and 2.5 Hz), 7.70 (dd, 1H, *J* = 7 Hz and 1.5 Hz), 7.63 (dd, 1H, *J* = 7 Hz and 2 Hz), 7.50-7.47 (m, 1H), 7.43-7.40 (m, 3H), 7.28-7.25 (m, 1H), 7.16 (d, 1H, *J* = 16 Hz), 4.44 (t, 2H, *J* = 7.5 Hz), 3.70 (t, 4H, *J* = 6.5 Hz), 2.78 (t, 2H, *J* = 3 Hz), 2.55 (t, 4H, *J* = 4 Hz), 2.31 (s, 3H); **^{13}C NMR** ($CDCl_3$, 125 MHz,) δ (ppm): 154.5, 153.5, 149.6, 147.8, 140.7, 140.4, 137.4, 133.3, 133.2, 133.0, 131.6, 128.2, 126.1, 124.6, 123.3, 122.9, 122.1, 120.6, 120.5, 120.4, 119.4, 119.0, 108.9, 108.8, 66.9, 56.6, 54.0, 41.1, 18.38; **HRMS**: MS Calcd. for $C_{31}H_{30}N_4O$, 474.24 ; Found 475.2492 ; $[M + H]^+$

25: **^{1}H NMR** ($CDCl_3$, 500 MHz, TMS) δ (ppm): 8.78 (d, 1H, *J* = 2 Hz), 8.51 (s, 1H), 8.36 (d, 1H, *J* = 8.5 Hz), 8.30 (d, 1H, *J* = 8 Hz), 8.26 (d, 1H, *J* = 1 Hz), 8.13 (d, 1H, *J* = 7.5 Hz), 8.00 (dd, 1H, *J* = 6 Hz and 2.5 Hz), 7.70 (dd, 1H, *J* = 7 Hz and 1.5 Hz), 7.62 (dd, 1H, *J* = 7 Hz and 2 Hz), 7.50-7.47 (m, 1H), 7.43-7.40 (m, 3H), 7.28-7.25 (m, 1H), 7.16 (d, 1H, *J* = 16 Hz), 4.33 (t, 2H, *J* = 7.5 Hz), 3.67 (t, 4H, *J* = 6.5 Hz), 2.39 (s, 3H), 2.37-2.32 (m, 6H), 1.96-1.90)m, 2H), 1.59-1.54 (m, 2H); **^{13}C NMR** ($CDCl_3$, 125 MHz) δ (ppm): 154.5, 153.5, 149.6, 147.8, 140.8, 140.4, 137.4, 133.3, 133.2, 132.9, 131.6, 128.0, 125.9, 124.5, 123.3, 122.8, 122.0, 120.6, 120.5, 120.4, 119.2, 119.0, 108.9, 108.9, 66.9, 58.3, 53.6, 42.9, 26.7, 24.1, 18.3; **HRMS**: MS Calcd. for $C_{33}H_{34}N_4O$, 502.27 ; Found 503.2801 ; $[M + H]^+$

26: **^{1}H NMR** ($CDCl_3$, 500 MHz, TMS) δ (ppm): 8.78 (d, 1H, *J* = 2 Hz), 8.51 (s, 1H), 8.36 (d, 1H, *J* = 8.5 Hz), 8.30 (d, 1H, *J* = 8 Hz), 8.25 (d, 1H, *J* = 1 Hz), 8.13 (d, 1H, *J* = 7.5 Hz), 8.00 (dd, 1H, *J* = 6 Hz and 2.5 Hz), 7.70 (dd, 1H, *J* = 7 Hz and 1.5 Hz), 7.63 (dd, 1H, *J* = 7 Hz and 2 Hz), 7.50-7.47 (m, 1H), 7.43-7.40 (m, 3H), 7.28-7.25 (m, 1H), 7.16 (d, 1H, *J* = 16 Hz), 4.44 (t, 2H, *J* = 7.5 Hz), 3.69 (t, 4H, *J* = 6.5 Hz), 2.34 (s, 3H), 2.29-2.26 (m, 4H), 1.90 (t, 2H, *J* = 7.5 Hz), 1.47-1.42 (m, 2H), 1.40-1.34 (m, 6H); **^{13}C NMR** ($CDCl_3$, 125 MHz) δ (ppm): 154.5, 153.5, 149.6, 147.8, 140.8, 140.5, 137.4, 133.4, 133.2, 133.0, 131.7, 127.9, 125.9, 124.5, 123.2, 122.8, 122.0, 120.6, 120.5, 119.2, 119.0, 108.9, 108.8, 66.9, 58.9, 53.7, 43.1, 28.9, 27.2, 27.1, 26.3, 18.39; **HRMS**: MS Calcd.. for $C_{35}H_{38}N_4O$, 530.30 ; Found 531.3119 ; [M + H]+

Synthesis of 2-(2-(2-methoxyethoxy)ethoxy)ethyl 4-methylbenzenesulfonate (28)

Sodium hydroxide (12 g) was dissolved in 50 mL water taken in a 250 mL round bottom flask. To this 15 g triethylene glycol monomethyl ether (dissolved in 20 mL THF) was added dropwise and stirred well at ice cold temperature. *p*-toluenesulfonyl chloride (30 g) dissolved in 50 mL THF was added drop wise to this reaction mixture at the ice cold temperature. The stirring was continued for 6 more hours. The reaction mixture was added to water taken in a beaker and extracted with water. The organic layer was washed several times with water to remove all sodium hydroxide present. The organic layer was then concentrated and dried under reduced pressure. The product was obtained as colourless liquid. Yield: 60 %. The product was directly used for the next reaction.

Preparation of 9-(2-(2-(2-methoxyethoxy)ethoxy)ethyl)-9H-carbazole (29)

A solution of carbazole (5 g, 29.9 mmol) in dry DMF was added drop wise under argon atmosphere at 0 °C to a suspension of NaH (2.145 g, 149 mmol) in DMF (10 mL). The resulting white suspension was stirred for 30 min. A solution of **28**

(12.29 g, 38.87 mmol) in dry DMF (20 mL) was added drop wise and the reaction mixture was stirred at ambient temperature for 60 h. The mixture was then poured in to 500 mL of ice water to give a brown suspension that was washed with hexane and extracted with ethyl acetate. The crude solution was then dried under reduced pressure and purified by column chromatography (SiO2, 80% Ethyl acetate/Hexane). Yield: 77%.

29: **^{1}H NMR** ($CDCl_3$, 500 MHz, TMS) δ (ppm): 8.10 (d, 2H, *J* = 8 Hz), 7.48 – 7.45 (m, 2H), 7.39 (d, 2H, *J* = 8 Hz), 7.25 – 7.22 (m, 2H), 4.51 (t, 2H, *J* = 6 Hz), 3.89 (t, 2H, *J* = 6 Hz), 3.55 – 3.42 (m, 8H), 1.65 (s, 3H); **^{13}C NMR** ($CDCl_3$, 125 MHz,) δ (ppm): 134.1, 122.8, 121.7, 109.6, 71.8, 71.2, 70.64, 70.5, 69.3, 57.4; **ESI MS**: MS Calcd for $C_{19}H_{23}NO_3$, 313.17 ; Found 314.20; $[M + H]^+$

Synthesis of 9-(2-(2-(2-methoxyethoxy)ethoxy)ethyl)-9H-carbazole-3-carbaldehyde (30)

$POCl_3$ (6.3 mL, 68.4 mmol) and dry DMF (5 mL, 68.4 mmol) were taken in a two neck round bottom flask in an inert atmosphere and at 0 °C. The mixture was stirred well for 2 h. A light yellow colour indicated the formation of the ylide. After 2 h, the compound **29** (1 g, 3.13 mmol) dissolved in dry DMF (10 mL) was added to the ylide at 0 °C and the stirring continued for 6 h. Then the reaction mixture was poured into ice and stirred well. The mixture was boiled at 80 °C and dilute NaOH solution was added. The reaction mixture was cooled to room temperature and the crude product was extracted with dichloromethane and dried over anhydrous Na_2SO_4. The purification was done by column chromatography (SiO_2, 4 % MeOH/EtOAc). Yield: 60 %.

30: **^{1}H NMR** ($CDCl_3$, 500 MHz, TMS) δ (ppm): 10.08 (s, 1H), 8.61 (d, 1H, *J* = 1 Hz), 8.12 (d, 1H, *J* = 7.5 Hz), 8.09 (dd, 1H, *J* = 7 Hz, and 1.5 Hz), 7.54- 7.51 (m, 1H), 7.48- 7.45 (m, 2H), 7.33- 7.26 (m, 1H), 4.51 (t, 2H, *J* = 6 Hz), 3.89 (t, 2H, *J* = 6 Hz), 3.55- 3.42 (m, 8H), 1.65 (s, 3H); **^{13}C NMR** ($CDCl_3$, 125 MHz,) δ (ppm): 189.1, 139.8, 135.4, 126.7, 119, 109.6, 71.8, 71.2, 70.64, 70.5, 69.3, 57.4; **ESI MS**: MS Calcd for $C_{20}H_{23}NO_4$, 341.16 ; Found 341.19 ; $[M]^+$

Synthesis of (E)-9-(2-(2-(2-methoxyethoxy)ethoxy)ethyl)-3-(2-(5'-methyl-[2,2'-bipyridin]-5-yl)vinyl)-9H-carbazole (31)

The monophosphonate ester derivative (**13**) (200 mg, 0.624 mmol) was taken in a two neck RB flask in an inert atmosphere; dry THF (20 mL) was added. NaH (76 mg) dissolved in dry THF (10 mL) was added dropwise to it using a pressure equalizer at 0 °C. The stirring was continued for 15 min. Then the aldehyde derivative (**20**) (213 mg, 0.624 mmol) dissolved in dry THF (20 mL) was added dropwise using a pressure equalizer. The mixture was ten refluxed at 60 °C for 12 h. Excess NaH was quenched by adding methanol and the crude solution was then poured in to water and then extracted with DCM. The organic layer was collected, dried under reduced pressure and the residue was purified by column chromatography (SiO_2, 6 % MeOH/DCM). Yield: 78%.

31: **^{1}H NMR** ($CDCl_3$, 500 MHz, TMS) δ (ppm): 8.78 (d, 1H, *J* = 2 Hz), 8.51 (q, 1H, *J* = 0.5 Hz), 8.36 (d, 1H, *J* = 8.5 Hz), 8.30 (d, 1H, *J* = 8 Hz), 8.25 (d, 1H, *J* = 1 Hz), 8.12 (d, 1H, *J* = 7.5 Hz), 8.00 (dd, 1H, *J* = 6 Hz and 2.5 Hz), 7.69 (dd, 1H, *J* = 7 Hz and 1.5 Hz), 7.62 (dd, 1H, *J* = 7 Hz and 2 Hz), 7.48-7.46 (m, 1H), 7.43 – 7.40 (m, 3H), 7.28- 7.25 (m, 1H), 7.16 (d, 1H, *J* = 16 Hz), 4.51 (t, 2H, *J* = 6 Hz), 3.89 (t, 2H, *J* = 6 Hz), 3.55- 3.42 (m, 8H), 2.40 (s, 3H), 1.65 (s, 3H); **^{13}C NMR** ($CDCl_3$, 125 MHz,) δ (ppm): 154.5, 153.5, 149.6, 147.8, 141.1, 140.7, 137.47, 133.3, 131.7, 128.2, 126, 124.5, 123.35, 122.9, 122.05, 120.69, 120.50, 119.4, 118.9, 109.1, 109.1, 71.8, 71, 70.6, 70.5, 69.3, 58.9, 18.4; **ESI MS**: MS Calcd. for $C_{32}H_{33}N_3O_3$, 507.25 ; Found 508.2606 ; $[M + H]^+$

2.5.2 Measurements

Optical Measurements: Electronic absorption spectra were recorded on a Shimadzu UV-2600 UV-Vis spectrophotometer and emission studies were performed on Horiba Fluorolog — 3 Jovin Yoon. The stock solution of all the molecules and $Zn(ClO_4)_2$ was prepared in dry acetonitrile. The pH solutions were made by using phosphate buffer/ MES buffer and pH was adjusted using dilute HCl/NaOH solution.

Determination of the detection limit: The detection limit was calculated based on the fluorescence titration curve of **CBL2** in the presence of Zn^{2+} (0–10 μM). The fluorescence intensity of **CBL2** and the standard deviation of the blank measurement were determined three times. The detection limit was calculated with the following equation:

$$\text{Detection limit} = 3\sigma/k$$

where σ is the standard deviation of the blank measurement, and k is the slope between the fluorescence intensity and Zn^{2+} concentrations.

Cell Culture: The human cancer cell line HeLa (cervical cancer) was obtained from American Type Culture Collection (ATCC, Manassas, VA, USA). The fibroblast-like murine pre-adipocyte cell line 3T3L1 was obtained from the Inter-University Centre for Genomics and Gene Technology, University of Kerala (Thiruvananthapuram, India). Cells were maintained in DMEM with 10% FBS and under an atmosphere of 5% CO_2 at 37 ^{o}C.

Cytotoxicity Experiments: The growth inhibition capacity of the probe **CBL2** was evaluated on cancer (HeLa) and normal cells (3T3 L1) by 3-(4,5-dimethylthiazol-2-yl)-2,5-diphenyltetrazolium bromide (MTT) assay as previously reported. Cell suspension of $5x10^3$ cells/well (100 μL) were seeded in a 96 well plate and 100 μL of **CBL2** at various concentrations (1 μM to 1M) and doxorubicin (Dox,1 μM) was similarly added as a positive control. The plates were then incubated for 24 h in a CO_2 incubator. After incubation, 20 μL MTT (5 mg/mL) was added to each well and incubation was continued for an additional 2 h. The insoluble formazan crystals formed were solubilized by the addition of 100 μL MTT lysis buffer (SDS and dimethyl formamide) followed by an incubation of 4 h and the absorbance was measured at 570 nm using a microplate spectrophotometer (BioTek, Power Wave XS).

$\text{Proliferation [\%]} = A_{sample} / A_{control} \text{ x } 100$

$\text{Inhibition [\%]} = 100 - \text{\% Proliferation}$

Subcellular Colocalization Imaging: For fluorescence imaging, the culture medium was removed and the cells were washed with phosphate buffered saline

(PBS pH 7.4) twice. For labeling of lysosomes and mitochondria, HeLa cells were treated with Lyso-Tracker Red (50 nM) and Mito-Tracker Red (100 nM) in PBS (pH 7.4), 20 min prior to imaging and for nuclear staining, cells were treated with Hoechst 33342 (1 μg/mL) in PBS, 15 min prior to imaging. The cells were then co-stained with 10 μM **CBL2** for 20 min and fluorescent images were acquired as described above. Images were collected in the wavelength range of 440-480 nm (blue) for Hoechst 33342 and 640−700 nm (red) for Lyso-Tracker Red and Mito-Tracker Red. Similarly co-localization experiments were also performed with non-targetd probe **CBG** (1 mM) against Lysotracker as explained above. Fluorescence imaging experiments were performed under an inverted fluorescence microscope using a green, red and yellow channel (Olympus 1 X 51, Singapore). The fluorescence was collected in the wavelength range of 540-580 nm (green), 590-650 nm (yellow) and 640−700 nm (red), respectively. Image processing was performed with Progress software. Image analysis was performed with Image J and Matlab R2014a software. The co-localization was calculated using Pearson´s correlation coefficient (r) and Manders overlap coefficients (R). The Pearson´s correlation and Manders overlap coefficients (r and R, respectively) are defined by

$$r = \frac{\sum (S1i - S1mean) \times (S2i - S2mean)}{\sqrt{\sum (S1i - S1mean)^2 \times (S2i - S2mean)^2}}$$

$$R = \frac{\sum S1i \times S2i}{\sqrt{\sum (S1i)^2 \times \sum (S2i)^2}}$$

where S1i represents signal intensity of pixels in the channel 1 and S2i represents signal intensity of pixels in the channel 2; S1mean and S2 mean reflect the average intensities of these respective channels. r is invariant to background and intensity scales, and thus, a robust estimator for co-localization. All data were expressed as mean ± standard deviation.

Intracellular pH Dependent Studies: Cells (HeLa) were incubated at 37 ^{0}C for 30 min in high K$^+$ buffer (30 mM NaCl, 120 mM KCl, 1 mM CaCl$_2$, 0.5 mM MgSO$_4$, 1 mM Na$_2$HPO$_4$, 5 mM glucose , 20 mM sodium acetate, 20 mM

MES) of various pH values (pH 4- 7). Next 25 μL (10 μM), a H^+/K^+ antiporter Nigericin was added and incubated for 15 min to equilibrate the intracellular pH with the pH buffer. The cells were then incubated with 25 μL of the probe **CBL2** (10 μM) for 30 min, washed and observed under an inverted fluorescence microscope using a green and yellow channel (Olympus 1X51, Singapore). Image processing was performed with Progress software and Image analysis was performed with Image J.

Zn^{2+} Generation and Chelation Studies: The efficiency and sensitivity of **CBL2** towards varying concentration of intracellular Zn^{2+} were evaluated using intracellular zinc generators and chelators. HeLa cells (60% confluent cultures in serum free medium) were treated with a membrane permeable metal ion chelator *N,N,N′,N′*-Tetrakis(2-pyridylmethyl)ethylenediamine (TPEN, 20 μM) for 20 min (25μL). Similarly, cells were incubated with hydrogen peroxide (H_2O_2, 50 μM) for 30 min which is a strong oxidant and an endogenous Zn^{2+} generator. Further, another set of experiment was performed on cells after subjecting them to TPEN exposure (20 μM) for 20 min after their treatment with H_2O_2, (50 μM) for 30 min. Subsequently, cells were incubated with **CBL2** ($c = 1 \times 10^{-5}$ M) for 30 min, washed and observed under an inverted fluorescence microscope after counter staining with Hoechst 33342 as described above.

Tracing Intracellular pH Changes with Regulators. HeLa cells grown under serum free conditions were incubated with various regulators proven to alter cellular H^+ concentration. HeLa cells were exposed to a 200 μM chloroquine (20 μL) solution for 30 min which can cause an increase in lysosome pH. Similarly, HeLa cells were incubated with 100 nM bafilomycin (30 μL) for 60 min. Dexamethasome can cause a decrease in the cytoplasmic pH and could initiate apoptosis at higher concentrations. In order to study the apoptosis, cells were incubated with 25 μL dexamethasome (2 μM) for 30 min. Along with the respective treatments, **CBL2** ($c = 1 \times 10^{-5}$ M) was also incubated with the cells and kept at 37 ^{0}C, washed and observed under an inverted fluorescence microscope as mentioned before.

Intracellular Zn^{2+} Variation During Apoptosis: It was established that the Zinc chelator TPEN at higher concentration could induce ROS formation through Zinc depletion and initiate DNA damage and subsequent apoptosis. For this HeLa cells were nutrient starved and was treated with 25 μL TPEN (30 μM) for 6-24 h under an atmosphere of 5% CO_2 at 37 ^{o}C. After the respective treatment period is over, cells were incubated with **CBL2** and images were observed as described before. In order to confirm TPEN induced apoptosis, acridine orange –ethidium bromide staining assay was perfomed on cells after TPEN treatment. Acridine orange-ethidium bromide dual staining is commonly used to detect apoptosis in vitro based on the differential uptake of two fluorescent DNA binding dyes by viable and nonviable cells and the experiments were performed as described previously. Cells were observed under an inverted fluorescence microscope in the green channel (Olympus 1X51, Singapore) to view apoptotic or non-apoptotic cells. Apoptotic cells will change the color from green to yellow/red, which is associated with other apoptotic features such as the presence of apoptotic bodies, damaged cell membrane, and nuclear condensation. Further, the effect of Zn^{2+} on apoptosis induced by a known chemotherapeutic agent (Dox) which is not an ion chelator was also investigated in the same manner as mentioned above after administration of 1 μM Dox for the above mentioned intervals.

Statistical Analysis: The data are expressed as the mean ± standard deviation (SD) of three replicates. Images were analysed using Image J software (version 1.48, NIH, USA) and MATLAB R 2014a software (The MathWorks, Inc. USA) using custom made algorithms.

2.6 References

(1) (a) Luzio, J.P.; Pryor, P.R;, Bright, N.A. *Nat. Rev. Mol. Cell Biol.* **2007**, *8*, 622–632. (b) Luzio, J. P.; Pryor, P. R.; Bright, N. A. *Nat. ReV.* **2007**, *8*, 622–632.

(2) (a) Saftig, P.; Klumperman, J. Nat. Rev. Mol. Cell Biol. 2009, 10, 623–635. (b) Safig, P.;Klumperman, J. *Nat. Rev.* **2009**, *10*, 623–635. (c) Fehrenbacher, N.; Jaattela, M., *Cancer Res*. **2005**, *65*, 2993–2995.

(3) Jhaveri, A.; Torchilin, V. *Expert Opin. Drug Deliv*. **2015**, *3*, 49–70.

(4) Cesen, M.H.; Pegan, K.; Spes, A.; Turk, B. *Exp. Cell Res*. **2012**, *318*, 1245–1251.

(5) Appelqvist, H.; Waster, P.; Kagedal, K.; Ollinger, K. *J. Mol. Cell Biol*. **2013**, *5*, 214–226.

(6) Glunde, K.; Foss, C. A.; Takagi, T.; Wildes, F.; Bhujwalla, Z. *Bioconjugate Chem*. **2005**, *16*, 843–851.

(7) Morales, A. R.; Yanez, C. O.; Schafer-Hales, K. J.; Marcus, A. I.; Belfield, K. D. *Bioconjugate Chem*., **2009**, *20*, 1992–2000.

(8) Liang, Y.; Xie, Y.-X.; Li, J.-H. *J. Org. Chem*. **2006**, *71*, 379–381.

(9) Wang, X.; Nguyen, D. M.; Yanez, C. O.; Rodriguez, L.; Ahn, H.-Y.; Bondar, M. V.; Belfield, K. D. *J. Am. Chem. Soc*. **2010**, *132*, 12237–12239.

(10) Fan, J.; Dong, H.; Hu, M.; Wang, J.; Zhang, H.; Zhu, H.; Suna, W.; Peng, X. *Chem. Commun*. **2014**, *50*, 882–884.

(11) Chen, L.; Wu, J.; Schmuck, C.; Tian, H. *Chem. Commun*. **2014**, *50*, 6443—6446.

(12) (a) Perez-Sala, D.; Collado-Escobar, D.; Mollinedo, F. *J. Biol. Chem*. **1995**, *270*, 6235–6242. (b) Gottlieb, R. A.; Nordberg, J.; Skowronski, E.; Babior, B. M. *Proc. Natl. Acad. Sci*. **1996**, *93*, 654–658. (c) Gottlieb, R. A.; Dosanjh, A., *Proc. Natl. Acad. Sci. U.S.A.* **1996**, *93*, 3587–3591.

(13) (a) Lakadamyali, M.; Rust, M. J.; Babcock, H. P.; Zhuang, X. *Proc. Natl. Acad. Sci. U.S.A.* **2003**, *100*, 9280-9285. (b) Adie, E. J.; Kalinka, S.; Smith, L.; Francis, M. J.; Marenghi, A.; Cooper, M. E.; Briggs, M.; Michael, N. P.; Milligan, G.; Game, S. *BioTechniques* **2002**, *33*, 1152–1156.

(14) (a) Janecki, A. J.; Montrose, M. H.; Zimniak, P.; Zweibaum, A.; Tse, C. M.; Khurana, S.; Donowitz, M., *J. Biol. Chem*., **1998**, *273*, 8790–8798; (b) Yuli, I.; Oplatka, A., *Science*, **1987**, *235*, 340–342.

(15) (a)) Izumi, H.; Torigoe, T.; Ishiguchi, H.; Uramoto, H.; Yoshida, Y.; Tanabe, M.; Ise, T.; Murakami, T.; Yoshida, T.; Nomoto, M.; Kohno, K. *Cancer Treatment ReV*. **2003**, *29*, 541–549. (b) Davies, T. A.; Fine, R. E.; Johnson, R. J.; Levesque,

C. A.; Rathbun, W. H.; Seetoo, K. F.; Smith, S. J.; Strohmeier, G.; Volicer, L., *Biochem. Biophys. Res. Commun*. **1993**, *194*, 537–543.

(16) Zhu, H.; Fan, J.; Xu, Q.; Li, H.; Wang, J.; Gaob, P.; Peng, X. *Chem. Commun*. **2012**, *48*, 11766–11768.

(17) Wan, Q.; Chen, S.; Shi, W.; Li, L.; Ma, H. *Angew. Chem. Int. Ed*. **2014**, *53*, 10916 –10920.

(18) Frederickson, C. J.; Koh, J.-Y.; Bush, A. I., *Nat. Rev. Neurosci*., **2005**, *6*, 449–462.

(19) Frederickson, C. J. *Int. Rev. Neurobiol*. **1989**, *31*, 145–238.

(20) Chen, Y.; Bai,Y.; Han, Z.; He, W.; Guo, Z. *Chem. Soc. Rev*. **2015**, *44*, 4517–4546.

(21) Xu, Z.; Yoon, J.; Spring, D. R. *Chem. Soc. Rev*. **2010**, *39*, 1996–2006.

(22) Xue, L.; Li, G.; Zhu, D.; Liu, Q.; Jiang, H. *Inorg. Chem*. **2012**, *51*, 10842−10849.

(23) Sreenath, K.; Yuan, Z.; Allen, J. R.; Davidson, M. W.; Zhu, L. *Chem. Eur. J*. **2015**, *21*, 867–874.

(24) Zhu, H.; Fan, J.; Zhang, S.; Cao, J.; Song, K.; Ge, D.; Dong, H.; Wang, J.; Peng, X. *Biomater. Sci*. **2014**, *2*, 89–97.

(25) Lee, H.-J.; Cho, C.-W.; Seo, H.; Singha, S.; Jun, Y. W.; Lee, K.-H.; Jung, Y.; Kim, K.-T.; Park, S.; Baed, S. C.; Ahn, K. H. *Chem. Commun*. **2016**, *52*, 124-127.

(26) (a) Mizusawa, K.; Takaoka, Y.; Hamachi, I. *J. Am. Chem. Soc*. **2012**, *134*,13386–13395. (b) Qiao, J.; Liu, Z.; Tian, Y.; Wu, M.; Niu, Z. W. *Chem. Commun*. **2015**, *51*, 3641–3644. (c) Yang, Q. Y.; Ye, Z. J.; Zhong, M. L.; Chen, B.; Chen, J.; Zeng, R. J.; Wei, L.; Li, H. W.; Xiao, L. H. *Acs Appl. Mater. Inter*. **2016**, *8*, 9629–9634. (d) Anees, P.; Sreejith, S.; Ajayaghosh, A. *J. Am. Chem. Soc*. **2014**, *136*, 13233–13239. (e) Kartha, K. K.; Babu, S. S.; Srinivasan, S.; Ajayaghosh, A. *J. Am. Chem. Soc*. **2012**, *134*, 4834–4841.

(27) (a) Mu, C. J.; LaVan, D. A.; Langer, R. S.; Zetter, *Acs Nano* **2010**, *4*, 1511–1520. (b) Huo, M.; Ye, Q. Q.; Che, H. L.; Wang, X. S.; Wei, Y.; Yuan, J. Y. *Macromolecules* **2017**, *50*, 1126–1133. (c) Shen, J. S.; Li, D. H.; Ruan, Y. B.; Xu,

S. Y.; Yu, T.; Zhang, H. W.; Jiang, Y. B. *Luminescence* **2012**, *27*, 317–327. (d) Wang, Q.; Li, Z.; Tao, D. D.; Zhang, Q.; Zhang, P.; Guo, D. P.; Jiang, Y. B. *Chem.Commun*. **2016**, *52*, 12929–12939. (e) Ren, C. H.; Zhang, J. W.; Chen, M. S.; Yang, Z. M. *Chem. Soc. Rev*. **2014**, *43*, 7257–7266. (f) Nair, L. V.; Philips, D. S.; Jayasree, R. S.; Ajayaghosh, A. *Small* **2013**, *9*, 2673–2677. (g) Guo, J.; Zhuang, J.; Wang, F.; Ragupathi, K. R.; Thayumanavan, S. *J. Am. Chem. Soc*. **2014**, *136*, 2220–2223.

Chapter 3

Lysosome Targeting Cyclometalated Ir(III) Complexes with Extended π-Conjugation as Potential Sensitizer for Photodynamic Therapeutic Applications

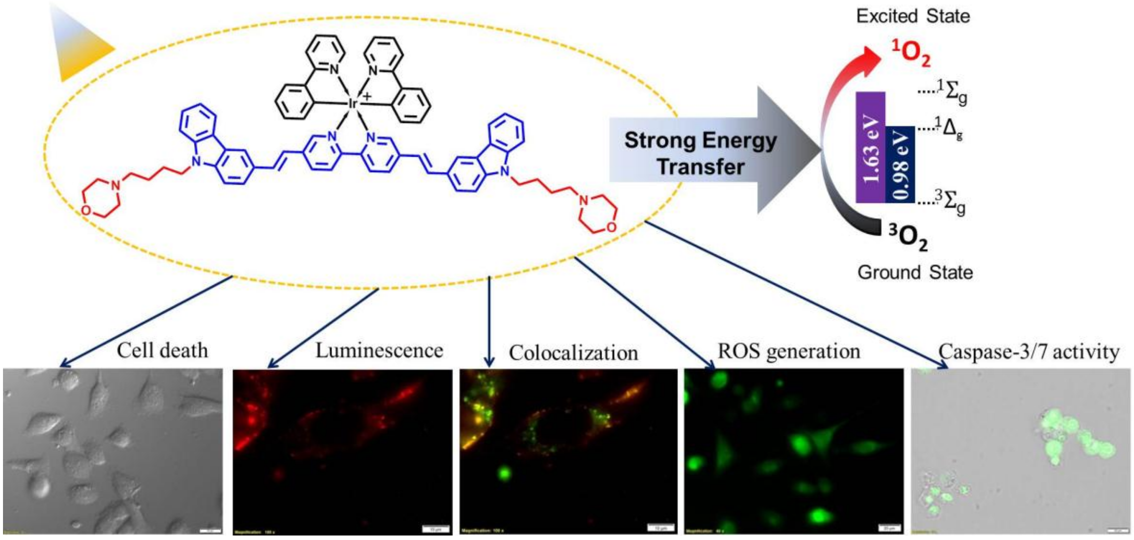

3.1. Abstract

Cyclometalated Ir(III) complexes facilitate efficient intersystem crossing due to their large spin-orbit coupling value which leads to quantitative/higher population of the triplet excited state of the molecule. This property of Ir(III) complexes make them potential candidates as photosensitizers for photodynamic therapy of tumors and skin diseases. However, the molar absorption coefficient in the visible spectral region is small, which limits their therapeutic applications. Here we report two cyclometalated Ir(III) complexes, ***IrL1*** *and* ***IrL2*** *having good molar absorption coefficient values in the visible region. We carried out detailed photophysical studies including triplet quantum yield, singlet oxygen quantum yield and*

*photostability, clearly revealing the efficiency of **IrL2** over **IrL1** as PS. **IrL2** localizes mainly in lysosome and displayed notable PDT effect in MDA-MB-231 cells, due to efficient generation of reactive oxygen species with a quantum yield of 0.79 at pH 4. The mechanism of cell death was studied through caspase-3/7 and flow cytometry analyses that clearly established the apoptotic pathway.*

3.2. Introduction

Photodynamic therapy is a clinically approved non-invasive therapeutic strategy which can be employed for cancer treatment. PDT reagents are inactive when they are alone and can transfer its triplet energy to $^3O_2$ which in turn is converted to $^1O_2$ upon photoexcitation.[1,2] These reactive oxygen species thus formed is used to cure the disease and thus is used as an attractive non-invasive modality for cancer treatment. Organometallic complexes based on ruthenium (Ru) and platinum (Pt) have been developed as PDT reagents and overcome most of the limitations associated with commercial PDT drugs based on hematophorphyrin derivatives.[3] Later, it was observed that Ru(II) complexes result in long cell permeation time and require relatively high concentration because of its poor cell permeability. Also, Pt (II) complexes were found to induce side effects at unintended sites.[4]

In the past decade, there has been a significant increase in the use of cyclometalated Ir(III) complexes for biological applications including cancer research.[5] Ir(III) usually facilitates efficient intersystem crossing due to its large spin-orbit coupling value which leads to quantitative/higher population of the triplet excited state of the molecule. The cellular uptake of the cyclometalated Ir(III) polypyridine complexes are high due to its greater lipophilicity.[6] The inherent cytotoxicity of these cyclometalated Ir(III) complexes has been circumvented by the incorporation of ligands including polyethylene glycol linkage or specific organelle targeting group.[7]

The molar absorption coefficient in the visible spectral region are small, which limits Ir(III) complexes to be used as triplet PSs for therapeutic applications.[8] The weak absorptivity of the cyclometalated Ir(III) complexes in the visible spectral region is due to two reasons (i) the lack of coordination ligands that show strong absorption of visible light. For example, the typical diimine ligand, 2,2'-bipyridine, shows absorption only in the UV region. (ii) The typical $S_0 \rightarrow {}^1$MLCT transition is featured by weak absorption.[9] Furthermore, these complexes usually show a short T_1 lifetime. An approach to prepare Ir(III) complex that shows strong absorption in the visible region is to attach a visible light-harvesting chromophore, to the coordination center. However, this method generally does not lead to the formation of Ir(III) complexes having effective absorption of visible light, *i.e.*, the excitation energy harvested by the chromophore cannot be funneled efficiently to the coordination center or the triplet excited state manifold.[10]

Transition metal complexes showing strong absorption in the visible region can be prepared by introducing π-conjugation between the coordination center and the light-harvesting antenna, or by direct metalation of the light-harvesting ligand.[11-16] The chromophore of Bodipy, dipyrrinato ligand is generally used for the preparation of Ir(III) complexes that shows strong absorption in the visible range (complexes **1**-**7**, Figure 3.1).[12] All these complexes show strong absorption around 470-485 nm (ε = 38000 M^{-1} cm^{-1}). There is an earlier report on Bodipy-containing Ir(III) complex, **8** which shows strong absorption of visible light (ε = 83600 M^{-1} cm^{-1} at 501 nm) and a long lived Bodipy-localized ^{3}IL state (τ_T = 25 μs).[13] However, the π-core of the Bodipy unit is not directly linked to the coordination center, thus the heavy atom effect is not prominent. Connecting the π-core of Bodipy to the Ir(III) coordination center *via* alkyne bond may improve ISC. Following this idea, Zhao *et al.*, prepared two Ir(III) complexes, **9** and **10** where the Bodipy unit is tethered to the ligand in **9** (no π-conjugation exists between the coordination center and the Bodipy unit).[14] In **10**, however, the Bodipy unit is directly π-conjugated to the coordination center *via* a C-C triple bond. Strong absorption of the visible light was observed for both **9** (ε = 71400 M^{-1} cm^{-1} at 499 nm) and **10** (ε = 83000 M^{-1} cm^{-1} at 527 nm). Singlet oxygen quantum yield for **10** was found to be 97% and that of **9** was 52% which indicated the efficiency of ISC. These results indicate that attaching a fluorophore to the coordination center *via* a π-conjugation linker is a useful method for the design of Ir(III) complexes that show effective strong absorption of visible light.

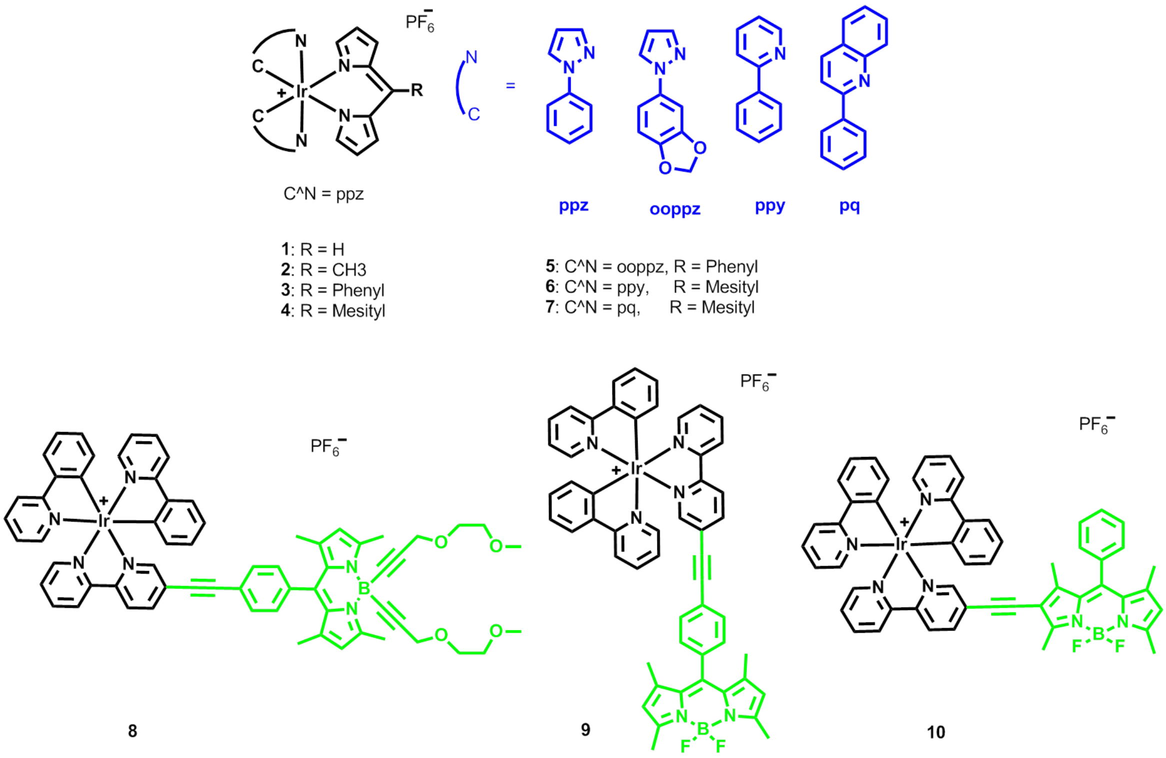

Figure 3.1: Molecular structures of **1-1**

Yang and coworkers designed and synthesized a phosphorescent cationic Ir(III) complex (**11**) with a donor-π-donor type unit as a N^N ligand and 2-phenylpyridine as a C^N ligand.[15] The complex **11** exhibits an intense absorption peak centered at ~ 450 nm with a large molar extinction coefficient (ε) ~ 2.4 × 10^4 M^{-1} cm^{-1} and also have highly efficient orange-red phosphorescence located at 620 nm with a quantum efficiency of ~3% in PBS buffer solution at room temperature. The singlet oxygen generation ($^1O_2$) by **11** was observed by 730 nm continuous wave (CW) laser irradiation owing to its reverse saturable absorption property, which was confirmed by the $^1O_2$ scavenger of 1,3-diphenylbenzo[*c*]furan (DPBF) and ESR spectra. The photodynamic therapy effect of **11** *in vivo* by a 730 nm CW laser was further assessed by histological examination and immunohistochemistry.

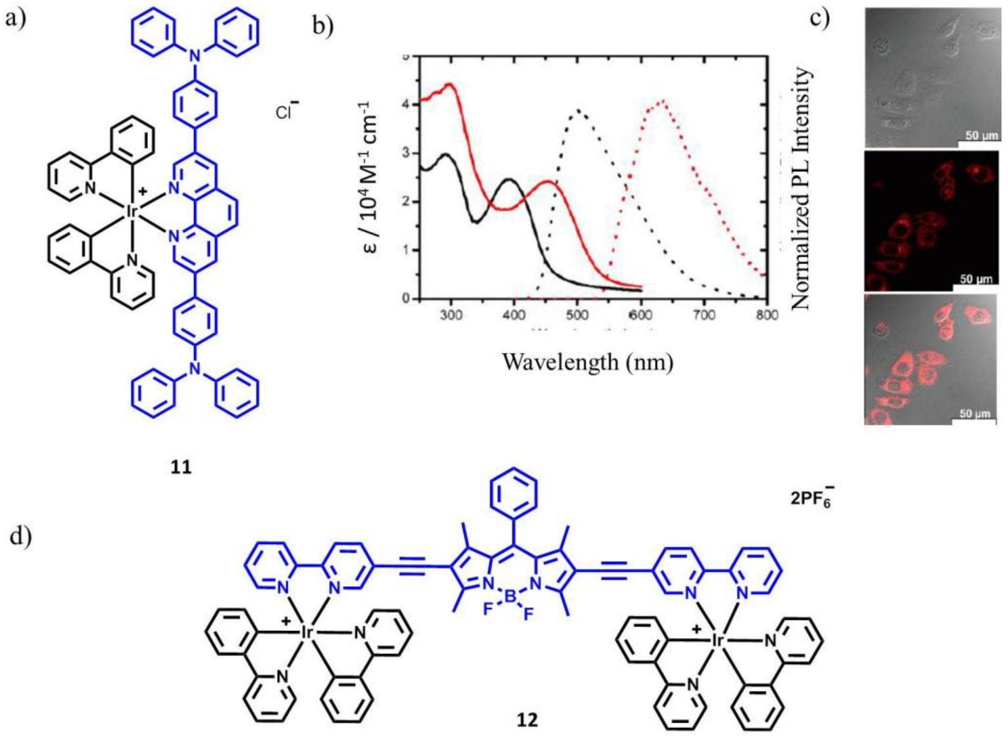

Figure 3.2: (a) Molecular structure of compound **11**. (b) Absorption spectra of the N^N ligand (black solid line) and **11** (red solid line) and phosphorescence spectra of the N^N ligand (black dashed line) and **11** (red dashed line) in DMSO/PBS (1/49 v/v) solution. (d) Molecular structure of **12**.

Drape *et al*., have reported Bodipy bridged binuclear Ir(III) complex **12**.[16] The strong visible light-harvesting ability of **12** is due to the presence of a second metal center, and hence performs better than their mononuclear transition metal analogues. The fluorescence of the Bodipy moieties was substantially quenched by efficient intersystem crossing. The strong intraligand (^{3}IL) character of the T_1 state is responsible for the long-lived triplet excited states of the complex. The authors also prepared a binuclear Ru-complex where Ir was replaced by Ru in **12**. This complex was used as a triplet PS for two triplet–triplet energy transfer related processes, TTA (Triplet–Triplet Annihilation) upconversion and singlet oxygen generation. In both applications, **12** exhibited improved performance when compared to other reported complexes. With DPA as a triplet acceptor, **12** shows a high upconversion quantum yield (FUC = 25.5%). The singlet oxygen quantum yield of **12** was observed to be 74.9%. The photodynamic activity of the complex **12** was studied in the HeLa cells and showed minimal cytotoxicity in the dark. The complex **12** exhibits unusual low energy and intense absorption and hence is an effective PS for PDT. The cytotoxicity was found to increase up on laser irradiation and the cell death mechanism follows the apoptotic pathway.[16]

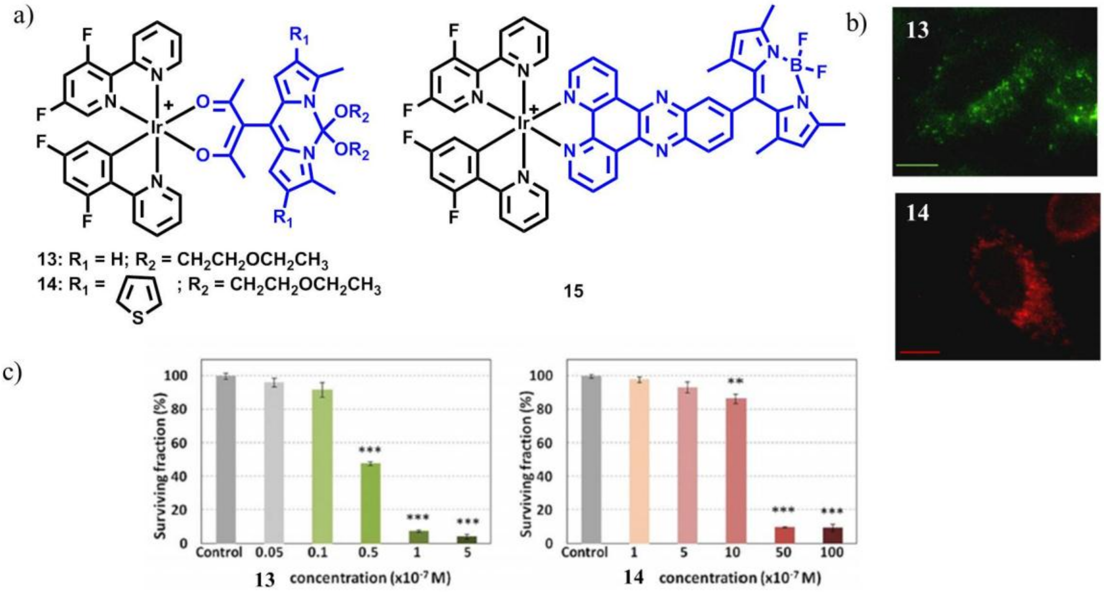

Figure 3.3: (a) Molecular structures of **13-15**. (b) Internalized **13** and **14** detected inside HeLa cells after incubation for 24 h with 5 x 10^{-7} M. Scale bar: 5 µm. (c) HeLa cells survival after exposure for 24 h to **13** and **14** at different concentrations followed by 6.8 J cm^{-2} of green or red light irradiation (for **13** and **14**, respectively). Cell viability was evaluated by MTT assay 24 h after each treatment.

The biscyclometalated Ir(III) complexes reported by Palao and co-workers have Bodipy-based ancillary ligands, where the Bodipy unit is grafted to different chelating cores (acetylacetonate for **13** and **14**, and bipyridine for **15**) at the meso position.[17] These complexes with the Bodipy moiety directly grafted to acetylacetonate (**13** and **14**) exhibit higher absorption coefficients (ε = 4.46 x 10^4 M^{-1} cm^{-1} and 3.38 x 10^4 M^{-1} cm^{-1} at 517 nm and 594 nm, respectively), higher moderate fluorescence emission (ϕ_{fl} = 0.08 and 0.22 at 528 nm and 652 nm, respectively) and, in particular, more efficient singlet oxygen generation upon visible-light irradiation (ϕ_Δ = 0.86 and 0.59, respectively) than that exhibited by **15** (ϕ_Δ = 0.51, but only under UV light). Phosphorescence emission, nanosecond time-resolved transient absorption, and DFT calculations suggest that Bodipy-localized long-lived ^{3}IL states are populated for **13** and **14**. *In vitro* PDT activity studied for

13 and **14** in HeLa cells shows that such complexes are efficiently internalized into the cells, exhibiting low dark- and high photocytoxicity, even at significantly low complex concentration, making them potential therapeutic agents.[17]

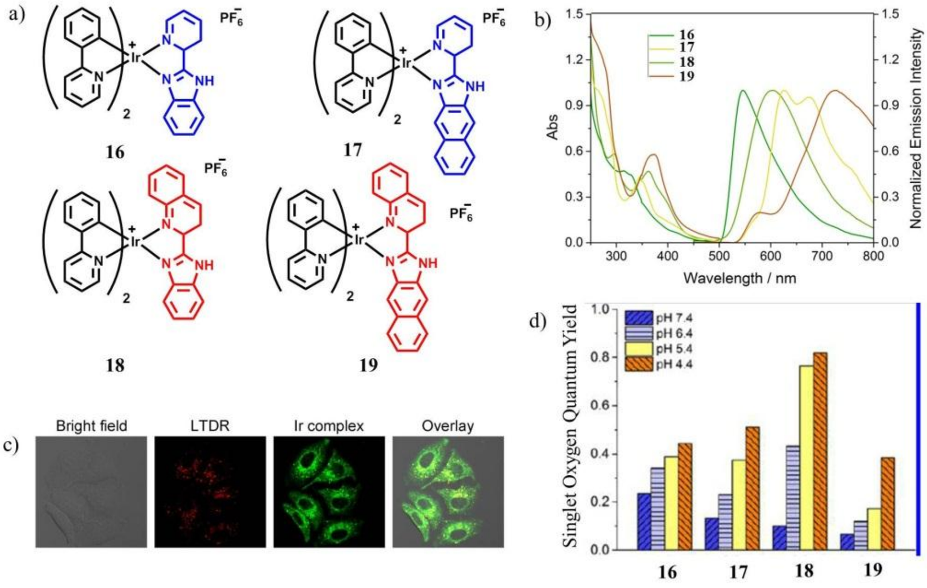

Figure 3.4: (a) Molecular structures of **16-19**. (b) UV-Vis spectra and fluorescence emission spectra of **16-19** (20 μM) in acetonitrile at 298 K. The Ir(III) complexes were excited at 405 nm. (c) Colocalization of **16** with Lysotracker Red (10 μM, 1 h) and LTDR (Lyso Tracker Deep Red)(150 nM, 0.5 h, λ_{ex} = 633 nm). (d) pH-dependent $^1O_2$ quantum yields of **16−19** in PBS. Ir(III) complexes were excited at 425 nm by an light-emitting diode light array (4 mW cm^{-2}, 300 s).

Mao and co-workers have reported four phosphorescent cyclometalated Ir(III) complexes containing benzimidazole moiety (**16-19**) (Figure 3.4). Among the four Ir(III) complexes, **19** have the maximum value of molar extinction coefficient, 3.12 x 10^4 M^{-1} cm^{-1} at 380 nm.[18] These complexes show potent antimetastatic and lysosome-damaged PDT effects. The complexes **16-19** can inhibit several key cancerous events, including cell migration, invasion, colony formation, and *in vivo* angiogenesis. Because of their pH-dependent phosphorescence, they show an enhanced emission in lysosomes. Upon low-energy irradiation, **16-19** can initiate cancer cell apoptosis through ROS elevation, caspase activation, and lysosomal damage. The complex **19** also shows potent *in vivo* antitumor effect after PDT. The major problem associated with these PSs is the weak absorption in the visible region. Thus, synthesis of organelle targeted

Ir(III) complexes having high absorption coefficient in the visible region is of great significance.

As we mentioned earlier, the incorporation of highly conjugated chromophore is considered as one of the best methods to achieve high molar extinction coefficient in the visible region. In Chapter 2, we discussed about the lysosome targeting organic probe, **20** (Figure 3.5a) for lysosome targeted pH and Zn^{2+} imaging.[19] Previously, we have reported a highly efficient two photon active Zn^{2+} imaging probe **21** as shown in the Figure 3.5b.[20] The molar extinction coefficients reported for the molecules are 4.15 x 10^4 M^{-1} cm^{-1} at 362 nm for **20** and 7.3 x 10^4 M^{-1} cm^{-1} at 400 nm for **21**. Considering the red shifted absorption of **21** when compared to **20**, we have designed two new Ir(III) complexes **29** (**IrL1**) and **30** (**IrL2**) in which the lysosome targeting moiety, morpholine is attached.

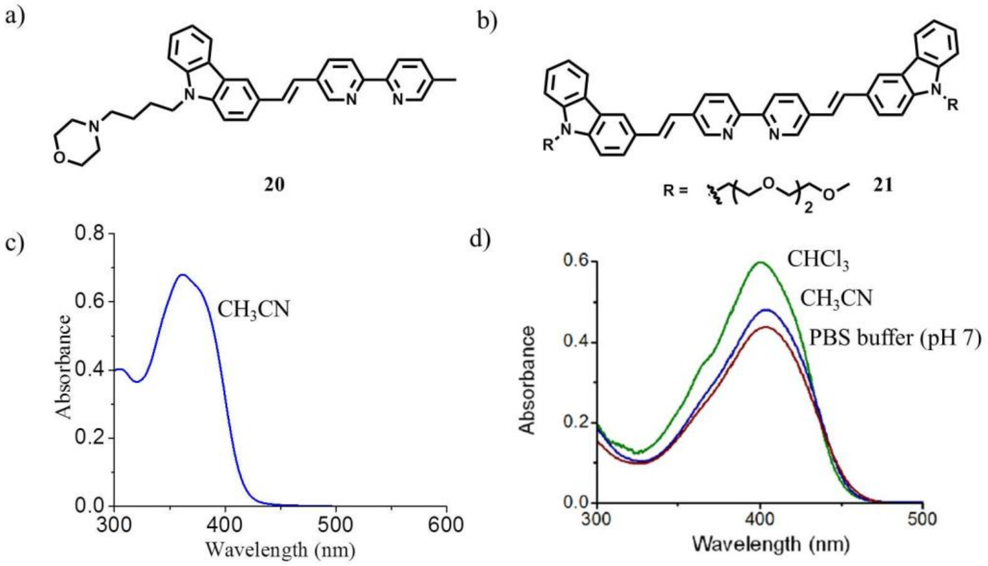

Figure 3.5: (a) and (b) Molecular structure of **20** and **21** respectively. (c) Absorption spectrum of **21** in acetonitrile (c = 10 μM). (d) Absorption spectra of **22** in chlor oform, acetonitrile and PBS buffer (pH 7) (c = 6 μM).

Generally, small molecule based targeting groups or ligand modification is used for specific organelle targeting since the peptide based targeting moieties are limited for enzymatic degradation.[21] Lysosomes are digestive compartment of the cell in pH range of 4.5-6, containing more than 60 types of acid hydrolases that are involved in the degradation of bio-macromolecules into low molecular weight materials.[22] The presence of morpholine group in the complex helps the probe to localize in the lysosome through lysosomotropism.[23]

Among the two cyclometalated Ir(III) complexes, **IrL1** (**29**) and **IrL2** (**30**), **IrL2** showed better photophysical properties such as high triplet and singlet oxygen quantum yields. Accumulation of **IrL2** in lysosome was proved by colocalization with Lyso Tracker Green. The photodynamic therapy study in MDA-MB-231 cells showed good cytotoxicity upon photoexcitation when compared to the control, $[Ru(bpy)_3]Cl_2$.

3.3 Results and Discussion

3.3.1 Synthesis and Characterization

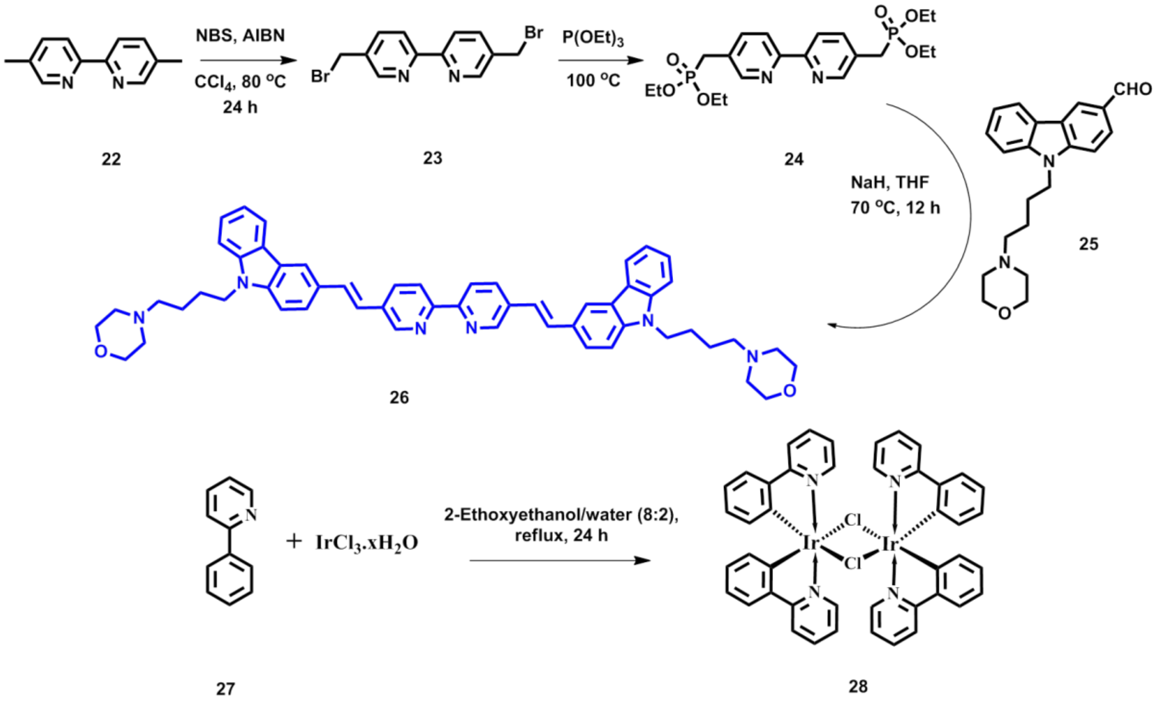

Scheme 3.1: Synthesis of ligand **26** and Ir(III) dimer **28** (The synthetic protocol for **25** is described in the Chapter 2, section 2.3.1).

Considering the requirement of an effective PS having good molar extinction coefficient value in the visible region, we choose ligands **20** and **26** for preparing the targeted complexes **29** and **30** respectively. The ligands were synthesized by multistep synthetic strategy as shown in the Scheme 3.1, where the synthesis of ligand **20** was explained in the Chapter 2, section 2.3.1. The morpholine moiety facilitates targeting of lysosome whereas the 2,2'-bipyridine react with Ir(III) dimer to form the complex.

The cyclometalated intermediate Ir(III) dimer **28** was prepared as per reported procedure. Reactions of **20** (or **26**) and **28** in a 3:1 (v/v) mixture of ethanol/dichloromethane under argon atmosphere and reflux condition followed by anion exchange with NH_4PF_6 resulted in **IrL1** (**29**) (or **IrL2** (**30**)). The purification was performed using silica gel column chromatography followed by precipitation in dichloromethane/hexane mixture with 42 % yield. The details of the synthetic steps are shown in Scheme 3.1 and 3.2.

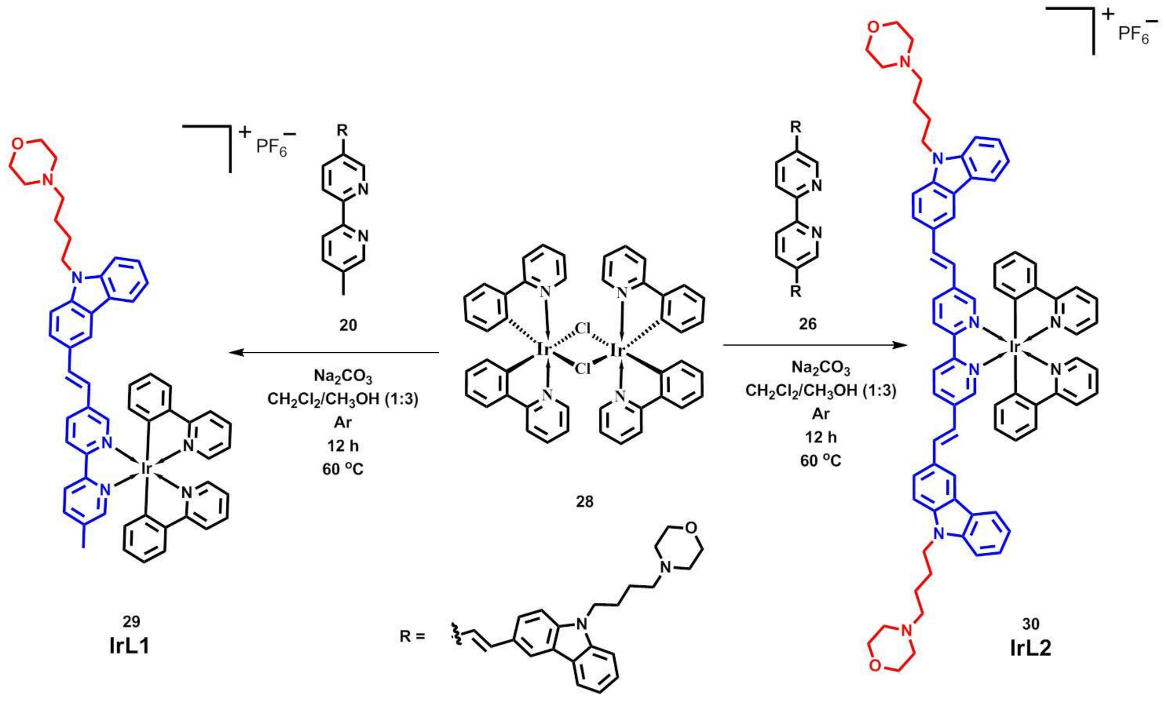

Scheme 3.2: Synthesis of cyclometalated Ir(III) complexes **IrL1** (**29**) and **IrL2** (**30**).

The final molecules and intermediates were characterized by ^1H NMR, ^{13}C NMR and HRMS analyses. The HRMS, both in the positive mode (1003.3675 corresponding to $C_{55}H_{50}IrN_6O$; $[M]^+$ (**IrL1**) and 1321.5445 corresponding to $C_{76}H_{72}IrN_8O_2$; $[M]^+$ (**IrL2**) and in the negative mode 144.9643 corresponding to PF_6^- for both **IrL1** and **IrL2**) were in agreement with the calculated values of 1003.37 , 1321.54 and 144.96 respectively. The melting point of **IrL1** and **IrL**2 was observed to be 212 ± 1 ^{o}C and 285 ± 1 ^{o}C, respectively. Elemental analysis was comparable with the calculated value as shown in the Table 3.1. ^{1}H NMR and ^{13}C NMR spectra of **IrL1** and **IrL2** were in agreement with their chemical structures.

3.3.2 Photophysical Properties

The photophysical characteristics of the complexes, **IrL1** and **IrL2** were investigated in organic and aqueous solutions such as acetonitrile and phosphate buffer, respectively. Generally cyclometalated Ir(III) complexes show low molar extinction coefficient in the visible region and hence, singlet oxygen production at visible light irradiation is lower and limits the application of these complexes for PDT applications. In our study, interestingly both **IrL1** and **IrL2** showed intense absorption in the visible region with high molar extinction coefficients (ε = 2.82 x 104 M^{-1} cm^{-1} at 410 nm and ε = 5.41 x 10^{4} M^{-1} cm^{-1} at 460 nm, respectively) (Figure 3.6a).

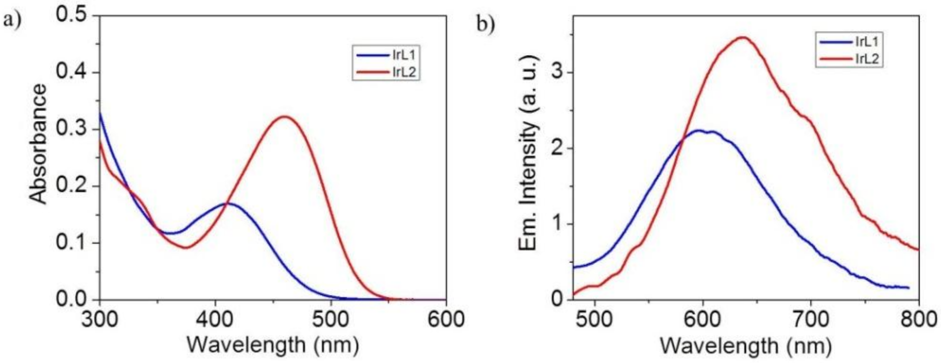

Figure 3.6: (a) Absorption and (b) emission of **IrL1** and **IrL2** in acetonitrile (*c* = 6 μM, λ_{ex} = 420 nm for **IrL1** and 460 nm for **IrL2**).

Both, **IrL1** and **IrL2** showed emission maximum at 600 nm and 640 nm in acetonitrile, when excited at 420 nm and 460 nm, respectively (Figure 3.6b). The relatively high emission life time of 500 ns and 800 ns for **IrL1** and **IrL2**, respectively, in acetonitrile indicated the phosphorescent emission of the complex. The respective phosphorescence quantum yield of **IrL1** and **IrL2** in acetonitrile was found to be 0.011 and 0.018 (absolute quantum yield). The absorption spectra were broadened when we measured in PBS buffer at pH 7 due to the formation of aggregates at 6 µM concentration (Figure 3.7). Absorption maximum remained same in all the pH conditions and then we monitored pH dependent emission. On changing pH from 4 to 9, the emission intensity was almost unaltered, which shows that the protonation at morpholine nitrogen has no influence in emission intensity.

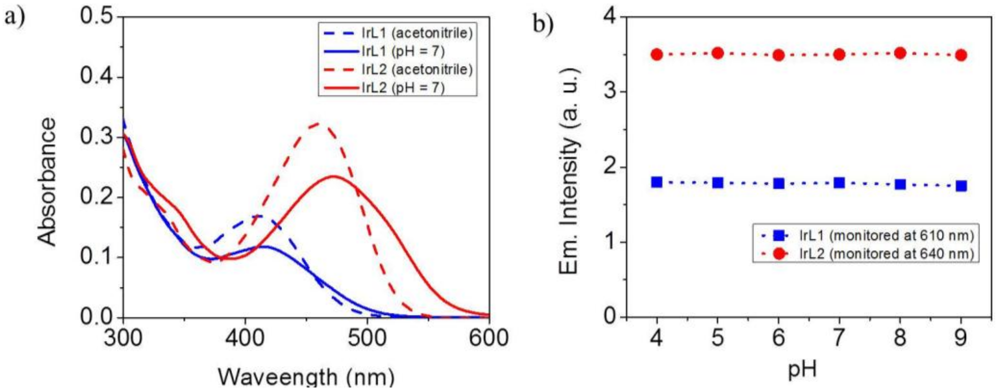

Figure 3.7: (a) Absorption spectra of **IrL1** and **IrL2** in PBS buffer (pH = 7, dashed line corresponds to the absorption in acetonitrile for a comparison, *c* = 6 µM). (b) pH Dependent emission change of **IrL1** (λ_{ex} = 420 nm) and **IrL2** (λ_{ex} = 460 nm) in PBS buffer.

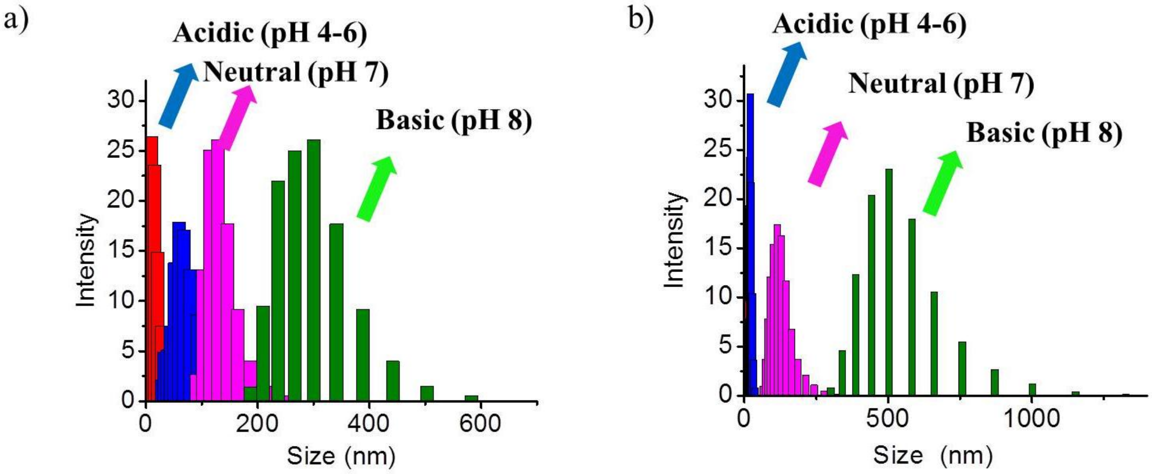

Figure 3.8: DLS analysis of (a) **IrL1** and (b) **IrL2** in different pH from 4-8 (*c* = 6 µM).

The detailed investigation on aggregation of **IrL1** and **IrL2** was carried out using DLS analysis. As shown in Figure 3.8, the size of the aggregates increased with increasing pH for both **IrL1** and **IrL2**. The aggregate size was observed to be less in the acidic pH which is due to the morpholine group attached to the PS where protonation at the morpholine nitrogen favors better solubility at lower pH. While comparing **IrL1** and **IrL2**, in the acidic pH, size of the aggregates is less for **IrL2**. The presence of two morpholine groups in **IrL2** leads to higher protonation and better solubility. The size of the aggregates is tabulated in the Table 3.2.

Compound	pH 4	pH 5	pH 6	pH 7	pH 8
IrL1	27	35	60	100	270
IrL2	10	14	25	95	450

Table 3.2: pH Dependent size (nm) variation of **IrL1** and **IrL2** in different pH from 4 – 8 (*c* = 6 μM).

3.3.3 Energy transfer efficiency

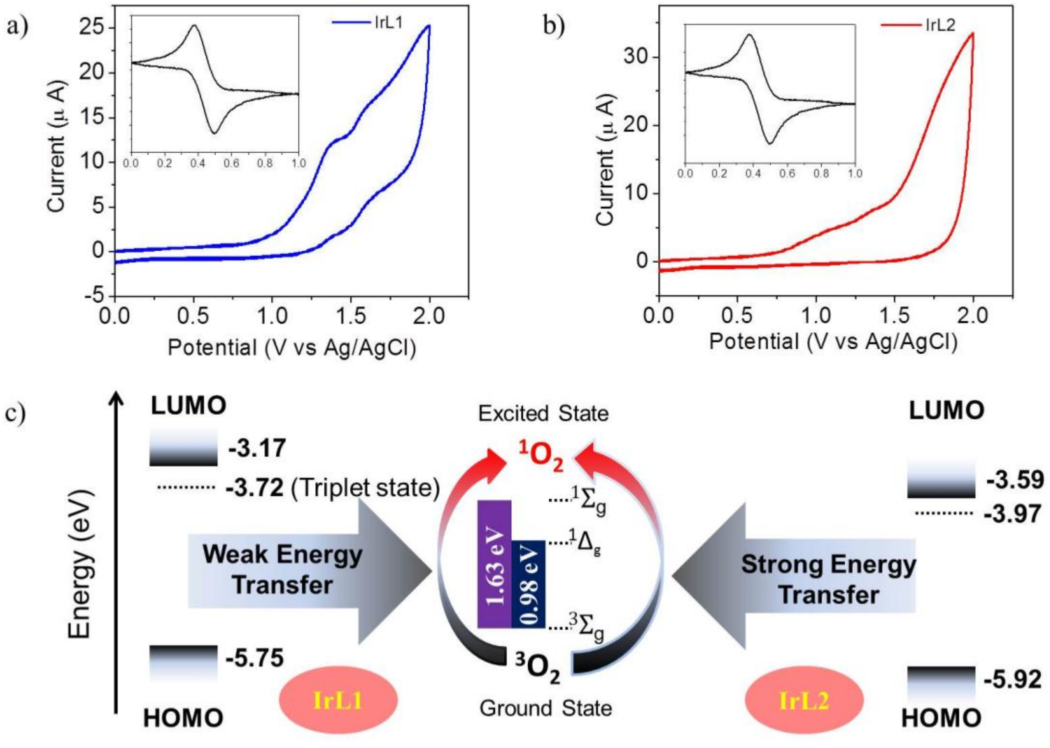

Figure 3.9: Cyclic voltammetry analysis of (a) **IrL1** and (b) **IrL2** at a scan rate of 50 mV/s in tetrabutylammonium hexafluorophosphate electrolyte dissolved in acetonitrile and insets show the CV of the reference, ferrocene. (c) The calculated energy levels of HOMO, LUMO and triplet state of **IrL1**, **IrL2** and ground state oxygen ($^3O_2$) absorption.

Cyclic voltammetry measurements were performed to determine the oxidation potential and the HOMO of **IrL1** and **IrL2** while band gap was calculated from the onset of absorption. The HOMO was measured by the onset potential of the Ir(III) complex with a ferrocene reference using the equation, HOMO = $-(E_{\text{onset-of-Ir(III)}}$ *vs.* $E_{\text{onset-of-ferrocene}}) - 4.8$ eV.[24] The triplet energy levels were obtained from the emission maximum. Two excited states of singlet oxygen ($^1\Sigma g$ for 762 nm and $^1\Delta g$ for 1268 nm) associated to the absorption energy from ground state oxygen are shown in Figure 3.9. From Figure 3.9c, it is clear that, the singlet and triplet energy difference of **IrL2** is highly favorable for the efficient energy transfer to molecular oxygen for singlet oxygen generation when compared to **IrL1**.

3.3.4 Characterization and Quantification of the Triplet Excited States

The Ir(III) derivatives due to their efficient energy transfer to triplet oxygen have immense potential as efficient sensitizers in photodynamic therapy. Since the photodynamic activity of the PSs is expected to involve the generation of singlet oxygen, we aim at studying the excited state properties of **IrL1** and **IrL2**. In order to characterize the transient intermediates such as triplet excited states in these systems, we carried out nanosecond laser flash photolysis of **IrL1** and **IrL2** under similar conditions.[25] Both the derivatives have sufficient absorption at 355 nm making it possible to excite them directly with the third harmonic of the Nd:YAG laser. Figure 3.10 shows the transient absorption spectrum of **IrL1** and **IrL2** in acetonitrile obtained after 355 nm laser excitation (500 ns, 60 mJ/pulse). Upon excitation, **IrL2** showed a fairly strong transient absorption with a maximum at 760 nm, with a bleach in the region corresponding to its ground state absorption. The transient absorption peak for **IrL1** was observed at 660 nm. The transient formed from **IrL1** and **IrL2** within the laser pulse, decayed by a first-order process and led to the recovery of the ground state absorption, thereby ruling out the formation of any permanent products or degradation of the PS under these conditions. To characterize the transients involved, we checked the transient absorption after purging with oxygen under similar conditions. We observed that the transient absorption was readily quenched by dissolved oxygen, suggesting the triplet energy transfer to triplet oxygen.

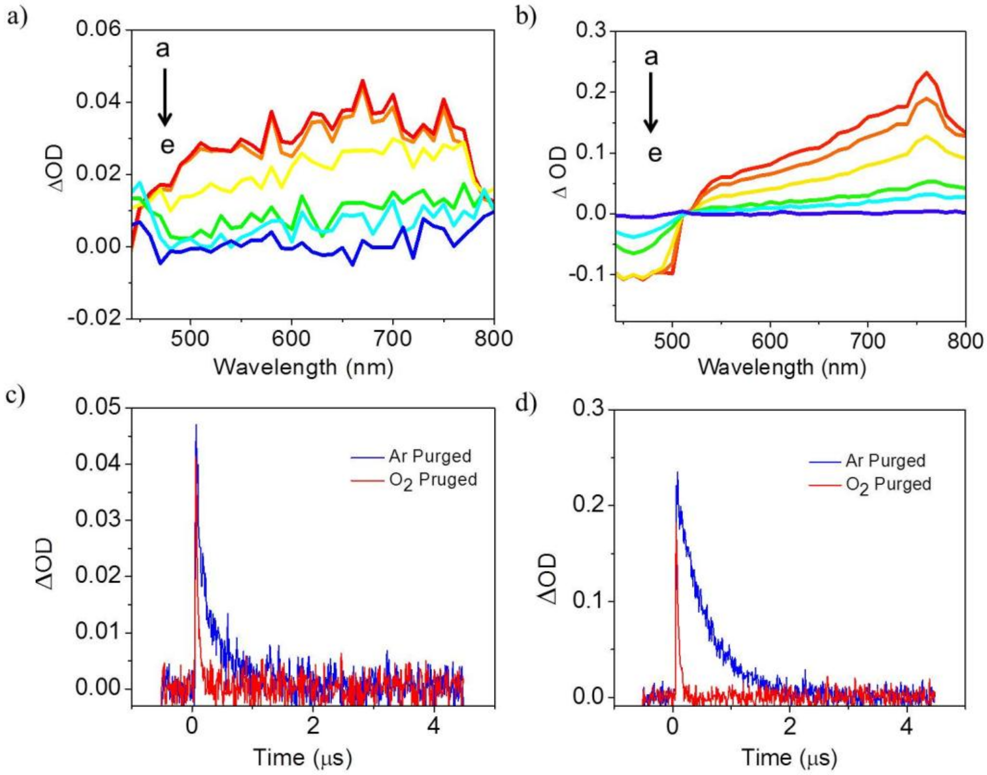

Figure 3.10: Transient absorption spectra of (a) **IrL1** and (b) **IrL2** (6 μM) following 355 nm laser pulse excitation; time-resolved absorption spectra recorded at (a) 0.19, (b) 0.39, (c) 0.83, (d) 1.7, and (e) 4.6 μs. The transient decay of (c) **IrL1** and (d) **IrL2** monitored at 660 nm and 760 nm, respectively (Ar-purged and O_2 purged).

Further, the formation of triplet excited state was confirmed and quantified by quenching the transients using β-carotene, a well-known triplet excited state quencher. Upon addition of β-carotene, which possesses a low energy level triplet excited state, we observed a quenching of the transient absorption, accompanied by the growth of a new transient absorption at 515 nm, corresponding to β-carotene triplet excited state. Since the intersystem crossing efficiency in β-carotene is negligible, the formation of the β-carotene triplet excited state upon laser excitation of **IrL1** and **IrL2** clearly confirms the involvement of triplet excited states of these PSs. Furthermore, the triplet excited state quantum yield

(ϕ_T) of **IrL1** and **IrL2** was measured by energy transfer to β-carotene using tris(bipyridyl)-ruthenium(II) complex as the reference. The quantum yield value was found to be 0.91 ± 0.02 for **IrL2** and 0.65 ± 0.02 for **IrL1**.

3.3.5 Singlet Oxygen Quantification

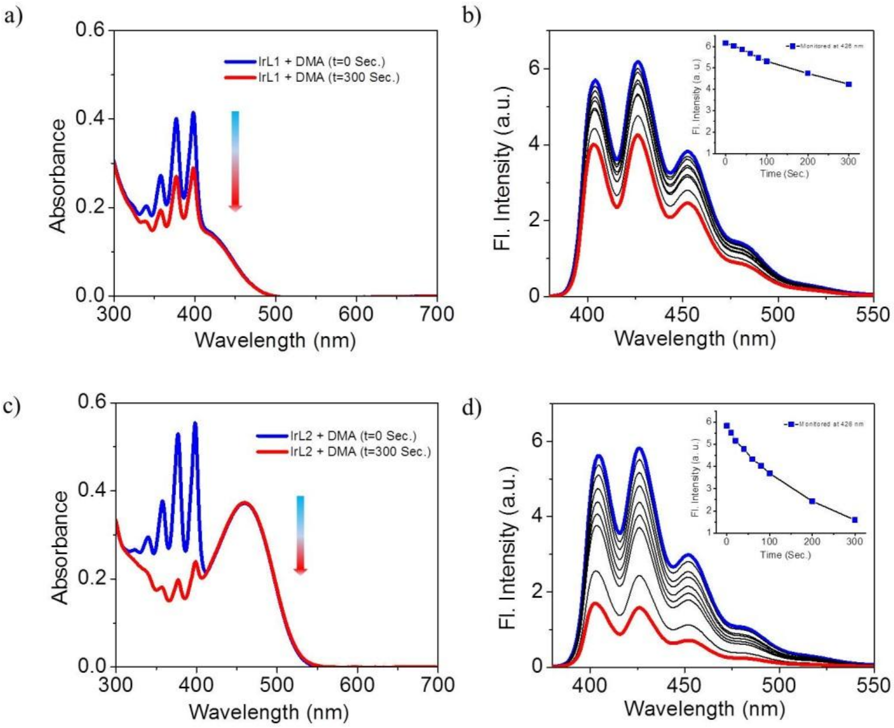

Figure 3.11: (a, c) Absorption (b, d) emission change of DMA in presence of **IrL1** and **IrL2** upon irradiation (t = 0-300 s) in acetonitrile and insets show the secondary plot (t = 0 - 300 s, λ_{ex} = 360 nm, $c_{(DMA)}$ = 10 μM and $c_{(IrL1/IrL2)}$ = 6 μM).

Enhanced triplet quantum yields are always favorable for the efficient generation of singlet oxygen. Hence, the efficiency of the singlet oxygen generation upon photoexcitation by the complexes **IrL1** and **IrL2** were examined. 9,10-Dimethyl anthracene (DMA) was used as the singlet oxygen scavenger and the absorption and emission was monitored in the presence of **IrL1** and **IrL2**. As shown in the Figure 3.11, the decrease in absorption and emission of DMA is more for **IrL2** when compared to **IrL1** on irradiating with 420 nm long pass filter over a period of 0-300 s.

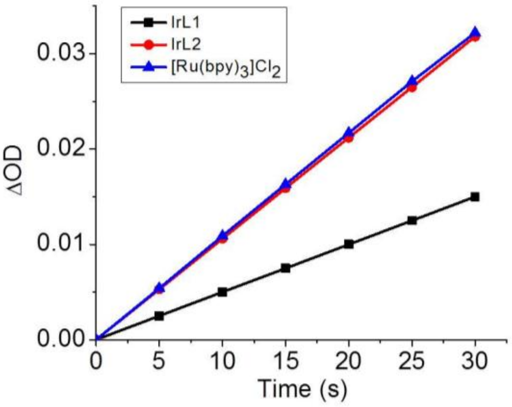

Figure 3.12: Quantum yield calculation of **IrL1** and **IrL2** using DMA in methanol and [Ru(bpy)$_3$]Cl$_2$ as the reference standard. Here we took the optically matched solution of the three PSs and the change in absorbance of DMA was monitored in each time interval during irradiation (t = 0-30 s, λ_{irr} = 420 nm long pass filter, $c_{(DMA)}$ = 10 μM).

The quantum yields of singlet oxygen generation were determined indirectly by monitoring the photo-oxidation of 9,10-dimethyl anthracene through absorption spectroscopy.[26] A solution of the PS (**IrL1** and **IrL2**) and DMA was irradiated using 420 nm long pass over a period of 0-30 s, and the decrease in the absorption peak at 360 nm of DMA was calculated in each time interval of 5 s. The quantum yields for the generation of singlet oxygen were evaluated for **IrL2** or **IrL1** taking reference sensitizer [Ru(bpy)$_3$]Cl$_2$ (Φ_Δ = 0.83), under similar conditions. Yields for the generation of singlet oxygen were calculated by plotting the reduction in absorbance (ΔOD) of DMA in presence of **IrL1** or **IrL2** as well as [Ru(bpy)$_3$]Cl$_2$, against the irradiation time. The plot showed a good linearity as shown in the Figure 3.12. From the slope and by knowing the singlet oxygen generation quantum yield of the reference sensitizer (ϕ_Δ = 0.83), we have calculated the quantum yields of singlet oxygen generation for **IrL1** (0.58 ± 0.02) and **IrL2** (0.85 ± 0.02).

We checked the quantum yields for $^1O_2$ production of **IrL1** and **IrL2** under light irradiation (420 nm) in aerated buffer solutions (PBS buffer) using steady state method with 9,10-anthracenediyl-bis-(methylene)dimalonic acid (ABDA) as the $^1O_2$ indicator and [Ru(bpy)$_3$]Cl$_2$ as the standard (Figure 3.13). The quantum yield value of the standard is found to be constant in all the pH range (ϕ_Δ = 0.18).

The singlet oxygen quantum yield of **IrL1** was low when compared to that of **IrL2** under all pH conditions. Also, it is observed that the singlet oxygen quantum yield was reduced on increasing the pH from acidic to alkaline. This is due to the formation of aggregates on increasing the pH as discussed earlier.

Mao *et al.*, have reported similar phenomenon in Ir(III) complexes where the ligands are designed to target the lysosome.[27] However, the detailed explanation for variable singlet oxygen quantum yield was not studied. In this study, we found that the variable solubility of **IrL1** and **IrL2** in different pH buffer regulated the quantum yields for $^1O_2$ production.

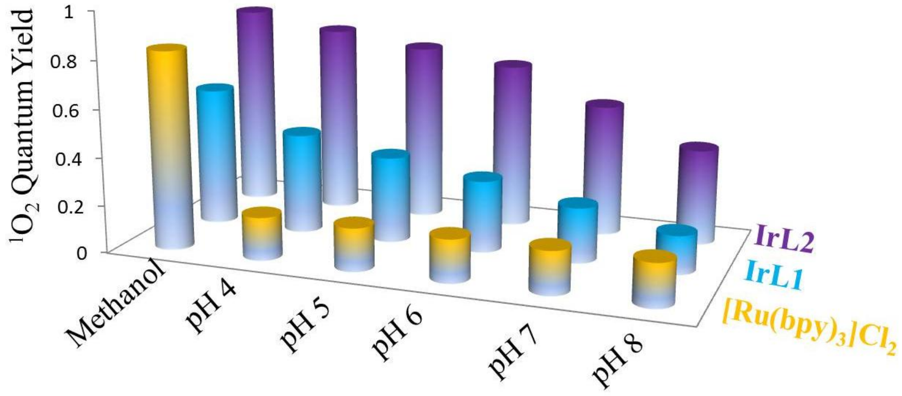

Figure 3.13: Singlet oxygen quantum yield in methanol and different pH for **IrL1** and **IrL2** using ABDA (*c* = 100 μM). The value is constant in all pH range for the reference standard, $[Ru(bpy)_3]Cl_2$. The quantum yield values for **IrL1** and **IrL2** change with pH (4(0.42/0.79), 5(0.36/0.74), 6(0.3/0.7), 7(0.23/0.55) and 8(0.16/0.44), respectively) (error limit = ± 0.005).

The pH dependent singlet oxygen quantum yield change was again confirmed by the pH dependent emission change of ABDA in presence of **IrL1** and **IrL2** upon irradiation for 300 s. From Figure 3.14 and 3.15, it is clear that the efficiency of generation of singlet oxygen by **IrL2** is high when compared to **IrL1**. Also the emission intensity was found to decrease on increasing the pH.

Thus, it is anticipated that **IrL1** and **IrL2** can photosensitize $^1O_2$ production more efficiently in the acidic region like lysosome and tumor tissues. To further confirm the singlet oxygen generation, we also monitored singlet oxygen luminescence at 1270 nm (Figure 3.16). For direct measurement of singlet

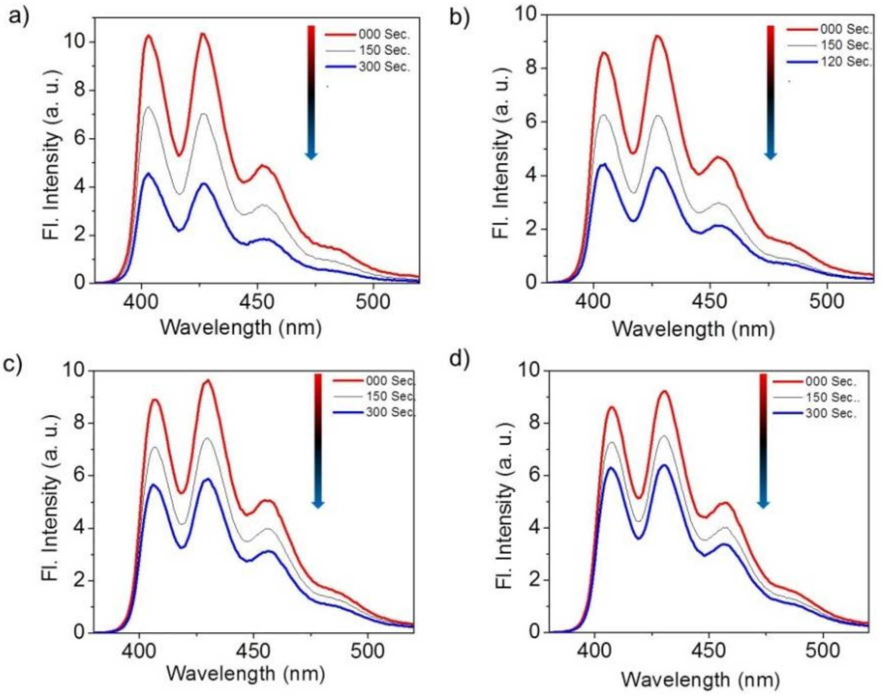

Figure 3.14: pH dependent emission change of ABDA (100 μM) in presence of **IrL1** (6 μM) in different pH a) pH 4, b) pH 5, c) pH 6 and d) pH 7 (λ_{ex} = 360 nm, λ_{irr} = 420 nm long pass filter).

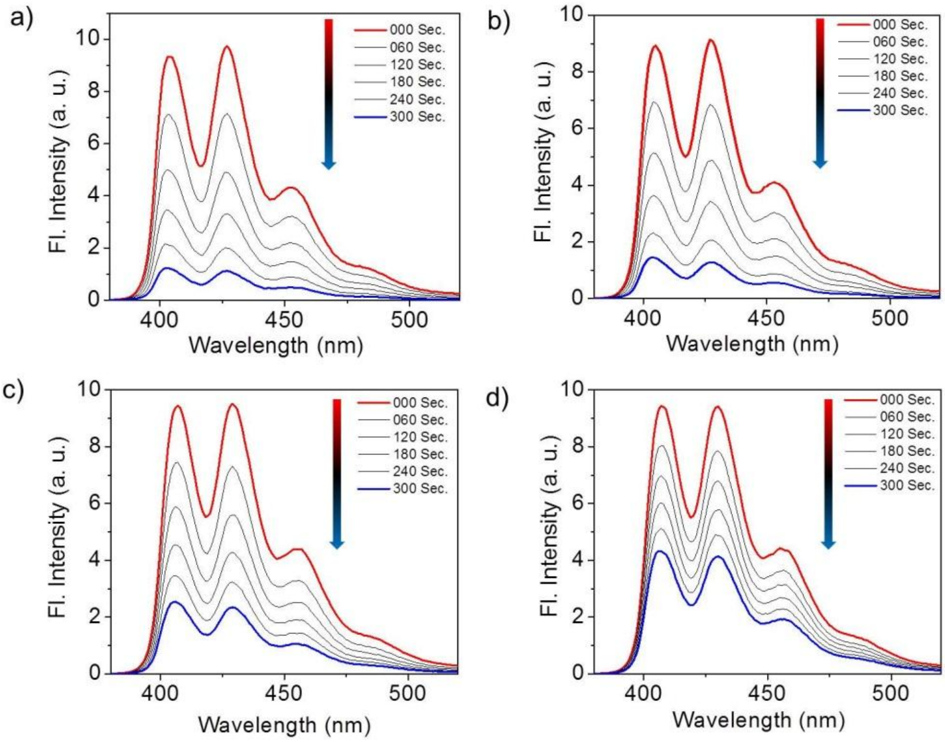

Figure 3.15: pH dependent emission change of ABDA (*c* = 100 μM) in presence of **IrL2** (6 μM) in different pH a) pH 4, b) pH 5, c) pH 6 and d) pH 7 (λ_{ex} = 360 nm, λ_{irr} = 420 nm long pass filter).

oxygen through NIR luminescence method, we used Fluorolog-3 spectrofluorimeter connected with an NIR detector and 450 W, Xenon lamp as light source.

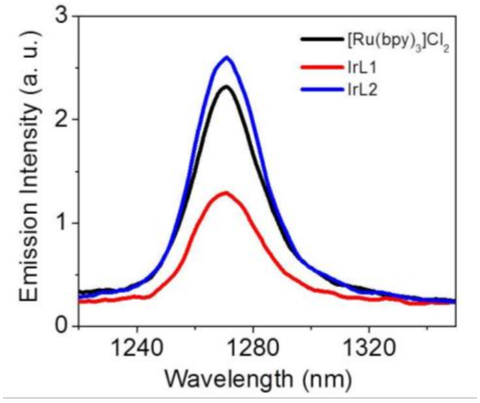

Figure 3.16: Singlet oxygen luminescence spectra in presence of **IrL1**, **IrL2** and [Ru(bpy)$_3$]Cl$_2$ (optically matched solutions) in acetonitrile (λ_{ex} = 450 nm).

3.3.6 Photostability

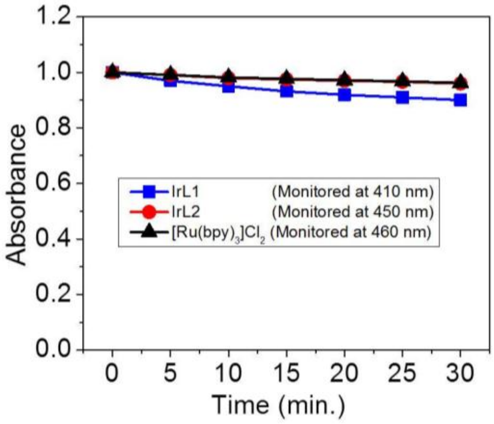

Figure 3.17: Photostability of **IrL1** and **IrL2** compared with the standard; [Ru(bpy)$_3$]Cl$_2$ in acetonitrile and the absorption maximum was monitored against irradiation time (t = 0-30 min).

Photostability is one of the foremost criteria for developing a good photosensitizer. The absorption spectra was monitored for both the PSs along with the standard ([Ru(bpy)$_3$]Cl$_2$) on irradiation using 420 nm long pass filter over a period of 0-30 min. The change in absorption was plotted against time as shown in the Figure 3.17. **IrL2** showed better photostability when compared to **IrL1** and comparable photostability with the standard ruthenium dye.

3.3.7 MTT Assay

From the photophysical properties and singlet oxygen quantum yield values, we regarded **IrL2** as the best probe to be of use in the biological system. To investigate the *in vitro* photodynamic efficacy of **IrL2** in cells, we have adopted 3-(4,5-dimethylthiazol-2-yl)-2,5-diphenyl-tetrazolium bromide (MTT) assay, which is a standard colorimetric technique used for the measurement of cellular proliferation (cell growth). MTT is yellow in color, but when reduced, it transforms to purple formazan by cellular reductase enzymes present in living cells (Scheme 3.2). The standardization of laser power was done by evaluation of the cell morphology changes and MTT assay as shown in the Figure 3.18. The cell morphology was found to be maintained in the laser power of 0.25 W and slowly degrades on increasing the power. The same result was confirmed by MTT assay in each laser power. Based on the results, a power of 0.25 W was chosen for further studies.

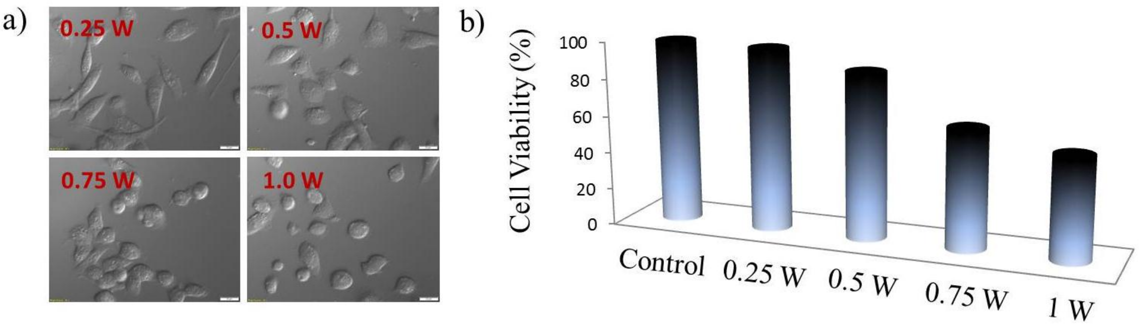

Figure 3.18: (a) The bright field images of MDA-MB-231 cells on irradiation with different laser power at 532 nm. (b) Laser power dependent MTT assay (error limit = ± 3%).

The concentration dependent MTT assay was done to analyze the toxicity of **IrL2** in the absence of light. The results showed more than 97% cell viability up to a concentration of 12 µM, confirming non-cyototoxicity of **IrL2** at lower concentration. Above 12 µM, the cell viability was found to decrease as shown in the Figure 3.19.

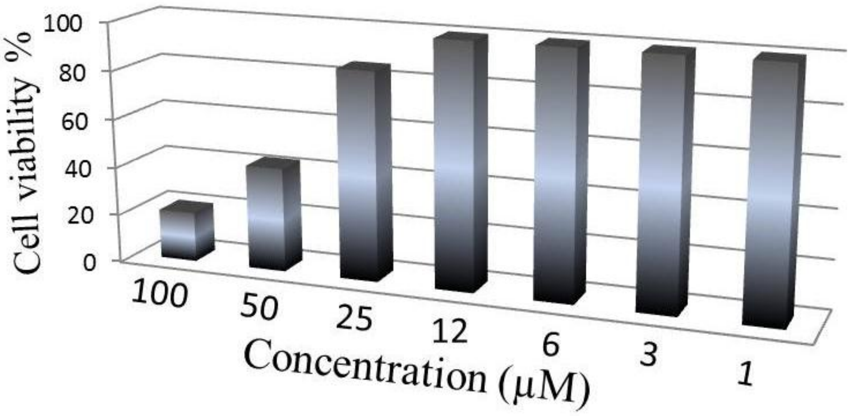

Figure 3.19: Cell viability of MDA-MB-231 cells after 24 h incubation with **IrL2** at different concentrations. Cells were cultured in DMEM (10% FBS) at 37 °C, at 5% CO_2. Spectra were measured at 570 nm (error limit = ± 3%).

To determine the photocytotoxicity of **IrL2**, we have carried out the MTT assay by irradiating with the probe at different concentrations. It was observed that the cell viability at lower concentration of **IrL2** at pH 7 noticeably reduced to 60% up on 30 s of irradiation, due to photodynamic effect. At the same time, the standard $[Ru(bpy)_3]Cl_2$ showed relatively high cell viability in similar conditions. We carried out the same experiment in three different concentrations and even with 1 μM of **IrL2**, the cell viability decreased much on irradiation (Figure 3.20). Based on the above results, we choose 1 μM concentration of **IrL2** for further studies.

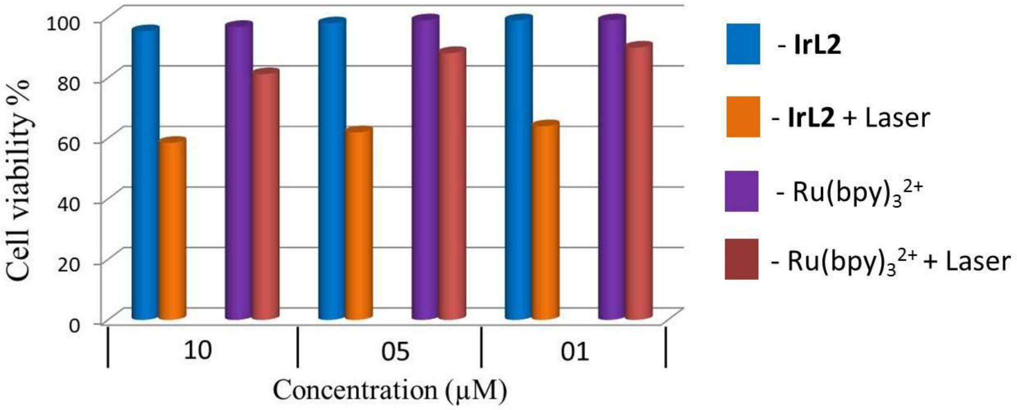

Figure 3.20: PDT effect evaluated by the MTT assay. Viability of MDA-MB-231 cells upon treatment with different concentrations of **IrL2** and $[Ru(bpy)_3]Cl_2$ (10, 5 and 1 μM) in the absence and presence of laser (532 nm, 0.25 W, t = 30 s) (error limit = ± 3%).

3.3.8 Cellular Uptake

After standardizing the optimal non-toxic concentration of **IrL2**, cellular uptake efficiency with respect to time was assessed. From three different incubation times, the best uptake efficiency was observed to be at 1 h incubation, when concentration was 1 µM (Figure 3.21). From Figure 3.21, it is clear that **IrL2** has the tendency to go to the nucleus. This is due to the presence of highly conjugated planar ligand present in the PS as discussed in Chapter 1, section 1.13. For all experiments hence forth, **IrL2** incubation time is chosen as 1 h and concentration as 1 µM.

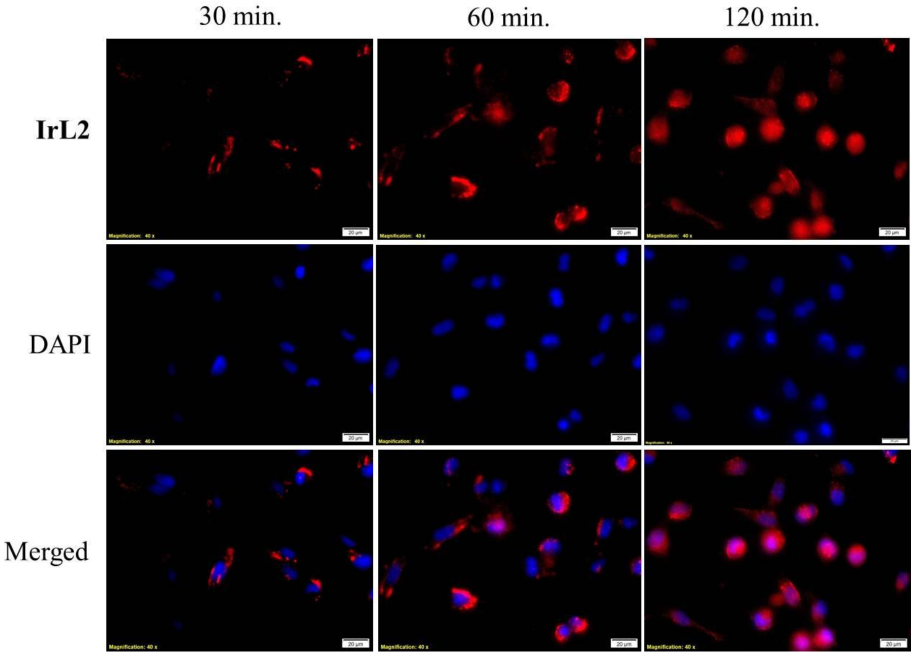

Figure 3.21: The time dependent uptake of **IrL2** by MDA-MB-231 cells at different time points (30-120 min). The merged images show the localization of **IrL2** in nucleus.

3.3.9 Intracellular Localization

The intracellular localization of **IrL2** was studied using Lyso Tracker Green and Mito Tracker Green. The results showed that, **IrL2** localizes mainly in the lysosome with a Pearson coefficient of 0.79 (Figure 3.22). The high value is due to the presence of two morpholine groups present in **IrL2** which helps to accumulate in the lysosome. It was mentioned in Chapter 1 that the inherent cationic property of the Ir(III) complexes helps the probe to accumulate in the mitochondria. In the present case, we calculated the colocalization with Mito Tracker Green as shown in Figure 3.22. The Pearson's coefficient of 0.21 clearly shows lesser extent of localization within mitochondria. The lysosomal localization of **IrL2** will help to generate localized ROS which can damage the most important cell organelle, thereby leading to cell death.

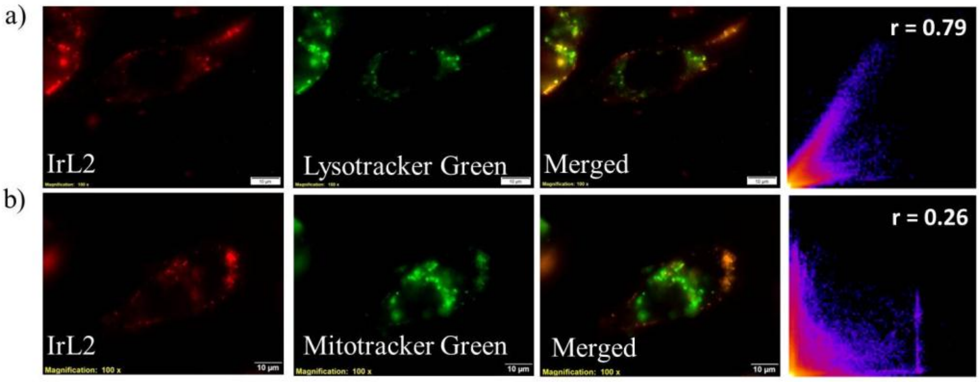

Figure 3.22: Colocalization study of **IrL2** with (a) Lyso Tracker Green and (b) Mito Tracker Green. The merged images show good overlap with Lysotracker Green with a Pearson's correlation coefficient, r = 0.79.

3.3.10 Reactive Oxygen Species Generation

To understand the involvement of reactive oxygen species (ROS), we quantified the generation of ROS in cells during the PDT treatment with **IrL2**, using 2',7'-dichlorodihydrofluorescein diacetate (H_2DCFDA) assay.[28] In the reduced form, H_2DCFDA is non-fluorescent, but esterases mediated hydrolysis followed by cellular oxidation of acetate groups results in a green fluorescent derivative (DCF). When MDA-MB-231 cells were treated with **IrL2** and irradiation followed by the addition of H_2DCFDA, we observed fluorescence in ca. 80% of cells. As shown in Figure 3.23, images showed a gradual and steady increase of ROS production in the cells with increase in the time interval of laser irradiation. In contrast, **IrL2** in the dark did not show any green fluorescence which establishes the photodynamic effect.

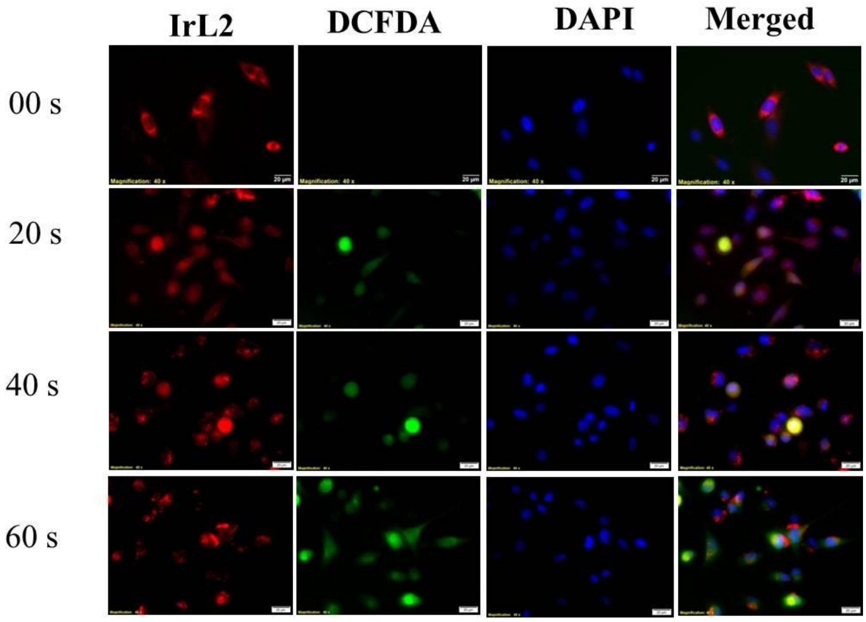

Figure 3.23: Singlet oxygen generation in the cellular level through DCFDA study. Time dependent increase in green emission shows that the increased production of singlet oxygen is proportional to laser irradiation.

Under control experiments without laser, no ROS production was observed suggesting that the synthesized **IrL2** do not cause any stress to the cells, in the absence of laser. Quantitative measure of the emission intensity also shows increased activity on laser irradiation time (Figure 3.24).

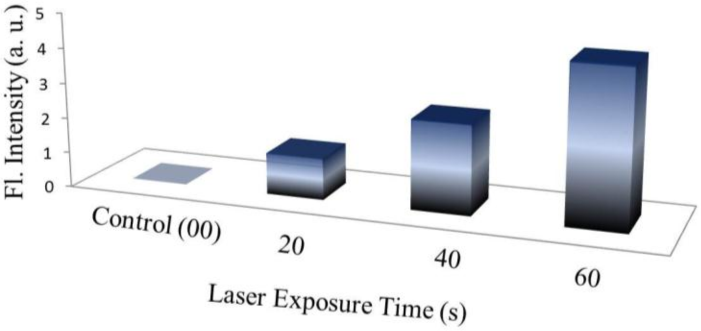

Figure 3.24: Quantitative analysis of fluorescence intensity obtained from DCFDA images. Gradual increase in the green fluorescence intensity is observed.

3.3.11 Nuclear Response – Cell Death Confirmation

The cells were treated with **IrL2** together with the staining agent, Hoechst and monitored the fluorescence intensity in different conditions (Figure 3.25). The fluorescence intensity from the nucleus was observed to decrease after treatment with **IrL2** and laser irradiation indicating major nuclear damage which is a robust proof of progressive cell death. In contrast, the control experiments (dark and light condition) showed negligible nuclear damage.

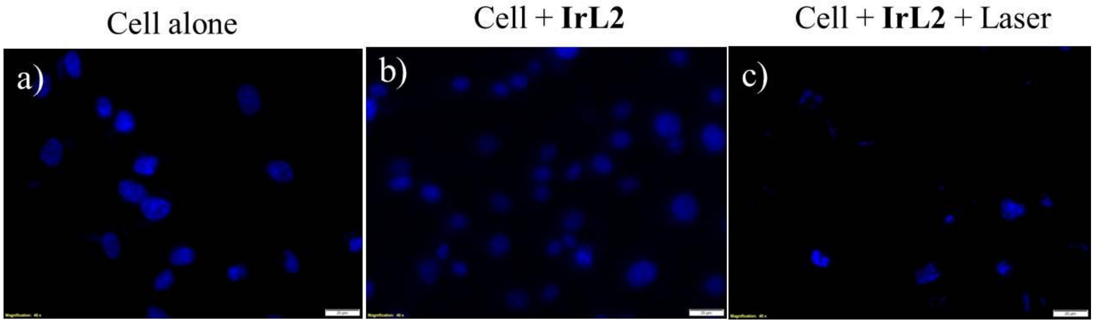

Figure 3.25: Confirmation of nuclear damage by Hoechst staining in MDA-MB-231 cells- a) control, b) in presence of **IrL2** and c) in presence of **IrL2** and laser.

3.3.12 Mechanism of Cell Death

On laser irradiation, **IrL2** exhibited high photodynamic activity in cancer cells. Encouraged by this observation, we made an attempt to understand the cell death mechanism. The two types of cell death mechanisms include (i) necrosis, which is caused by factors external to the cell, such as infection, toxins, or trauma which result in the unregulated digestion of cell components and (ii) apoptosis, which is a naturally occurring programmed and targeted cause of cellular death. The activation of caspase-3/7 has been identified as one of the key events in apoptosis. As compared with the control cells in the dark, negligible increase in caspase-3/7 activity was detected in cells treated with **IrL2** or with light irradiation. The green emission from the nucleus was found to increase with the increase in irradiation time confirming that the mechanism of cell death was through apoptosis. A quantitative evaluation of caspase-3/7 activity in MDA-MB-231 cells after treatment with **IrL2** was also carried out at the same condition as shown in the Figure 3.26. A similar finding of increased green emission from **IrL2** treated cells in the presence of light was observed when compared to both the controls.

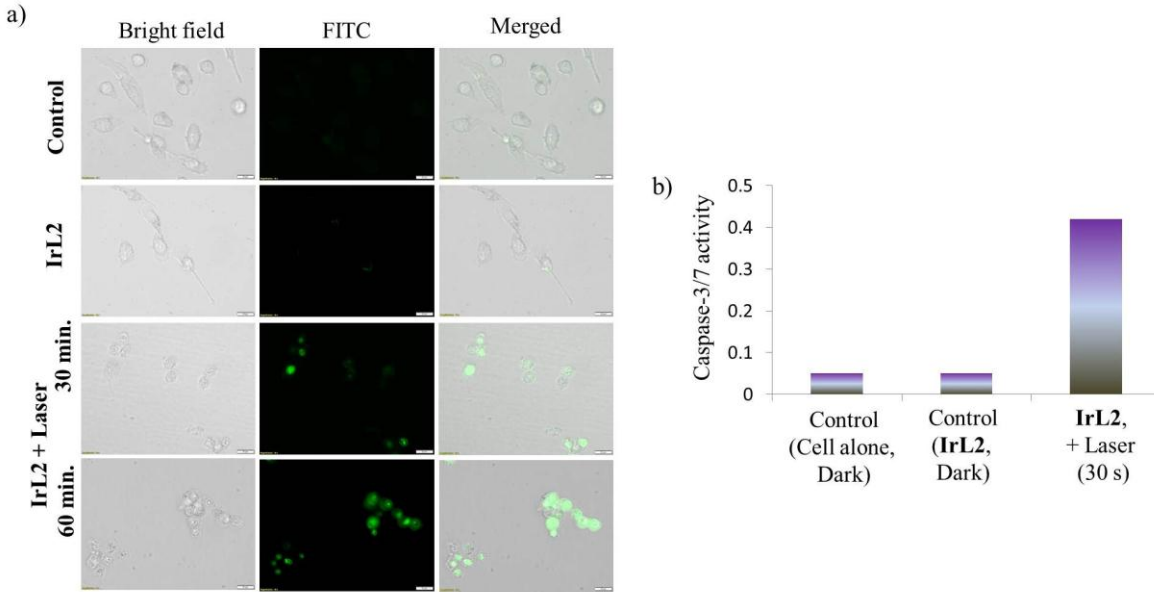

Figure 3.26: (a) Detection of caspase-3/7 activity in MDA-MB-231 cells treating with **IrL2** in the absence and presence of light (c = 1 μM, 1 h). The time dependent fluorescence spectra were recorded with caspase-3/7 green detection reagent with 5 nM caspase-3/7 staining dye and imaging was done in specific time interval. (b) Quantitative detection of caspase-3/7 activity in MDA-MB-231 cells after treatment with **IrL2** in the absence and presence of light.

To understand the mechanism of the PDT activity and cellular damage induced by **IrL2**, we performed Annexin V-FITC/PI assay using flow cytometric analysis. For this, Annexin V-FITC was used together with propidium iodide (PI). Annexin V conjugated with fluorescein isothiocynate (FITC) to label phosphatidylserine sites on the membrane surface and this phosphatidylserine, a marker of apoptosis is on the outer leaflet of the plasma membrane during apoptosis, whereas the PI can only pass through dead cells. The cell populations at different phases of cell death, namely, viable (Annexin V-FITC (-ve)/PI (-ve)), early apoptotic (Annexin V-FITC (+ve)/PI (-ve)) and necrotic or late-stage apoptotic (Annexin V-FITC (+ve)/PI (+ve)) were examined at different drug doses. The lower left quadrant (Q3) of each panel showed the viable cells, since they were negative for both Annexin V-FITC and PI, whereas the lower right quadrants (Q4) represent the apoptotic cells (Annexin V-FITC (+ve)/PI (-ve)). The data produced by the FACS (Fluorescence Assisted Cell Sorting) analysis showed highest percentage of late apoptotic cells on irradiation (t = 30 s) when compared with the dark control (Figure 3.27). This observation confirms the capability of **IrL2** to induce apoptosis in cancer cells upon laser irradiation. On the contrary, the control cells showed very less number of apoptotic and necrotic cells.

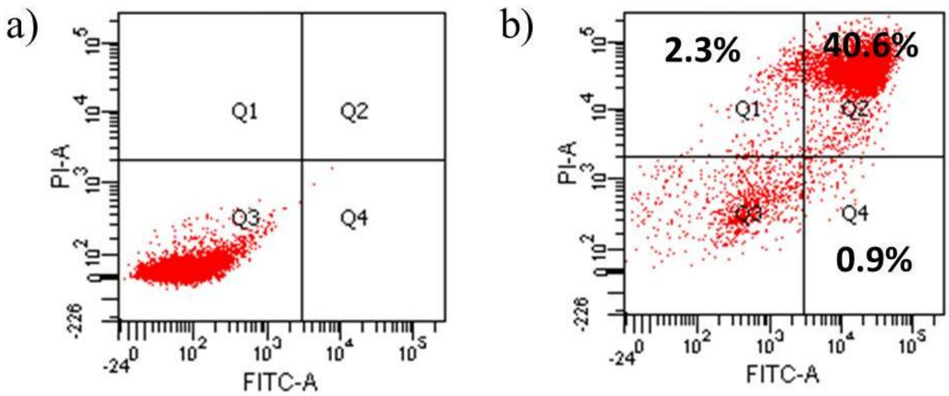

Figure 3.27: Flow cytometric quantification of annexin V and propidium iodide double-labeled MDA-MB-231 with **IrL2** for 2 h in the absence (a) and presence (b) of light (c = 10 μM, λ_{irr} = 532 nm).

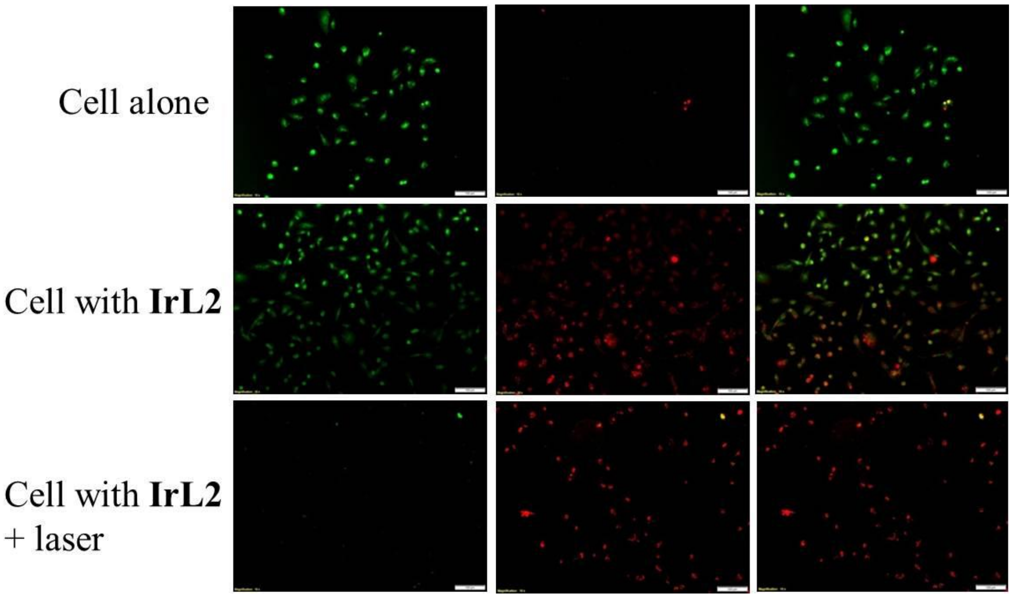

Figure 3.28: Live-dead cell assay of MDA-MB-231 cells during PDT; control, **IrL2** and **IrL2** + laser. The decrease in green emission in the first column indicates the cell death and since **IrL2** is red emissive, red emission cannot be compared with the standard.

The apoptotic pathway was again investigated through the live-dead cell assay with the nucleic acid binding dyes acridine orange (AO) and PI. Here, PI could stain only dead nucleated cells to generate red fluorescence and AO stained all live and dead nucleated cells to show green fluorescence. Figure 3.28 shows the fluorescence image from the cells in various conditions. The control shows only green emission since all the cells are alive. On treating with **IrL2**, cells showed red emission due to the emission from the PS. After irradiation, since **IrL2** is red emissive, the cell death is understood through the decrease in emission intensity in the green channel (Figure 3.28), due to the more uptake of PI in the dead cells.

3.4 Conclusions

We have developed two cyclometalated Ir(III) complexes, **IrL1** and **IrL2** as PDT agents for cancer cells. Both the PSs exhibit good molar extinction coefficient in the visible region which improve the efficiency of PDT in cells. The triplet quantum yield, energy transfer efficiency and singlet oxygen quantum yield values clearly establish the high efficiency of **IrL2** when compared to **IrL1**. The presence of two morpholine units in **IrL2** helps to accumulate in the lysosome. The MTT assay in MDA-MB-231 cells showed the non-cytotoxicity of **IrL2** at lower concentrations and in dark control. The generation of reactive oxygen species in the cellular level was studied through DCFDA fluorescence study. Finally, the mechanism of cell death was analyzed through caspase-3/7 activity and flow cytometry which establish the apoptotic pathway. Overall, this work provides a new insight into the development of cyclometalated Ir(III) complexes as organelle targeted PDT agents having better efficiency.

3.5 Experimental Section

3.5.1 Materials and methods

Unless otherwise stated, all starting materials and reagents were purchased from commercial suppliers (Sigma Aldrich, Alfa Aesar, Fluka, Merck or Spectrochem) and used without further purification. DAPI, Lyso Tracker Green, Mito Tracker Green were also purchased from Sigma Aldrich. Reactions were monitored with thin layer chromatography on silica gel 60 F254 (0.2 mm; Merck) using UV light source at 254 nm and 365 nm. Normal-phase chromatography was carried out using silica gel (particle size: 60-120 mesh and 100-200 mesh). ^{1}H-NMR spectra were recorded on Bruker Advance 500 NMR spectrometers, and chemical shifts are expressed in parts per million (ppm). Cell imaging was carried out in an Epifluorescent Inverted microscope. Acetonitrile used for photophysical measurements was dried over P_2O_5 and freshly distilled prior to use to ensure extreme dry condition. PBS buffer was used for pH dependent studies.

3.5.2 Synthesis and characterization

Preparation of diethyl 5,5'-bis(bromomethyl)-2,2'-bipyridine (23)

To a solution of 5,5'-methyl-2,2'-bipyridine (**22**) (2 g, 10.85 mmol) in 50 mL of dry carbontetrachloride was added *N*-bromosuccinimide (3.86 g, 21.7 mmol) and AIBN (100 mg). The reaction mixture was refluxed for 12 h at 80 ^{o}C. After the completion of the reaction, the mixture was filtered in the hot condition and the solvent was removed under reduced pressure. The crude was then purified by column chromatography (SiO_2, 8% EtOAc/DCM) to give a white solid. Yield: 63 %.

^{1}H NMR ($CDCl_3$, 500 MHz, TMS) δ (ppm): 8.62 (d, *J* = 1.5 Hz, 2H), 8.34 (d, *J* = 8 Hz, 2H), 7.79 (dd, *J* = 8 Hz, 2.5 Hz), 4.47 (s, 4H). **^{13}C NMR** ($CDCl_3$, 125 MHz,) δ (ppm): 153.25, 150.28, 136.24, 129.87, 120.22, 34.23. **ESI MS**: MS Calcd for $C_{12}H_{11}$ BrN_2, 262.01; Found 262.01 (100%) and 264.01 (98%).

Preparation of diethyl tetraethyl ([2,2'-bipyridine]-5,5'-diylbis(methylene)) bis (phosphonate) (24)

The biphosphonate (**24**) was prepared by the reaction of the corresponding dibromo- derivative (**23**) (1 g, 2.92 mmol) with 2.4 mL (11.69 mmol) of triethyl phosphite at 100 ^{o}C for 12 h followed by the removal of the unreacted triethyl phosphite under vacuum. Yield: 90%.

^{1}H NMR ($CDCl_3$, 500 MHz, TMS) δ (ppm): 8.56 (s, 2H), 8.34 (d, *J* = 8 Hz, 2H), 7.79 (dd, *J* = 8 Hz, 2.5 Hz, 2H), 4.2 (q, *J* = 7 Hz, 8H), 3.08 (s, 4H), 1.32 (t, *J* = 7 Hz, 12H); **^{13}C NMR** ($CDCl_3$, 125 MHz,) δ (ppm): 153.55, 150.24, 135.44, 126.21, 119.18, 65.32, 38.43, 19.21; **ESI MS**: MS Calcd. for $C_{20}H_{30}N_2O_6P_2$, 456.16 ; Found 457.16.

Preparation of 5,5'-bis((E)-2-(9-(4-morpholinobutyl)-9H-carbazol-3-yl)vinyl)-2,2'-bipyridine (26)

The phosphonate ester derivative (**24**) (200 mg, 0.438 mmol) was taken in a two necked RB in inert atmosphere, dry THF (20 mL) was added and dissolved well. To this solution NaH (70 mg) dissolved in dry THF (10 mL) was added drop wise using a pressure equalizer at 0 °C. The stirring continued for 15 min. Then the aldehyde derivative (**25**) (324.09 mg, 0.964 mmol) dissolved in dry THF (20 mL) was added dropwise using a pressure equalizer. The mixture was refluxed at 60 °C for 12 h. The excess NaH was quenched by adding methanol and the crude productwas then poured to water and then extracted with DCM. It is dried under reduced pressure and purified by column chromatography (SiO_2, 10% MeOH/DCM). Yield: 70%.

^{1}H NMR ($CDCl_3$, 500 MHz, TMS) δ (ppm): 8.81 (d, *J* = 2 Hz, 2H), 8.43 (d, *J* = 8 Hz, 2H), 8.27 (s, 2H), 8.14 (d, *J* = 7.5 Hz, 2H), 8.02 (dd, *J* = 7 Hz, 1.5 Hz, 2H), 7.50-7.40 (m, 4H), 7.28-7.26 (m, 4H), 7.17 (d, *J* = 16.5 Hz, 2H), 4.35 (t, *J* = 7 Hz, 4H), 3.69 (t, *J* = 4.5 Hz, 8H), 2.39-2.34 (m, 12 H), 1.96-1.91 (m, 4 H), 1.62-1.58 (m, 4H). **^{13}C NMR** ($CDCl_3$, 125 MHz,) δ (ppm): 154.26, 147.94, 140.84, 140.51, 133.50, 132.97, 131.80, 128.05, 126.01, 124.62, 123.33, 122.89, 122.05, 120.88, 120.53, 119.29, 199.09, 108.98, 100.00, 66.85, 58.31, 53.61, 42.99, 37.21, 26.78, 24.07. **ESI MS**: MS Calcd. for $C_{54}H_{56}N_6O_2$, 820.45; Found 821.45.

Synthesis of dimer (28)

$IrCl_3.xH_2O$ (224.36 mg, 0.75 mmol) and 2-phenylpyridine (244 mg, 1.6 mmol) were dissolved in 20 mL of 2-ethoxyethanol and water (8:2) mixture and refluxed at 140 °C for 24 h. After the solution was cooled, addition of 40 mL of H_2O gave a yellow precipitate that was filtered and washed with diethyl ether. The crude product was used for next reaction without further purification.

Synthesis of IrL1 and IrL2 (29 and 30)

28 (1.0 eq.) and **20** (or **26**) (2.6 eq.) and sodium carbonate (11.0 eq.) were stirred overnight in 1:3 dichloromethane/ethanol (40 mL) at 60 °C under argon atmosphere. The solvent was removed by evaporation under reduced pressure. The crude product obtained was poured into a solution of NH_4PF_6 in water and extracted with dichloromethane (3 x 50 mL). The combined organic layers were dried over Na_2SO_4. A crude residue was obtained after removal of the solvent. The desired complex was obtained as an orange powder after the purification of crude product by silica column chromatography using DCM/methanol in a 9:1 ratio (for **IrL1**) (7:3 for **IrL2**) as the eluent. The product is reprecipitated in CH_2Cl_2/Hexane. Yield: 40% for **IrL1** and 43% for **IrL2**.

29: **^{1}H NMR** ($CDCl_3$, 500 MHz, TMS) δ (ppm): 8.14(dd, *J* = 8 Hz, 6 Hz, 2H), 7.94 (d, *J* = 6.5 Hz, 2H), 7.77-7.44 (m, 4H), 7.61 (d, *J* = 7.5 Hz, 2H), 7.59-7.55 (m, 2H), 7.92 (d, *J* = 1.5 Hz, 2H), 7.46-7.42 (m, 3H), 7.06-7.03 (m, 4H), 6.99-6.93 (m, 2H), 7.48 (d, *J* = 8 Hz, 2H), 7.41 (d, *J* = 8.5 Hz, 4H), 6.79 (d, *J* = 16 Hz, 2H), 4.32 (t, *J* = 7 Hz, 2H), 2.5 (s, 3H), 1.74-1.52 (m, 4H).**^{13}C NMR** ($CDCl_3$, 125 MHz,) δ (ppm): 150.28, 147.83, 142.43, 141.26, 137.54, 136.26, 134.31, 133.26, 133.11, 129.62, 127.52, 127.14, 126.11, 125.31, 122.11, 120.86, 119.82, 108.72, 107.42, 67.11, 62.74, 57.11, 56.43, 28.24, 26.11, 18.40.

30: **^{1}H NMR** ($CDCl_3$, 500 MHz, TMS) δ (ppm): 8.61(d, *J* = 8 Hz, 2H), 8.29 (dd, *J* = 6.5 Hz, 2 Hz, 2H), 8.21-8.12 (m, 2H), 8.11 (d, *J* = 7.5 Hz, 2H), 7.96 (d, *J* = 8 Hz, 2H), 7.92 (d, *J* = 1.5 Hz, 2H), 7.80-7.76 (m, 2H), 7.64 (d, *J* = 5.5 Hz, 4H), 7.58-7.56 (m, 2H), 7.48 (d, *J* = 8 Hz, 2H), 7.41 (d, *J* = 8.5 Hz, 4H), 7.37 (d, *J* = 8.5 Hz, 2H), 7.28-7.26 (m, 2H), 7.15-7.13 (m, 4H), 7.08-7.01 (m, 2H), 6.79 (d, *J* = 16 Hz, 2H), 6.4 (d, *J* = 7.5Hz, 2H), 4.33 (t, *J* = 7 Hz, 4H), 3.67-3.55 (m, 12 H), 2.34 (t, *J* = 7 Hz, 12H), 1.92 (t, *J* = 7.5 Hz, 4H). **^{13}C NMR** ($CDCl_3$, 125 MHz,) δ (ppm): 150.12, 150.00, 144.52, 142.81, 141.81, 141.22, 141.00, 138.94, 138.21, 133.21, 128.94, 127.52, 126.98, 125.12, 122.21, 121.14, 119.28, 119.21, 112.21, 110.21, 108.45, 67.34, 62.09, 56.43, 56.64, 28.21, 25.98.

3.5.3 Calculation of triplet excited state quantum yields

The triplet excited state quantum yields (ϕ_T) of the iridium (III) complexes were determined by an earlier reported procedure of energy transfer to β-carotene, using $Ru(bpy)_3^{2+}$, as the reference molecule.[15] For these experiments, optically matched solutions of $Ru(bpy)_3^{2+}$ and the iridium (III) complexes at 355 nm, were mixed with a known volume of β-carotene solution (end concentration of β-carotene was fixed at *ca.* 2.0 x 10^{-4} M). The transient absorbance of the β–carotene triplet, generated by the energy transfer from $Ru(bpy)_3^{2+}$ or the Iridium (III) complexe's triplet excited state, was monitored at 515 nm. Comparison of plateau absorbance (ΔA) following the completion of sensitized triplet formation, properly corrected for the decay of the donor triplet excited state in competition with energy transfer to β-carotene, enabled us to estimate ϕ_T of the triplet excited states based on the following equation.

$$\phi_T^{ir} = \frac{\phi_T^{ref} \text{ x } \Delta A^{ir} \text{ x } K_{obs}^{ir} \ (K_{obs}^{ref} - K_0^{ref})}{\Delta A^{ref} \text{ x } K_{obs}^{ref} \ (K_{obs}^{ir} - K_0^{ir})}$$

wherein, superscripts 'ir' and 'ref' designate compound **Ir-Bp-Ly** and $Ru(bpy)_3^{2+}$, respectively, K_{obs}, is the pseudo-first-order rate constant for the growth of the β-carotene triplet and K_0 is the rate constant for the decay of the donor triplet, in the absence of β-carotene, observed in solutions containing $Ru(bpy)_3^{2+}$ or a porphyrin at the same optical density (OD = 0.1) as those used for sensitization.

3.5.3 Singlet oxygen quantum yield

The quantum yield (ϕ_s) for singlet oxygen ($^1O_2$) in methanol was measured by 9,10-dimethyl anthracene (DMA), a powerful $^1O_2$ indicator. $[Ru(bpy)_3]Cl_2$ was used as the standard, which has a known $^1O_2$ quantum yield of 0.83 in methanol. Using 1 mM stock solutions, we prepared optically matched solutions for Ir(III) complex and $[Ru(bpy)_3]Cl_2$ in methanol. DMA stock solution was prepared as 100 mM in methanol and it was added in Ir(III) complex solution. Then, total concentration ratio of Ir(III) complexes and DMA was made to 1:10. This solution was then irradiated using a 420 nm long pass filter in the irradiation chamber for 10-60 s and the attenuation of absorbance from DMA deactivation by irradiation was recorded in each 10 s. The experiment was repeated for the standard also. ϕ_s value for the complex is obtained by the following equation.

$$\phi_s = \frac{\phi_r \text{ x } m_s \text{ x } F_r}{m_r \text{ x } F_s}$$

In the above equation, 's' indicates the sample and 'std' represents the standard, 'S' is the slope of DMA absorbance difference and 'F' is from $F = 1 - 10^{-OD}$. Optical density (OD) was measured from the optically matched solution of the complex and standard.

Scheme 3.3: Singlet oxygen addition reaction with DMA

The singlet oxygen generation quantum yield was measured in different pH also using the same method and standard. In this case, we took the water soluble derivative of the anthracene derivative, 9,10-anthracenediyl-bi(methylene)dimalonic acid (ABDA).

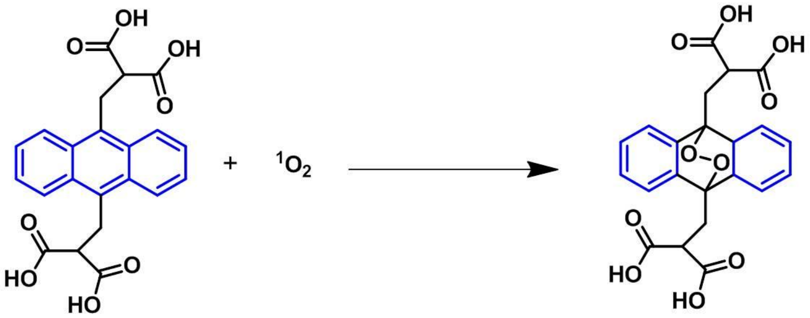

Scheme 3.3: Singlet oxygen addition reaction with ABDA

3.5.4 MDA MB-231 cell line culture

MDA MB-231 cells are basal epethelial cells which is isolated from breast tumor of humans. These cells were cultured using DMEM medium which was supplemented with 10% PBS and 1% anti-anti. After thawing from cryo-preservation, the cells were added to fresh medium to 5x dilution. Centrifugation at 3000 rpm for 3 min was done and the cell pellet was re-suspended in 1 mL of complete DMEM medium. This cell suspension was seed into DMEM medium in a T-25 flask and incubated for 24 h in 5% CO_2 incubator at 37 ^oC. After the specific incubation the cells were observed for healthy growth. After reaching the specified confluency (80-90%) the cells were trypsinized using 0.25% (w/v) trypsin - 0.53 mM EDTA solution. After 5 min incubation with trypsin at 37 ^oC the cells were collected by adding 1 mL of complete medium. The trypsinized cells were pipetted to separate the individual cells. Centrifugation was carried out for 3 min at 3000 rpm to get the cell pellet. This pellet was again re-suspended in 1 mL of complete medium and was pipetted thoroughly. This cell suspension was used to seed the required flasks and plates.

3.5.5 MTT Assay

MDA-MB-231 cells were seed into 96 well plates and then incubated for 24 h at 37 ^oC. After incubation the cells where added with different concentrations of **IrL2**. The different concentrations of material used ranges from 100 μM to 1.0 μM. The cells were incubated with these concentrations and were given for 24 h incubation. After this, the medium was replaced with 90 µL of fresh medium and 10 µL MTT reagent (5 mg/mL) was added. And incubated for 4 h, after that the medium with MTT was removed. The well were then added with 100 µL of DMSO and kept for 30 min incubation. The absorbance of colour developed was then determined using micro plate reader at 570 nm.

3.5.6 MTT Assay with laser irradiation

After culturing of MDA MB-231 cells in 96 well plates, the cells were exposed to different powers (0.25W, 0.5 W. 0.75 W and 1 W) of laser irradiations for 30 s each. After irradiation, the cells were allowed to incubate for 24 h. After the specific incubation, the cells were added with fresh serum free medium and MTT reagent was added along with it. Then, 100 µL of DMSO was added to each well after 30 min incubation with MTT reagent. The cells were allowed to develop color for 30 min and then recorded at 570 nm using a micro plate reader. Imaging of the cells after reading was also done after removing the DMSO and adding 1x PBS.

3.5.7 MTT Assay with Laser Irradiation

The cells were seeded into 96 well plates and then incubated for 24 h at 37 ^{o}C. After incubation, the cells were added with 1.0, 0.75, 0.5, 0.25 µM concentrations of **IrL2** and $[Ru(bpy)_3]Cl_2$. Incubation was done for 1 h and the medium was replaced with fresh medium. Then, 532 nm laser irradiation (0.25 W) was given to cells for 30 s and again incubation was carried out for another 30 min. 10 µL of MTT reagent (5 mg/mL) of DMSO was added to all the wells and was incubated for 4 h. After the incubation of the MTT reagent, 100 µL of DMSO was added to all wells. After 30 min the absorbance was recorded at 570 nm using a micro plate reader.

3.5.8 Cellular Uptake Studies

Uptake efficiency of **IrL2** was performed to standardize the time enquired for the maximum uptake of material by the cells. After 24 h incubation at 37 ^{o}C, the cells were treated with 1 µM concentration of **IrL2** at different time points. The treatments were given for 30, 60, 120 min. After each time point incubation, the fluorescence images of the cells were captured using selective filter sets such as HcRED and DAPI in epifluorescence microscope.

3.5.9 Colocalization

Colocalization studies were carried out using both Mito Tracker Green and Lyso Tracker Green. The cells were seeded and cultured on glass cover slips and were incubated with **IrL2** for 1 h in serum free medium. After the incubation the medium was replaced with fresh medium and 5 µL of Mito Tracker Green and Lyso Tracker Green. This was again kept for another 30 min. After the whole incubation the cells were washed with PBS. The cover slips were then mounted on a clear glass slide using glycerin. The images were taken at 100x using a fluorescent microscope.

3.5.10 Intracellular ROS generation

The cells were seed into 6 well plates and incubated in a CO_2 incubator for 24 h. After the 1 µM concentration of **IrL2**, cells were again incubated for 1 h. This was followed by washing the cells with PBS and replacing it with fresh serum free media. Then irradiation was given for different time intervals ranging from 20 - 60 s. Without laser irradiation, a control was also maintained which contains IrL2 alone. After the irradiation, the cells were incubated for 30 min. Following this, 25 µL DCFDA reagent was added and incubated for another 30-45 min. The cells were washed and the colorless serum free fresh media was added to wells. Images were taken to find out the different rates of ROS generation using a fluorescent microscope with available filter sets (FITC, HcRED and DAPI).

3.5.11 Nucleus (DAPI) staining

Cells were seeded in 4 well dish and provided with required incubation conditions and time. After the cells have grown to full size, material was introduced into two wells. After 1 h of incubation of **IrL2**, the medium containing the material was removed and washed witrh PBS. Laser irradiation was given to one of the wells with material incubated cells. DAPI stain was then added to all the wells and incubated for 10 min. Again PBS wash was given, then fresh colorless serum free media was added and images were then taken at 40 x (DAPI).

3.5.12 Caspase-3/7 green detection – imaging

The cells were cultured in the specific culture conditions. After specific cell density was attained, the cells were incubated with **IrL2** and exposed to laser (0.25W, 30 sec). After the treatments, the cells were given 30 min of incubation so that the cells could start apoptosis. After this incubation, the cells were treated with 5 nM concentration of caspase-3/7 staining dye. After 30 min incubation, cells were washed and imaged (40x, FITC and BF)

3.5.13 Caspase-3/7 green detection – quantitative

The cells were cultured in 96 well plate and the experiments were carried out when the required cell density was attained. The test wells were treated with optimum concentration of material and irradiated with 0.25 W; 532 nm laser for 30 s. In order to compare the result, control with cell alone and with **IrL2** (without laser irradiation) were also incubated. After the treatment, the cells were washed with PBS and serum free media was added along with caspase-3/7 dye. After 30 min incubation with dye, the plate was read for fluorescence emission using a micro plate reader (excitation 350 ± 20 nm, emission 440 ± 20 nm).

4.5.14 Flow Cytometry Analysis

Alexa Fluor® 488 Annexin V/Dead Cell Apoptosis Kit was used to carry out this analysis and the protocol was followed as prescribed by the manufacturer. Cells were seeded into culture dish (6 well plates) and then incubated for 24 h to attain complete growth. Afterwards, the cells were given a media change and **IrL2** was added to 4 wells out of the 6 wells. The remaining 2 wells were considered as control. After the material incubation for 1 h, the cells were washed with PBS and again fresh media was added. All the 4 wells with material added were irradiated with 532 nm laser for 30 s. The cells were then collected and washed with PBS using centrifugation and suspended in 100 μL of 1 x binding buffer. The suspension of cells was then added with 5 µL of Annexin V conjugate and 2 µL of PI (100 µg/mL). The cells were then incubated for 15 min at 37 ºC. After incubation, the cells were washed with 1x binding buffer and again suspended in 500 μL of 1x binding buffer. The cells were then analyzed using FACS.

4.5.15 Live-Dead Cell Assay

The specific cell line was seeded into culture plates and allowed to grow for 24 h at standard culture conditions. After the growth period, the cells were added with the optimum concentration of **IrL2** and given 1 h incubation in serum free media. A cell alone and with material (without laser) was also incubated. The test well was irradiated with 532 nm laser for 30 s and again kept for incubation for 30 min.

Fresh serum free media along with acridine orange- propidium iodide mixture (1:1 in 1x PBS) was added and incubated. After incubation, the cells were washed and imaged under fluorescence microscope.

3.6 References

(1) (a) Lo, K. K.-W.; Ng, D. C. -M.; Chung, C. -K. *Organometallics* **2001**, *20*, 4999−5001. (b) Lo, K. K.-W.; Hui, W.-K.; Chung, C.-K.; Tsang, K. H.-K.; Lee, T. K.-M.; Li, C.-K.; Lau, J. S.-Y.; Ng, D. C.-M. *Coord. Chem. Rev*. **2006**, *250*, 1724−1736. (c) Stinner, C.; Wightman, M. D.; Kelley, S. O.; Hill, M. G.; Barton, J. K. *Inorg. Chem*. **2001**, 40, 5245−5250. (d) Barry, N. P. E.; Sadler, P. J. Chem. Soc. Rev. 2012, 41, 3264−3279.

(2) Celli, J. P.; Spring, B. Q.; Rizvi, I.; Evans, C. L.; Samkoe, K. S.; Verma, S.; Pogue, B. W.; Hasan, T. *Chem. Rev*. **2010**, *110*, 2795−2838.

(3) (a) Josefsen, L. B.; Boyle, R. W. *Met. Based Drugs* **2008**; 276109-276123. (b) Ali, H.; van Lier, J. E. *Chem. Rev*. **1999**, *99*, 2379−2450. (c) Liu, Z.; Habtemsrism, A.; Pizarro, A. M.; Fletcher, S. A.; Kisova, A.; Vrana, O.; Salassa, L.; Bruijnincx, P. C.; Clarkson, G. J.; Brabec, V.; Sadler, P. J. *J. Med. Chem*. **2011**, *54*, 3011−3026. (d) Liu, Z.; Romero-Canelon, I.; Qamar, B.; Hearn, J. M.; Habtemariam, A.; Barry, N. P.; Pizarro, A. M.; Clarkson, G. J.; Sadler, P. J. *Angew. Chem. Int. Ed*. **2014**, *53*, 3941−3946. (e) Leung, C. H.; Zhong, H. J.; Yang, H.; Cheng, Z.; Chan, D. S.; Ma, V. P.; Abagyan, R.; Wong, C. Y.; Ma, D. L. *Angew. Chem. Int. Ed*. **2012**, *51*, 9010−9014. (f) Okamura, N.; Nakamura, T.; Yagi, S.; Maeda, T.; Nakazumi, H.; Fujiwarab, H.; Kosek, S. *RSC Adv*. **2016**, *6*, 51435−51445.

(4) (a) Demas, J. N.; Harris, E. W.; McBride, R. P. *J. Am. Chem. Soc*. **1977**, *99*, 3547−3551. (b) Mulazzani, Q. G.; Jiun, H.; Hoffmann, M. Z.; Ford, W. E.; Rodgers, M. A. *J. Phys. Chem*. **1994**, *98*, 1145−1150. (c) Connick, W. B.; Gray, H. B. *J. Am. Chem. Soc*. **1997**, *119*, 11620−11627. (d) Anhalagan, V.; Srivastava, T. S. *J. Photochem. Photobiol. A: Chem*. **1995**, *89*, 113−119.

(5) (a) Yogo, T.; Urano, Y.; Ishitsuka, Y.; Maniwa, F.; Nagano, T. *J. Am. Chem. Soc*. **2005**, *127*, 12162−12163. (b) Stacy, O. J.; Pope, S. J. A. *RSC Adv*. **2013**, *3*, 25550−25564.

(6) (a) Ruggi, A.; van Leeuwen, F. W. B.; Velders, A. H. *Coord. Chem. Rev*. **2011**, *255*, 2542−2554; (b) Steunenberg, P.; Ruggi, A.; van den Berg, N. S.; Buckle, T.; Kuil, J.; van Leeuwen, F. W. B.; Velders, A. H. *Inorg. Chem*. **2012**, *51*, 2105−2114; (c) Cao, J,-J.; Tan, C. -P.; Chen, M.-H.; Wu, N.; Yao, D.-Y.; Liu, X.-G.; Jia, L.-N.; Mao, Z.-W. *Chem. Sci*. **2017**, *8*, 631–640.

(7) Li, S. P.-Y.; Liu, H.-W.; Zhang, K. Y.; Lo, K. K.-W. *Chem. -Eur. J*. **2010**, *16*, 8329−8339.

(8) Zhao, J.; Wu, W.; Sun, J.; Guo, S. *Chem. Soc. Rev*. **2013**, *42*, 5323−5351.

(9) (a) Vezzu, D. A. K.; Ravindranathan, D.; Garner, . W.; Bartolotti, L.; Smith, M. E.; Boyle, P. D.; Huo, S. *Inorg. Chem*. **2011**, *50*, 8261−8273. (b) Flamigni, L.; Barbieri, A.; Sabatini, C.; Ventura, B.; Barigelletti, F., *Photochemistry and Photophysics of Coordination Compounds II*, 143−203. (c) Deaton, J. C.; Young, R. H.; Lenhard, J. R.; Rajeswaran, M.; Huo, S. *Inorg. Chem*. **2010**, *49*, 9151—9161. (d) Hallett, A. J.; Kariuki, B. M.; Pope, S. J. A. *Dalton Trans*. **2011**, *40*, 9474−9481.

(10) Kam-Wing, K.; Zhang, K. Y. *RSC Adv*. **2012**, *2*, 12069−12083.

(11) (a) Wu, W.; Sun, J.; Ji, S.; Wu, W.; Zhao, J.; Guo, H. *Dalton Trans*. **2011**, *40*, 11550−11561. (b) Liu, Y.; Wu, W.; Zhao, J.; Zhang, X.; Guo, H. *Dalton Trans*. **2011**, *40*, 9085−9089. (c) Rachford, A. A.; Goeb, S.; Ziessel, R.; Castellano, F. N. *Inorg. Chem*. **2008**, *47*, 4348−4355. (d) Lanoe, P.-H.; Fillaut, J.-L.; Toupet, L.; Gareth Williams, J. A.; Bozec, H. L.; Guerchais, V. *Chem. Commun*. **2008**, 4333−4335.

(12) Hanson, K.; Tamayo, A.; Diev, V. V.; Whited, M. T.; Djurovich, P. I.; Thompson, M. E. *Inorg. Chem*. **2010**, *49*, 6077−6084.

(13) Rachford, A. A.; Ziessel, R.; Bura, T.; Retailleau, P.; Castellano, F. N. *Inorg. Chem*. **2010**, *49*, 3730−3736.

(14) Sun, J.; Zhong, F.; Yi, X.; Zhao, J., *Inorg. Chem*. **2013**, *52*, 6299–6310.

(15) Xue, F.; Lu, Y.; Zhou, Z.; Shi, M.; Yan, Y.; Yang, H.; Yang, S. *Organometallics* **2015**, *34*, 73−77.

(16) Wang, J.; Lu, Y.; McGoldrick, N.; Zhang, C.; Yang, W.; Zhaob, J.; Draper, S. M. *J. Mater. Chem. C* **2016**, *4*, 6131−6139.

(17) Palao, E.; Sola-Llano, R.; Tabero, A.; Manzano, H.; Agarrabeitia, A. R.; Villanueva, A.; Ljpez-Arbeloa, C.; Mart&nez- Mart&nez, V.; Ortiz, M. J. *Chem. Eur. J.* **2017**, *23*, 10139–10147.

(18) Wang, F. -X.; Chen, M. -H.; Lin, Y. -N.; Zhang, H.; Tan, C. -P.; Ji, L. -N.; Mao, Z. -W. *ACS Appl. Mater. Interfaces* **2017**, *9*, 42471−42481.

(19) Sudheesh, K. V.; Joseph, M. M.; Philips, D. S.; Samanta, A.; Maiti, K. K.; Ajayaghosh, A. *ChemSelect* **2018**, *28*, 2416−2422.

(20) Divya, K. P.; Sreejith, S.; Ashokkumar, P.; Yuzhan, K.; Peng, Q.; Maji, S. K.; Tong, Y.; Yu, H.; Zhao, Y.; Ramamurthy, P.; Ajayaghosh, A. *Chem. Sci*. **2014**, *5*, 3469−3474.

(21) Qiu, K.; Chen, Y.; Rees, T. W.; Ji, L.; Chao, H., *Coord. Chem. Rev*., **2018**, DOI: 10.1016/j.ccr.2017.10.0220010-8545

(22) (a) Luzio, J. P.; Pryor, P. R.; Bright, N. A., *Nat. Rev. Mol. Cell Biol.*, **2007**, *8*, 622–632. (b) Saftig, P.; Klumperman, J. *Nat. Rev. Mol. Cell Biol*. **2009**, *10*, 623–635. (c) Cesen, M. H.; Pegan, K.; Spes, A.; Turk, B. *Exp. Cell Res*. **2012**, *318*, 1245–1251.

(23) (a) Paine, P. L.; Moore, L. C.; Horowitz, S. B. *Nature* **1975**, *254*, 109–114. (b) Galindo, F.; Burguete, M. I.; Vigara, L.; Luis, S. V.; Kabir, N.; Gavrilovic, J.; Russell, D. A. *Angew. Chem*. **2005**, *117*, 6662–6666. (c) Huang, H.; Yu, B.; Zhang, P.; Huang, J.; Chen, Y.; Gasser, G.; Ji, L.; Chao, H. *Angew. Chem. Int. Ed*. **2015**, *54*, 14049–14052.

(24) Nam, J. S.; Kang, M. G.; Kang, J.; Park, S. Y.; Lee, S. J. C.; Kim, H. T.; Seo, J. K.; Kwon, O. H.; Lim, M. H.; Rhee, H. W.; Kwon, T. H. *J. Am. Chem. Soc*. **2016**, *138*, 10968−10977.

(25) (a) Wang, C.; Lystrom, L.; Yin, H.; Hetu, M.; Kilina, S.; McFerland, S. A.; Sun, W., *Dalton Trans*. **2016**, *45*, 16366−16378. (b) Sun, Y.; Joyce, L. E.; Dickson, N. M.; Turro, C. *Chem. Commun*. **2010**, *46*, 2426−2428.

(26) Gutierrez, M. I.; Martinez, C. G.; Garcia-Fresnadillo, D.; Castro, A. M.; Orellana, G.; Braun, A. M.; Oliveros, E., *J. Phys. Chem. A* **2003**, *107*, 3397−3403.

(27) He, L.; Li, Y.; Tan, C.-P; Ye, R. -R.; Chen, M. -H.; Cao, J.-J.; Ji, L.-N.; Mao, Z. -W. *Chem. Sci*. **2015**, *6*, 5409−5418.

(28) LeBel, G. P.; Ischiropoulos, H.; Bondy, S. G. *Chem. Res. Toxicol*. **1992**, *5*, 227−231.

Chapter 4

A Cyclometalated Ir(III) Complex as Lysosome Targeted Photodynamic Therapeutic Agent for Integrated Imaging and Therapy in Cancer Cells

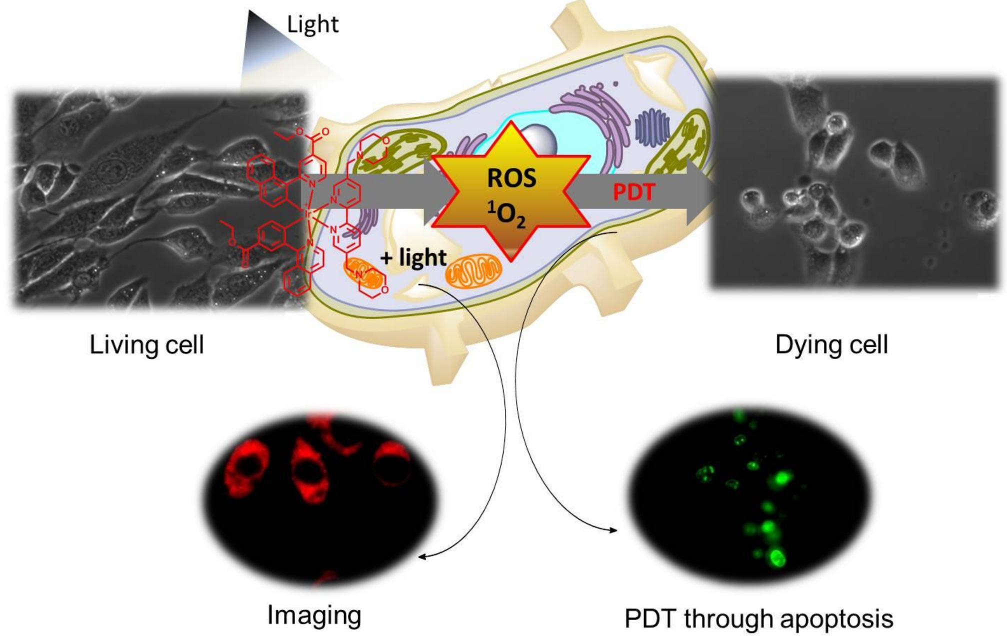

4.1 Abstract

Organelle targeted photosensitizers having luminescence properties are potential theranostic agents for simultaneous luminescence imaging and photodynamic therapy. Herein, we report a water soluble luminescent cyclometalated Ir(III) complex, ***Ir-Bp-Ly*** *as lysosome targeted theranostic probe.* ***Ir-Bp-Ly*** *exhibits exceptional photophysical properties of good triplet state quantum yield (0.90 in methanol), singlet oxygen generation quantum yield (0.71 at pH 4) and long lifetime (1.47μs). Interestingly,* ***Ir-Bp-Ly*** *localizes mostly in the lysosome because of the presence of morpholine units, suggesting its potential as a Lyso Tracker.* ***Ir-Bp-Ly*** *displayed notable PDT effect in C6 glioma cells, as these PS efficiently generated reacting oxygen species owing to the close proximity of energy levels corresponding to the triplet states of* ***Ir-Bp-Ly*** *and molecular oxygen ($^3O_2$). The*

mechanism of cell death was studied through caspase-3/7 and flow cytometry analysis that clearly established the apoptotic pathway.

4.2 Introduction

Photodynamic therapy is a minimally invasive treatment that destroys target cells when irradiated with light of a suitable wavelength in presence of oxygen and a photosensitizer, generating highly reactive singlet oxygen.[1] PSs are not restricted solely to therapeutic generation of singlet oxygen, they also tend to emit in the near infrared region which is useful for *in vivo* imaging.[2] A fluorescently detectable photosensitizer is beneficial for aiding in defining and adjusting parameters during PDT treatment. If the malignant tissue retains the PS, the target site will light up to provide opportunities for therapy and imaging.[3] The fluorescence/phosphorescence spectra of a PS may differentiate normal and malignant regions, acting as an image-guidance tool. Luminescent signatures may also be used as an optical biopsy, differentiating benign and malignant disease avoiding standard histological evaluation.[4]

Luminescent PSs can aid in determining its localization and degree of uptake by diseased tissue. The PS characteristics can be further exploited in PSs that are only active in the presence of a target molecule upon which luminescence and singlet oxygen production occur.[5] PSs that are not phototoxic outside activation or target sites would therefore be more useful as imaging probes due to a reduction in non-specific phototoxicity. Another utility of PSs is that they may be conjugated to agents from other imaging modalities. Radio-labeled PSs and magnetic resonance imaging (MRI) contrast agent-conjugated PSs are known in the literature which provide a multifunctional probe with the capabilities of two imaging modalities (fluorescence/phosphorescence imaging and positron emission tomography/MRI) as well as therapeutic function.[6] The schematic representation of a theranostic photosensitizer is given in the Figure 4.1.

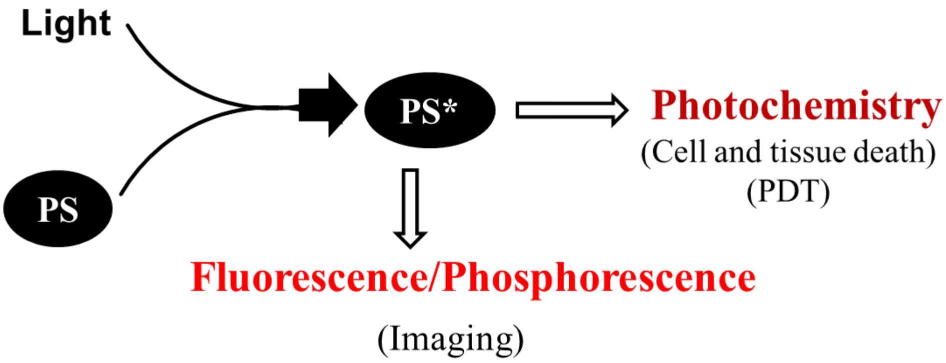

Figure 4.1: Schematic representation of PDT where PS is a photoactivatable multifunctional agent, which upon light activation can serve as both an imaging agent and therapeutic agent.

Recently, cyclometalated Ir(III) complexes have received much attention as potential theranostic agents. However, to date, a very few cyclometalated Ir(III) complexes are reported for specific imaging of the subcellular organelles including nucleus, cytoplasm, mitochondria, lysosome, endoplasmic reticulum, etc. along with therapeutic applications.[7] When these agents are specific to organelles, especially lysosomes, mitochondria, etc., which play crucial role in cell apoptosis, these offer an insight into intracellular dynamic.[8] Thus, targeted theranostic agents are suitable for widespread applications since the biological functions can be disrupted upon photo activation.[9]

The various methods used for organelle targeting are discussed in Chapter 1, section 1.6. In 2014, He *et al.*, have developed two Ir(III) complexes, **LysoIr1** (**1**) and **LysoIr2** (**2**) (Figure 4.2), as one- and two photon-excited theranostic agents.[10] It is found that both **1** and **2** show pH sensitive phosphorescence in disodium hydrogen phosphate/citric acid buffer solutions, which is ascribed to the protonation/deprotonation of the secondary amine of the indole rings on the β-carboline ligands. The authors then evaluated their pH-dependent emission properties in the two-photon mode. The maximum two-photon absorption cross-sections (δ_{max}, λ_{ex} = 810 nm) were measured to be 958 and 972 GM at pH 3.4 for **1** and **2**, respectively. The subcellular distribution was analyzed by calculating the Pearson's colocalization coefficient and which indicated lysosome selectivity.

Authors also show the specific visualization of lysosomes during the autophagic process in live cells without any additional labeling operations using **2**.

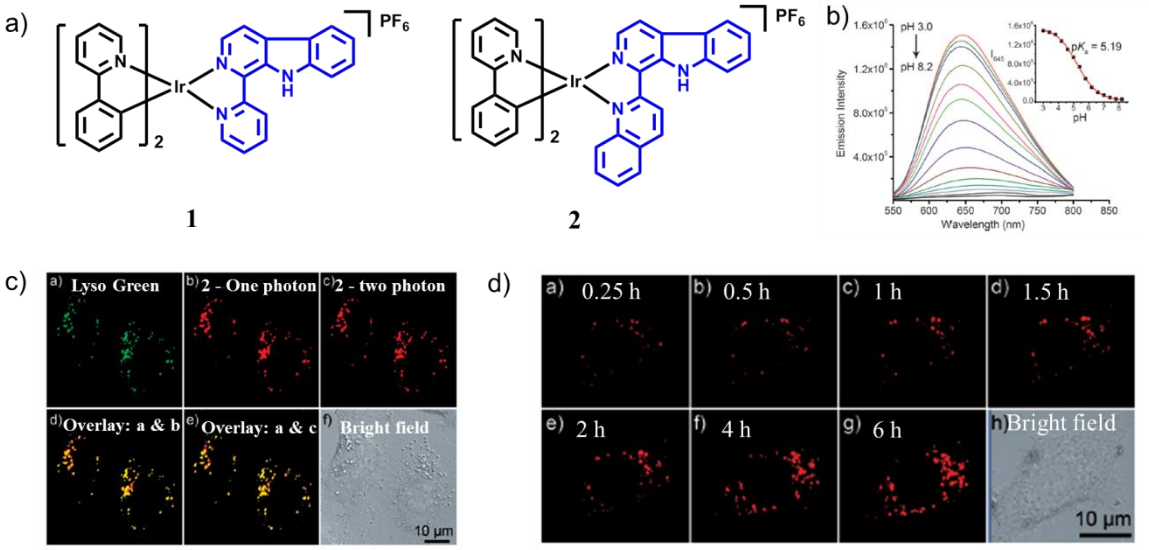

Figure 4.2: (a) Molecular structure of **1** and **2**; (b) pH-sensitive emission spectra of **2** (10 µm, λ_{ex} = 420 nm) in disodium hydrogen phosphate/citric acid buffer solutions. Inset: A plot of emission intensity of **2** at 645 nm versus different pH values; (c) One- and two-photon images of A549 cells co-labeled with **2** (10 µm, 1 h) and Lysotracker Green (150 nm, 0.5 h); (d) Two-photon excited real-time tracking of lysosomes in A549 cells stained with **2** (10 mm) at 37 °C for different time intervals.

In 2015, the same group reported four cyclometlated Ir(III)-β-carboline complexes with pH responsive singlet oxygen production and lysosome-specific imaging properties.[11] These complexes show enhanced phosphorescent emission and $^1O_2$ generation in tumor/lysosome-related acidic environments (pH < 6.5). For example, the phosphorescence quantum yield of **4** increased significantly from 0.019 at pH 7.4 to 0.092 at pH 3.0. The pH-sensitive emission of these complexes could be contributed by the protonation/deprotonation processes of the imidazolyl/benzimidazolyl-NH and the indolyl-NH on the β-carboline ligands, which cause pH-dependent switching from the interligand-charge-transfer (ILCT) state to highly emissive triplet ligand-to-ligand charge-transfer (^{3}LLCT)/triplet metal-to-ligand charge-transfer (^{3}MLCT) excited states. Unlike the ϕ_Δ of $[Ru(bpy)_3]Cl_2$ (bpy = 2,2'-bipyridine), which was almost constant at different pH values, the ϕ_Δ of **3-6** displayed a marked reliance on the pH of the solutions.

Notably, the ϕ_{Δ} of **4** increased from 0.05 at pH 7.4 to 0.51 at pH 3.0. The authors also demonstrated that **4**-mediated PDT induces a caspase-dependent apoptosis through lysosomal damage. The pH responsive phosphorescence of complex **4** was used to monitor the lysosomal integrity upon PDT, which provides a reliable and convenient method for *in situ* monitoring of therapeutic effect and real-time assessment of treated outcome.

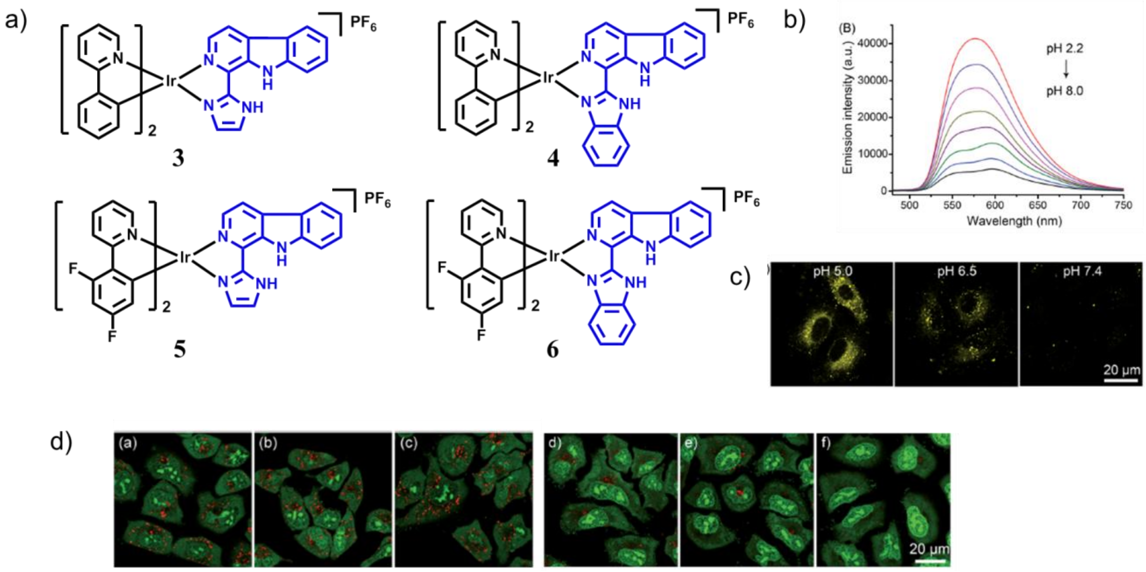

Figure 4.3: Chemical structures of lysosome targeting theranostic probes, **3**-**6**. (b) pH-sensitive emission spectra of **4** (20 µM, λ_{ex} = 405 nm). (c) pH-dependent phosphorescent images of **4**-labeled A549 cells (10 µM, λ_{ex} = 405 nm, λ_{em} = 580 ± 30 nm). (d) Observation of lysosomal disruption in A549 cells caused by **4**-mediated PDT by acridine orange (5 mM) staining.

Huang *et al.*, designed and synthesized two Ir(III) complexes, (**7**) and (**8**) that specifically stain the mitochondria and lysosomes of living cells.[12] Both complexes exhibited long-lived phosphorescence, which is sensitive to oxygen quenching. The luminescent quantum efficiencies of **7** and **8** were 0.13 and 0.15 in water, respectively. The singlet oxygen quantum yields of **7** and **8** were calculated to be 0.17 and 0.21 using methylene blue (MB; ϕ_{Δ} = 0.52 in DMF) as a standard. The photocytotoxicity of the complexes was evaluated under normoxic and hypoxic conditions. The results showed that HeLa cells treated with the mitochondria-targeted complex, **7** maintained a slower respiration rate, leading to a higher intracellular oxygen level under hypoxia. As a result, this complex exhibited an improved PDT effect compared to the lysosome-targeted complex, especially under hypoxia conditions, suggestive of a higher practicable potential of mitochondria-targeted PDT agents in cancer therapy.

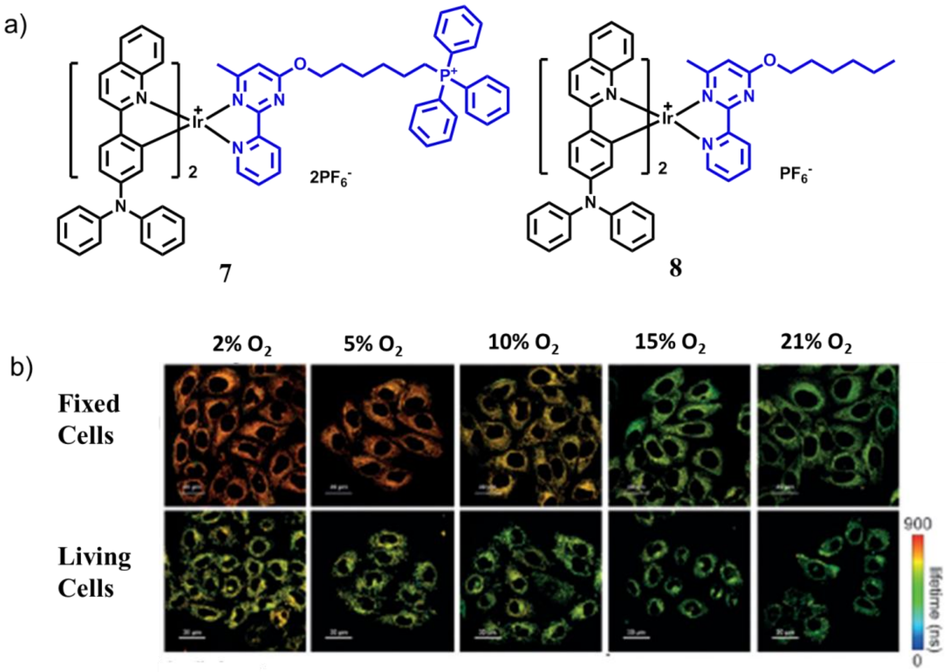

Figure 4.4: Chemical structure of mitochondria and lysosome targeting theranostic probes, **7** and **8**. (b) PLIM images of a) **7**-loaded fixed and living HeLa cells. The cells were incubated with the complexes (5 μm) at 37 °C for 12 h. The images were taken under different oxygen partial pressures. λ_{ex} = 405 nm, f = 0.5 MHz. All of the images share the same scale bar of 30 μm. Images were taken at 37 °C.

In 2016, Lim, Rhee, Kwon and coworkers have designed and synthesized four Ir(III) complexes and studied the effect of ligand on theranostic applications, **9-12** (Figure 4.5).[13] The Ir(III) complexes are effective as PDT agents at low concentrations with low-energy irradiation ($\leq$ 1 J cm^{-2}) because of the relatively high $^1O_2$ quantum yield (> 0.78), even with two photon activation. Based on the onset points of UV-Vis spectrum and the oxidation potentials measured by CV, the singlet energy levels and the corresponding energy band-gap were calculated. Authors compared the energy level of each of the four Ir(III) complexes and ground state oxygen ($^1O_2$) absorption to explain the efficiency of energy transfer. Furthermore, ϕ_p of the Ir(III) complexes was observed to be highly dependent on their ligands [**11** (0.53 ± 0.05) > **9** (0.46 ± 0.02) > **12** (0.11 ± 0.01) > **10** (0.011 ±

0.001)]. The singlet oxygen quantum yield was also found to vary largely depending on the ligands [**11** (0.95 ± 0.04) > **12** (0.78 ± 0.04) > **10** (0.37 ± 0.01) > **9** (0.32 ± 0.04)]. Apart from these, the tuning of emission from blue to NIR was also made possible by the authors by choosing appropriate ligands as shown in Figure 4.5. The complexes **11** and **12** effectively triggered the death of cancer cells through spatiotemporal cytotoxic activity *via* their ROS generation ability localized at the endoplasmic reticulum (ER), even under low concentration (≤ 2 μM) and weak light energy (≤ 1 J cm^{-2}). Additionally, **11** efficiently induced cancer cell death by two photon irradiation.

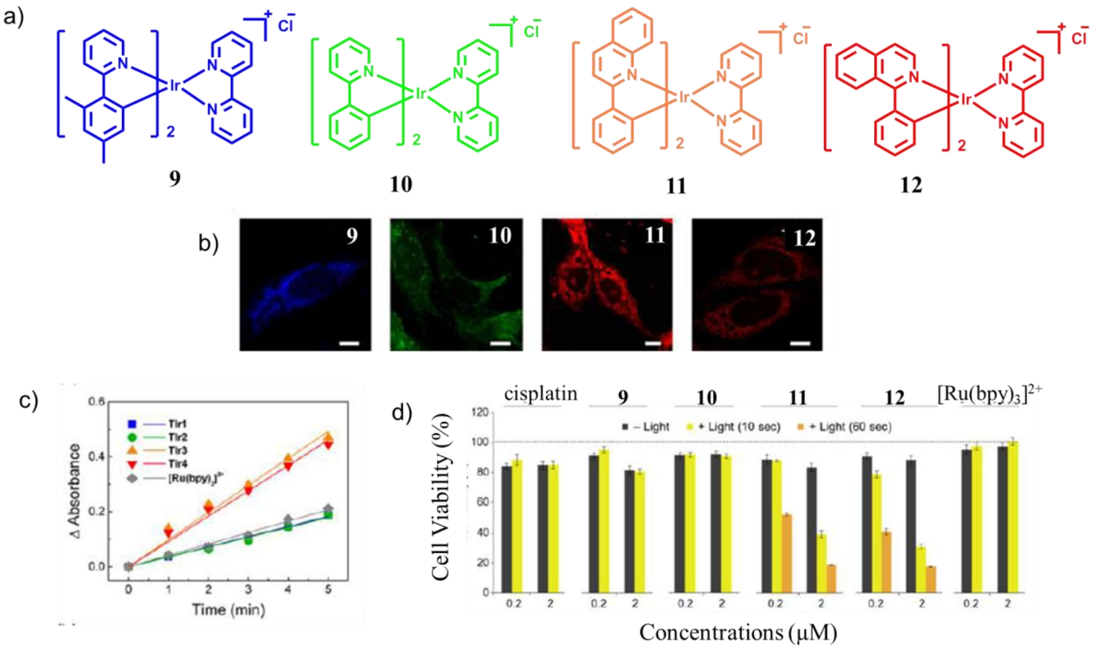

Figure 4.5: (a) Chemical structures of ER targeting probes **9-12**. (b) Two-photon optical imaging of **9**, **10**, **11**, and **12** using confocal laser scanning microscopy. Scale bar = 10 μm. (c) Singlet oxygen assay using the absorbance attenuation ($\Delta A = A_s - A_f$) of 9,10-anthracenediyl-bis(methylene)dimalonic acid (ABDA) under light exposure. The slope corresponds to the absolute amount of $^1O_2$. (d) Viability of human ovarian cancer SKOV-3 cells upon treatment with Ir(III) complexes, cisplatin, and $[Ru(bpy)_3]^{2+}$.

Apart from fluorescence or phosphorescence imaging techniques, life time imaging were also used along with theranostic probes.[14] Recently, modifications in the Ir(III) complexes helped to improve the quality of the probe. Generally Ir(III) complexes containing bipyridyl ligands are having inherent cationic nature and therefore without any further modification or targeting group, they are capable of localizing in mitochondria.[15] One of the recent works make use of coumarin-appended phosphorescent cyclometalated Ir(III) complexes for targeting mitochondria. These complexes have rich photophysical properties, which facilitates the study of their intracellular fate.[16] All the three complexes were found to specifically target mitochondria and show much higher antiproliferative activities than cisplatin against various cancer cells including cisplatin-resistant cells. The complexes **13-15** can penetrate into human cervical carcinoma (HeLa) cells quickly and efficiently, and they can carry out theranostic functions by simultaneously inducing and monitoring the morphological changes in mitochondria. Mechanistic studies showed that **13-15** exert their anticancer efficacy by initiating a cascade of events related to mitochondrial dysfunction. Genome-wide transcriptional and Connectivity Map analyses reveal that the cytotoxicity of complex **15** is associated with pathways involved in mitochondrial dysfunction and apoptosis.

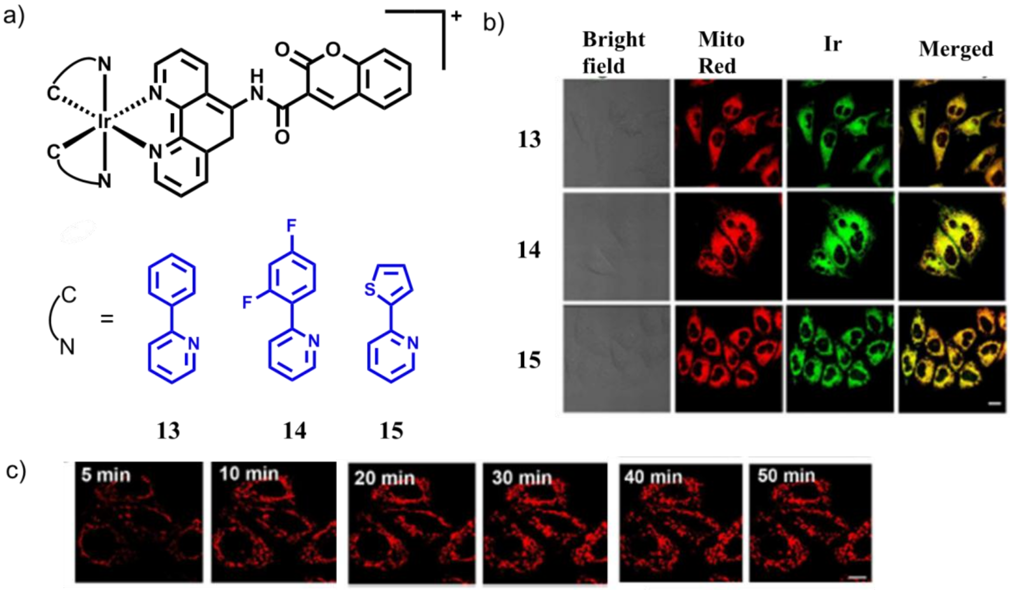

Figure 4.6: (a) Molecular structures of **13-15**. (b) Confocal microscopic images of HeLa cells colabeled with **13−15** (10 μM, 30 min) and MTDR (150 nM, 30 min). **13−15** were excited at 405 nm, MTDR was excited at 633 nm. The phosphorescence/fluorescence was collected at 600 ± 20 nm, 530 ± 20 nm, 630 ± 20 nm, 665 ± 20 and 668 ± 20 nm for **13**, **14**, **15** and MTDR respectively. Scale bar: 20 μm. (c) Real-time tracking of mitochondria in HeLa cells stained with 10 μM **15** at 37 °C for different time intervals. Scale bar: 10 μm.

The design and synthesis of organelle targeting probe for theranostic applications is a major area of research. The selection of ligands, targeting group, aqueous solubility, bio-compatibility and the photophysical properties of the probe are highly important to achieve the best outcome. With a thorough literature precedence, we designed a Ir(III) complex, **Ir-Bp-Ly**, having morpholine attached bipyridine ligand to target lysosome which can increase cellular uptake. Our probe gives a good triplet quantum yield and high singlet oxygen generation efficiency when compared with other reported lysosome targeting Ir(III) complexes in the lysosomal pH window (pH 4.5 -6).[10,11] The detailed cell imaging studies shows good value of Pearson's colocalization coefficient with Lyso Tracker Green and the cell death mechanism shows apoptotic pathway, which is highly desirable for PDT applications.

4.3 Results and Discussion

4.3.1 Synthesis and Characterization

Considering the requirement of an effective theranostic probe in aqueous medium with high triplet quantum yield, high ROS generation capability, specific imaging at subcellular level and cancer cell damaging capability upon light illumination , we have synthesized the **Ir-Bp-Ly** complex as shown in Scheme 4.1 and 4.2. For this purpose, the bipyridine ligand **18** was prepared by reacting the corresponding 5,5'-bis(bromomethyl)-2,2'-bipyridine with morpholine in reflux condition (Scheme 4.1). The cyclometalated intermediate Ir(III) dimer **22** was prepared as per the reported procedure.[13] Reaction of **18** and **22** in 3:1 (v/v) mixture of ethanol/DCM under argon atmosphere and reflux condition followed by anion exchange with NH_4PH_6 resulted in **Ir-Bp-Ly**. The purification was performed using silica gel column chromatography followed by precipitation in DCM/hexane mixture with 38% yield. The high resolution mass spectrum (HRMS), both in the positive (1099.37243 corresponding to $C_{56}H_{54}IrN_6O_6^+$; $[M]^+$) and negative (144.96452 corresponding to PF_6^-; $[M]^-$) mode was in agreement with the

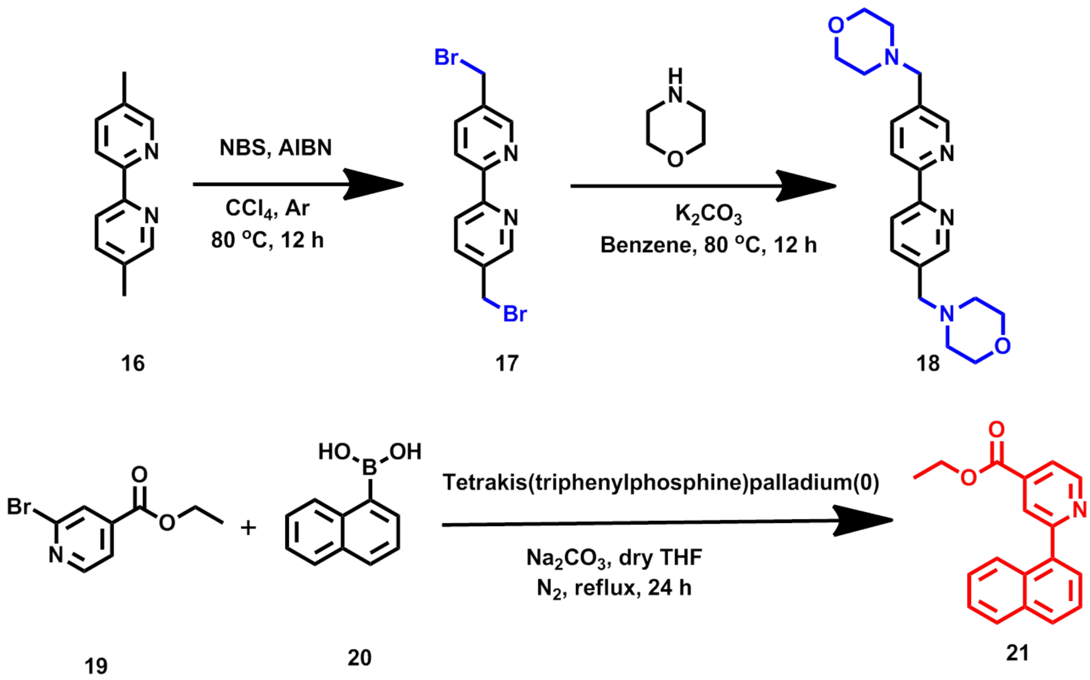

Scheme 4.1: Synthesis ligands **18** and **21.**

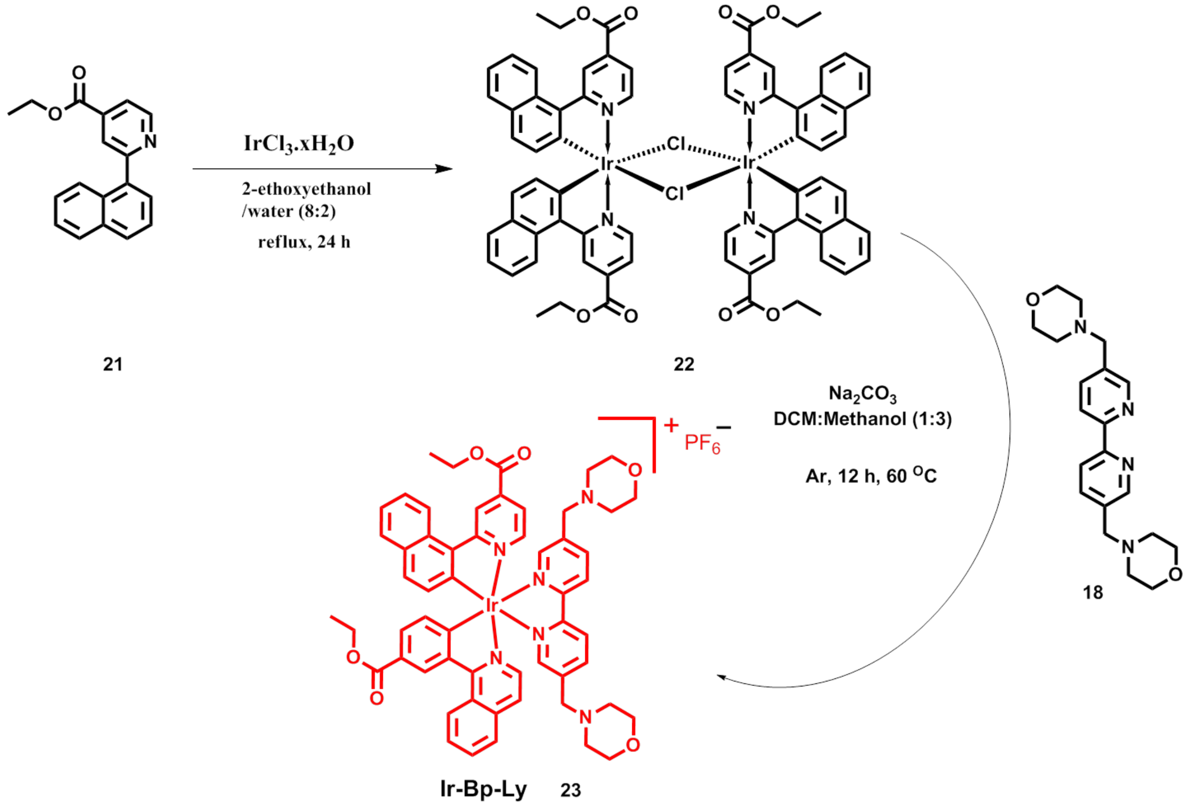

Scheme 4.2: Synthesis of complex **Ir-Bp-Ly.**

calculated values of 1099.37 and 144.96, respectively. The melting point of **Ir-Bp-Ly** was observed to be 195 ±1 °C. The elemental analysis was in good agreement with the calculated values as % C = 54.15 (54.06), % H = 4.83 (4.37) and % N = 6.71 (6.75), where the experimental value is given along with the calculated value in the bracket. ^{1}H NMR and ^{13}C NMR spectra of **Ir-Bp-Ly** were in agreement with their respective chemical structure.

The ligand 2-(naphthalen-1-yl)pyridine with ester functional groups were incorporated with Ir(III) center, for enhanced aqueous solubility. Furthermore, ancillary ligand, bipyridine attached morpholine units were integrated to render a cationic Ir(III) complex with aqueous solubility, efficient cellular uptake and subcellular localization.[17]

4.3.2 Photophysical Properties

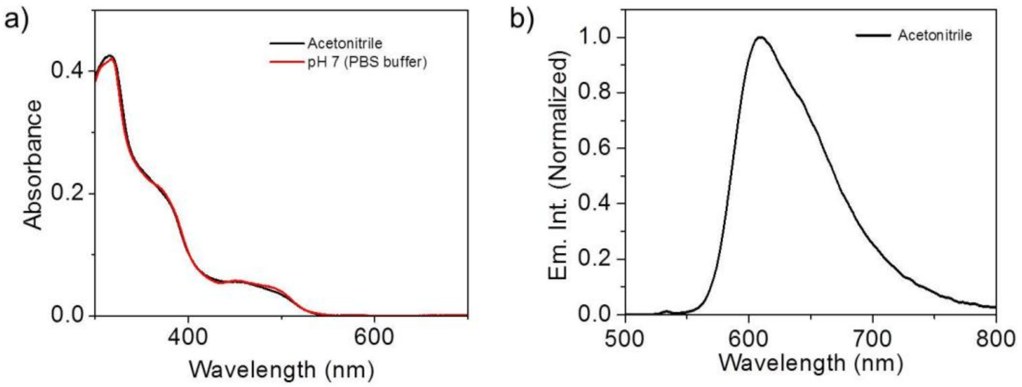

Figure 4.7: (a) Absorption of **Ir-Bp-Ly** in acetonitrile and PBS buffer (pH 7) and (b) Emission of **Ir-Bp-Ly** in acetonitrile (c = 10 μM, λ_{ex} = 460 nm).

The UV-Vis spectrum of **Ir-Bp-Ly** (c = 10 μM) exhibited strong absorption bands at 316 and 369 nm having extinction coefficients (ε) of 4.2 x 10^4 and 1.9 x 10^4 M^{-1} cm^{-1} respectively, which were assigned to spin-allowed ligand centered (^{1}LC) π-π* transition for cyclometalated (C-N) and ancillary (N-N) ligands, respectively (Figure 4.7). The relatively low-energy bands around 440 to 510 nm with the extinction coefficients (ε) of 6110-2124 M^{-1} cm^{-1} is attributed to the mixed singlet and triplet metal-to-ligand charge transfer (^{1}MLCT and ^{3}MLCT) and ligand-to-ligand charge transfer (LLCT) transitions.[18]

Ir-Bp-Ly exhibited a red emission in acetonitrile (615 nm) (Figure 4.7) and PBS buffer (620 nm) upon excitation at 465 nm (Figure 4.8). The long emission life time of 1.47 μs in acetonitrile can be ascribed to triplet emission from the complex. The emission intensity of **Ir-Bp-Ly** in acetonitrile was increased upon purging the solution (c = 10 μM) with argon suggesting the presence of dissolved molecular oxygen which favors triplet energy transfer (Figure 4.8).

The pH dependent luminescence spectra showed no remarkable change in emission intensity within lysosomal pH (Figure 4.8) indicating that the **Ir-Bp-Ly** is suitable for lysosome (pH 4.5 -5.5) imaging. The small change in luminescence intensity at pH 4 and 5 is due to the electron transfer to the protonated morpholine at lower pH as Chao and co-workers have explained in their recent publication.[19] The photoluminescence quantum yield of 0.11 ± 0.001 (absolute quantum yield) for **Ir-Bp-Ly** in PBS buffer (pH 7) proves that it is an effective bio-imaging agent in physiological conditions.

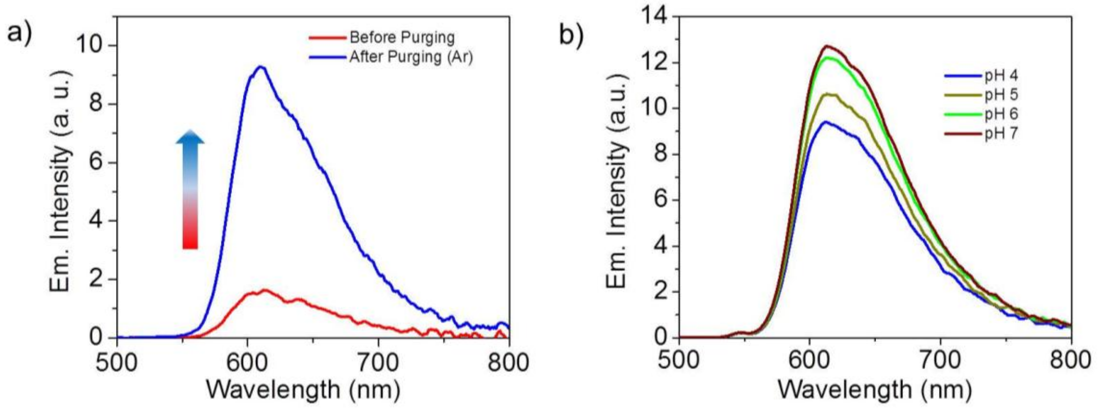

Figure 4.8: (a) The emission intensity change of **Ir-Bp-Ly** before and after purging with argon (purging for 10 minutes). (b) Emission spectra of **Ir-Bp-Ly** in different pH (4, 5, 6 and 7) (PBS buffer, c = 10 μM, λ_{ex} = 460 nm).

4.3.3. Energy Transfer Efficiency

Cyclic voltammetry measurements were performed to determine the oxidation potential and the HOMO of **Ir-Bp-Ly**. The HOMO was measured from the onset potential of the **Ir-Bp-Ly** complex with a ferrocene reference (inset in Figure 4.9) using the equation, HOMO = $-(E_{\text{onset of Ir(III)}}$ vs $E_{\text{onset of ferrocene}}) - 4.8$ eV. The energy band gap was measured from the onset peak of the absorption spectrum and the triplet energy level was obtained from the emission maximum. Two excitation states of singlet oxygen ($^1\Sigma g$ for 762 nm and $^1\Delta g$ for 1268 nm) associated to the absorption energy from ground state oxygen are presented in Figure 4.9.[13] The energy transfer efficiency was calculated from the triplet energy level and the singlet energy level as the complexes show high spin-orbit coupling and the calculated values are compared with the literature values.[13] From Figure 4.9, it is clear that, the energy difference of **Ir-Bp-Ly** is favorable for energy transfer to molecular oxygen that facilitates singlet oxygen generation.

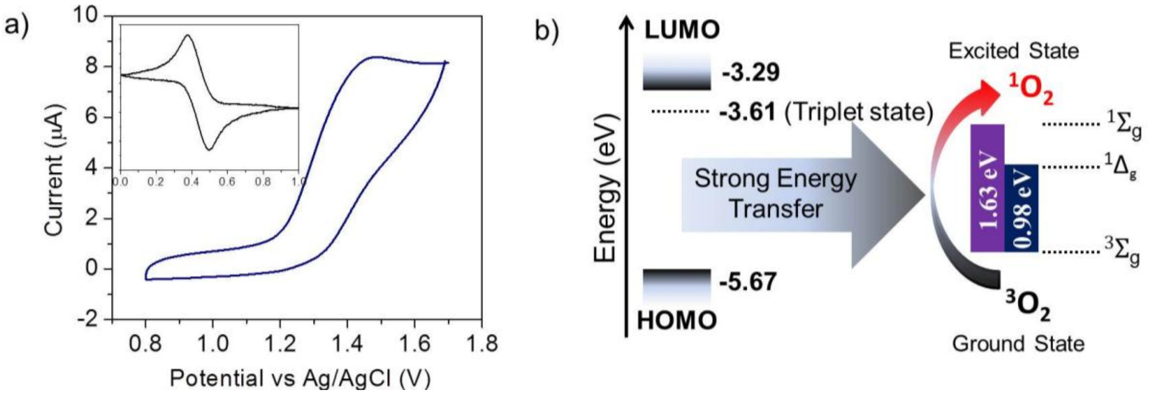

Figure 4.9: (a) Cyclic voltammetry analysis of **Ir-Bp-Ly** at a scan rate of 50 mV/s in tetrabutylammonium hexafluorophosphate electrolyte dissolved in acetonitrile. The inset is the CV of the reference ferrocene. (b) The calculated energy levels of HOMO, LUMO, triplet state (dashed line) of **Ir-Bp-Ly** and ground state oxygen ($^3O_2$) absorption.

4.3.4. Photostability

Photostability of the photosensitizer is a major concern for applying them in biological system. When irradiated with 450 nm band pass filter for 30 min with an interval of 5 min each, **Ir-Bp-Ly** exhibited a comparable photostability to the standard, $[Ru(bpy)_3]Cl_2$ (Figure 4.10) which is an advantage for imaging applications.

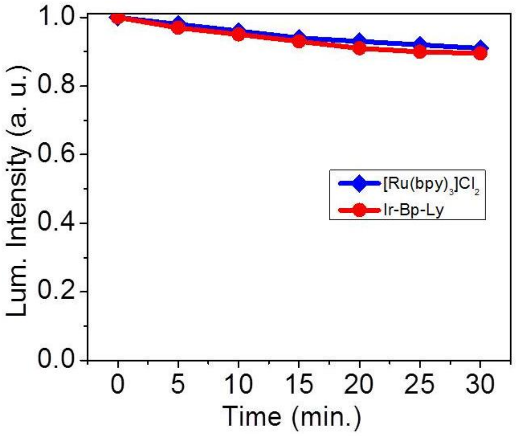

Figure 4.10: Photostability of **Ir-Bp-Ly** compared with the standard; $[Ru(bpy)_3]Cl_2$ at pH 4 and absorbance was monitored at 460 (λ_{irr} = 450 nm and t = 0 to 30 min)

4.3.5 Characterization and Quantification of the Triplet Excited States

Nanosecond transient absorption technique was used to investigate the triplet excited state absorption, lifetime and triplet state quantum yield.[20] The transient decay and the transient absorption peaks of **Ir-Bp-Ly** in acetonitrile (laser excitation 355 nm, 500 ns, 60 mJ per pulse) appeared at 410 and 550 nm as shown in the Figure 4.11.

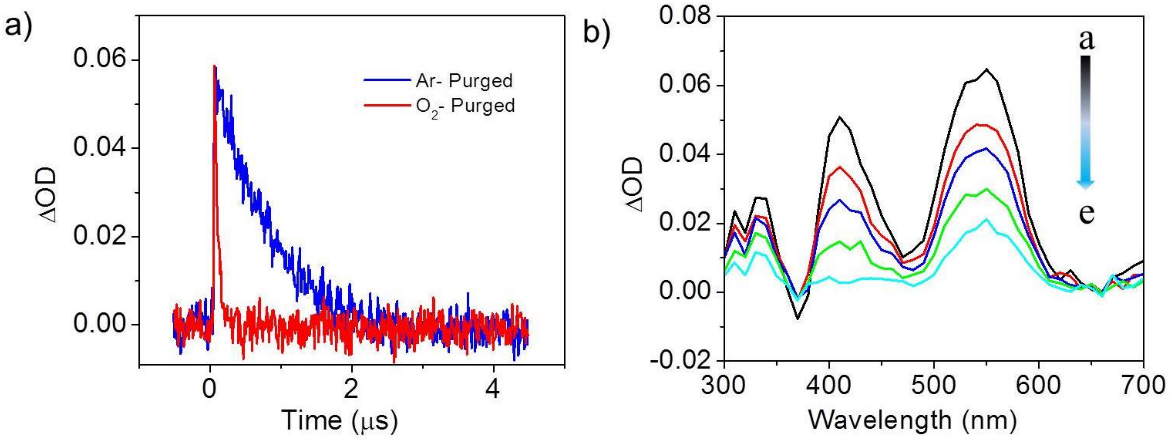

Figure 4.11: (a) The transient decay of **Ir-Bp-Ly** (10 μM) at 550 nm (Ar- purged) and the quenching of transient signal on purging with oxygen. (b) Transient absorption spectra of **Ir-Bp-Ly** (10 μM) following 355 nm laser pulse excitation; time resolved spectra recorded at a) 0.122, b) 0.322, c) 0.482, d) 0.752 and e) 1.142 μs.

The transient intermediate formed upon laser excitation decayed by a first-order process and led to the recovery of the ground-state absorption (Figure 4.11), thereby ruling out the formation of any permanent products and/or degradation of the molecule under these conditions. Also, it was observed that the dissolved oxygen readily quench the transient absorption, indicating that the transient species is generated from the triplet excited state. The triplet quantum yield was determined by the triplet-triplet energy transfer to β–carotene by using $[Ru(bpy)_3]Cl_2$ as the reference (ϕ_s = 0.90 ±0.005). The detailed experimental procedure is given in the experimental section.

4.3.6 Singlet Oxygen Generation and Quantification

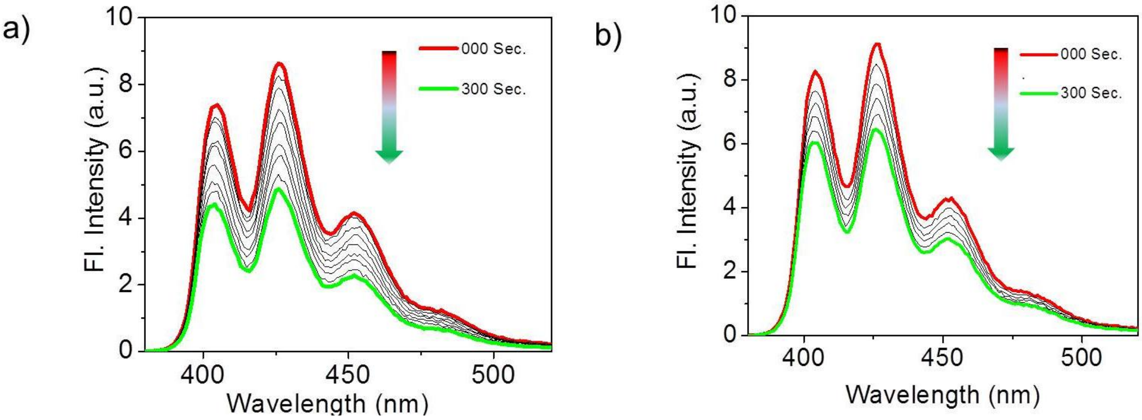

Figure 4.12: Emission change of DMA along with a) **Ir-Bp-Ly** b) $[Ru(bpy)_3]Cl_2$ (optically matched solutions) on irradiation using 420 nm long pass filter (λ_{ex} = 360 nm, $c_{(DMA)}$ = 10 μM).

The enhanced triplet quantum yield of **Ir-Bp-Ly** is favorable for the efficient singlet oxygen generation through energy transfer. Hence, we examined the efficacy of the **Ir-Bp-Ly** complex in comparison with the optically matched standard, $[Ru(bpy)_3]Cl_2$ (ϕ_Δ = 0.83) in acetonitrile. Figure 4.12 shows that the decrease in emission intensity at 425 nm of 9, 10-dimethyl anthracene is more for **Ir-Bp-Ly** when compared to the reference upon irradiation with 420 nm long pass filter for a period of 0-300 s.

The singlet oxygen quantum yield was calculated indirectly from the absorption change of DMA during irradiation along with **Ir-Bp-Ly** where

$[Ru(bpy)_3]Cl_2$ was taken as the standard having $\phi_\Delta = 0.84$ in methanol. The plot of ΔOD of DMA in presence of **Ir-Bp-Ly** against the irradiation time (Figure 4.13) showed very good linearity, indicating the efficiency of the complex for singlet oxygen generation. From the slope and singlet oxygen generation quantum yields (ϕ_Δ) of the reference sensitizer, we calculated the quantum yield of singlet oxygen generation of **Ir-Bp-Ly** to be 0.84 ± 0.005.

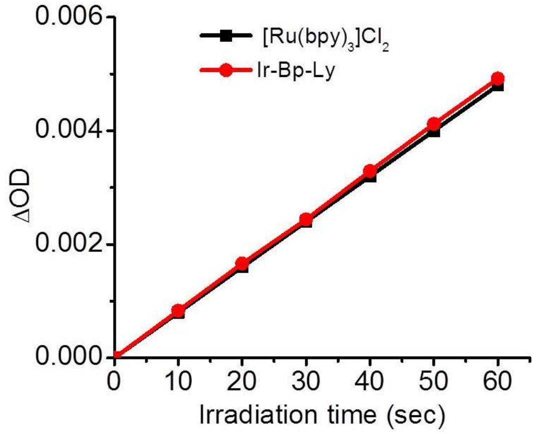

Figure 4.13: Singlet oxygen ($^1O_2$) assay using the absorbance attenuation ($\Delta A = A_s - A_f$) of DMA under light exposure (optically matched solutions of the complexes and $c_{(DMA)}$ = 10 μM).

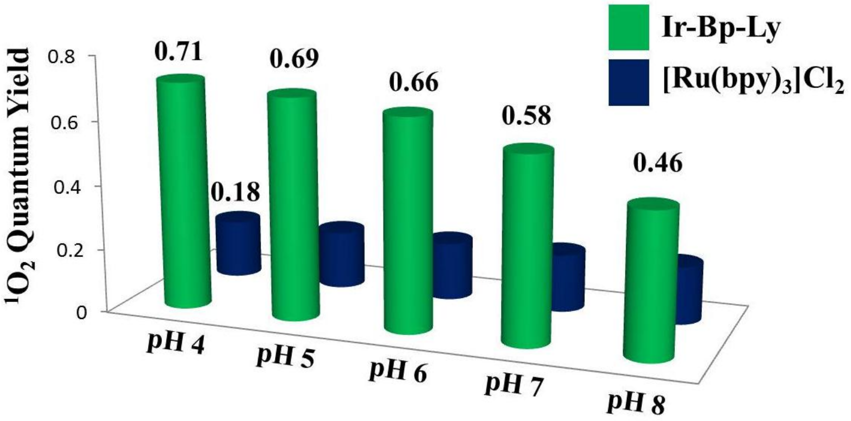

Figure 4.14: Singlet oxygen quantum values of **Ir-Bp-Ly** in different pH along with the standard. The calculation was done by monitoring the absorption change of ABDA on irradiation along with the optically matched solutions ($c_{(ABDA)}$ = 100 μM) (error limit = ± 0.005).

The singlet oxygen quantum yield of **Ir-Bp-Ly** was also evaluated in aerated buffer solutions (PBS buffer) using steady state method in which decrease in absorbance of 9,10-anthracenediyl-bis-(methylene)dimalonic acid (ABDA) was measured on irradiation and the values were compared with $[Ru(bpy)_3]Cl_2$ as the standard (Figure 4.14). The singlet oxygen quantum yield, Φ_Δ of $[Ru(bpy)_3]Cl_2$ was only 0.18, whereas the ϕ_Δ of **Ir-Bp-Ly** was observed to be very high (ϕ_Δ = 0.71 ± 0.01) within lysosomal pH windows (pH 4-5.5) on comparison with the literature values. Hence, **Ir-Bp-Ly** can photosensitize $^1O_2$ production more efficiently in the acidic environments of lysosomes and tumor tissues.

On increasing the pH, especially in the alkaline region, the singlet oxygen quantum yield was found to decrease. We did the DLS analysis and confirmed the formation of nanoparticles in the alkaline pH. Above pH 7, the protonation of morpholine nitrogen is disfavored which leads to the formation of aggregates as shown in Figure 4.15. Interestingly, these aggregates also generate singlet oxygen, although less when compared to that in acidic conditions. However, this does not limit the application of **Ir-Bp-Ly** since these are highly efficient in the acidic environment of lysosomes and tumor tissues where the pH is < 5.

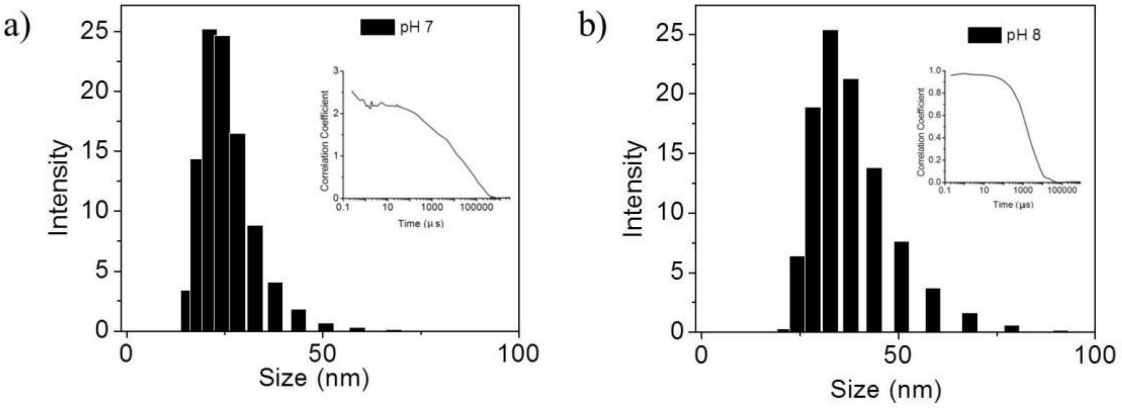

Figure 4.15: DLS analysis of **Ir-Bp-Ly** at pH 7 and 8 (c = 10 μM, PBS buffer)

The high efficiency of singlet oxygen production by **Ir-Bp-Ly** in the acidic region is again confirmed by the decay of ABDA in different pH as shown in Figure 4.16. The decay is high in the acidic pH when compared to the standard on irradiation experiment for about 30 min. The photostability of ABDA was measured by monitoring the emission maximum at 426 nm when irradiated using 420 nm long pass filter for 30 min at pH 5. From Figure 4.16, it is clear that ABDA is highly photostable.

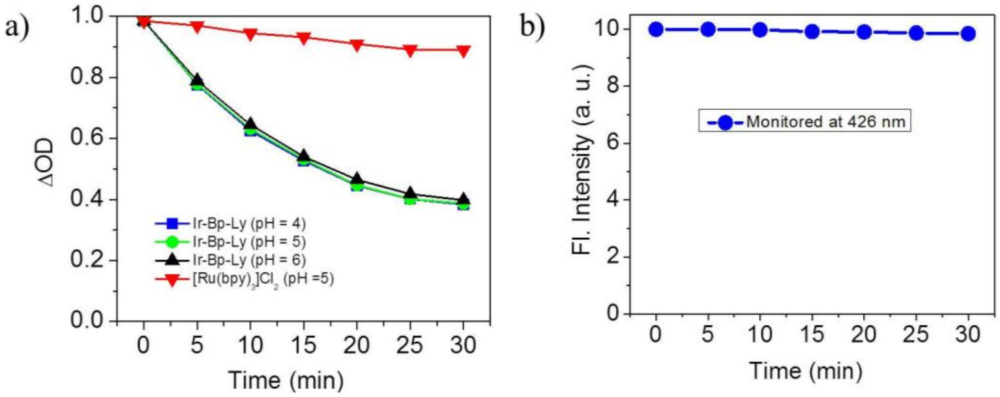

Figure 4.16: (a) Decay of ABDA (c = 100 μM) on irradiation in presence of optically matched solutions of Ir-Bp-Ly and $[Ru(bpy)_3]Cl_2$ at different pH (PBS buffer, t = 0-30 min). (b) Photostability of ABDA

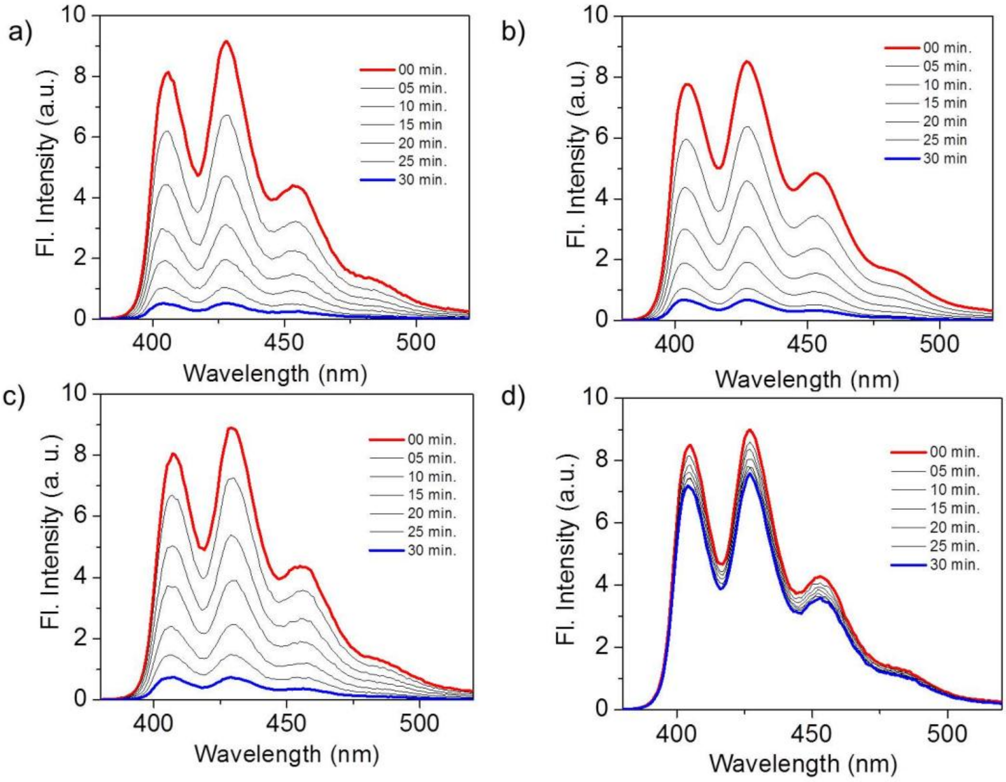

Figure 4.17: : The emission intensity change of ABDA on irradiation along with **Ir-Bp-Ly** at a) pH 4, b) pH 5, c) pH 6 and d) $[Ru(bpy)_3]Cl_2$ at pH 4 (λ_{ex} = 360 nm, $c_{(ABDA)}$ = 100 μM)

Emission intensity change of ABDA on irradiation in presence of **Ir-Bp-Ly** and $[Ru(bpy)_3]Cl_2$ at various time intervals from 0-30 min was studied. The singlet oxygen generation activity of **Ir-Bp-Ly** in the acidic pH was again confirmed by the quenching of emission intensity in the acidic region compared to the standard as shown in the Figure 4.17. Decay of ABDA in presence of $[Ru(bpy)_3]Cl_2$ is less in the acidic pH. It also confirms the higher activity of **Ir-Bp-Ly** in the aqueous media when compared to the standard.

In the biological environment, **Ir-Bp-Ly** can also undergo various interactions with the biomolecules which in turn can affect the efficiency of the PS. The activity of the probe was again checked in the presence of various biologically relevant analytes including metal ions (Zn^{2+}, Na^{+}, Fe^{3+} and Ca^{2+}), thiols (cysteine and homocystein) etc., however, no significant variation was observed (Figure 4.18).

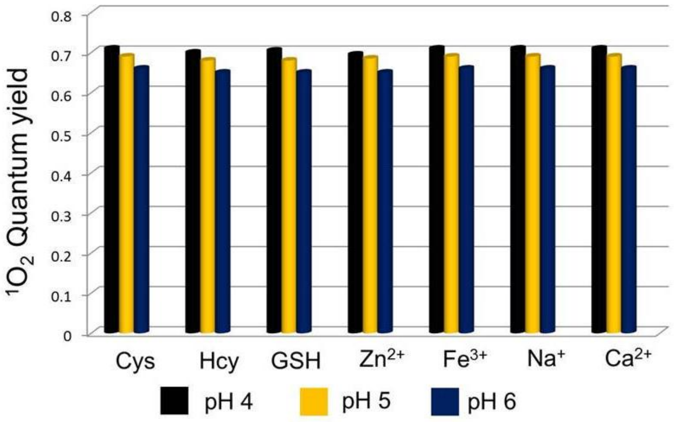

Figure 4.18: Singlet oxygen quantum yield values of **Ir-Bp-Ly** in presence of biologically relevant analysts (we checked metal ions like Mg^{2+}, Mn^{2+}, Cu^{2+}, Co^{2+}, K^{+} etc., and obtained similar results as shown above) at different pH values(error limit = ± 0.005).

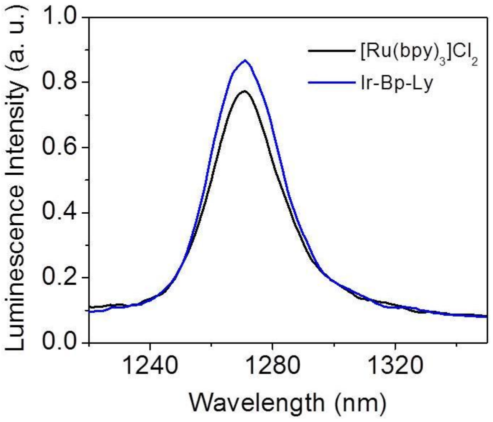

Figure 4.19: Singlet oxygen luminescence spectra in presence of **Ir-Bp-Ly** and $[Ru(bpy)_3]Cl_2$ (optically matched solutions) in acetonitrile (λ_{ex} = 465 nm).

To further confirm the singlet oxygen generation, we used a direct method by monitoring singlet oxygen luminescence at 1270 nm. For the direct measurement of singlet oxygen through NIR luminescence method, Fluorolog-3 spectrofluorimeter connected with an NIR detector and 450 W Xenon lamp as the light source was used. To obtain the singlet oxygen luminescence at 1270 nm in the steady-state, we prepared optically matched solutions of the **Ir-Bp-Ly** and a common reference sensitizer, $[Ru(bpy)_3]Cl_2$. The singlet oxygen generation was confirmed by the NIR emission at 1270 nm as shown in the Figure 4.19.

4.3.7 MTT Assay

The PDT efficacy of **Ir-Bp-Ly** was examined in C6 glioma cells using a 3-(4,5-dimethylthiazole-2-yl)-2,5-diphenyl tetrazolium bromide (MTT) assay and compared with a standard photoactivatable reagent, $[Ru(bpy)_3]^{2+}$. The standardization of laser power was done by evaluating the cell morphology changes and MTT assay as shown in the Figure 4.20. The cell morphology is preserved at a laser power of 0.25 W and slowly vanished on increasing power. The same result was confirmed by the MTT assay in each laser power. Based on the results, a power of 0.25 W was chosen for further studies (Figure 4.20).

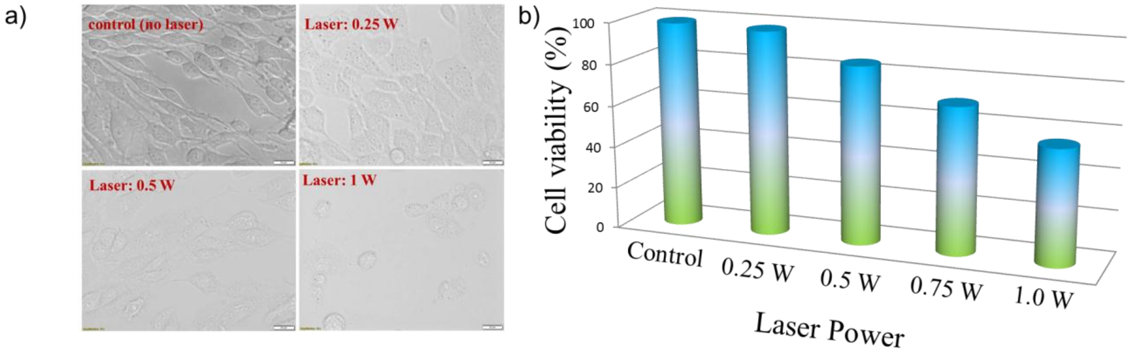

Figure 4.20: (a) The bright field images of C6 glioma cells on irradiation with different laser power at 532 nm. (b) Laser power dependent MTT assay (c = 1 μM) (error limit = ± 2%).

The optimum concentration of **Ir-Bp-Ly** for the cells to have minimum toxicity in the absence of light was checked through MTT assay. The concentration dependent MTT assay showed more than 97% cell viability up to a concentration of 1 μM, confirming the non-cytotoxicity of **Ir-Bp-Ly** at lower concentrations. However, on increasing the concentration, decreasing cell viability was observed even with 10 μM. Therefore, we choose lower concentration for imaging and therapeutic studies.

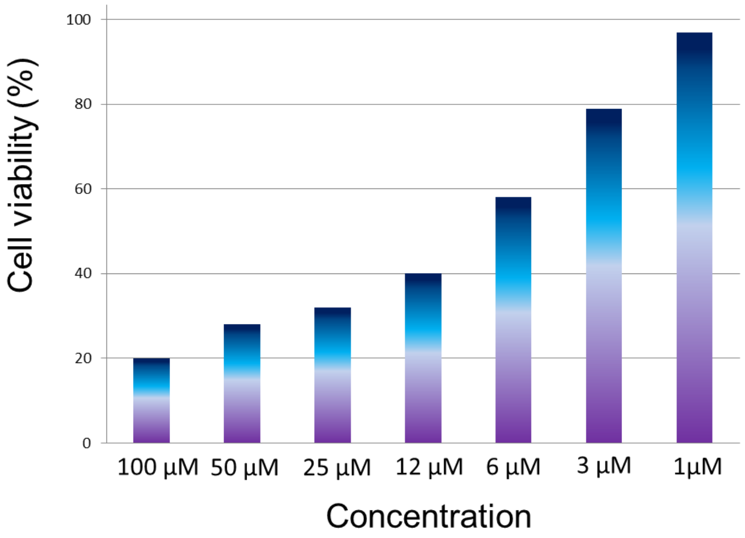

Figure 4.21: Cell viability of C6 glioma cells after 24 h incubation with **Ir-Bp-Ly** at different concentrations. Cells were cultured in DMEM (10% FBS) at 37 °C, at 5 % CO_2. Spectra were measured at 570 nm (error limit = ± 3%).

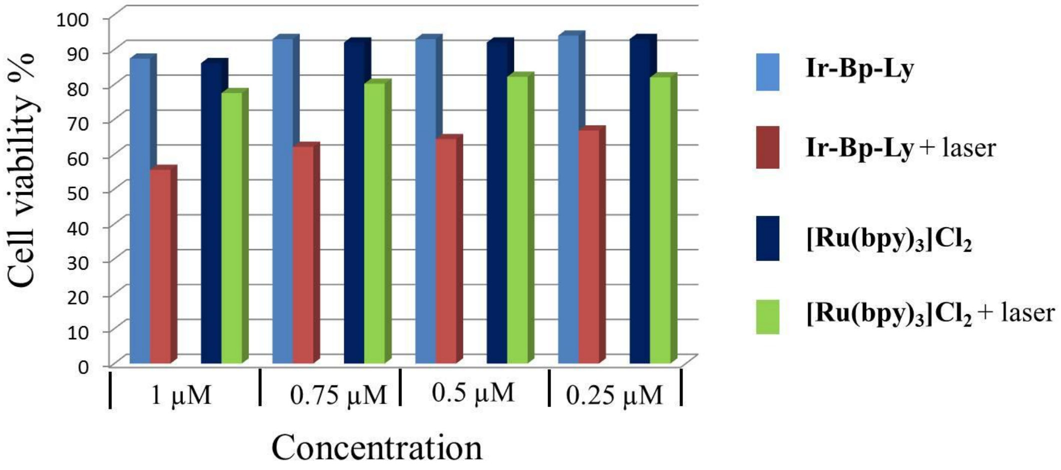

Figure 4.22: PDT effect evaluated by the MTT assay. Viability of C6 glioma cells upon treatment with different concentrations of **Ir-Bp-Ly** and $[Ru(bpy)_3]^{2+}$ (1, 0.7, 0.5 and 0.25 μM) in the absence and presence of laser (532 nm, 0.25 W) for 30 s (error limit = ± 3%).

The preliminary studies of the photosensitizer, **Ir-Bp-Ly** in the cellular system were performed with MTT assay on irradiation. It was observed that the cell viability at lower concentration of **Ir-Bp-Ly** at pH 7 was noticeably reduced to 60% upon 30 s of laser irradiation, due to photodynamic effect. Whereas the standard $[Ru(bpy)_3]^{2+}$ showed relatively high cell viability (80%) at similar conditions. Figure 4.22 shows the effect of laser in different concentrations of **Ir-Bp-Ly** and shows that, in lower concentrations also **Ir-Bp-Ly** is highly toxic on irradiation. Based on the above results we choose the concentration of 0.5 µM for further studies.

4.3.8 Cellular Uptake

After standardizing the optimal non-toxic concentration of **Ir-Bp-Ly**, cellular uptake efficiency with respect to time was assessed. From three different incubation times, the best uptake efficiency was observed to be 2 h incubation, when the concentration was 0.5 µM (Figure 4.23). For all the experiments hence forth, the material incubation time is chosen as 2 h and concentration as 0.5 µM.

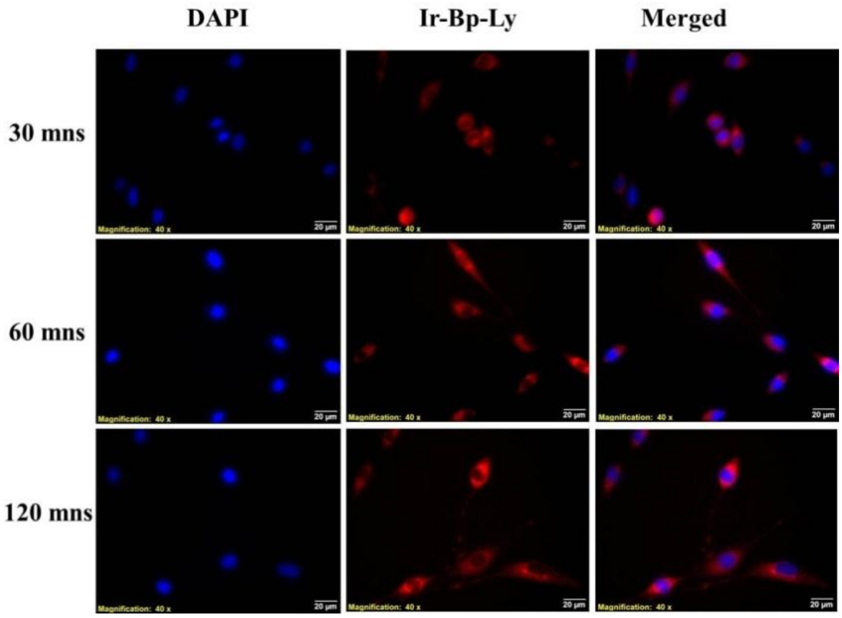

Figure 4.23: The time dependent uptake of **Ir-Bp-Ly** by C6 glioma cells at different time points (30 to120 min). First column shows the nuclear staining, second column with the probe and third one is the merged image.

4.3.9 Intracellular Localization

Subsequent to the cell uptake study, co-localization experiment was conducted to confirm the intracellular localization with Lyso-Tracker Green and Mito-Tracker Green. The results show that, **Ir-Bp-Ly** localizes mainly in the lysosome with a Pearson coefficient of 0.86 (Figure 4.24). We also compared the co-localization of **Ir-Bp-Ly** with Mito-Tracker Green to evaluate the specific subcellular targeting and the Pearson's correlation value, r = 0.28 (Figure 4.24b) clearly indicates that **Ir-Bp-Ly** rarely co-localize to mitochondria. The lysosomal localization of **Ir-Bp-Ly** will help to generate localized ROS, which causes for damaging the most important cell organelle, leading to the cancer cell death.

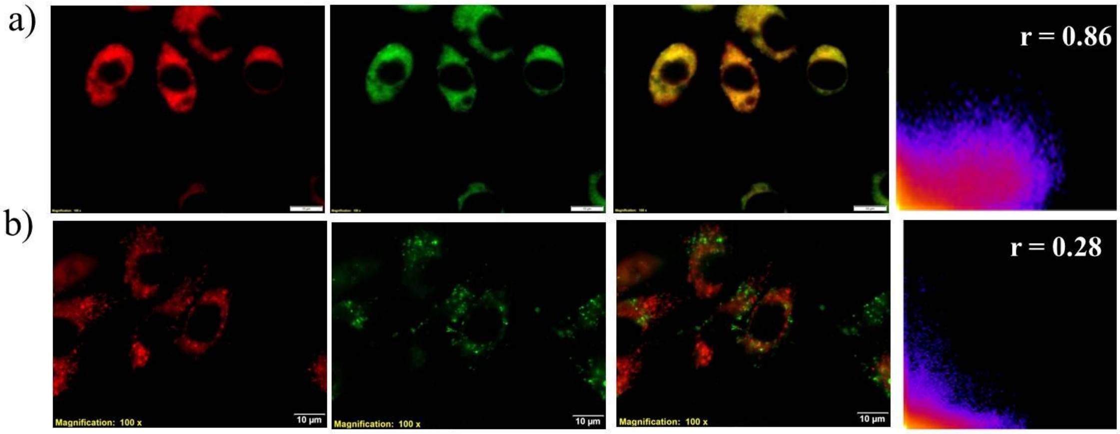

Figure 4.24: Co-localization study of **Ir-Bp-Ly** with a) Lyso Tracker Green and b) Mito Tracker Green. The merged images show good overlap with Lyso Tracker Green with a Pearson´s correlation coefficient, r = 0.86.

4.3.10 Reactive Oxygen Species Generation

After the intracellular localization is confirmed, the efficiency of ROS generation in the cells was evaluated using the optimized concentration and incubation period of the material. ROS generated by **Ir-Bp-Ly** with laser was detected using 2',7'-dichlorodihydro fluorescein diacetate (H_2DCFDA) staining.[21] The non-flourescent molecule, H_2DCFDA, upon reaction with the ROS present in cellular system converted to DCF which is green fluorescent in nature. Thus, the intracellular generation of ROS can be monitored by the green emission from DCF. As shown in the Figure 4.25, the green emission is absent in the control where the cell is incubated with **Ir-Bp-Ly** and H_2DCFDA only.

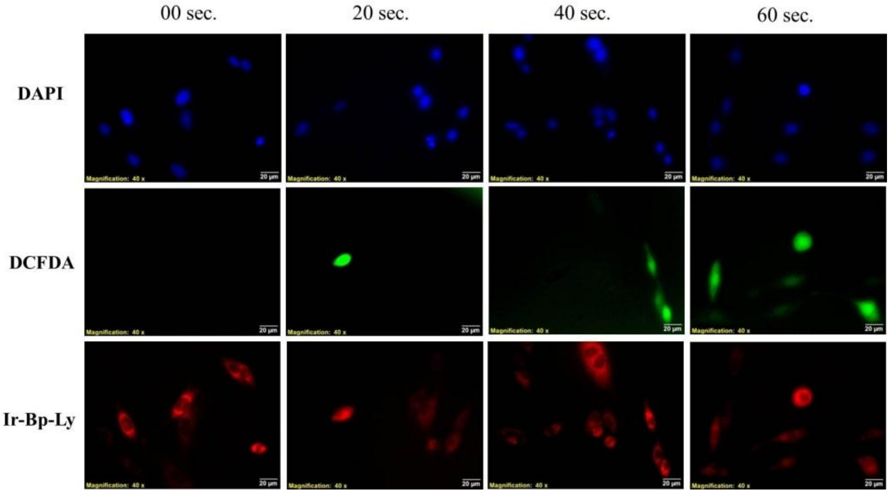

Figure 4.25: Singlet oxygen generation in the cellular level through DCFDA study. Time dependent increase in green emission shows that the increased production of singlet oxygen is proportional to duration of laser irradiation.

In the next stage, there was a gradual, but steady increase in ROS production within the cells proportional to the duration of laser irradiation from 20-60 seconds (Figure 4.25) facilitating PDT in cancer cells. Under control experiments without laser, no ROS production was observed suggesting that the developed **Ir-Bp-Ly** do not cause any stress to the cells, in the absence of laser. The quantitative measure of the emission intensity also showed increased activity on laser irradiation time (Figure 4.26)

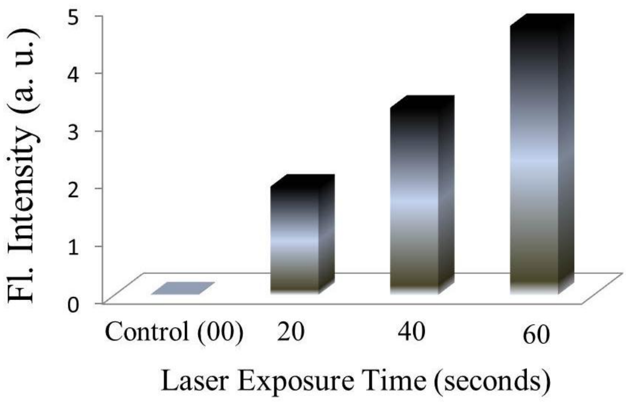

Figure 4.26: Quantitative analysis of fluorescence intensity obtained from DCFDA images. Gradual increase in the green fluorescence intensity is observed.

4.3.11 Nuclear Response- Cell Death Confirmation

On proving the ROS generation efficiency of **Ir-Bp-Ly**, its effect on cell nucleus was also evaluated by specifically staining the nucleus with Hoechst. The fluorescence intensity from the nucleus was observed to decrease after treatment with **Ir-Bp-Ly** and laser irradiation indicating a major nuclear damage which is a robust proof of progressive cell death. On the contrary, the control experiments (dark and **Ir-Bp-Ly** alone) showed negligible nuclear damage (Figure 4.27).

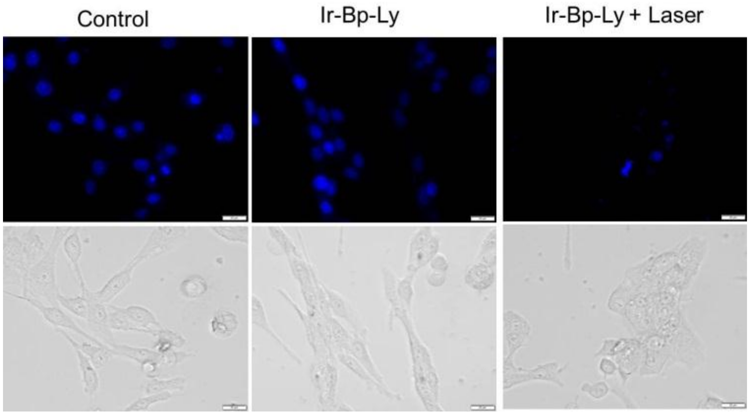

Figure 4.27: Confirmation of nuclear damage by Hoechst staining in C6 glioma cells; control, in presence of **Ir-Bp-Ly** and in the presence of **Ir-Bp-Ly** with laser irradiation. Corresponding bright field images are also shown.

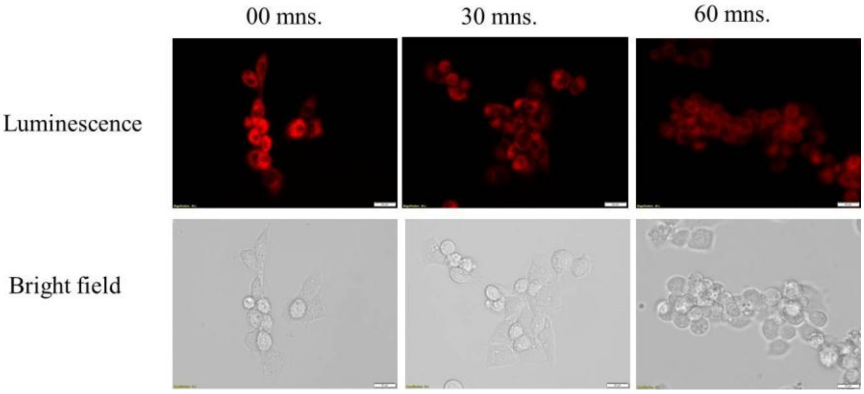

Figure 4.28: Time dependent luminescence change during PDT along with the bright field images using **Ir-Bp-Ly**.

The cell death was also monitored by the time dependent luminescence change and the corresponding bright field images after laser irradiation are shown in Figure 4.28. Both these results also suggest that **Ir-Bp-Ly** along with laser irradiation is capable of inducing cell death in cancer cells. Thus, **Ir-Bp-Ly** alone can be used to monitor the lysosomal integrity during apoptosis.

4.3.12 Mechanism of Cell Death

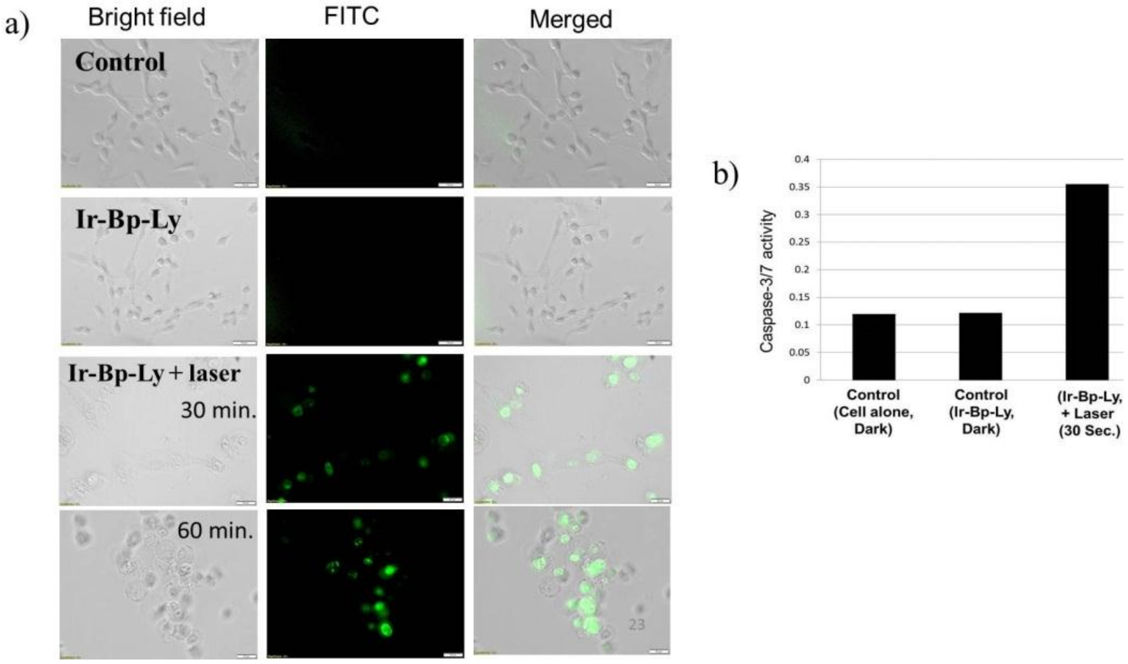

Figure 4.29: (a) Detection of caspase-3/7 activity in C6 glioma cells after treating with **Ir-Bp-Ly** in the absence and presence of light (c = 0.5 μM, 2 h). The time dependent fluorescence spectra were recorded with caspase-3/7 green detection reagent; cells were treated with 5 nM caspase-3/7 staining dye and imaging was done in specific time interval. (b) Quantitative detection of caspase-3/7 activity in C6 glioma cells after treatment with **Ir-Bp-Ly** in the absence and presence of light.

On laser irradiation, **Ir-Bp-Ly** exhibited high photodynamic activity in cancer cells. Encouraged by this observation, we have made an attempt to understand the cell death mechanism. Lysosomes are found to be involved in most of the crucial functions of any cells, such as macromolecular digestion, and any damage to these organelles can be fatal to the cell. The activation of caspase-3/7 protein was evaluated as it is identified as one of the key events in apoptosis. As compared with the control cells in the dark, noticeable increase in caspase-3/7 activity was detected in cells treated with **Ir-Bp-Ly** with irradiation. Similarly, the green emission from the nucleus was found to increase with the increasing irradiation time confirming the mechanism of cell death was through apoptosis. The increase in the fluorescence indicates that apoptosis progresses with time after laser irradiation.

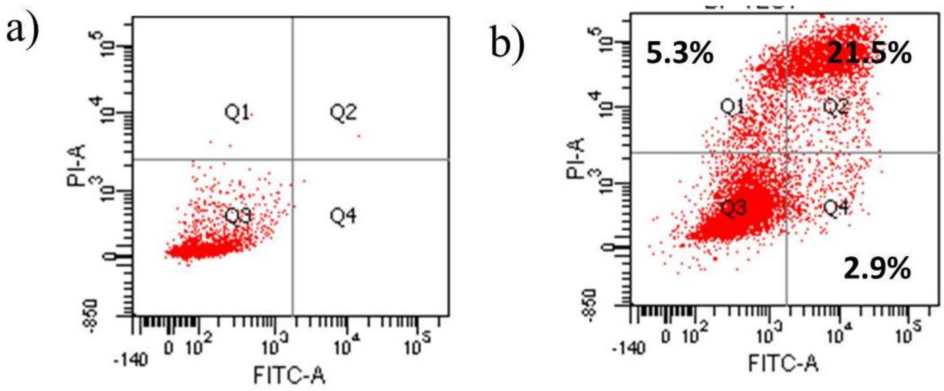

Figure 4.30: Flow cytometric quantification of annexin V and propidium iodide double-labeled C6 glioma cells treated with **Ir-Bp-Ly** for 2 h in the absence (a) and presence (b) of light (*c* = 0.5 μM).

A quantitative evaluation of caspase-3/7 activity in C6 glioma cells after treatment with **Ir-Bp-Ly** was also carried out in the same conditions. An increased green emission was also found from the **Ir-Bp-Ly** treated wells in the presence of light when compared to both the controls (Figure 4.29). Again, the activation of apoptosis in treated cells was quantified by flow cytometric analysis. The cells were double labelled with Alexa Fluor® 488 Annexin V/Dead Cell Apoptosis Kit. The data produced by the Fluorescence Assisted Cell Sorting (FACS) analysis showed highest percentage of late apoptotic cells on irradiation (t = 30 sec.) when compared with the dark control (Figure 4.30). This observation confirms the capability of **Ir-Bp-Ly** to induce apoptosis in cancer cells upon laser irradiation. On the contrary, the control cells showed very less number of apoptotic and necrotic cells.

The apoptotic pathway was again investigated through the live-dead cell assay. Figure 4.31 shows the fluorescence image from the cells in various conditions. The control shows only green emission since all the cells are alive. On treating with **Ir-Bp-Ly**, cells show red emission which is from the photosensitizer. After laser irradiation, since **Ir-Bp-Ly** is red emissive, the cell death is understood from the decrease in emission intensity in the green channel as shown in Figure 4.31.

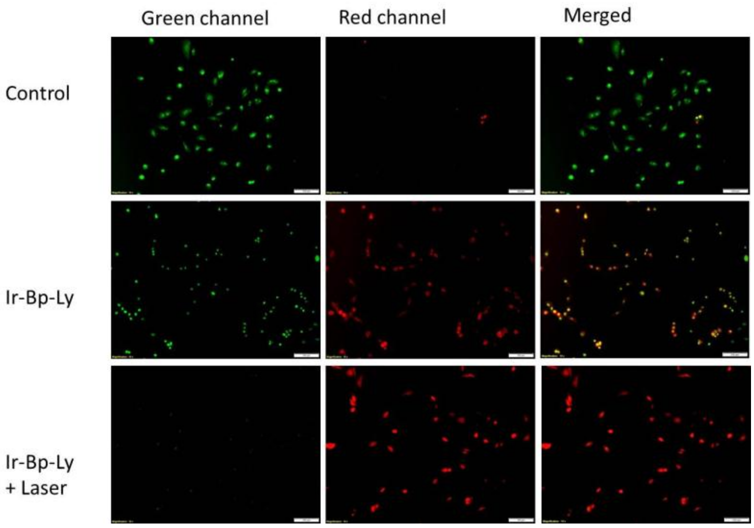

Figure 4.31: Live-dead assay of C6 glioma cells during PDT; control, **Ir-Bp-Ly** and **Ir-Bp-Ly** + laser. The decrease in green emission in the first column indicates the cell death.

4.4 Conclusions

We developed a water soluble cyclometalated Ir(III) complex, **Ir-Bp-Ly** as a PDT agent for cancer cells *via* suitable ligand design strategy. It exhibits high triplet quantum yield of 0.9 and efficient ROS generation because of photoexcited energy levels matching with molecular oxygen. The photophysics of **Ir-Bp-Ly** indicate its selective imaging applicability to lysosome and cell death through cytotoxic activity *via* localized ROS generation. The singlet oxygen quantum yield in acidic environment (ϕ_{Δ} = 0.71 at pH 4) shows its efficacy at lysosomal pH windows. In living cells, the **Ir-Bp-Ly** localizes specifically to the lysosome with minimum or no cytotoxicity at low concentration (≤ 0.25μM) and noticeable cytotoxicity was caused on laser irradiation due to the formation of ROS that leads to apoptosis. **Ir-Bp-Ly** mediated PDT studies in C6 glioma cells through fluorescent imaging and FACS analysis specify that the apoptotic cell death is through lysosomal and nuclear damage. Overall, this work provides new insights into the development of cyclometalated Ir(III) complexes as organelle targeted theranostic agents.

4.5 Experimental Section

4.5.1 Materials and methods

Unless otherwise stated, all starting materials and reagents were purchased from commercial suppliers (Sigma Aldrich, Alfa Aesar, Fluka, Merck or Spectrochem) and used without further purification. DAPI, Lyso Tracker Green and Mito Tracker Green were also purchased from Sigma Aldrich. Reactions were monitored using thin layer chromatography on silica gel 60 F254 (0.2 mm; Merck) using UV light source at 254 nm and 365 nm. Normal-phase chromatography was carried out using silica gel (particle size: 60-120 mesh and 100-200 mesh). ^{1}H-NMR spectra were recorded on Bruker Advance 500 NMR spectrometers, and chemical shifts are expressed in parts per million (ppm). Cell based assays and imaging were carried out in an Epifluorescent Inverted microscope (Olympus lX83 Inverted Fluorescence Microscope) at Division of Bio-photonics and Imaging Laboratory, Sree Chitra Tirunal Institute for Medical Sciences and Technology, Trivandrum. Acetonitrile used for photophysical measurements was dried over P_2O_5 and freshly distilled prior to use to ensure extreme dry condition. PBS buffer was used for pH dependent studies.

4.5.2 Synthesis and characterization

Synthesis of diethyl 5,5'-bis(bromomethyl)-2,2'-bipyridine (17)

To a solution of 5,5'-methyl-2,2'-bipyridine (**16**) (1.5 g, 10.85 mmol) in 50 mL of dry carbontetrachloride was added NBS (2.89 g, 16.2 mmol) and AIBN (100 mg). The reaction mixture was refluxed for 12 h at 80 ^oC. After the completion of the reaction, the mixture is filtered in the hot condition and the solvent was removed under reduced pressure. The crude product was then purified by column chromatography (SiO_2, 4% EtOAc/DCM) to give a white solid. Yield: 67%.

^{1}H NMR ($CDCl_3$, 500 MHz, TMS) δ (ppm): 8.68 (d, 2H, *J* = 2.5 Hz), 8.39 (d, 2H, *J* = 8 Hz, 7.85 (dd, 2H, *J* = 5.5 Hz, *J* = 2.5 Hz), 4.53 (s, 4H.); **^{13}C NMR** ($CDCl_3$, 125 MHz) δ (ppm): 153.25, 150.63, 129.42, 120.71, 35.21

Synthesis of 5,5'-bis(morpholinomethyl)-2,2'-bipyridine (**18**):

Compound **17** (400 mg, 1.1767 mmol) and activated K_2CO_3 (973 mg, 7.06 mmol) were taken in a 100 mL round bottom flask and 50 mL benzene was added. The mixture was stirred well for 10 min. Morpholine (4 mL, 4.706 mmol) was added and the mixture was refluxed for 12 h at 80 ^{o}C. The solvent was removed and product was purified by column chromatography (SiO_2, 4 % MeOH/DCM) to give light yellow colored solid. Yield: 76 %. **^{1}H NMR** ($CDCl_3$, 500 MHz, TMS) δ (ppm): 8.53 (d, 2H, *J* = 1.5 Hz), 8.27 (d, 2H, *J* = 8 Hz, 7.73 (dd, 2H, *J* = 6 Hz, *J* = 2 Hz), 3.65 (t, 8 H, *J* = 4.5 Hz), 3.50 (s, 4H), 2.41 (t, 8 H, *J* = 4.5 Hz); **^{13}C NMR** ($CDCl_3$, 125 MHz,) δ (ppm): 153.21, 150.45, 136.25, 129.44, 120.71, 66.72, 58.6, 35.72; **ESI MS**: MS Calcd for $C_{20}H_{26}N_4O_2$ is 354.21; Found 355.21

Synthesis of ethyl 2-(naphthalen-1-yl)isonicotinate (**21**):

One equivalent of ethyl 2-bromoisonicotinate (1 g, 4.346 mmol) with 1.2 equivalents of naphthalen-1-ylboronic acid (0.893 g, 5.216 mmol) and catalytic amount of tetrakis(triphenylphosphine)palladium(0) were dissolved in 25 mL of dry THF. A solution of 5% Na_2CO_3 (10 mL) was added and the mixture was refluxed with stirring for 24 h, under nitrogen atmosphere. After cooling, the mixture was poured into water and extracted with ethyl acetate. The organic layer was dried over Na_2SO_4. The solvent was removed under reduced pressure to give a crude residue. The crude product was then purified by silica column chromatography with ethyl acetate/ n-hexane (1: 9) as the eluent to give the final product. Yield = 70%.

^{1}H NMR ($CDCl_3$, 500 MHz, TMS) δ (ppm): 8.93 (dd, 1H, *J* = 4 Hz, *J* = 1 Hz), 8.15 (t, 1H, *J* = 1 Hz), 8.05 (t, 1H, *J* = 1 hz), 8.04 (d, 1H, *J* = 2 Hz), 7.93-7.88 (m, 3H), 7.62 (dd, 1H, *J* = 5.5 hz, *J* = 1.5 Hz), 7.52 – 7.46 (m, 2 H), 4.42 (q, 2H, *J* = 7 Hz), 1.40 (t, 3 H, *J* = 7.5 Hz); **^{13}C NMR** ($CDCl_3$, 125 MHz,) δ (ppm): 165.24, 160.34, 150.28, 138.33, 137.69, 133.95, 131.02, 129.05, 128.45, 127.73, 126.74, 126.03, 125.32, 125.29, 124.23, 121.18, 61.91, 14.23

Synthesis of dimer (**22**):

$IrCl_3{\cdot}xH_2O$ (224.36 mg, 0.75 mmol) and ethyl 2-(naphthalen-1-yl)isonicotinate (L1) (350 mg, 1.58 mmol) were dissolved in 20 mL of 2-ethoxyethanol and water (8:2) mixture and refluxed at 140 °C for 24 h. The solution was cooled followed by the addition of 40 mL of H_2O resulting in a reddish brown precipitate that was filtered and washed with diethyl ether. The crude product was used for the next reaction without further purification Yield: 55%).

Synthesis of the complex, Ir-Bp-Ly (23):

23 (1.0 eq.), **18** (2.6 eq.), and sodium carbonate (11.0 eq.) were stirred overnight in 1:3 dichloromethane /ethanol (40 mL) at 60 °C under argon atmosphere. The solvent was removed by evaporation under reduced pressure. The crude product obtained was poured into a solution of NH_4PF_6 in water and extracted with DCM (3 × 50 mL). The combined organic layers were dried over Na_2SO_4. A crude residue was obtained after removal of the solvent. The desired complex was obtained as an orange powder after the purification of crude product by silica column chromatography using DCM/methanol in a 9/1 ratio as an eluent. The product is then re precipitated in DCM/hexane. Yield: 38%.

^{1}H NMR (CD_3CN, 500 MHz, TMS) δ (ppm): 9.04 (d, 2H, *J* = 2Hz), 8.61 (d, 2 H, *J* = 8.5 Hz), 8.42 (d, 2 H, *J* = 8.5 Hz), 7.94 (dd, 4H, *J* = 5.5 Hz, J = 0.5 Hz), 7.85 – 7.83 (m, 4 H), 7.66 (dt, 2 H, *J* = 5.5 Hz, *J* = 1.5 Hz), 7.47 – 7.43 (m, 4 H), 7.41 (d, 2 H, *J* = 8 Hz), 6.46 (d, 2 H, *J* = 10.5 Hz, 4.44 (q, 4 H, *J* = 7 Hz), 3.37 – 3.01 (m, 10 H), 1.95 – 1.93 (m, 10 H), 1.42 (t, 6 H, *J* = 7.5 Hz); **^{13}C NMR** ($CDCl_3$, 125 MHz,) δ (ppm): 169.25, 164.01, 156.72, 154.33, 149.87, 149.61, 139.99, 139.26, 136.35, 131.80, 131.47, 130.11, 129.60, 128.03, 124.97, 124.08, 122.96, 121.77, 121.08, 66.36, 62.62, 59.14, 52.17, 14.22.;**ESI MS**: MS calcd. for $C_{56}H_{54}IrN_6O_6$, 1099.37; Found 1099.37243; $[M]^+$ MS Calcd. for PF_6, 144.96; Found 144.96452.

4.5.3 Measurements

Optical measurements

Electronic absorption spectra were recorded on a Shimadzu UV-2600 UV-Vis spectrophotometer and emission studies were performed on Horiba Fluorolog-3 Jovin Yoon. pH Changes were achieved by phosphate buffer and pH was adjusted by adding required amount of HCl/NaOH solution

4.5.4 Cell culture methods

4.5.4.1 C6 Cell line culture

C6 glioma cells are glial cells which is isolated from the brain tumor tissue of Rattus norvegicus. These cells were cultured using F-12K basal medium which was supplemented with 10% PBS and 1% anti-anti. After thawing from cryo-preservation, the cells were added to fresh medium to 5x dilution. Centrifugation at 3000 rpm for 3 min was done and the cell pellet was re-suspended in 1 mL of complete F-12K medium. This cell suspension was seeded into F-12K medium in a T-25 flask and incubated for 24 h in 5% CO_2 incubator at 37 ºC. After the specific incubation, the cells were observed for healthy growth. After reaching the specified confluency (80-90%), the cells were trypsinized using 0.25% (w/v) Trypsin - 0.53 mM EDTA solution. After 5 min incubation with trypsin at 37 ºC, the cells were collected by adding 1 mL of complete medium. The trypsinized cells were pipetted well to separate the individual cells. Centrifugation was carried out for 3 min at 3000 rpm to get the cell pellet. This pellet was again re-suspended in 1 mL of complete medium and was pipetted thoroughly. This cell suspension was used to seed the required flasks and plates.

4.5.4.2 MTT assay

C6 cells were seeded into 96 well plates and incubated for 24 h at 37 ºC. After incubation, the cells were added with different concentrations of our material of interest. The different concentrations of material used ranges from 0.25 μM to100 μM. The cells were incubated with these concentrations and were given 24 h of incubation in serum free medium. After this, the medium was replaced with 90 μL of fresh medium and 10 μL MTT reagent (5 mg/mL) was added. This combination was given 4 h incubation and after that the medium with MTT was removed. The wells were then added with 100 μL of DMSO and kept for 30 min incubation. The absorbance of color developed was then determined using micro plate reader at 570 nm.

4.5.4.3 MTT assay: laser power optimization

After culturing of C6 cells in 96 well plates, the cells were exposed to different powers (1.0, 0.75, 0.50, 0.25 W) of laser irradiations for 30 s each. After irradiation, the cells were allowed to incubate for 24 h. After the specific incubation, the cells were added with fresh serum free medium and MTT reagent was added along with it. 100 μL of DMSO was added to each well after the 30 min incubation with MTT reagent. The cells were allowed to develop color for 30 min and then read at 570 nm using a micro plate reader. Imaging of the cells after reading was also done after removing the DMSO and adding 1x PBS

4.5.4.4 MTT assay with laser irradiation

C6 cells were seeded into 96 well plates and then incubated for 24 h at 37 ºC. After incubation, the cells where added with 1.0, 0.75, 0.5, 0.25 µM concentrations of **Ir-Bp-Ly** and $[Ru(bpy)_3]Cl_2$. $[Ru(bpy)_3]Cl_2$ was used as a standard to compare the efficiency of our material. Incubation was done for 2 h and after that the medium was replaced with fresh medium. Then, 532 nm laser irradiation (0.25 W) was given to cell for 30 s and again incubation was carried out for another 30 min. 10 µL of MTT reagent (5 mg/mL) was added to all the wells and was incubated for 4 h. After the incubation of the MTT reagent, 100 µL of DMSO was added to all wells. After 30 min the absorbance was recorded at 570 nm using a micro plate reader.

4.5.4.5 Cellular uptake studies

Uptake efficiency of **Ir-Bp-Ly** was performed to standardize the time enquired for the maximum uptake of material by the cells. After 24 h incubation at 37 ºC, the cells were treated with 0.5 µM concentration of material at different time points. The treatments were given for 30, 60, 120 min. After each time point incubation, the fluorescence images of cells were captured using selective filter sets such as HcRED and DAPI in epifluorescence microscope.

4.5.4.6 Colocalization studies

Colocalization studies were carried out using both Mito Tracker Green and Lyso Tracker Green. The cells were seeded and cultured on glass cover slips and then incubated with **Ir-Bp-Ly** for 2 h in serum free medium. After incubation, the medium was replaced with fresh serum free medium and 5 µL of Lyso Tracker green. This was again kept for another 30 min. After the whole incubation, the cells were washed with PBS. The cover slips were then mounted on a clear glass slide using glycerin. The images were taken at 100 x using a fluorescent microscope.

4.5.4.7 Intracellular ROS generation

The cells were seeded into 6 well plates and incubated in a CO_2 incubator for 24 h. After incubation, 0.5 µM of **Ir-Bp-Ly** was added and incubated for 2 h. After incubation, the cells were washed with PBS and replaced with fresh serum free media. Then irradiation was given for different time intervals ranging from 20 - 60 sec. Without laser irradiation, a control was also maintained which contains **Ir-Bp-Ly** alone. After the irradiation, the cells were incubated for 30 mins at 37 ºC. Following this, 25 µM DCFDA reagent was added and incubated for another 30-45 minutes. Cells were then washed and colorless serum free media was added to wells. Images were taken to find out the different rates of ROS generation using a fluorescent microscope with available filter sets (FITC, HcRED and DAPI).

4.5.4.8 Nucleus (DAPI) staining

Cells were seeded in 4 well dish and provided with required incubation conditions and time. After the cells have grown to full size, material was introduced into two wells. After the 2 h material incubation, the medium containing the material was removed and given PBS washes. Laser irradiation was given to one of the wells with material incubated cells. DAPI stain was then added to all the wells and incubated for 10 min. Again PBS wash was given, then Fresh colorless serum free media was added and images were then taken at 40 x (DAPI).

4.5.4.9 Caspase-3/7 green detection – imaging

The cells were cultured in the specific culture conditions. After specific cell density was attained, the cells were incubated with **Ir-Bp-Ly** and exposed to laser (0.25W, 30 sec). After the treatments, the cells were given 30 min of incubation so that the cells could start apoptosis. After this incubation, the cells were treated with 5 nM concentration of caspase-3/7 staining dye. After 30 mins incubation, cells were washed and imaged (40 x, FITC, BF).

4.5.4.10 Caspase-3/7 green detection – quantitative

The cells were cultured in 96 well plate and when the required cell density was attained, experiments were carried out. The test wells were treated with optimum concentration of material and irradiated with 0.25 W; 532 nm laser for 30 sec. In order to compare the result, a control with cell alone and cell treated with **Ir-Bp-Ly** (without laser irradiation) were also incubated. After the incubation, all the wells were washed with 1 x PBS and added with serum free media along with caspase-3/7 dye. After 30 min incubation with dye, the plate was read for fluorescence emission using a micro plate reader (excitation 350 ± 20 nm, emission 440 ± 20 nm).

4.5.4.11 Flow cytometry analysis

Alexa Fluor® 488 Annexin V/Dead Cell Apoptosis Kit was used to carry out this analysis and the protocol was followed as prescribed by the manufacturer. Cells were seeded into culture dish (6 well plates) and then incubated for 24 h to attain complete growth. Afterwards, the cells were given a media change and **Ir-Bp-Ly** was added to 4 wells out of the 6 wells. The remaining 2 wells were considered as control. After the material incubation for 2 h, the cells were washed with PBS and again fresh media was added. All the 4 wells with material added were irradiated with 532 nm laser for 30 s. The cells were then collected and washed with PBS using centrifugation and suspended in 100 µL of 1x binding buffer. The suspension of cells was then added with 5 µL of annexin V conjugate and 2 µL of PI (100 µg/mL). The cells were then incubated for 15 min at 37 ºC. After incubation, the cells were washed with 1x binding buffer and again suspended in 500 µL of 1x binding buffer. The cells were then analyzed using FACS.

4.5.4.12 Live-dead cell assay

The specific cell line was seeded into culture plates and allowed to grow for 24 h at standard culture conditions. After the growth period, the cells were added with the optimum concentrations of **Ir-Bp-Ly** and given 2 h incubation in serum free media. A cell alone and with material (without laser) was also incubated. The test well was irradiated with 532 nm laser for 30 s and again kept for incubation for 30 min. Fresh serum free media along with acridine orange- propidium iodide mixture (1:1 in 1x PBS) was added and incubated. After incubation, the cells were washed and imaged under fluorescence microscope.

4.6 References

(1) (a) Dougherty, T. J.; Grindey, G. B.; Fiel, R.; Weishaupt, K. R.; Boyle, D. G. *J. Natl. CancerInst.* **1975,** *55*, 115–121. (b) Dougherty, T. J.; Kaufman, J. E.; Goldfarb, A.; Weishaupt, K. R.; Boyle, D.; Mittleman, A. *Cancer Res.* **1978**, *38*, 2628–2635. (c) Kelly, J. F.; Snell, M. E.; Berenbaum, M. C. *Br. J. Cancer* **1975**, *31*, 237–244. (d) Kelly, J. F.; Snell, M. E. *J. Urol. 1976*, **115**, 150–151. (e) Dougherty, T.; Gomer, C.; Henderson, B.; Jpri, G.; Kessel, D.; Korbelik, M.; Moan, J.; Peng, Q. *J. Nat. Cancer Inst*. **1998**, *90*, 889-905. (f) Dolmans, D.; Fukumura, D.; Jain, R. K. *Nat. Rev. Cancer* **2003**,*3*, 380–387.

(2) Lovell, J. F.; Liu, T. W. B.; Chen, Juan; Zheng, G., *Chem. Rev*. **2010**, *110*, 2839–2857.

(3) (a) Wilson, B. C.; Patterson, M. S. *Phys. Med. Biol*., **2008**, *53*, R61–109. (b) Josefsen, L. B.; Boyle, R. W. *Met. Based Drugs* **2008**, *2008*, 276109–276133.

(4) Lovell, J. F.; Zheng, G. *J. Innov. Opt. Health Sci*. **2008**, *1*, 45–61.

(5) Mehraban, N.; Freeman, H. S. *Materials* **2015**, *8*, 4421-4456.

(6) (a) Vaidya, A.; Sun, Y.; Ke, T.; Jeong, E.; Lu, Z. *Magn. Reson. Med*. **2006**, 56, 761-767. (b) Pandey, S. K.; gryshunk, A. L.; Sajjad, M.; Zheng, X.; Chen, Y.; Abouzeid, M. M.; Morgan, J.; Charamisinau, I.; Nabi, H. A.; Oseroff, A.; Pandey, R. K. *J. Med. Chem*. **2005**, *48*, 6286-6295.

(7) (a) Chen, Y.; Qiao, L.; Ji, L.; Chao, H. *Biomaterials* **2014**, *35*, 2–13. (b) Qiu, K.; Huang, H.; Liu, B.; Liu, Y.; Huang, Z.; Chen, Y.; Ji, L.; Chao, H. *A. C. S. Appl, Mater. Interfaces* **2016**, *8*, 12702–12710. (c) Li, S. P.-Y.; Lau, C. T.-S.; Louie, M.-W.; Lam, Y.-W.; Cheng, S. H.; Lo, K. K.-W. *Biomaterials* **2013**, *34*, 7519–7532. (d) Cao, R.; Jia, J.; Ma, X.; Zhou, M.; Fei, H. *J. Med. Chem*. **2013**, *56*, 3636–3644. (e) Mandal, S.; Poria, D. K.; Ghosh, R.; Ray, P.S.; Gupta, P. *Dalton Trans*. **2014**, *43*, 17463–17474. (f) Ho, C.-L.; Wong, K.-L.; Kong, H.-K.; Ho, Y.-M.; Chan, C. T.-L.; Kwok, W.-M.; Leung, K. S.-Y.; Tam, H.-L.; Lam, M. H.-W.; Ren, X.-F.; Ren, A.-M; Feng, J.-K.; Wong, W.-Y. *Chem. Commun*. **2012**, *48*, 2525–2527. (g)

Qiu, K.; Chen, Y.; Rees, T. W.; Ji, L.; Chao, H. *Coord. Chem. Rev*. **2016**, *310,* 16–40.

(8) (a) Fulda, S.; Galluzzi, L.; Kroemer, G. *Nat. Rev. Drug. Discovery* **2010**, *9*, 447-464. (b) Kromer, G.; Jaattela, M. *Nat. Rev. Cancer* **2005**, *5*, 886-897. (c) Pieczenik, S. R. *J. Neustadt, Exp. Mol. Pathol*. **2007**, *83,* 84–92. (d) Appelqvist, H.; Waster, P.; Kagedal, K.; Ollinger, K. *J. Mol. Cell Biol*. **2013**, *5*, 214–226. (e) Safting, P.; Klumperman, J. *Nat. Rev. Mol. Cell Biol*. **2009**, *10*, 623–635.

(9) (a) Ackroyd, R.; Kelty, C.; Brown, N.; reed, M. *Photochem. Photobiol*. **2001**, *74*, 656–.669. (b) Georgakoudi, I.; Solban, N.;Novak, J.; Rice, W.; Wei, X.; Hasan, T.; Lin, C. *Cancer Res*. **2004**, *64*, 5044–5047. (c) Zheng, X.; Sallum, U. W.; Verma, S.; Athar, H.; Evans, C. L.; Hasan, T. *Angew. Chem. Int. Ed*. **2009**, *48*, 2148–2151. (d) Borle, F.; radu, A.; Monnier, P.; van den Bergh, H.; Wagnieres, G. *Photochem. Photobiol*. **2003**, *78,* 377–383. (e) Celli, J. P.; Spring, B. Q.; Rizvi, I.; Evans, C. L.; Samkoe, K. S.; Vema, S.; Pogue, B. W.; Hasan, T. *Chem. Rev*. **2010**, *110*, 2795–2838.

(10) He, L.; Tan, C.-P.; Ye, R.-R.; Zhao, Y.-Z.; Liu, Y.-H.; Zhao, Q.; Ji, L.-N.; Mao, and Z.-W. *Angew. Chem. Int. Ed*. **2014**, *53*, 12137 –12141.

(11) He, L.; Li, Y.; Tan, C.-P.; Ye, R.-R.; Chen, M.-H.; Cao, J.-J.; Ji, L.-N.; Mao, Z.-W. *Chem. Sci*. **2015**, *6*, 5409–5418.

(12) Lv, W.; Zhang, Z.; Zhang, K. Y.; Yang, H.; Liu, S.; Xu, A.; Guo, S.; Zhao, Q.; Huang, W. *Angew. Chem. Int. Ed*. **2016**, *55*, 9947 –9951.

(13) Nam, J. S.; Kang, M.-G.; Kang, J.; Park, S.-Y.; Lee, S. J. C.; Kim, H.-T.; Seo, J. K.; Kwon, O.-H.; Lim, M. H.; Rhee, H. W.; Kwon, T.-H. *J. Am. Chem. Soc*. **2016**, *138*, 10968−10977.

(14) Shi, H.; Sun, H.; Yang, H.; Liu, S.; Jenkins, G.; Feng, W.; Li, F.; Zhao, Q.; Liu, B.; Huang, W. *Adv. Funct. Mater*. **2013**, *23*, 3268–3276.

(15) (a) Tang, T. S.-M.; Leung, K.-K.; Louie, M. -W.; Liu, H.-W.; Cheng, S.-H.; Lo, K. K.-W. *Dalton Trans*. **2015**, *44*, 4945–4956. (b) Qiu, K; Liu, Y.; Huang, H.; Liu, C.; Zhu, H.; Chen, Y.; Ji, L.; Chao, H. *Dalton Trans*. **2016**, *45*, 16144–16147.

(16) Ye, R. -R.; Tan, C. -P.; Jia, L. -N.; Mao, Z. -W. *Dalton Trans*. **2016**, *45*, 13042–13051.

(17) (a) Lo, K. K. -W.; Zhang, K. Y. *RSC Adv*. **2012**, *2*, 12069–12083. (b) Stacey, O. J.; Pope, S. J. A. *RSC Adv*. **2013**, *3*, 25550–25564.

(18) Cao, J.-J.; Tan, C.-P.; Chen, M,-H.; Wu, N.; Yao, D.-Y.; Liu, X.-G.; Ji, L.-N.; Z, Mao,-W. *Chem. Sci*. **2017**, *8*, 631–640.

(19) Qiu, K.; Ke, L.; Zhang, X..; Liu, Y.; Rees, T. W.; Ji, L.; Diao, J.; Chao, H. *Chem. Commun*. **2018**, DOI: 10.1039/x0xx00000x.

(20) (a) Wang, C.; Lystrom, L.; Yin, H.; Hetu, M.; Kilina, S.; McFerland, S. A.; Sun, W., *Dalton Trans*. **2016**, *45*, 16366–16378. (b) Sun, Y.; Joyce, L. E.; Dickson, N. M.; Turro, C. *Chem. Commun*. **2010**, *46*, 2426–2428.

(21) LeBel, G. P.; Ischiropoulos, H.; Bondy, S. G. *Chem. Res. Toxicol*. **1992**, *5*, 227–231.

Papers Presented at Conferences (Posters/Oral)

1. Fluorimetric and Colorimetric Detection of a Nitroaromatic Explosive Using Squaraine Dye. D. S. Philips, **Sudheesh K. V**, and A. Ajayaghosh*

   Paper presented at a National Conference on “Advance Technologies for Material Processing and Diagnostics” organized by Indian Society of Analytical Scientists (ISAS) on September 18-20, 2014, Eranakulam, Kerala, India. (Best Poster Award)

2. A Squaraine Based Sensor for the Detection of Atmospheric CO_2, Biomolecule and Nitroaromatic Compound. D. S. Philips, **Sudheesh K. V**, C. H. Suresh and A. Ajayaghosh*

   Paper presented at ANASAT-2015, a National Conference of “Analytical Science for Technological Excellence an Environmental Sustainability” organized by Indian Society of Analytical Scientists (ISAS) on September 24-26, 2015, Munnar, Kerala, India. (**Best Poster Award**).

3. Fluorescence Imaging of Lysosomal Zn(II) Ion and the Apoptosis Study in Cancer Cells Using an Aggregation Based Probe. **Sudheesh K. V** and A. Ajayaghosh*

   Paper presented at a National Conference on “Critical and Strategic materials for Advanced Technologies” organized by rare Earths Association of India (REAI) on March 09-11, 2017, Munnar, Kerala, India. (**Best Poster Award**).

4. Cyclometalated Ir(III) Complex as a Lysosome Targeted Potential Sensitizer for Photodynamic Theerapy and Bioimaging. **Sudheesh K. V** and A. Ajayaghosh *

   Oral presentation at a National Conference On “Innovations and Emerging Advances in Analytical Science and Technology” ” organized by Indian Society of Analytical Scientists (ISAS) on February 8-10, 2018, Kumarakam, Kottayam, Kerala, India. (**Best Oral Presentation Award**)

List of Publications from the Thesis

1. pH-Controlled Nanoparticles Formation and Tracking of Lysosomal Zinc Ions in Cancer Cells by Fluorescent Carbazole–Bipyridine Conjugates. **Sudheesh, K. V**.; Joseph, M. M.; Philips, D. S.; Samanta, A.; Maiti, K. K.; Ajayaghosh, A. *ChemistrySelect* **2018**, *3*, 2416 – 2422
2. A Cyclometalated Ir(III) Complex as Lysosome Targeted Photodynamic Therapeutic Agent for Integrated Imaging and Therapy in Cancer Cells. **Sudheesh, K. V**.; Jayaram, P. S.; Samanta, A.; Bejoymohandas, K. S.; Jayasree, R. S.; Ajayaghosh, A. *Chem. Eur. J.* **2018** (Accepted article. DOI: 10.1002/chem.201801918).
3. Lysosome Targeting Cyclometalated Ir(III) Complexes with Extended π-Conjugation as Potential Sensitizer for Photodynamic Therapeutic Applications. **Sudheesh, K. V**.; Jayaram, P. S.; Samanta, A.; Jayasree, R. S.; Ajayaghosh, A. (under preparation)

List of Publications from Other Related Works

4. A protein–dye hybrid system as a narrow range tunable intracellular pH sensor. Anees, P.; **Sudheesh, K. V**.; Jayamurthy, P.; Chandrika, A. R.; Omkumar, R. V.; Ajayaghosh, A. *Chem. Sci*. **2016**,*7*, 6808-6814.
5. An Unsymmetrical Squaraine Dye based Chemical Platform for Multiple Analyte Recognition. Philips, D. S.; Ghosh, S.; Sudheesh, K. V.; Suresh, C. H.; Ajayaghosh, A. *Chem. -Eur. J*. **2017**, *23*, 17973-17980.